



Durham E-Theses

M.A.R.S.: The momentum spectrum of muons to 800 GeVc in the vertical direction

Whalley, M. R.

How to cite:

Whalley, M. R. (1974) *M.A.R.S.: The momentum spectrum of muons to 800 GeVc in the vertical direction*, Durham theses, Durham University. Available at Durham E-Theses Online: <http://etheses.dur.ac.uk/8234/>

Use policy

The full-text may be used and/or reproduced, and given to third parties in any format or medium, without prior permission or charge, for personal research or study, educational, or not-for-profit purposes provided that:

- a full bibliographic reference is made to the original source
- a [link](#) is made to the metadata record in Durham E-Theses
- the full-text is not changed in any way

The full-text must not be sold in any format or medium without the formal permission of the copyright holders.

Please consult the [full Durham E-Theses policy](#) for further details.

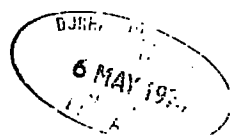
M.A.R.S.-The Momentum Spectrum of Muons to
800 GeV/c in the Vertical Direction

by

M.R. Whalley, B.Sc.

A Thesis submitted to the
University of Durham for the
Degree of Doctor of Philosophy

March, 1974



ABSTRACT

The sea-level vertical muon differential momentum spectrum has been measured using the Durham spectrograph MARS in the region 20 GeV/c to 500 GeV/c. The instrumental biases have been studied in detail and allowances made for the particle detector inefficiencies to render to measurement absolute.

A simple muon production and propagation model has been used to predict the pion and kaon production spectra from the muon spectrum measurements. It has been found impossible to fit, with any degree of significance, a constant exponent power law pion and kaon production spectrum, having a reasonable value of the K/ π ratio (0.15). A better fit is obtained if the exponent is allowed to increase with momentum, and in particular a model with two values of the exponent has been fitted.

The muon spectrum has been extrapolated both above and below 500 GeV/c and 20 GeV/c respectively, and at low momenta good agreement is found with the recent "form fit" of De et al. (1972). The present results are compared with previous and contemporary measurements of the muon spectrum with the conclusion that there is no evidence, from other recent measurements, that they are incorrect. Comparison with surveys of indirect measurements at higher energies however suggest that the muon spectrum cannot continue in this enhanced fashion much beyond 1000 GeV.

Finally an absolute integral rate experiment has been performed using MARS as a range spectrograph, and the intensity above 7.12 GeV/c is found to be in agreement with a previous similar measurement made with the instrument. Further it is concluded that the intensity at this momentum is in agreement with the extrapolation of the differential spectrum measurements below 20 GeV/c.

PREFACE

The work presented in this thesis represents that carried out in the period 1970-1973 while the author was a research student under the supervision of Dr. M.G. Thompson in the Cosmic Ray Group of the Physics Department of the University of Durham.

The MARS spectrograph was in an advanced stage of construction when the author joined the group in 1970, most of the electronic circuitry and the magnets themselves having been constructed. Since then the author has played a part in the construction and running of the instrument, for the purpose of the work described in this thesis, and has been solely responsible for the analysis and interpretation of the experimental data relating to the muon spectrum. The work described in this thesis in fact represents the first stage of the MARS spectrograph programme, the measurements having been made with the "low momentum" system which is eventually to be used as the momentum selector system for the "high momentum" (up to 5000 GeV/c) measurements.

Preliminary results from these analyses have been presented at the XIII International Cosmic Ray Conference in Denver, U.S.A., (Ayre et al., 1973). The work in this thesis represents further analyses and interpretation of the data.

CONTENTS

	Page
ABSTRACT	i
PREFACE	ii
CHAPTER 1 INTRODUCTION	
1.1 Historical Background	1
1.2 Importance of Cosmic Ray Studies	2
1.3 The Primary Spectrum	3
1.4 Nuclear Interactions	5
1.5 Propagation through the Atmosphere	6
1.6 Absolute Determinations of the Spectrum	7
1.7 The MARS Experiment	8
CHAPTER 2 THE MARS SPECTROGRAPH	
2.1 Introduction	11
2.2 General Description	11
2.3 The Magnetic Field	14
2.3.1. The Magnetic Blocks	14
2.3.2. Measurements of the Field	15
2.3.3. The Trajectory of Muons in the Magnetic Field	15
2.4 The Scintillation Counters	16
2.5 The High Voltage Pulsing System	16
2.6 The Momentum Selector Trays	17
2.7 The Momentum Selector	19
2.8 RUDI	19
2.8.1. Introduction	19
2.8.2. Definition of Deflection	19
2.8.3. Operation of RUDI	21
2.8.4. Final Output from RUDI	25
2.9 Checking the Electronic Circuits	26
2.10 The Role of the Author and the Present Experiment	27
CHAPTER 3 THE MOMENTUM SPECTRUM - METHOD OF DATA ANALYSIS	
3.1 Introduction	28
3.2 Factors Involved in Calculating the Trial Deflection Spectrum	28
3.2.1. The Momentum - Deflection Relationship	28
3.2.2. The Trial Momentum Spectrum	30

	page	
3.3	Corrections to the Spectrum	30
3.3.1.	The Effect of Multiple Coulomb Scattering	30
3.3.2.	The Overall Spectrograph Acceptance	31
3.3.3.	Rejection of Events	31
3.4	The Category Acceptance Function	40
3.4.1.	Definition	40
3.4.2.	Method A	41
3.4.3.	Method B	48
3.4.4.	Comparison of Methods A and B	49
3.5	Summary	50
CHAPTER 4	THE MOMENTUM SPECTRUM - RESULTS	
4.1	Introduction	51
4.2	The Deflection Spectrum	52
4.3	Expected Rates and Mean Momenta	52
4.4	Full-Field Runs	53
4.4.1.	Introduction	53
4.4.2.	Comparison of Observed Data with Expectation	54
4.4.3.	The Measured Spectrum	55
4.4.4.	The Effect of Varying the Burst Correction	55
4.5	Sources of Error	56
4.5.1.	Tray Alignment	56
4.5.2.	Other Sources of Error	59
4.5.3.	Combination of all Non-Statistical (Systematic) Errors	61
4.6	The Maximum Detectable Momentum	62
4.7	The Best Estimate of the Spectrum	63
CHAPTER 5	DERIVATION OF THE PION AND KAON PRODUCTION SPECTRA	
5.1	Introduction	66
5.2	Theoretical Model	67
5.2.1.	Introduction	67
5.2.2.	The Pion Spectrum in the Atmosphere	67
5.2.3.	The Muon Production Spectrum	69
5.2.4.	The Muon Spectrum at Sea Level	71
5.2.5.	The Effect of Including Kaon Decay	72
5.3	Comparison of the Predicted and Measured Muon Spectrum	73
5.3.1.	Method of Comparison	73
5.3.2.	All Pion Source	73
5.3.3.	Inclusion of Kaons	76

	Page
5.4 The Integral Intensity above 500 GeV/c	78
5.5 Conclusion	79
 CHAPTER 6 COMPARISON WITH OTHER RESULTS	
6.1 Introduction	80
6.2 Direct Determinations of the Muon Spectrum	81
6.2.1. Introduction	81
6.2.2. The Standard Comparison Spectrum	82
6.2.3. The Earlier Durham Measurements	83
6.2.4. The Work of the Nottingham Group	86
6.2.5. The Spectrum of the Kiel Group	88
6.2.6. The Dagapur Spectrum	90
6.2.7. Spectrum Measurements Presented at the Denver Conference	91
6.2.8. Conclusion from the Direct Measurements	93
6.3 Indirect Determinations of the Muon Spectrum	94
6.4 Summary	96
 CHAPTER 7 THE ABSOLUTE RATE EXPERIMENT	
7.1 Introduction	98
7.2 Reduction of the Magnetic Field to Zero	99
7.3 Measurement of the Efficiency of the Scintillation Counters	100
7.4 Measurement of the 3-fold Coincidence Rate	102
7.5 Absorbing Material in the Muon Beam	102
7.6 Corrections due to Instrumental Effects	104
7.6.1. Multiple Coulomb Scattering	104
7.6.2. Non-Vertical Angles of Incidence	107
7.6.3. Air Shower Triggers	108
7.6.4. Short Pulses in the Coincidence Unit	108
7.6.5. Random Coincidences	108
7.7 The Final Rate	109
7.8 Discussion	109
 CHAPTER 8 CONCLUSION AND FUTURE WORK	
8.1 Conclusion	112
8.2 Future Work	115
 APPENDIX A THE TRAJECTORY OF MUONS THROUGH THE MAGNET BLOCKS	116

	Page
APPENDIX B ; CALCULATION OF THE SPECTROGRAPH ACCEPTANCE	118
APPENDIX C MULTIPLE COULOMB SCATTERING IN THE IRON	121
ACKNOWLEDGMENTS	124
REFERENCES	125

CHAPTER 1

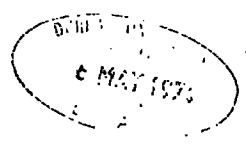
INTRODUCTION

1.1 Historical Background

The first indication of radiation from outside the earth came, at the beginning of the century, with the observation of a small conductivity in gases at electric field strengths at which they should have exhibited perfect insulation. The theory that this was due to natural radioactivity from the earth was disproved by the balloon borne experiments of Hess (1912) who showed that the ionization, measured with an electroscope, increased with altitude above certain height. To account for this, Hess proposed the revolutionary theory that it was due to radiation from outer space, later to be known as the 'Cosmic Radiation'.

At the time the radiation was assumed to be γ - rays, these constituting the only penetrating radiation known. Measurements made on the variation of the intensity at different geomagnetic latitudes, (the latitude effect), showed that the radiation was predominantly charged (Bothe and K lhorster, 1929) and a study of the rates of arrival from an easterly and westerly direction, (east-west effect), indicated a surplus from the latter, showing the greater proportion to be positively charged (Johnson and Street, 1933). The interpretation of both these effects is based upon the interaction of the charged particles with the earth's magnetic field, and the theory of St rmer of charged particles in a magnetic field has been extensively used in this direction (Johnson, 1938).

That all these particles could be electrons was doubtful when it was found they could be classified into hard and soft components on their ability to penetrate 15 cm of lead. The soft component was indeed shown to be electrons but the hard component was much too penetrating at the energies measured, using range-energy relations with cloud chambers, and they were subsequently identified as being particles intermediate in mass between



protons and electrons, and were named mu-mesons. Later the term meson was dropped when they were found not to belong to this class of elementary particles, and they were re-termed muons.

The study of cosmic radiation progressed rapidly over the next few decades. The bulk of the primary radiation (i.e. the radiation actually incident on the earth's atmosphere) was found to be protons which were observed to interact with atmospheric nuclei leading ultimately to the muons originally detected. Many new particles were discovered in this secondary radiation, notably the positron (Anderson, 1932), the antiparticle of the electron predicted by the Dirac theory, and the pion (Lattes et al., 1947) which proved to be the particle proposed by Yukawa to be responsible for the nuclear 'glue' which binds together nucleons in nuclei. Other more exotic particles, such as a so-called strange particle, the Λ^0 , were also discovered (Rochester and Butler, 1947).

1.2 Importance of Cosmic Ray Studies.

The study of cosmic rays naturally divides into two parts, the study of the actual primary radiation, and the study of the secondary radiation produced in the interactions of the primaries with the atmosphere. Investigation of the first is mainly carried on with detectors flown high in the atmosphere whilst the second is more able to be studied at ground level. In the second category there are again two main divisions, firstly the study of extensive air showers (electromagnetic cascades in the atmosphere emanating from the π^0 particles produced in the nuclear interactions high in the atmosphere), and secondly the study of individual particles, the most abundant being the muon; such a study being the subject of this thesis.

The properties of the muons generally measured are their momentum spectrum and charge ratio (the ratio of positive to negative particles), which are important for two main reasons. Firstly to study the properties of the muon itself, e.g. its electromagnetic interactions with matter, and secondly to combine the information with the cosmic ray primary spectrum and hence be able to infer something about the nuclear physics occurring in the

interactions of the primary nucleons with the atmospheric nuclei. Conversely, if the nuclear physics is known, then predictions can be made concerning the primary cosmic ray spectrum. In order to understand what is involved, consider first what is known, to date, about the various ingredients of the problem, that is the primary spectrum, the nuclear interactions of the particles, and the propagation of the secondary particles, produced in the interactions, through the atmosphere.

1.3 The Primary Spectrum

At energies $\sim 10^{10}$ eV where satellite measurements have been possible the composition of the radiation is found to be $\sim 88\%$ protons, $\sim 11\%$ helium nuclei, and $\sim 1\%$ heavier nuclei. A small proportion of other particles such as electrons and γ -ray quanta have also been detected, and it is known that there is a large flux of neutrinos which prove extremely difficult to detect due to their low cross section for interaction. Iron is the most abundant of the heavier nuclei though nuclei as large as uranium have been detected (Fowler et al., 1967). Comparison with universal abundances of the elements in the universe shows that there is an excess of the lighter elements (Li, Be, B) in cosmic rays, which are believed to come from the fragmentation of the heavier nuclei in passing through the small amount of matter ($\sim 4 \text{ g cm}^{-2}$) from their source to the earth. The actual source of cosmic radiation is still the subject of much speculation, the most generally acceptable theory being that they originate in supernova (e.g. the Crab Nebula), one of the difficulties with this being in the explanation of the attainment of the highest energies observed, ($\sim 10^{20}$ eV). Up to 10^{15} eV there does not seem to be any evidence for a change in composition.

Greisen (1965) has produced an integral energy spectrum which is shown in figure 1.1. The flux is found to decrease very rapidly with energy and to be isotropic at energies in excess of $\sim 2 \times 10^{10}$ eV. Measurements up to 10^{12} eV have been made using balloon and satellite borne detectors and as such are direct. At higher energies the measurements are generally less direct being based upon measurements of secondaries at sea level or mountain

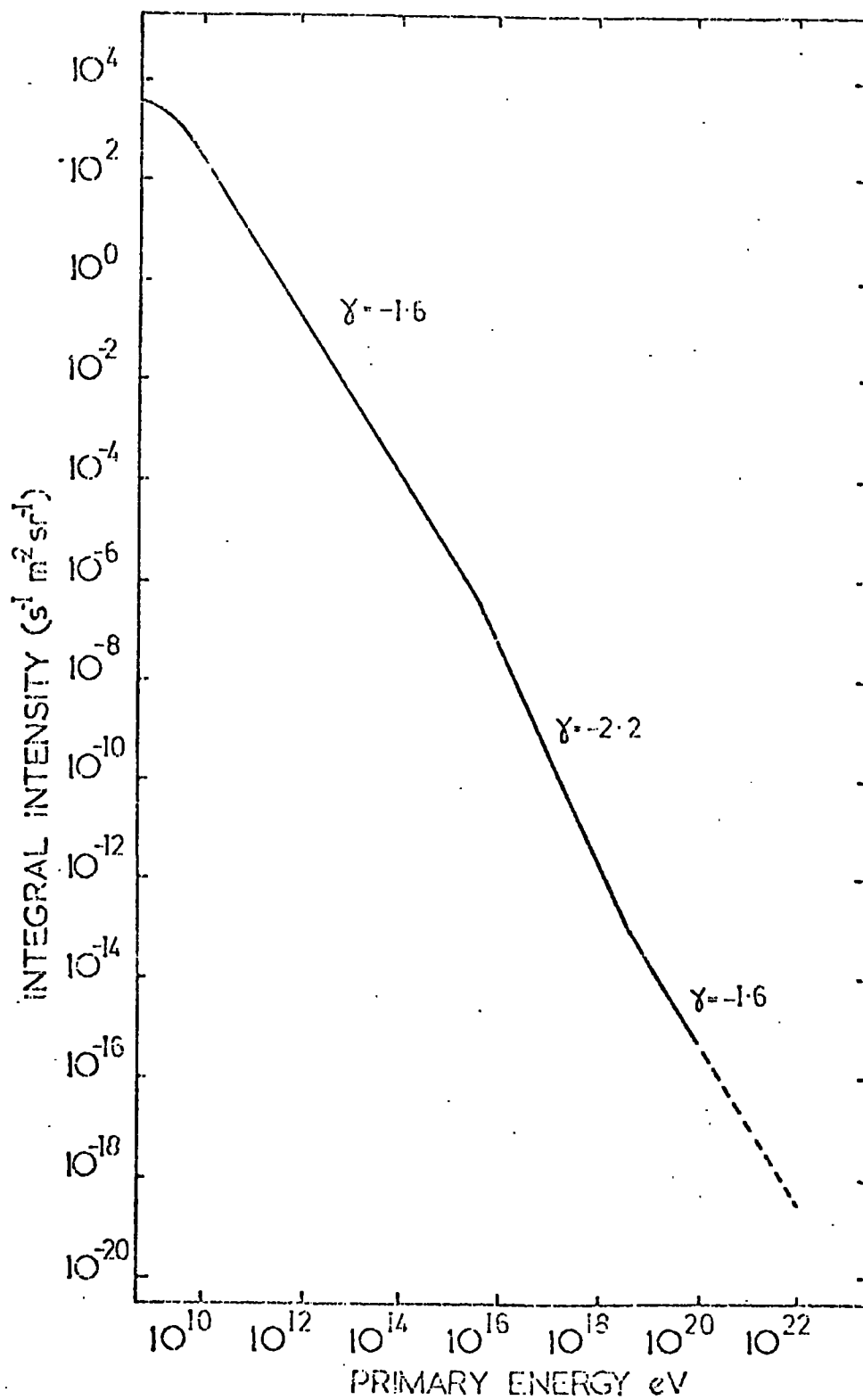


FIGURE 1.1 The Primary Cosmic Ray Spectrum (after Greisen, 1965).

altitudes. Some direct measurements have been made above 10^{12} eV with the PROTON series of satellites (Grigorov et al., 1971) but with results which so far have not met with universal acceptance, and which seem to give a steeper slope to the integral spectrum ($\gamma \sim 1.7$) with sharp steepening of the proton component above 10^{12} eV, a result which is contrary to the constancy of the composition. The experiments of Ryan et al. (1972), again with satellite detectors, also give a steeper slope (~ -1.75) in this region, though without the fall off of the proton component. At the highest energy, measurements are made from observations on extensive air showers, in general counting the number of particles. Measurements made near maximum shower development are the best, since there is least dependence on the interaction model used at that point, and it is found that the number of particles is roughly proportional to the primary energy, the absolute calibration depending upon the model used.

Below $\sim 3 \times 10^{15}$ eV Greisen gives the integral intensity as $10^{-4} (10^{14}/E)^{1.6} \text{ s}^{-1} \text{ m}^{-2} \text{ sr}^{-1}$ at which energy there is a dramatic change in slope from -1.6 to -2.2 , the intensity thereafter being given by $2 \times 10^{-10} (10^{17}/E)^{2.2} \text{ s}^{-1} \text{ m}^{-2} \text{ sr}^{-1}$. This change in slope is generally believed to be due to the inability of the galactic magnetic fields to contain the various types of particles as their rigidities are exceeded. At around 3×10^{18} eV the slope is again seen to revert back to -1.6 the intensity being given by Greisen as $4 \times 10^{-16} (10^{20}/E)^{1.6} \text{ s}^{-1} \text{ m}^{-2} \text{ sr}^{-1}$. Such an increase was believed to be due to an extragalactic component but since the discovery of the 2.7°K radiation in intergalactic space (Roll and Wilkinson, 1967), and as a consequence of the onset of photomeson interactions at $\sim 6 \times 10^{19}$ eV, a sharp cut off in the spectrum has been predicted (Greisen, 1966) at $\sim 10^{20}$ eV. Several primaries have been indirectly observed with such large energies (e.g. Suga et al., 1971) but due to the obvious difficulty in measuring such large air showers the results are in question. The point of this is that if primaries are observed with energies $> 10^{20}$ eV then they are most likely galactic and possible production mechanisms capable of creating these high energies have been cited as quasars or pulsars.

1.4 Nuclear Interactions

A cosmic ray nucleon on colliding with an atmospheric nucleus may interact producing secondary particles (mainly pions and kaons). The nucleon itself may or may not undergo charge exchange (i.e. a proton becoming a neutron or vice-versa), and on average will lose half its energy. Other particles such as the so called strange particles or particle-antiparticle pairs may also be produced but with such insignificant probability as to be negligible. Accelerators provide the best method for studying these interactions and so far the maximum energy attained is that of the CERN I.S.R. (intersecting storage rings), which have reached an equivalent laboratory energy of 1.5×10^{12} eV. The I.S.R. utilizes two colliding proton beams, and hence suffers from the disadvantage that only proton-proton interactions can be studied. For cosmic ray purposes neutron interactions, and nucleon-nucleus interactions are also of importance. Another accelerator which operates at fairly high energies is the conventional N.A.L. accelerator in the U.S.A.. This can accelerate protons to energies of 3×10^{11} eV, and has the advantage that different materials can be used as target material, which is closer to the nucleon-nuclei collisions occurring in the atmosphere.

Empirical models of nuclear interactions have been formulated in the past, the most extensively used (e.g. de Beer et al., 1966) being the C.K.P. model (Cocconi, Koester and Perkins, 1966), which was based upon accelerator measurements from the conventional CERN machine up to 3×10^{10} eV, and assumed an exponential distribution of energy among the secondary particles with some mean energy depending upon the incident particle energy. This model predicted an $E_p^{\frac{1}{4}}$ dependence of secondary particle multiplicity on the incident energy E_p . Modern ideas are along the lines of scaling (Feynman, 1969), which assumes a limiting shape to the energy distribution when the energy is expressed in the parameter x , which represents the actual energy divided by the maximum energy that the secondary could have. Thus x

varies between 0 and 1. A logarithmic dependence of multiplicity upon energy is predicted by this model. Some support for scaling has come from CERN I.S.R. results (see review by Jacob, 1973) though attempts to reconcile it with certain cosmic ray measurements, e.g. the charge ratio of muons at sea level, do not seem to be quite so successful, (Hume et al., 1973).

However what is becoming clear is that accelerator results are now approaching the energy regions where in co-operation with cosmic ray results they may produce some interesting ideas both as regards the nuclear physics, and the primary spectrum of the cosmic rays themselves.

1.5 Propagation through the Atmosphere

As indicated, the most important particles produced in the interactions are the pions and kaons, particularly those charged, since they potentially may decay into muons. The shape of the muon spectrum at sea level depends upon the way in which these particles propagate through the atmosphere. Apart from decaying into muons, the pions and kaons can also interact and hence be lost to the cause of muon production. This competition between interaction and decay depends upon the angle of incidence of the particle trajectory through the atmosphere, and upon the relevant energies involved. The angular dependence arises because of the density per unit path length decreasing at large angles and hence the interaction probabilities decreasing thus allowing more pions and kaons to decay into muons. This is the so called "Sec ϑ " enhancement at large angles. In opposition to this we have the fact that as the energy increases the cross section for nuclear interaction also increases, hence at high energy the muon intensity will decrease due to this increasing probability of an interaction. At very low energies the muon intensity also decreases due to the probability of the muon decaying into an electron. Due to the different properties of the pion and kaon, particularly their mass, at high energies and at large angles the muon spectrum becomes sensitive to the ratio of kaons to pions at production. Cosmic ray measurements of this ratio have been made in the past by comparing the spectrum at large angles with that in the vertical direction (e.g. Osborne, 1966) with the result that the ratio is found to lie between

0 and 40%. The uncertainty basically comes from the statistical uncertainty on the vertical spectrum measurements in the energy region >100 GeV where the spectrum is sensitive to the K/π ratio, and this provides another reason for studying the vertical muon spectrum. The I.S.R. measurements seem to indicate a K/π ratio of 15% in this energy region (bertin et al., 1972). In theory it should be possible with sufficient statistical precision, to measure the K/π ratio from the vertical spectrum alone, particularly at very high energies. However, so far no experiments have been reported which have had sufficient precision to enable this to be done.

A recent suggestion, which in part led to the building of several high energy cosmic ray muon spectrographs was that of the Utah group (Bergeson et al., 1963), who proposed from their observations, that there was some process by which muons were being produced directly from the primary interactions and not via pion or kaon production. The evidence for this X-process has since been disproved by the same group after modifications to their underground apparatus. However, as stated earlier, the effect did lead to the construction of several large spectrographs, of which the subject of this thesis is one, and the construction of which should prove to be well justified in other fields apart from the Utah effect.

1.6 Absolute Determination of the Spectrum

In order to be able to make a satisfactory comparison between the predicted primary spectrum and that observed, and consequently make some deductions about the nuclear interaction model assumed, it is necessary to know the absolute value of the predicted spectrum. This of necessity entails an absolute determination of the muon spectrum. In many previous experiments (e.g. Hayman and Wolfendale, 1962), workers have been unable to ascertain the absolute value of efficiencies of their apparatus, particularly using geiger tubes, or cloud chambers. Instead it had become practice to normalise the measured spectrum to some previously established value, using the differential point at 1 GeV/c as given by Rossi (the so called Rossi point), or to the integral intensity of Greisen at 0.3 GeV/c (the Greisen

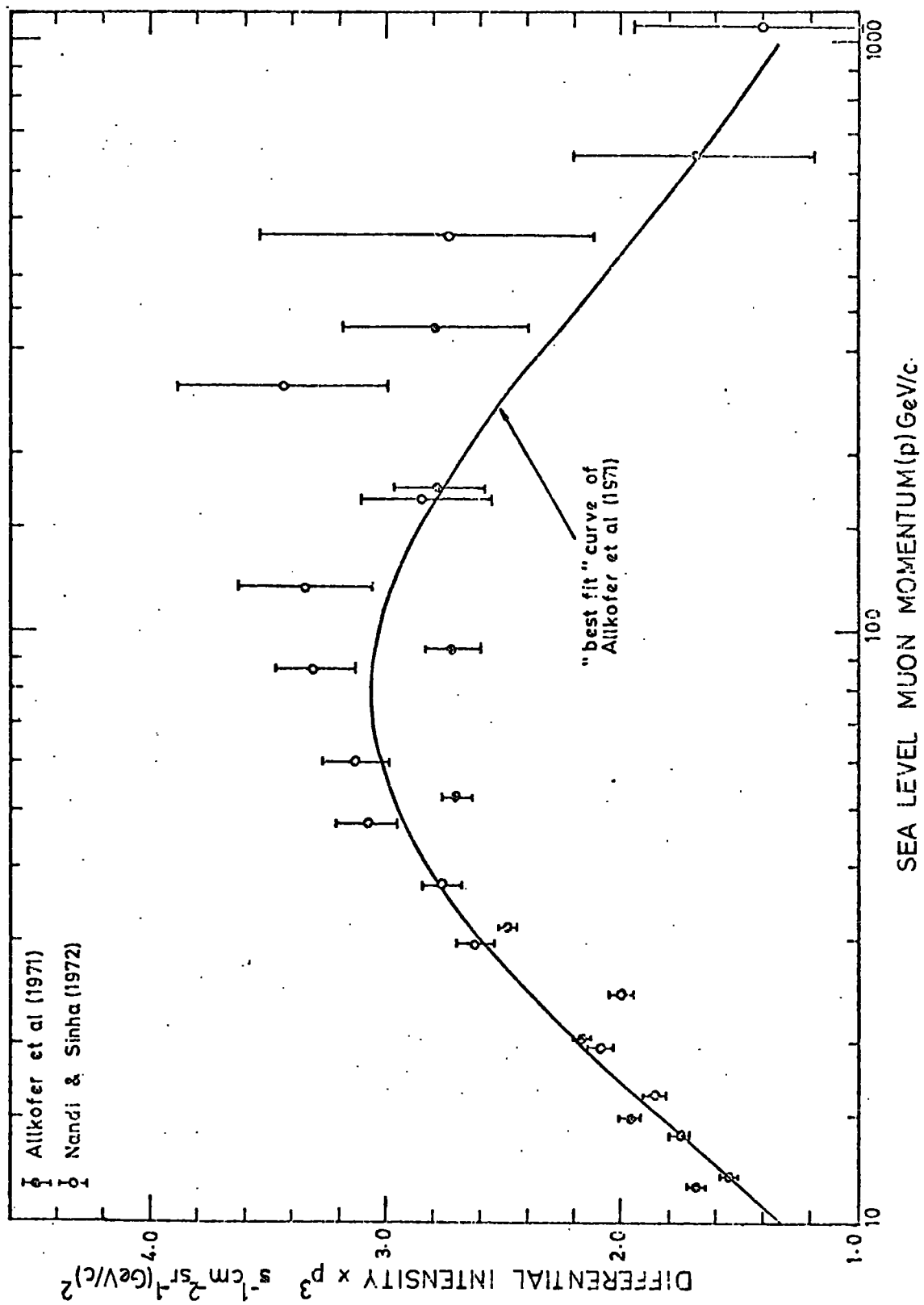


FIGURE 1.2 Two Recent Measurements of the Muon Sea Level Spectrum.

point). Recently a number of measurements, prompted by the work of Allkofer et al. (1970), have shown that the Rossi point is probably underestimated by $\sim 20\%$. This underestimation has been attributed to the scattering effect in the apparatus.

Another problem with normalisation is that if the measured spectrum does not happen to have energy values in the region of a previously established point, then it is necessary to normalise to some point on a different spectrum which has itself been normalised at yet a further point, thereby probably introducing systematic errors via the intermediate spectrum. It is more preferable if a spectrum can be attributed an absolute value in its own right. In this present work an attempt has been made to make the spectrum measurements absolute. Other absolute measurements have also been made in the last few years by several workers (e.g. Allkofer et al., 1971). The results of this, together with the recent determination by Nandi and Sinha (1972), are shown in figure 1.2 where they are plotted in terms of $P^3N(p)$. Also shown is the best fit line of Allkofer, which was fitted to data from 0.2 to 1000 GeV/c, assuming a constant exponent of the pion production spectrum and no kaon production. As can be seen the precision of these measurements is poor for >100 GeV/c and generally there is disagreement between the two even down to 20 GeV/c.

The present experiment, even though it does not extend the energy range covered at all, does increase the statistical accuracy in the higher energy regions quite appreciably, as well as doing away with the aforementioned problems of the absolute value. Also contained in this thesis are the results of an absolute integral rate experiment at ~ 7 GeV/c.

1.7 The MARS Experiment

In 1968 construction began on the 5000 GeV magnetic automated research spectrograph (MARS) at the University of Durham. Since that date, building has been in progress, and at various stages during the construction experiments have been performed with the apparatus as it stood at the time. The first of these experiments was in 1970 when events were photographed using the newly

installed flash-tube trays. This was primarily intended to test the various parts of the spectrograph, and preliminary results on the spectrum and charge ratio were published at the 1971 Cosmic Ray Conference at Hobart, Tasmania (Ayre et al., 1971(a)). Also from these, and other photographed events, an experiment was performed on the electromagnetic interactions of the muon in the iron magnet blocks, (Gruppen et al., 1972).

For a description of the spectrograph see Chapter 2, where it will be explained MARS consists of two momentum determining systems. One is the low resolution system which forms part of the instrument's momentum selection system, but which also provided the opportunity of spectrum and charge ratio measurements, before the instrument was completed. The results from this part of the experimental programme are the main subject of this thesis. The other momentum determining system is used for measuring the energies of the high energy particles, and at the time of writing has only just begun to operate, and it will be some time before results start to emerge from this high resolution system. Since MARS consists of a large mass of iron it was also possible, as mentioned, to do an absolute rate experiment; that is to measure the integral muon rate above the operative cut-off energy of the iron absorber. The results of one of these absolute rate experiments have also been presented at the Hobart Conference (Ayre et al., 1971(b)). As there was some disagreement between these results and those of other workers, notably Allkofer, it was decided at the beginning of 1973 to repeat the experiment completely independently. The results of this repeated experiment are presented in this thesis where it is concluded that in fact the previous measurements were correct.

The interpretation of the data from the low resolution system as regards the momentum spectrum have been the responsibility of the author and comprise the main body of this work. Preliminary results were presented at the Denver Conference on the spectrum (Ayre et al., 1973), since then the data have been re-analysed in greater detail, particularly with regard to the flash-tube efficiencies, and the momentum-deflection relationship. The conclusions reached are fundamentally the same as those in the above

publication but the numerical values will be found to be slightly different.

An important point which must be realised when considering the present work is that the MARS apparatus was not in fact designed for this experiment, and that this is only a very small part of the whole project. The spectrograph was designed to have a maximum efficiency in the very high energy region ~ 5000 GeV., and in this high energy region the analysis techniques will be quite different. However, due to the great statistical accuracy which could be obtained in the ~ 100 GeV region, and because there is some disagreement as to the shape and absolute height of the spectrum in this energy region, it was decided to utilise MARS to measure this region of the spectrum. In fact difficulties arose not with the statistical errors on the points but rather with the interpretation of what exactly happened as the particles traversed the spectrograph. This is a problem which will occur in all very large spectrographs, in which the instrumental biases become considerable, and may go some way to explaining some of the discrepancies which have appeared between some recent measurements of the muon spectrum.

CHAPTER 2

THE MARS SPECTROGRAPH

2.1 Introduction

The MARS spectrograph has been described in several other publications (Ayre, 1971, Ayre et al., 1972 (a), (b)), consequently in this chapter only a very brief description will be given with references to the other works at appropriate places. Attention will be concentrated mainly upon those elements particularly relevant to the understanding of the part of the experiment to be described, i.e. the aforementioned low resolution system. For completeness, however, initially an overall picture of spectrograph will be given.

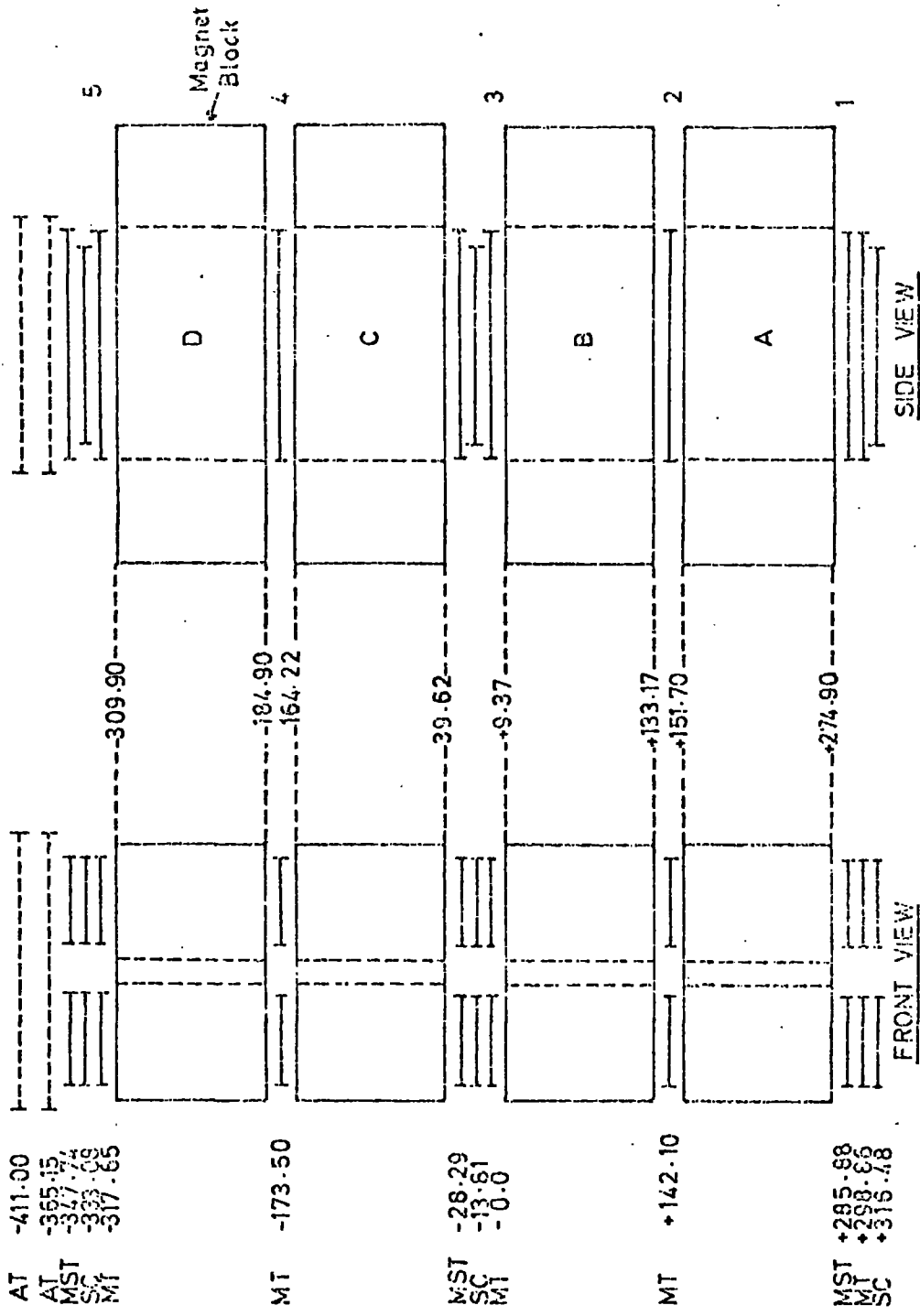
2.2 General Description

Figure 2.1 shows a front and side view of the spectrograph. In short MARS is a multilayer solid iron magnetic spectrograph consisting of four iron electromagnets, in the form of rectangular blocks, interleaved with particle detectors. The purpose of the magnets is to bend the particles track, the amount of bending being a measure of the particle's momentum, and the detectors are to locate this curved trajectory. As can be seen there are five detection levels containing the various detectors.

Essentially two types of detectors are employed :

- (a) Plastic (NE102A) scintillation counters to detect initially the passage of a muon through the spectrograph, (muons are justifiably assumed because of the great stopping power of the iron).
- (b) Neon flash-tubes to locate the trajectory of the muon.

The neon flash-tube, as introduced by Conversi and Cozzini (1955), consists of a long (~2m.) glass tube filled with neon gas. The passage of a charged particle through the gas causes ionization which on the application of a high voltage pulse across the tube (in this case ~10 kV



MST Momentum Selector Tray
 MT Measuring Tray
 SC Scintillation Counter

All dimensions are given in cm. and are accurate to 0.1cm.

FIGURE 2.1 The MARS Spectrograph.

for $\sim 3\mu\text{s}$) leads to a discharge along the tube, and the tube is said to have flashed. Two types of flash-tubes are used; (i) large diameter (~ 1.5 cm.) tubes located in the momentum selector trays, which as their name suggests are a part of the system for the selection of high momentum events, and comprise a part of the low resolution system, and (ii) small diameter (~ 0.55 cm.) tubes for the analysis of the high momentum events, and are contained in the so-called measuring trays. The small diameter tubes are able to locate the muon's trajectory to a much greater accuracy than the large diameter tubes, and hence form the high resolution system.

Figure 2.1 shows that the scintillation counters (SC) are located at the upper, middle, and lower levels, as also are the momentum selector trays (MST), whereas the measuring trays (MT) are located at each of the five levels. The reason for five measuring trays, when only three are strictly necessary to define the trajectory, is to combat the effect of the increasing probability of electrons accompanying the muon from the iron blocks, due to electromagnetic interactions of the muon in the iron, as the energy increases. An event is thus generally over-defined so that information can be 'lost' from up to two levels, but the event will still be useful. The m.d.m. (maximum detectable momentum) of the high resolution system with five measuring trays has been shown to be 5856 GeV/c (Ayre et al., 1972 (a)) and this only decreases to 1280 GeV/c with the worst possible combination of three trays (i.e. levels 1,2,3 or 3,4,5). Account of the variation of m.d.m. with tray configuration will have to be taken when the analysis of the high resolution system data is eventually made.

Also apparent from figure 2.1 is that the spectrograph comprises two separate halves, one set of detectors lying on the L.H.S. of the magnet blocks, and the other on the R.H.S. These are known as the blue and red sides respectively. Since flash-tubes have to be allowed time to recover (\sim seconds) between events, having two complete sets of detectors working independently means that whilst one side is recovering from the previous event, the other can still be operative, hence increasing the

overall collection rate.

With the detectors so far mentioned there is no facility for ascertaining the angle of the muon in the back plane, that is in the plane parallel to the magnetic field lines. For this purpose two other trays, the azimuthal trays (AT) are placed above the spectrograph, separated by ~45 cm., with the tube axes perpendicular to the magnetic field lines in each side of the spectrograph. The format of these trays is identical to those of the momentum selector, except that their width is very much larger, and the tubes are longer. Table 2.1 gives a brief description of the format of each of the different types of detector.

Finally the whole system is designed to be automatic and to this end the outputs from the flash-tubes are digitised. The method adopted is that of Ayre and Thompson (1969), and is described in detail in Ayre (1971). Briefly a small brass probe is placed in front of each flashtube and connected, through a resistor, to the input of an integrated circuit electronic memory. When a tube discharges a voltage pulse appears, due to the capacitative effect of the probe, at the input to the memory. The amplitude of the pulse is adjusted by means of a series resistor and sets the memory. There is a probe and memory for each tube. Both types of tube are digitised in the same way, different values of resistor being used to make the voltage compatible with that of the memories.

The information from the flash-tubes in the measuring trays and the azimuthal trays will be sent to an IBM 1130 computer for storage on magnetic disk, and then transferred to magnetic tape where it can be analysed at a later date on a large IBM 360 computer. The storing of the flash-tube data in the 1130 will take place only when a high momentum ($>200 \text{ GeV}/c$) is indicated by the momentum selector.

As remarked in chapter 1 the low resolution side of the system was originally designed to be the momentum selector alone. For this purpose the trajectory of the muon at each of the three M.S.T.'s is allocated to certain $\frac{1}{2}$ cm. cells, and the momentum selector ascertains whether or not

	SCINTILLATION COUNTER	MOMENTUM SELECTOR TRAY	MEASURING TRAY	AZIMUTHAL TRAY
NUMBER OF SUCH PER SIDE	3	3	5	2 (covering both the red and blue sides)
BASIC DETECTION ELEMENT	Plastic Scintillator. NE 102 A (75x176x5) cm.	Neon Flash-Tube. Int. diam. - 1.5 cm. Length - 200 cm.	Neon Flash -Tube. Int. diam. - 0.55 cm. Length - 200 cm.	Neon Flash -Tube. Int. diam. - 1.5 cm. Length - 250 cm.
GENERAL COMMENTS	Viewed by 4 photo- multipliers type 53AVP via triangular perspex light guides at each end (see fig 2.4).	4 layers containing 51 tubes each. Digitised. Tube pattern shown in fig 2.5.	8 layers containing 89 tubes each. Digitised. NOT USED IN PRESENT EXPERIMENT.	4 layers containing 118 tubes each Digitised.
SPECIFIC USE	Initial particle detection. Triggers rest of apparatus.	Initial low resolution momentum measurement for momentum selector and RUDI.	High resolution system. Data sent to IBM 1130 computer for analysis.	To measure angle in the back plane. Data sent to 1130.

TABLE 2.1 The Formats of the Detectors in MARS.

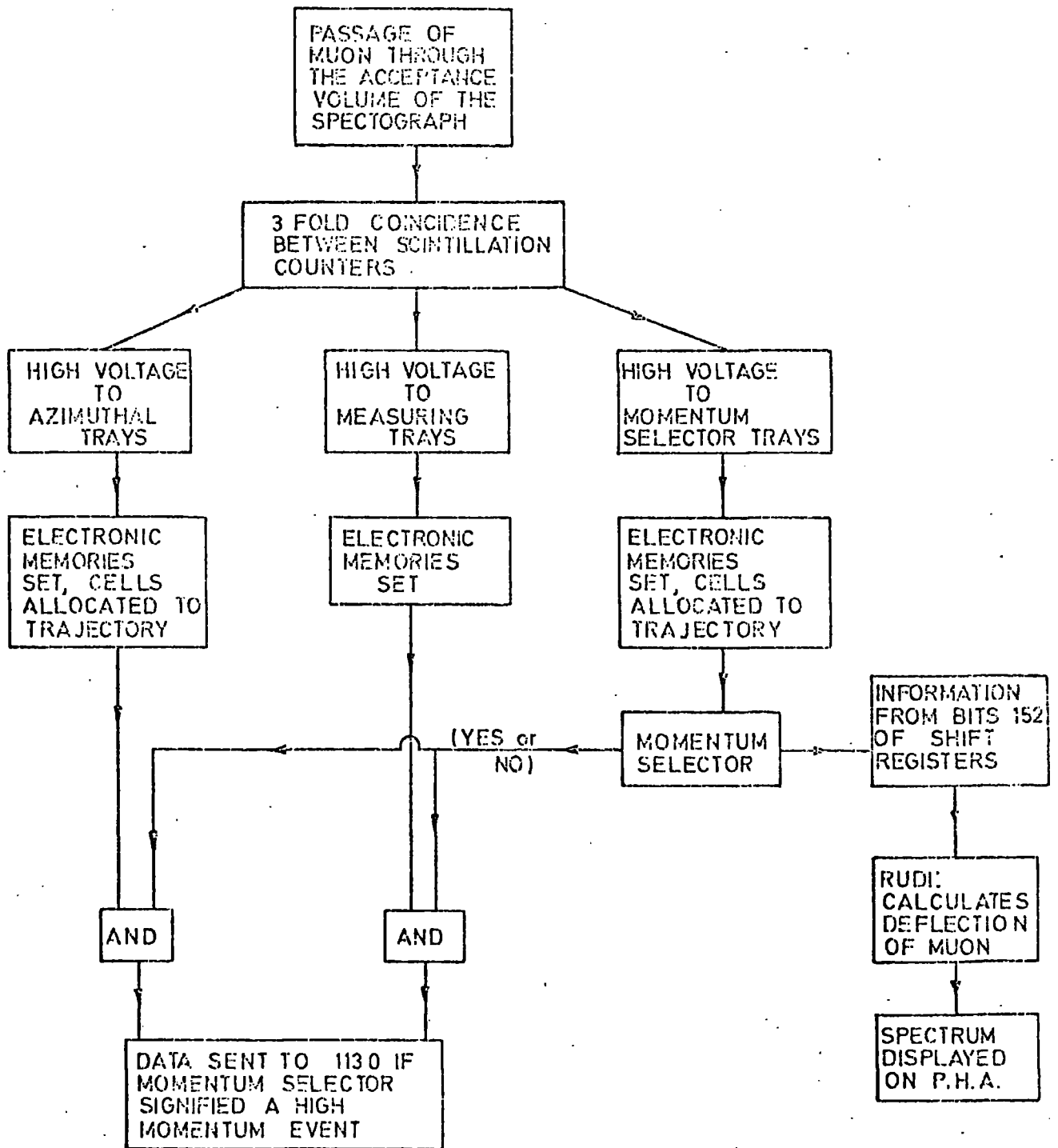


FIGURE 2.2 The Sequence of Events on the Passage of a Muon through the Spectrograph

any of these cells lie in a straight line, and hence is potentially a high momentum event. The event is only 'potentially' of high momentum since cells may be set off due to other particle tracks in the trays causing a low momentum event to appear to the momentum selector as one of high momentum. The important point of this method is that whilst pseudo-high momentum events may be signalled, no true high momentum events are lost, the pseudo-high momentum events being sorted out in the final analysis. The experiment which provides the main topic of this thesis uses the information contained in the cells corresponding to the muon track at each level, wherever possible, to find the momentum of the muon, and hence produce the momentum spectrum in the lower energy region ($<500\text{ GeV}/c$). In order to do this a device known as RUDI (restricted used digital instrument) was constructed which automatically takes the three cells from the momentum selector, and calculates the deflection of the particle, the output being stored in the memory of a multichannel analyser (PHA).

Figure 2.2 shows a flow diagram of the events which take place subsequent to the passage of a muon through the spectrograph assuming that it is still not paralysed by the previous event. The extreme R.H.S. of this diagram is important to what follows, and each of the relevant parts of the spectrograph are now considered in more detail.

2.3 The Magnetic Field

2.3.1 The Magnet Blocks

Figure 2.3 shows a diagram of one of the four magnet blocks. As can be seen they are of rectangular shape with a hole cut out of the centre. Each block comprises 78, $5/8$ " iron plates. Thick copper wire is wound around each arm of the magnet block as indicated producing, on the passage of a current through the windings, a toroidal magnetic field. The blocks are labelled A, B, C, and D from bottom to top, A and C being wired together in series as also are B and D. Each of these pairs are connected

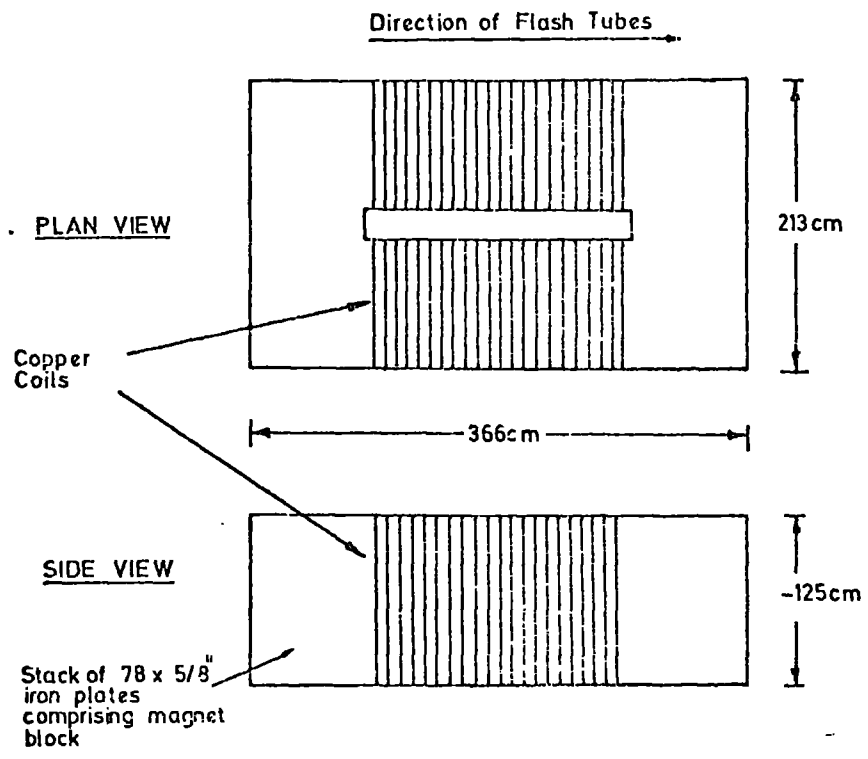


FIGURE 2.3 Plan and Side View of a Magnet Block.

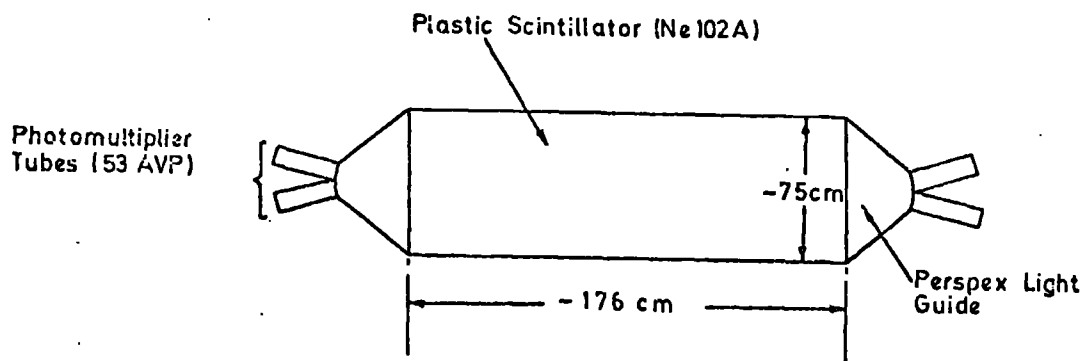


FIGURE 2.4 Plan View of a Scintillation Counter.

in parallel and driven by a 100 A x 100 V unstabilised D.C. supply. For a more detailed description see Ayre (1971).

2.3.2. Measurements of the Field

Two factors are important from the point of view of the spectrum measurement; (a) the exact magnitude of the field, and (b) how uniform it is over the sensitive region of the detectors.

In order to be able to answer (b), during the building of the magnets, holes were drilled and search coils placed at various positions in the blocks. The local field at these positions could then be found by measuring $\int Vdt$, when the magnetic field is reversed, using an X - Y plotter connected across the ends of the search coils. The average field in a block could also be measured in a similar way utilizing a large loop of wire around the entire arm of the magnet block. Using these methods it is found that the magnitude of the field is (16.3 ± 0.1) kG with a non-uniformity of $\pm 4\%$ over the sensitive region (Ayre, 1971). Since the non-uniformity is small, it may be neglected and the mean value of the field used.

The error quoted above on the magnitude of the field is based upon the analysis of several (25) measurements. Examination of the B-H curve for the magnet iron shows that a 10% variation in current at 50A will give rise to a variation of 1% in the field. Since it is known that the mains voltage varies by 6-7%, and the magnet power supply is unstabilised, it is thought that a more reasonable estimate of the error on the field is $(16.3 \text{ kG} \pm 1\%)$.

2.3.3 The Trajectory of Muons in the Magnetic Field

A particle of charge ze travelling with a velocity v in a magnetic field B is subject to a Lorentz force of magnitude :

$$|\text{Force}| = zevB \qquad 2.1$$

causing it to move in a circular trajectory. The inclusion of energy loss as the particle progresses changes the trajectory from circular

to spiral.

The equations, and method used to study the trajectory of the muon in the magnetic field are outlined in Appendix A.

2.4 The Scintillation Counters

As stated there are three scintillation counters in each side of the spectrograph; in the upper, middle and lower levels. Their construction is as indicated in table 2.1 and shown schematically in figure 2.4.

The outputs from the two diagonally opposite photo-multipliers are added together, and the resultant pulses passed through discriminators and a coincidence circuit producing an output when a particle has traversed the counter. The resultant pulses from each of the three counters are fed into a three-fold coincidence circuit which serves as the main trigger indicating the passage of a muon through the acceptance volume of the spectrograph.

The dimensions of the three scintillation counters on the blue side of the spectrograph are :

Upper : (176.15 x 75.0 x 5.0) cm.

Middle : (175.95 x 75.0 x 5.0) cm.

Lower : (176.25 x 75.0 x 5.0) cm.

the measurements being to ± 0.1 cm. The co-ordinates of the mid-planes of each are given in figure 2.1.

The three scintillation counters serve to define the overall acceptance of the spectrograph which, due to the bending of the particles in the magnetic field, varies with momentum. The calculation of this acceptance is discussed in Appendix B.

2.5 The High Voltage Pulsing System.

The three-fold coincidence from the scintillators is used to trigger, by means of a thyristor, a spark gap causing the discharge of a delay line across a resistor. This produces a square negative going pulse of amplitude

~ 10 kV and duration $\sim 3\mu\text{s}$. This pulse is applied to the electrodes of the momentum selector trays to discharge the flash-tubes which have been traversed by the muon. The inherent delay between the three-fold coincidence and the application of the high voltage pulse is $\sim 2\mu\text{s}$. A detailed description of the pulsing system is given by Ayre (1971).

A master reset pulse is applied to the majority of the electronic circuitry for the duration of the high voltage pulse to combat the effects of noise. When constructing the high voltage system it was found necessary to maintain very good earthing to reduce this noise, and the subsequent "pick-up".

2.6 The Momentum Selector Trays

Figure 2.5 shows a diagram of a section of the tube pattern in the MST's. As can be seen they consist of four layers of tubes staggered in such a way that, in combination with the electronic circuitry, the tray width is effectively divided into 152, $\frac{1}{2}$ cm. cells. These cells are defined at the middle of the third layer of flash-tubes, known as the measuring level, and the positions of the first four are also shown in figure 2.5. Between each layer of flash-tubes are the aluminium electrodes across which the high voltage pulse is applied. The electronic circuits which determine the cells are on circuit boards fastened, via edge connectors, to the front of the MST's. The memories corresponding to the tubes are also fastened to the MST's. The cell-allocating electronic logic primarily consists of a series of coincidence and anticoincidence circuits which allocate cells according to predetermined tube configurations. A detailed description of the electronic circuitry is given by Ayre (1971).

The cells corresponding to the predetermined flash-tube configurations were originally determined by considering trajectories within $+7^\circ$ and -7° to the vertical, and it was not possible to design the circuitry such that at all angles the trajectory is allocated to the correct cell. For the cases where a given configuration can be in either of two cells, that which

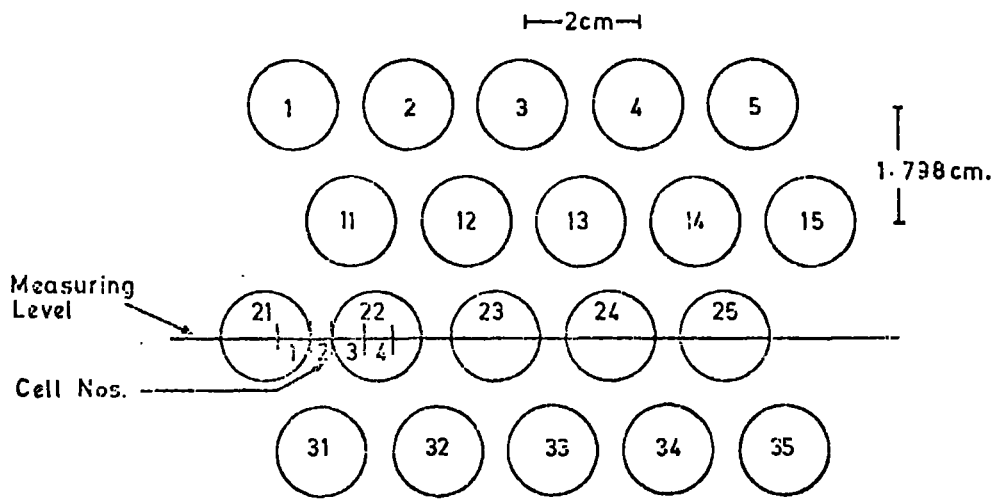


FIGURE 2.5 The Flash-Tube Pattern in the Momentum Selector Trays.

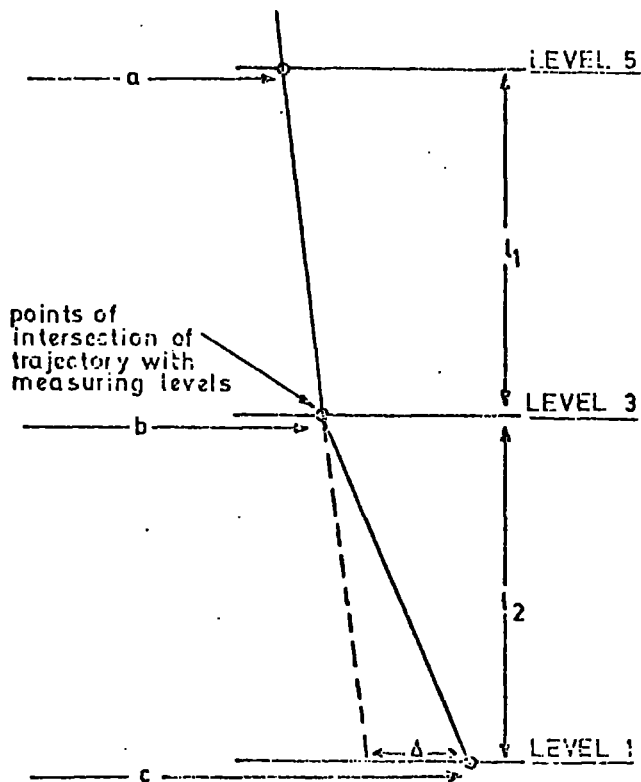


FIGURE 2.6 The Definition of Deflection.

has greater probability is allocated. Account of this is taken subsequently by the momentum selector which 'OR's' the cells together in threes at the top and bottom levels before a straight line comparison is made. Table 2.2 shows the cell allocations for the first four cells using the notation of figure 2.5. The celling is basically into groups of four, after which the electronics duplicates itself, hence it suffices to only consider these.

When designing the electronic celling, as said, trajectories were only considered out to $\pm 7^\circ$ to the vertical which is adequate for the primary use of the momentum selector. However at low energies

Cell No.	LAYER			
	1	2	3	4
	TUBES DISCHARGED			
1	1		21	31
1	1	11	21	31
1	1		21	
2	1	11		31
2		11		31
2	1			31
3	1	11	22	31
3		11	22	31
3	2	11	22	31
4	2	11	22	
4		11	22	
4		11	22	32
4	2	11	22	32

TABLE 2.2.

Relation between predetermined flash-tube configuration and allocated cells (for notation see figure 2.5.)

particles can traverse the trays at quite large angles, due to bending of the particle trajectory, particularly in the top and bottom levels. It

is found that at certain angles, not only may the wrong cell be allocated, but that sometimes more than one, or no cells may be given. This is discussed in more detail in Chapter 3, and must be taken into account when analysing data down to momenta ~ 20 GeV/c.

2.7 The Momentum Selector

The momentum selector contains three shift registers (A, B, C) corresponding to the three MST measuring levels (5,3,1), each of which has one 'bit' for each possible cell. Approximately $10 \mu\text{s}$ after a three-fold coincidence is detected the information from the MST's is gated down to the shift registers where the bits corresponding to the allocated cells are set to a '0' state. Next a clocking pulse of frequency ~ 1 MHz. is applied to the shift registers, shifting taking place towards the centre of the magnet for both blue and red sides. From the point of view of momentum selection itself, three-fold coincidence circuits are connected to all possible straight line configurations centred upon bits 76 and 152 of the middle shift register (B), the bits in the top and bottom being 'OR'ed together in threes to allow for wrong celling. Consequently after $\sim 76 \mu\text{s}$ the event is classified as being possibly due to a particle of high momentum. Of relevance to the present experiment is the cell information available at bit 152 of each shift register. This is utilized by RUDI as explained in the next section.

2.8 RUDI

2.8.1 Introduction

RUDI, as explained, is the name given to the device which calculates the deflection of the particle from the information contained in the shift registers of the momentum selector. Before one can describe its operation, the definition of deflection must be clarified.

2.8.2 Definition of Deflection

Consider figure 2.6 which shows the measuring levels of the MST's. Level 5 is the upper tray and 1 the lower. a, b, and c are the co-ordinates of the points of intersection of the particles track with the levels 5,3 and 1.

respectively, measured from some arbitrary vertical line. The deflection, Δ , is defined as the distance from the trajectory co-ordinate at level 1 to the point of intersection of the extrapolation of the straight line ab at that level, as indicated on the diagram. If l_1 and l_2 are the distances between levels 5 and 3, and 3 and 1 respectively, then it can be shown that Δ is given by :

$$\Delta = (a - 2b + c) + K(b - a) \quad 2.2.$$

where $K = 1 - l_2/l_1$

Now if n_a , n_b , and n_c are the allocated cell numbers at the three levels, it is seen that the quantity :

$$N = (n_a - n_b) - (n_b - n_c) = n_a - 2n_b + n_c \quad 2.3$$

is closely related to the deflection. Indeed for the case $l_1 = l_2$, i.e. a spectrograph having equal arms, then N is a correct estimate of Δ apart from the location error of $\frac{1}{2}$ cm at each level. In the present experiment the arms of the spectrograph differ by 4 cm, hence :

$$K = 1 - l_2/l_1 \sim \frac{4}{300} \sim 0.013$$

$(b-a)$ has values up to 76 cms and therefore $K(b-a)$ can be as great as -1 cm. This is large compared with deflections at high momenta (it will be shown later that for an incident momentum of 100 GeV/c, $\Delta \sim 4$ cms).

RUDI measures the quantity N , known as the category number, in equation 2.3, which is equivalent to the $a-2b+c$ in equation 2.2. Hence it must always be remembered in the analysis that N varies from the true deflection by the amount $K(b-a)$. In subsequent theoretical calculations of the deflection corresponding to different momenta, the deflection is always taken as that corresponding to $(b-a) = 0$. Hence, when considering any observables such as the frequency distributions of N , account must always be taken of the variation of N with $(b-a)$, that is with incident angle.

2.8.3 Operation of RUDI

The purpose of RUDI is to calculate from the allocated $\frac{1}{2}$ cm cells at each level, the sign, deflection, and incident angle of the triggering muons. Figure 2.7 shows a schematic diagram of the operation which is described in more detail in the following :

(a) Basic Operation.

The operation of RUDI is based upon the determination of two quantities. Firstly the arrival order of the '0' bits at elements 152 of the shift registers in the momentum selector, and secondly the contents of two scalars which count the clocking pulses used in the momentum selector for shifting. The counting of one, the scalar AB, is started by the arrival of either of the '0' bits from shift registers A or B, and stopped by the arrival of the other '0' bit. The second, the scalar BC is similarly controlled by the pulses from shift registers B and C.

(b) Checking for correct number of cells.

Obviously an event can only be analysed if there is one, and only one, cell in each of the shift registers, otherwise the position of the trajectory is ambiguous. This condition is checked automatically and the calculation of the deflection only proceeds if the condition is fulfilled.

(c) Determination of muon sign and deflection.

Examination of equation 2.3 shows that from the two numbers in the scalars, the category number N can be calculated. The deflection shown in figure 2.6 is only one of eight possible cases, having six different arrival orders of the '0' bit. These eight cases are shown in figure 2.8 where the three letters (e.g. ABC) indicate the arrival orders of the '0' bits at elements 152 of the three shift registers. The decision as to whether to add or subtract the two numbers is made by considering these arrival orders. The sign of the muon is also decided in this way, when possible, initially assuming the magnetic field to be positive. (A positive field is defined as having the lines of flux going into the front of the

Arrows indicate direction of information flow.

- Ch — indicates the checks made at various stages that events are being allocated to only one alternative.
- C — clocking (shifting) pulse from momentum selector.
- A — pulse from momentum selector indicating shifting has stopped and is utilized to begin the arithmetic if the correct number of cells have been received, and is delayed by 750 μs to provide "store" pulse to PHA.

All elements are reset immediately after the 3-fold coincidence between the scintillation counters.

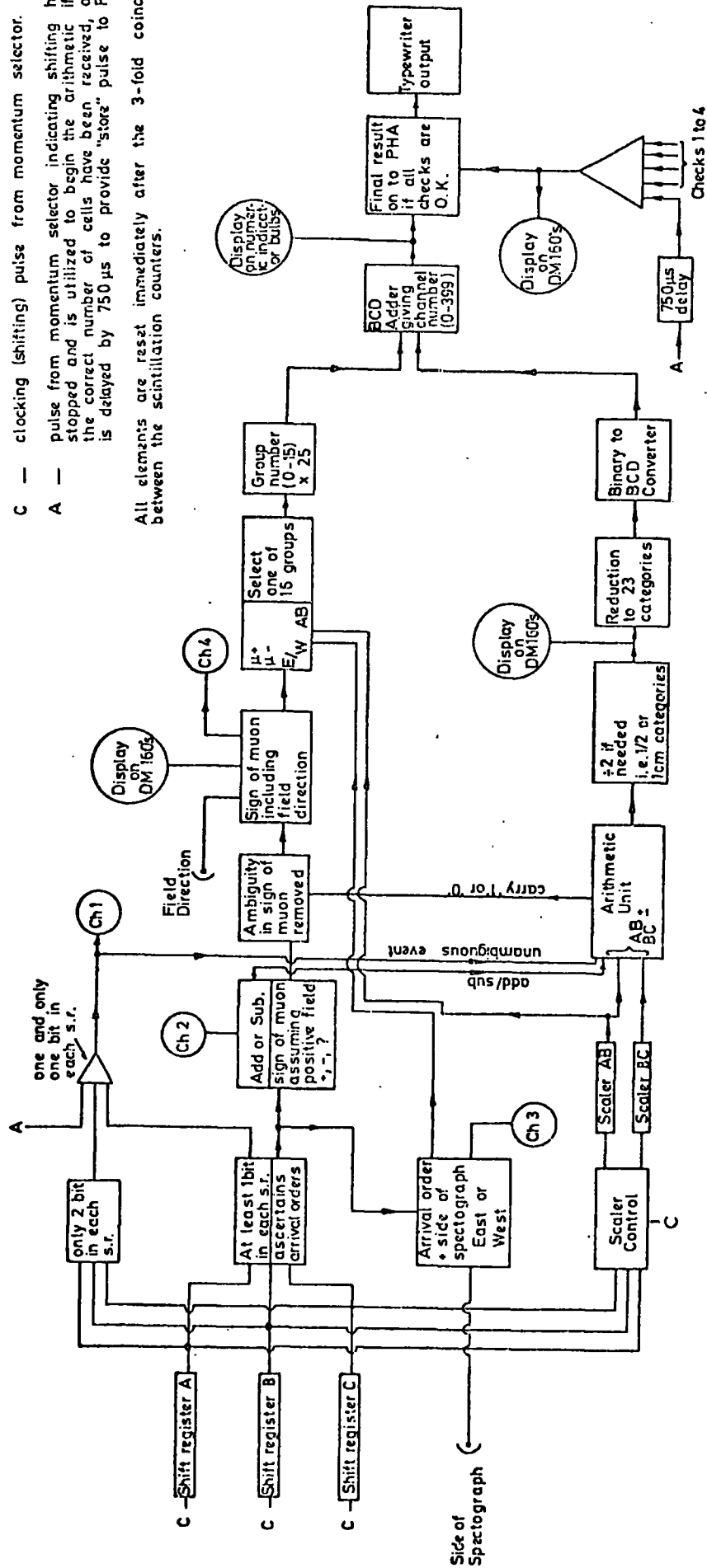


FIGURE 2.7 The Operation of RUDI.

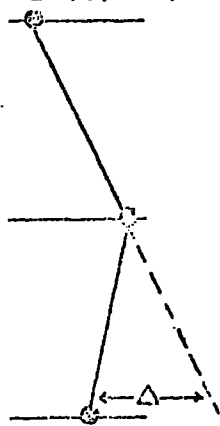
Level

5

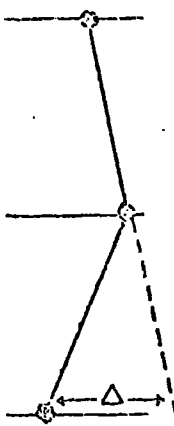
3

1

BCA (-ve)



BAC (-ve)

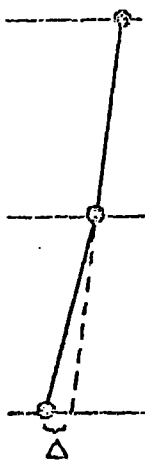


5

3

1

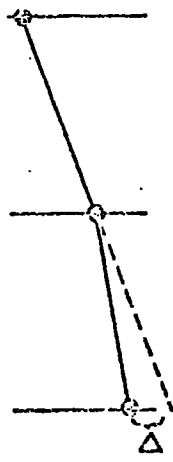
ABC (-ve)



ABC (+ve)



CBA (-ve)



CBA (+ve)

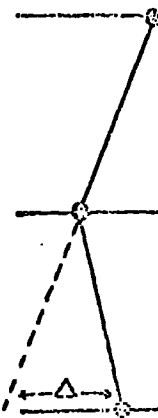


5

3

1

ACB (+ve)



CAB (+ve)

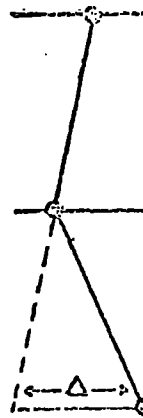


FIGURE 2.8 The Eight Possible Cases of Arrival Orders and Signs of Deflection.

blue side and out of the red side). Table 2.3 shows the six possible arrival orders, and the decision whether to add or subtract.

Arrival Order	Sign of Muon	Arithmetic
BCA	-	ADD
BAC	-	ADD
ABC	+/-	SUB
CBA	+/-	SUB
ACB	+	ADD
CAB	+	ADD

TABLE 2.3

Relation between the arrival orders at element 152, the sign of the muon, and the decision to add or subtract the numbers in the scalars.

At this point it should be noted that these rules apply to both sides (blue and red) of the spectrograph, since although shifting in both cases is towards the centre of the magnet (i.e. in opposite directions), the fields are also in opposite directions. As will be seen later, the only time when the side of the spectrograph has to be considered is in calculating the incident angle of the muons.

From table 2.3 it is seen that the general rule is : when B arrives second, subtract, otherwise add. For the addition cases, the sign of the muon is clear, whereas for the subtraction it is not. This ambiguity is resolved by considering the relative sizes of AB and BC. Subtraction is performed BC-AB, by taking the complement of AB (i.e. \overline{AB}) and adding it to BC., the addition being done by a 9 - bit binary adder. Two possible cases exist:

- (i) BC > AB. In the addition a "carry 1" appears at the 9th bit of the adder which must be added into the 1st bit to give the correct answer.
- (ii) BC < AB. In this case there is no carry, but the correct answer is

given by taking the complement of the final result.

$$\text{i.e. } BC > AB \quad |\Delta| = BC + \overline{AB} + "1" \quad 2.4$$

$$BC < AB \quad |\Delta| = \overline{BC + \overline{AB}} \quad 2.5$$

To resolve the ambiguity of sign, consider the case ABC. If $BC > AB$, then the particle will be negative (for a positive field). Thus the order ABC, plus the presence of a "carry 1" from the binary adder, are used to specify the particle as negative. For a positive muon, $BC < AB$, and consequently the order AEC, and the presence of "no carry" define the event as positive. In a similar way, the ambiguity for CBA is resolved. Table 2.4 shows a summary of the resolution of these ambiguities.

Arrival order	9th bit of adder	sign of muon
ABC	No carry	+
ABC	Carry 1	-
CBA	No Carry	-
CBA	Carry 1	+

TABLE 2.4.

The resolution of the ambiguities of sign for B arriving second.

The final decision as to the sign is made by considering the direction of the magnetic field which must be set up, by hand, on the instrument. For a positive, or zero field, the signs are unaltered, whilst for a negative field they are reversed. In order to deal with the case of zero deflection, the pulse from shift register E is delayed by an amount, insignificant relative to the clocking frequency. This allows the arrival orders to designate a sign to the deflection even though the sign of the muon will be indeterminate as the deflection will still be zero. A check is made that only one state shown in table 2.3 has been registered, and finally

a check is also made that only one sign has been allocated to the event.

(d) Determination of the incident direction

The incident direction is calculated by considering the arrival order of A and B together with the side of the spectrograph operative. In this way the event is categorised as being east or west. A further division is made into four ranges of AB (0-15, 16-31, 32-47, ≥ 48), by examining the magnitude of AB. A check is made that the muon is only allocated to one incident direction.

(e) Grouping of the spectra

The events are grouped into sixteen individual spectra as shown, according to charge, incident angle, and the four ranges of AB. Since the final output is to be displayed on a 400 channel analyser, there are at most 25 channels available for each. To accommodate this all categories larger than 22 are added together into category 23, making a total of 24 categories in all. The group numbers of the sixteen different spectra (0-15) are then multiplied by 25 and added to the category number to give the final channel number (0-399) into which the event is stored. In practice "1" is added to this number, to start the storing in channel 1 of the analyser. The relation between the channel numbers and the different grouping is shown in table 2.5.

	Channel numbers of different spectra			
	$0 \leq AB < 16$	$16 \leq AB < 32$	$32 \leq AB < 48$	$48 \leq AB$
μ^-E	0-24	25-49	50-74	75-99
μ^-W	100-	125-	150-	175-
μ^+E	200-	225-	250-	275-
μ^+W	300-	325-	350-	375-

TABLE 2.5.

Relation between individual groups and PHA channel numbers

(f) Changing the width of the categories

As explained in the previous section, because of the limited space on the PHA, all categories greater than 22 have been added together with the resultant loss of individual category information. With the $\frac{1}{2}$ cm categories this sets a lower limit to the spectrum measurement of ~ 40 GeV/c (as will be shown later). This can be reduced to ~ 20 GeV/c by adding the categories together in pairs (effectively dividing by two). This addition is carried out immediately after the full deflection has been calculated and is effected by simply dropping to "1" bit from the binary number. (In practice a plug containing the binary number is displayed by one spacing hence "losing" the "1" bit). Table 2.6 shows the relation between these "1 cm" categories and the basic $\frac{1}{2}$ cm categories.

$\frac{1}{2}$ cm categories.	1 cm categories.
0,+1	0
+2,+3	+1
+4,+5	+2
⋮	⋮
+42,+43	+21
+44,+45	+22

TABLE 2.6.

Relation between the $\frac{1}{2}$ cm and 1 cm categories

2.8.4 Final Output from RUDI

The allocated channel number (in BCD) is set up on the address lines to the PHA. Provided the conditions at the four checks (marked Ch on figure 2.8) are fulfilled then the pulse (A) from the momentum selector indicating the end of shift, which has been delayed by 750 μ s, is used to gate the channel number into the PHA, where it is stored. Also displayed

for each event on DM160 indicator bulbs, is the sign of the muon, and whether or not the event has been stored. The full deflection before reduction to categories 0-23 is also displayed in binary form together with the final channel number in decimal, the latter being on numeric indicator bulbs.

Figure 2.9 shows a typical output from an overnight run with RUDI, the field being in the negative direction. Indicated are the positions of the sixteen individual spectra.

2.9 Checking the Electronic Circuits

With such a complicated system it is very important to ascertain whether the different parts are working correctly. This was done at various stages during construction with specially designed devices which simulated experimental conditions.

(a) The flash-tube memories

These were tested individually by connecting the probes to earth in turn and noting whether the correct memory was set.

(b) The cell allocation logic

This was tested with a device in which the tube patterns could be set up by hand, with a series of switches. Each board was checked carefully and any faults rectified before installation in the spectrograph.

(c) The momentum selector

The momentum selector itself was tested by setting up all possible straight line combinations in turn with switches replacing the flash-tubes, and checking that a high momentum event was registered. The individual shift registers were checked by observing the allocated cell numbers for a random selection of events, and making sure the expected distribution was recorded.

(d) RUDI

RUDI was tested with a special test instrument which simulated deflections, and the outputs from the shift registers. All possible deflections were set up and a check made that the expected output was given. The results

of all these tests were that the instrument was working correctly and that it appeared to do so over long periods of time.

2.10 The Role of the Author and the Present Experiment

Obviously with an experiment of this complexity and size it cannot be the work of one person, rather a group of people working together. When the author joined the group in 1970 most of the electronic circuitry had been built. Since then the author has been active in the "marrying" together of the flash-tubes and the low resolution system (i.e. the momentum selector and RUDI) via a further study of the digitisation method. This resulted in a paper on 'the particle location along the length of a neon flash-tube', (Ayre et al., 1972 (c)) in which it was concluded that it may be possible, by timing the arrival of the pulses at the end of the flash-tube, to be able to locate the position of intersection of the muon's trajectory to ~ 10 cm, using the flash-tubes in MARS. The running of the apparatus has been carried out by various members of the group, including the author, and data was collected over a six month period utilizing the blue side MST's only. The analysis of this data to produce a momentum spectrum is described in the next two chapters and, as stated in chapter 1, has been the responsibility of the author. As the spectrograph is large, and the collection of data completely automatic then this analysis is a complicated procedure since instrumental effects become noticeable. Chapter 3 shows how the instrumental effects are handled, and chapter 4 gives the actual analysis of the results.

CHAPTER 3

THE MOMENTUM SPECTRUM - METHOD OF DATA ANALYSIS

3.1 Introduction

It is rarely possible in any complicated system to work from the data directly to the final results, the present work being no exception. The approach to the problem has to be from the opposite direction, that is to work from some initial assumption to predicted values for the quantities which are to be observed, and finally to compare these with the values actually observed. As a result of this comparison it is usually possible to say something about the assumption. Figure 3.1 shows a flow diagram of the analysis procedure. In short a trial momentum spectrum is adopted and converted into a deflection spectrum, which is then corrected for various instrumental effects. The probability of deflections being allocated to the different deflection categories is then calculated, and this folded into the corrected deflection spectrum to give the expected rates in each category. Knowledge of the exact live time of the experimental runs, and scintillation counter efficiencies, enable an absolute determination of the differential momentum spectrum to be made.

In order to be able to effect the analysis properly one must consider, in detail, how the instrument works, exactly what is being measured, and what effects any instrumental biases or inefficiencies have on the results. This chapter deals with the calculation of such effects, the next chapter showing how the expectation values are calculated, and their comparison with observations.

3.2 Factors Involved in Calculating the Trial Deflection Spectrum

3.2.1 The Momentum - Deflection Relationship.

Because MARS is a multilayer instrument, with interspersed detectors and gaps between the iron magnet blocks, any analytical expression for the

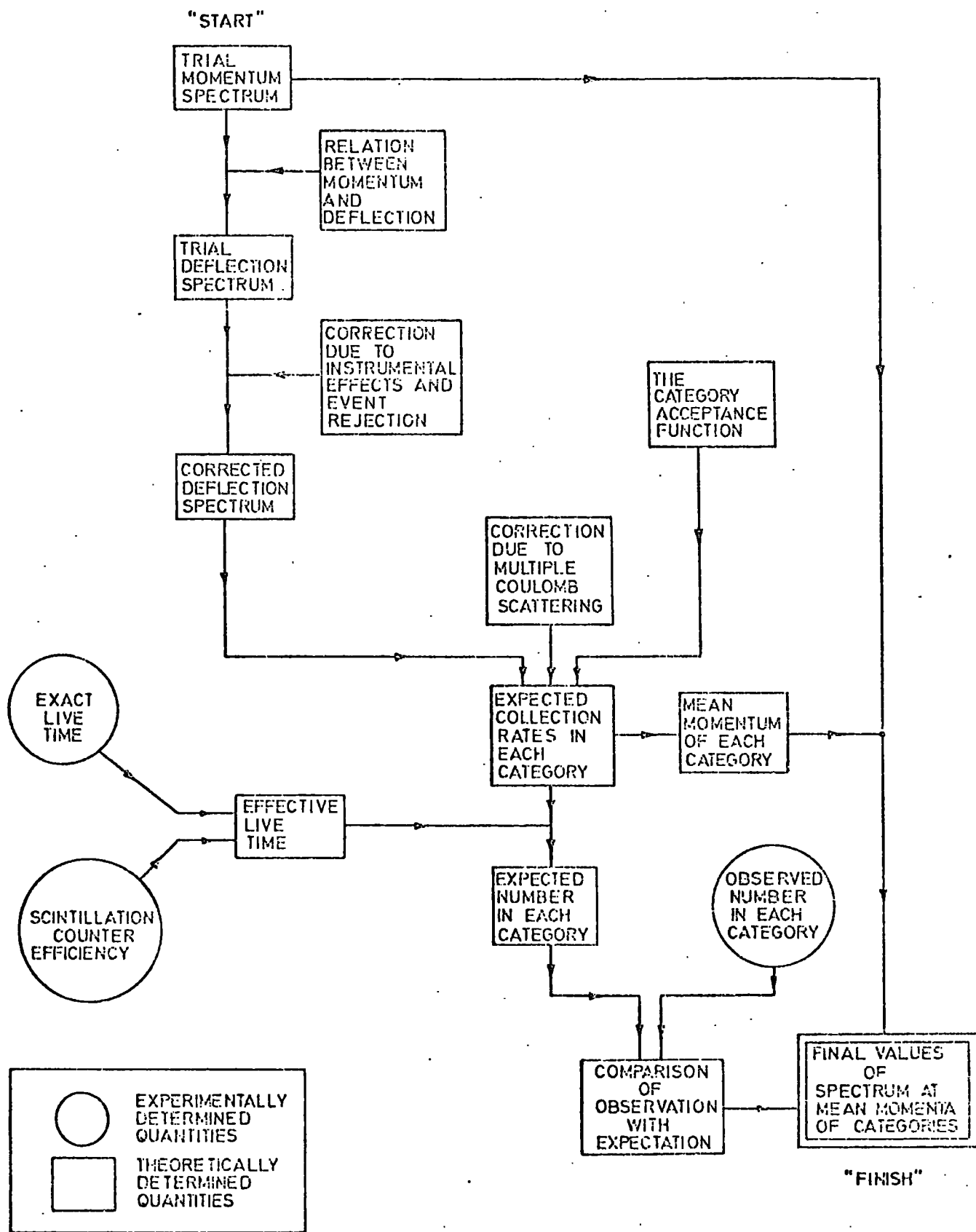


FIGURE 3.1 The Analysis Procedure.

trajectory of a muon through the spectrograph is very complicated, and impractical to use. The method adopted to study the relationship between momentum and deflection involved a computer simulation of events. In such a simulation, the incident angle and momentum of the muon could be varied and hence all possible trajectories considered. Initially a constant rate of energy loss was assumed, which was taken as the mean rate of energy loss sustained by a muon of that particular incident momentum in its passage through the spectrograph. This was found to be too inaccurate for the final results, consequently a variable loss was taken, which varied as the momentum decreased through the spectrograph. The values of energy loss of a muon in iron as a function of momentum have been calculated from the work of Sternheimer (1956) for ionisation loss, and Hayman et al. (1963) for bremsstrahlung, pair production, and nuclear losses, and are shown in figure 3.2.

Table 3.1 shows a sample of the results of the computer simulation. Values are taken for the case $(b-a) = 0$ since it is in this condition that the deflections measured by RUDI correspond to the true deflections (equation 2.2). This condition is used to define deflection throughout the analysis.

Incident Momentum p GeV/c	Deflection Δ cm.	$d\Delta/dp$ $\text{cm}(\text{GeV}/c)^{-1}$
10	64.5	13.38
20	24.08	1.511
30	14.84	0.5678
40	10.73	0.2956
50	8.402	0.1812
70	5.860	0.0880
100	4.050	0.0422
1000	0.3898	0.0003887

TABLE 3.1

Values deflection and $d\Delta/dp$ for given momenta.

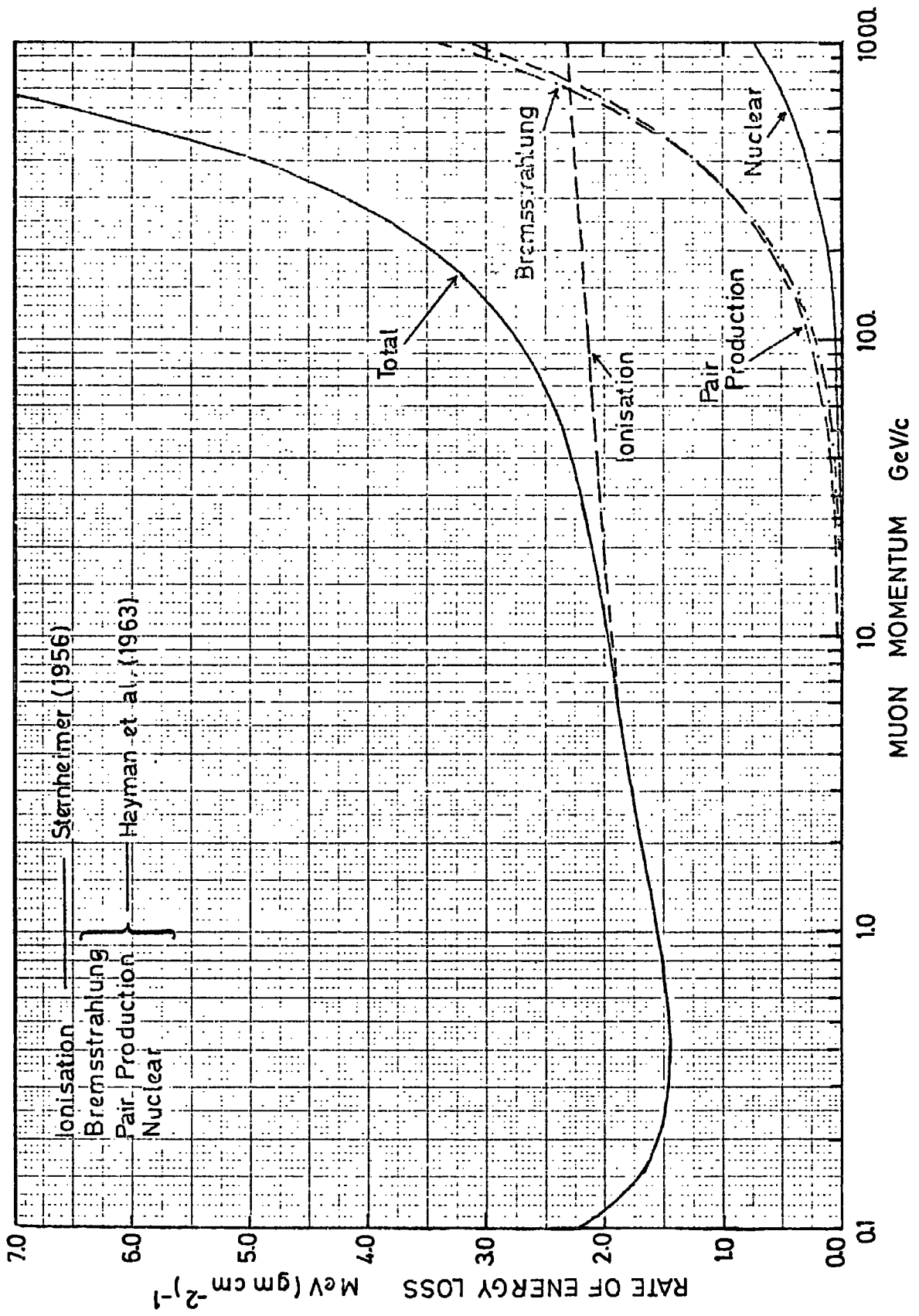


FIGURE 3.2 The Rate of Energy Loss of Muons in Iron.

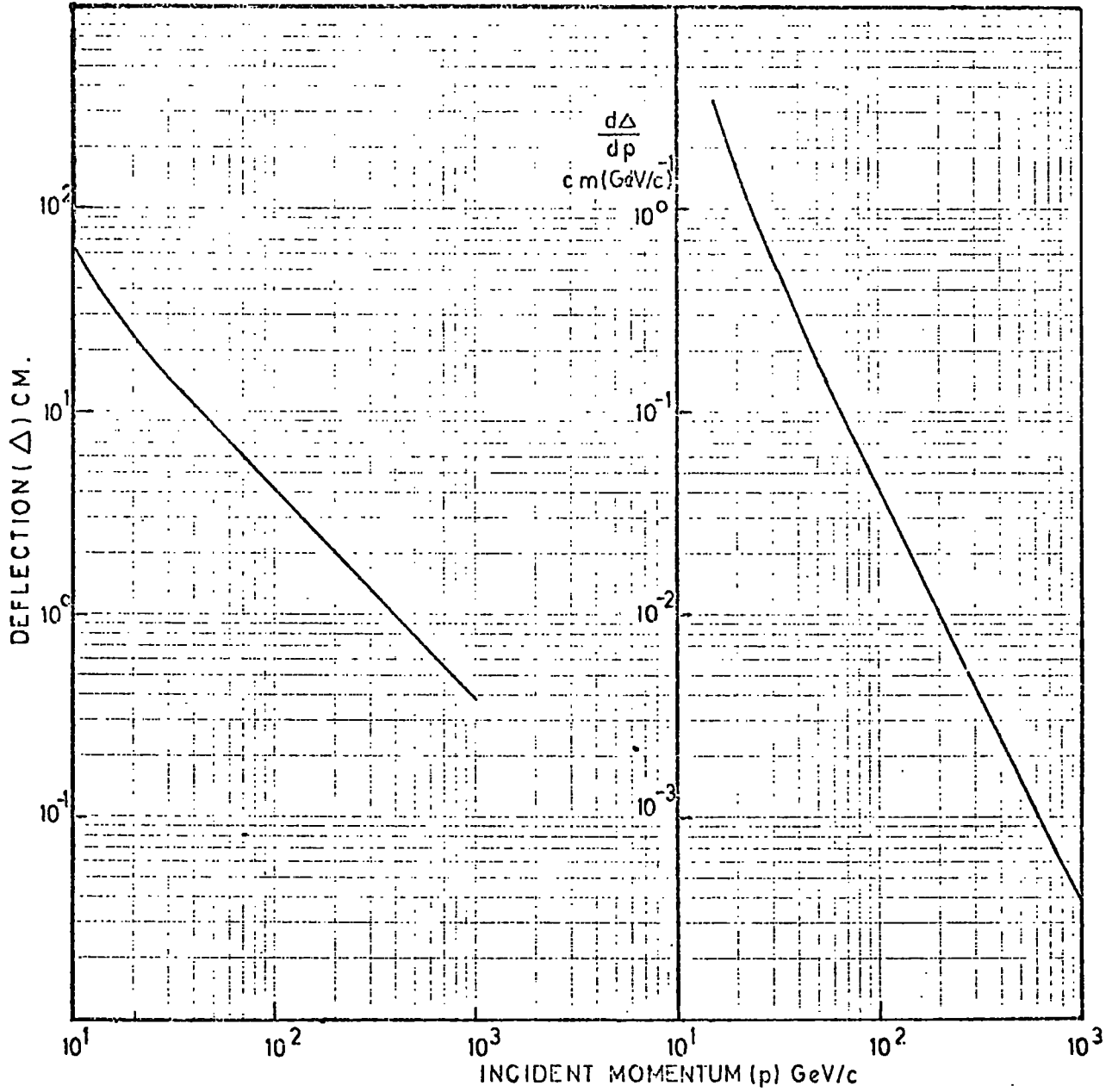


FIGURE 3.3 The Relation between Deflection (Δ), $d\Delta/dp$, and Momentum (p).

Also shown are values of the gradient of the momentum-deflection curve, $\frac{d\Delta}{dp}$, calculated by considering the deflections 1 GeV/c on either side of the momentum. These are required to calculate the deflection spectrum from the momentum spectrum according to the relation:

$$\frac{dN}{d\Delta} = \frac{dN}{dp} \cdot \frac{dp}{d\Delta} \quad 3.1$$

Figure 3.3 shows graphically the results in table 3.1

3.2.2 The Trial Momentum Spectrum

At the time of starting the analysis, the most recent absolute determination of the muon's momentum spectrum was that measured by the Kiel group (Allkofer et al., 1971). This was presented at the Hobart Cosmic Ray Conference, and as stated in chapter 1, was a best fit to the data from four different spectrographs ranging from 0.2 GeV/c to 1000 GeV/c. A curve drawn by the author through the points from 10 to 1000 GeV/c, given in the above publication as the best fit, is used in the present work as the trial spectrum. Table 3.2 shows the values assumed.

Also shown are values of $p^3N(p)$. This is used in preference to $N(p)$ alone in determining intermediate values as it varies much less rapidly than $N(p)$. Figure 3.4 shows a plot of p against $p^3N(p)$.

3.3 Corrections to the Spectrum.

3.3.1 The Effect of Multiple Coulomb Scattering

In traversing the iron in the spectrograph the muon suffers a considerable amount of multiple coulomb scattering. This was incorporated in the model of the spectrograph using the expressions given by Rossi and Greisen (1942). The equations used and the method of application to this situation are explained in Appendix C. It is found that the inclusion of the effect of scattering for a given momentum gives a range of values of deflection having a gaussian distribution with a mean deflection given by the value of deflection without scattering, and a standard deviation of 12% of that deflection. This 12% is constant over the whole range of momenta.

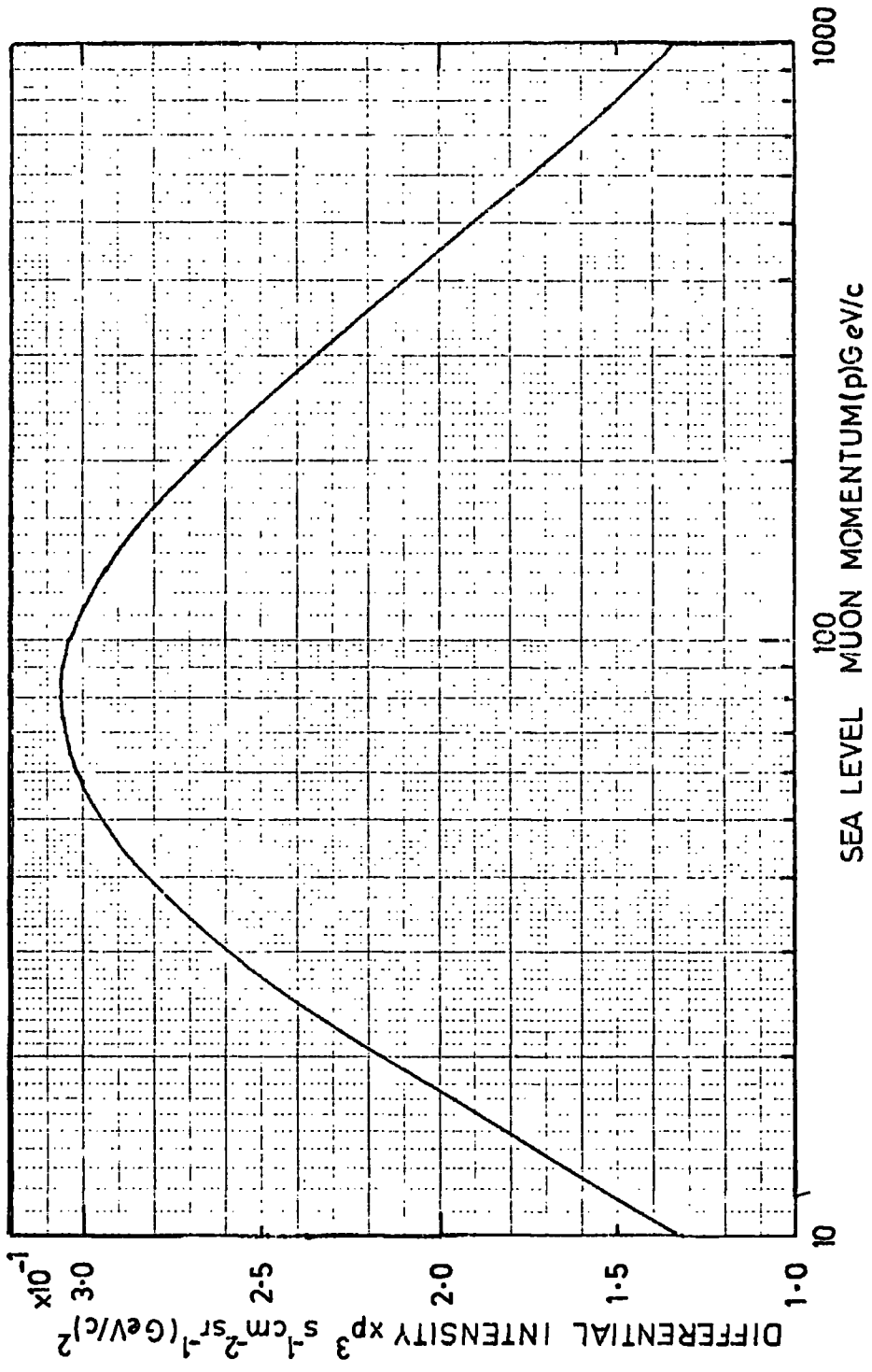


FIGURE 3.4 The Muon Momentum Spectrum (after Allkofer et al., 1971).

Momentum (p) GeV/c	Differential Rate $s^{-1} cm^{-2} sr^{-1} (GeV/c)^{-1}$	$p^3 \frac{dN}{dp}$
10	1.33×10^{-4}	0.1330
15	5.40×10^{-5}	0.1822
20	2.70×10^{-5}	0.2160
30	9.59×10^{-6}	0.2589
50	2.36×10^{-6}	0.2950
70	8.92×10^{-7}	0.3060
100	3.04×10^{-7}	0.3040
150	8.51×10^{-8}	0.2872
200	3.35×10^{-8}	0.2680
300	8.70×10^{-9}	0.2349
500	1.52×10^{-9}	0.1900
700	4.71×10^{-10}	0.1616
1000	1.34×10^{-10}	0.1340

TABLE 3.2.

The Trial Spectrum

Deflection Δ cm	$R(= N^1(\Delta)/N(\Delta))$	Δ cm	R
0.1	1.074	3.0	1.048
0.2	1.072	5.0	1.038
0.3	1.071	7.0	1.030
0.5	1.069	10.0	1.022
0.7	1.067	15.0	1.011
1.0	1.064	20.0	1.002
2.0	1.055		

TABLE 3.3

The effect of multiple coulomb scattering
upon the trial spectrum.

To calculate the effect upon the deflection spectrum one must fold the gaussian distributions into the deflection spectrum. i.e. if $N(\Delta)$ is the deflection spectrum then the spectrum corrected for multiple scattering, $N^1(\Delta)$, is given by :

$$N^1(\Delta) = \frac{1}{\sqrt{2\pi}} \int_{-\infty}^{+\infty} \frac{1}{\sigma} N(\Delta') \exp \left[-\frac{(\Delta' - \Delta)^2}{2\sigma^2} \right] d\Delta' \quad 3.2$$

where $\sigma = 0.12\Delta$

Values of the integral as a function of Δ are shown in table 3.3 and are plotted in figure 3.5. The fact that the correction factor falls to unity at ~ 20 cm. reflects the fact that the deflection spectrum has reached a maximum at around this value of deflection.

3.3.2 The Overall Spectrograph Acceptance

As is discussed in Appendix B, the trajectory of a muon traversing the magnetic field is curved, which causes a loss of low momenta particles due to their failure to fulfil the triggering requirements of passing through all three scintillation counters. Figure 3.6 shows a graph of the relative acceptance as a function of muon incident momentum. A particle of infinite momentum would travel in a straight line through the spectrograph, the acceptance for such a particle being $408 \pm 2 \text{ cm}^2 \text{ sr}$. In practice muons with momenta greater than 100 Gev/c reach this limiting value.

3.3.3 Rejection of Events

(i) Causes of Rejection.

In order to be able to allocate a deflection to an event, one must know, unambiguously, the position of the trajectory to within some defined limits, in this case nominally $\frac{1}{2}$ cm., at each of the levels. Since there are only three levels available in the momentum selector system, any loss of information at one of the levels is disastrous and renders the event completely unanalysable. This condition, that there be one and only one cell at each of the three levels, is built into RUDI, as explained in chapter 2, which automatically rejects any other events. Consequently one has to make

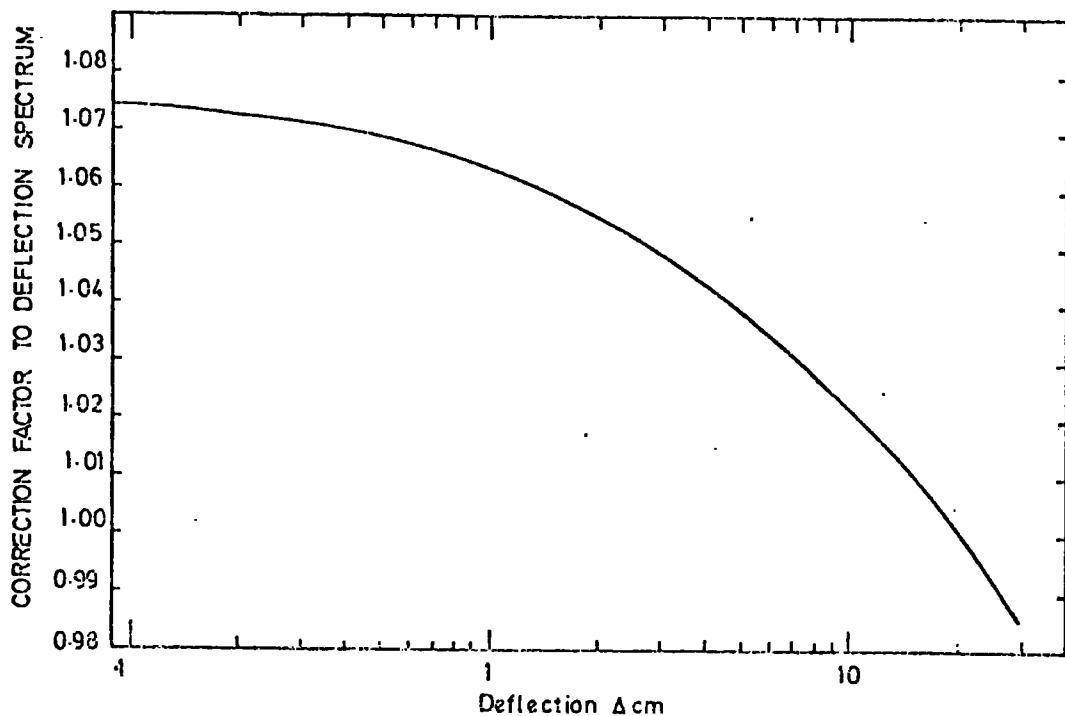


FIGURE 3.5 The Multiple Scattering Correction.

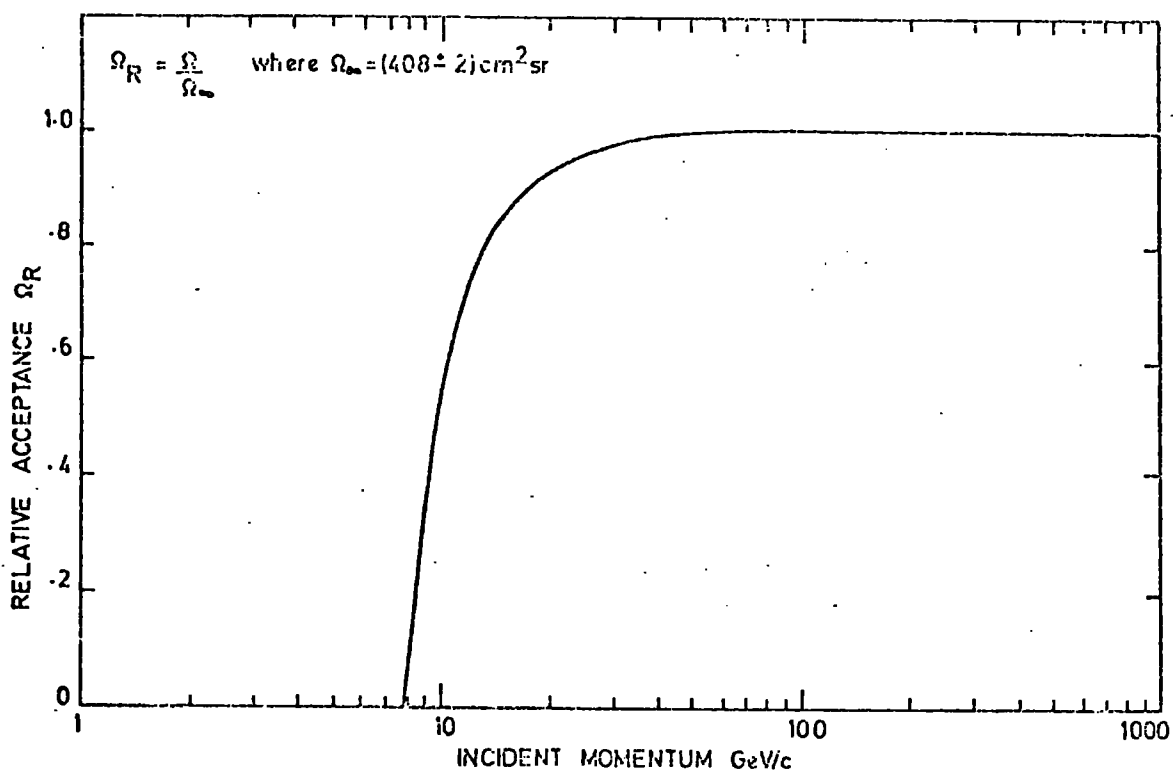


FIGURE 3.6 The Overall Spectrograph Acceptance.

a correction to the deflection spectrum for these rejected events. It is found that only ~60% of the events are unambiguously defined.

If all the effects which cause this contamination were independent of the muon's momentum, then the correction to be made to the data would be simply a raising of the spectrum by 1.67. However this is not the case, and a mixture of momentum independent and momentum dependent effects are found. The problem resolves itself into classifying the 40% unanalysable events into several categories, each category being associated with a certain type of contamination.

There are four factors which cause there to be a lack of triggered cells, or more than one triggered cell in the information from a given momentum tray :

- (a) The fact that the flash-tubes are inefficient can cause no cell to be set.
- (b) Muons traversing a tray at a large angle (usually muons of very low momenta) may cause either no cell, or alternatively more than one cell to be set in the tray.
- (c) Interactions of the muons in the iron blocks may cause one or more electrons to accompany the muon from the block, and may produce extra cells in levels 3 and 1. It is found that the probability of one electron accompanying the muon is virtually momentum independent, whilst the probability of two or more electrons depends strongly upon momentum. For this reason, in the analysis, the two effects are considered separately.
- (d) Extensive air shower particles and other spurious particles which traverse the trays together with the muon. This is particularly relevant to the top tray which has little absorber above it, whilst the other two trays are somewhat shielded by the magnet blocks.

(ii) Experimental Frequency of Number of Cells.

Any system which has to provide an instant analysis of the muon's deflection for high momentum selection purposes has to be completely

automatic. The system in this case was designed with this in mind; only later was it decided that a useful momentum spectrum could be measured with the same system. Consequently there is very little, if any, intermediate information on the events. All that is known for an event is into which deflection category it has been allocated. Ideally one would like to have information concerning the flash-tubes which had discharged, and which cells had been allocated at each level. This is not immediately available. It was decided however, that one piece of very useful information, easily extractable, was the rate of allocation of none, and greater than one cell at the different levels. Knowing these, together with various theoretical calculations and assumptions enables, amongst other effects, the inefficiencies of the flash-tubes to be estimated.

A simple device was constructed which counted pulses from an oscillator at a frequency of 10 MHz. The counting was controlled by the state of bit 152 of the shift register of the tray being examined. Counting only took place when a bit was a '0', which corresponds to an allocated cell. Hence if two cells were allocated, twice as many oscillations would be counted, etc.. Each tray was examined in turn, and for both field directions, there being about 500 events in each 'run'. The results for the various numbers of allocated cells are shown in table 3.4.

Level	% having no cells	% having more than one cell
5	6.3 ± .3	8.3 ± .3
3	2.7 ± .2	8.0 ± .3
1	11.9 ± .4	10.4 ± .4

TABLE 3.4

The observed frequencies of numbers of cells.

These refer to the values averaged over the two field directions.

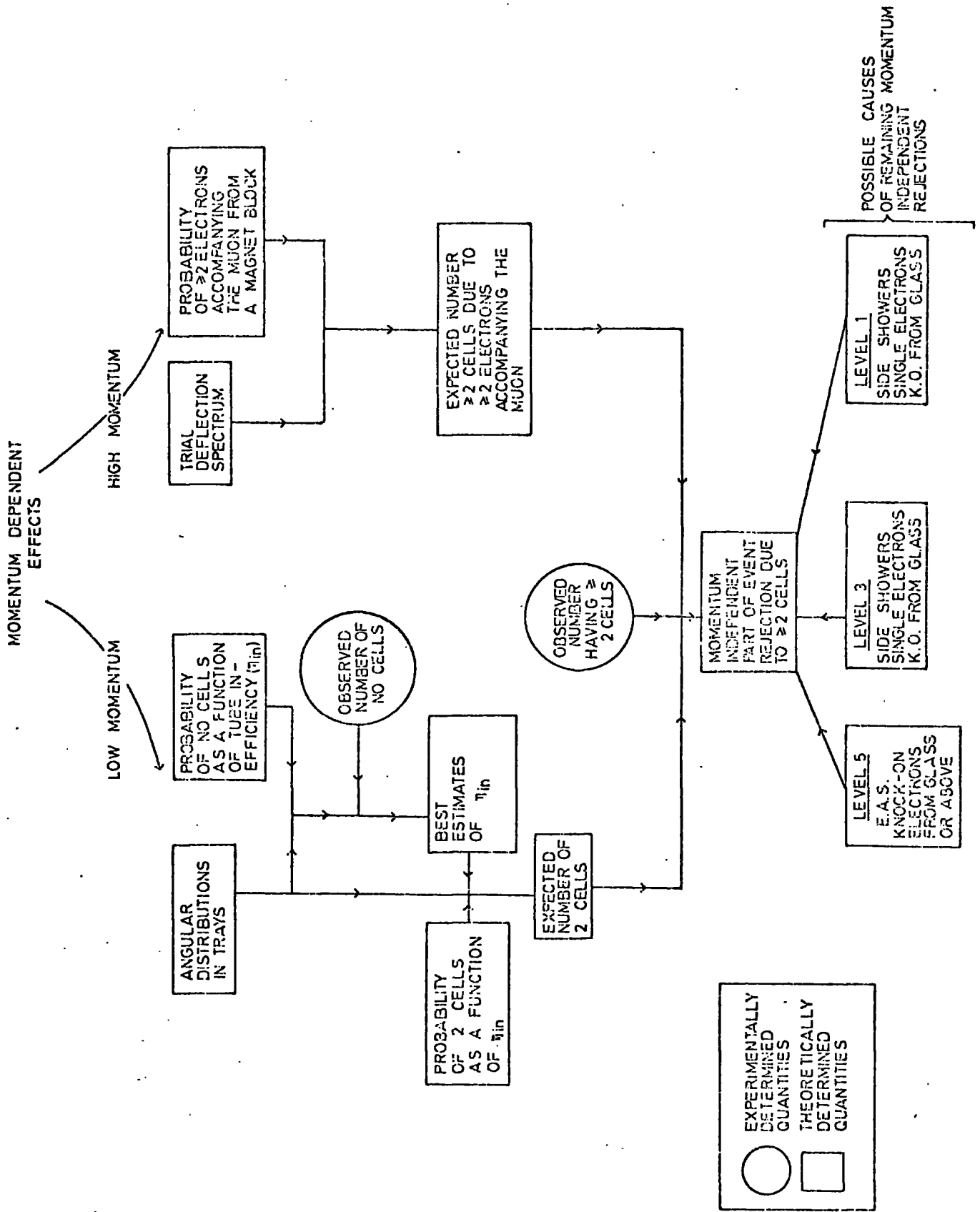


FIGURE 3.7 The Method of Calculation of Event Rejection by RUDI.

Since the spectrograph was in a state of further construction it was impractical to dismantle the trays to measure the flash-tube inefficiencies. However, as will be shown, using the above data in table 3.4 it is possible to estimate the inefficiencies of the tubes. Shown in figure 3.7 is a flow diagram which indicates the outline of how this problem is treated.

Division is made into momentum dependent and momentum independent effects as follows:

(iii) Momentum Dependent Rejections.

Momentum dependent rejection have two causes, one relating to low momentum events, and the other to events of high momentum.

(a) Low Momentum - Estimation of Flash-Tube Efficiencies.

At low momentum, particles traverse the trays with fairly large angles. Figure 3.8 shows graphs of the angular ranges in the upper and lower levels at four different momenta, 8, 10, 15, and 20 GeV/c. In the middle level the angles are small for all momenta having a range of from $+ 8^\circ$ to $- 8^\circ$. Since the celling logic was designed primarily for use in a momentum selector it was not required to be able to handle these large angled tracks, as high momenta events are fairly straight. In order to investigate the efficiency of the celling at large angles, a computer programme was written, which completely duplicated the logic of the electronic celling. The programme was tested and the results compared with the actual electronic circuits, together with an electronic checking unit with which the discharged tubes could be simulated and the allocated cells displayed. Using this programme together with a model of the tube pattern, the probabilities of various numbers of cells for different angles of incidence were examined. Figure 3.9 shows the results for the probability of none, one, and two cells being allocated. Also shown in the figure is the sign of angle conversion used throughout. These figures refer to 100% internally efficient tubes of internal diameter 1.53 cm., the mean diameter as given by Ayre (1971). Close examination of these probabilities, bearing in mind the results shown

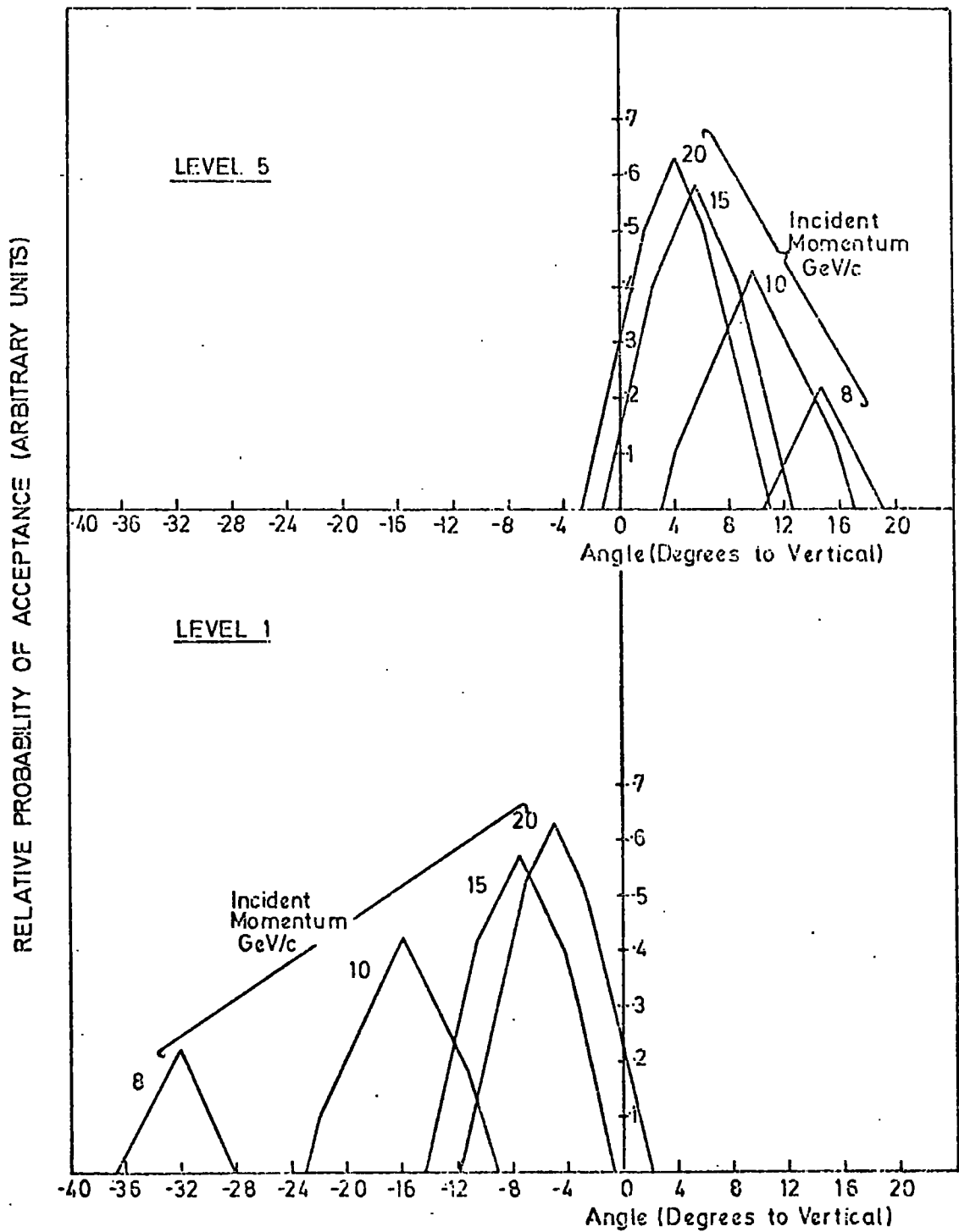


FIGURE 3.8 Angular Distributions in the Top and Lower Levels for Momenta of 8, 10, 15, and 20 GeV/c.

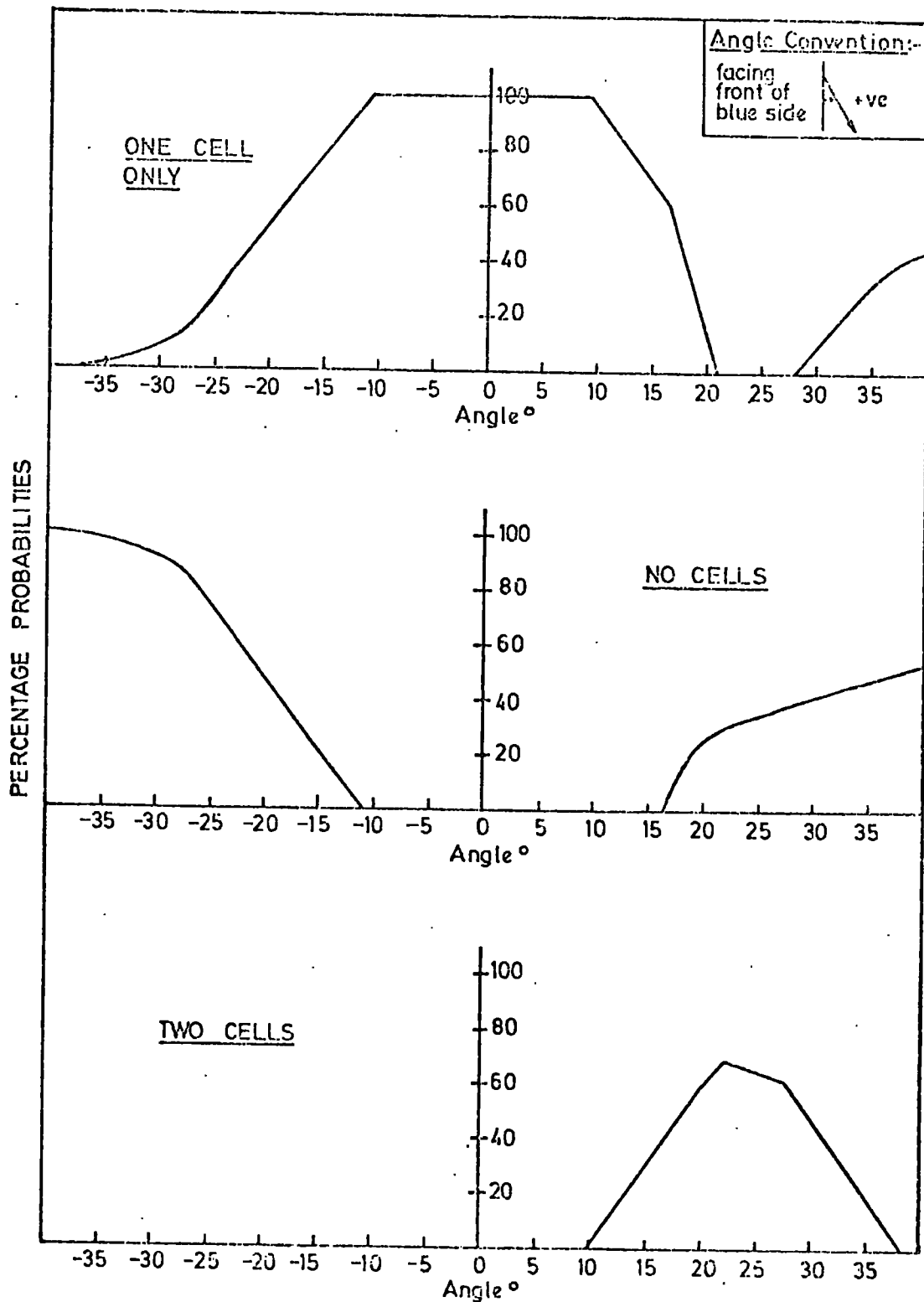


FIGURE 3.9 Probabilities of One, None, and Two Cells from a M.S.T. as a Function of the Angle of the Track to the Vertical.

in figure 3.8 on the angular distributions, indicate that there will be quite a large number of events in which the number of cells which are set is not unity, especially at low momenta. It is also to be noted that for angles less than 10° the electronic circuitry is 100% efficient at producing one and only one cell, which is adequate for the momentum selector itself.

The data shown in table 3.4 implicitly contain particles of all momenta. Hence in order to compare any theoretical values it is necessary to know the overall angular distributions of particle trajectories in the trays, integrated over all momenta. Ideally, these should be measured experimentally, but the only such information available were photographs of the tubes in the measuring trays taken during earlier runs with the spectrograph. It was found difficult to estimate the angles of the tracks in these trays, and it was felt that more accurate distributions could be obtained using a computer simulation of events. The passage of muons, with a momentum distribution taken from the spectrum of Allkofer et al. (1971), and incident isotropically from $+30^\circ$ to -30° , was modelled through the spectrograph and the distribution of angles from accepted events was calculated.

Figure 3.10 shows the results of a simulation of 1038 accepted events.

The angular distributions were then fed into the programme which simulated the celling logic, and the effect of varying the flash-tube efficiency investigated. The effect of reversing the signs of the angles was also examined which is the same as reversing the field. Each tube was assumed to be uniformly efficient across its entire diameter, since the form of the efficiency variation was not known, and could not be estimated easily. Figure 3.11 illustrates the results from these calculations. It shows the number of no cells, and of two cells which would be expected as a function of the flash-tube efficiency. By comparing the measured numbers of no cells, given in table 3.4, with these curves it is seen that the average efficiencies of the flash-tubes in each tray are :

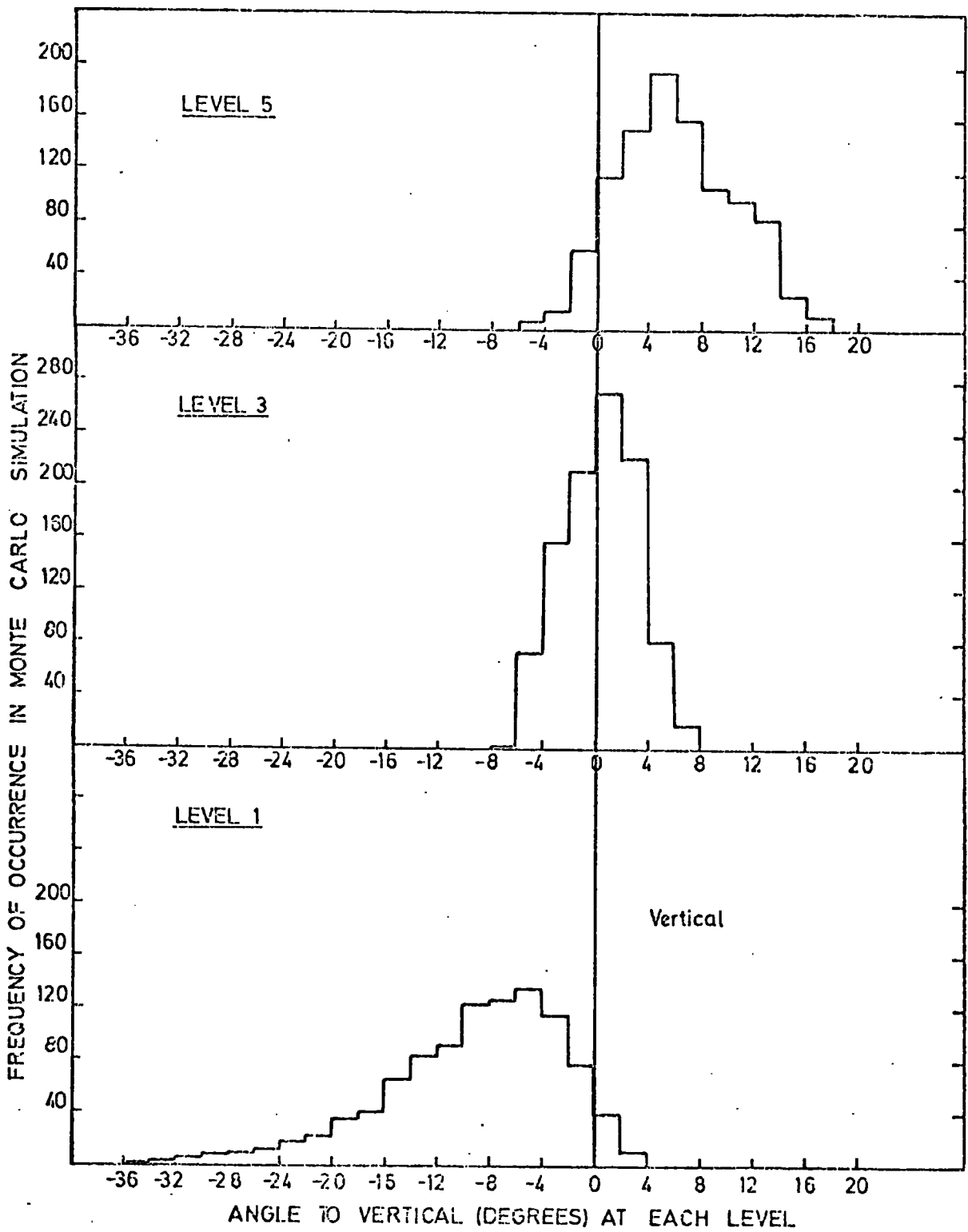


FIGURE 3.10 The Total Angular Distributions in all Three Levels (based upon a Monte Carlo Simulation).

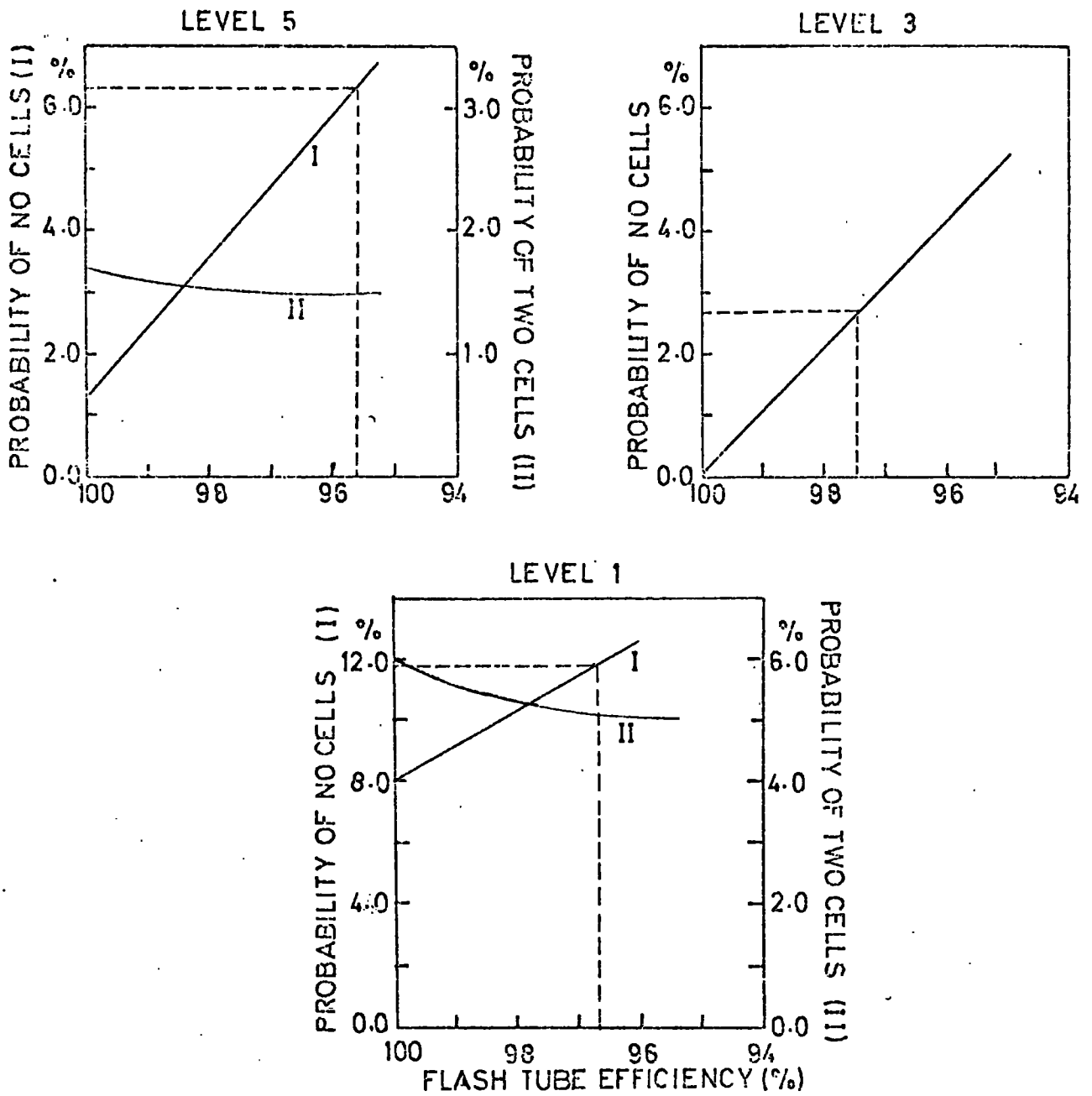


FIGURE 3.11 Probabilities of None, and Two Cells as a Function of Flash-Tube Efficiency (the Dashed Lines are at those Estimated at Each Level).

Level 5	:	$95.7 \pm .3\%$
Level 3	:	$97.4 \pm .2\%$
Level 1	:	$96.7 \pm .4\%$

The errors being those corresponding to the errors of the measured frequencies in table 3.4.

There is no reason to expect that each tray has the same efficiency, and the variation between them is only 1.8%. From figure 3.11 also can be read off the value of the rates of two allocated cells for the estimated tube efficiencies. These are :

Level 5	:	$1.5 \pm .01\%$
Level 3	:	$0.0 \pm 0.00\%$
Level 1	:	$5.1 \pm .02\%$

The errors on these values are very small due to the slow variation with flash-tube efficiency.

Also apparent from the figure is the fact that the probability of two cells falls slowly as the tube efficiency decreases. Some second order effect such as this is to be expected.

(b) High Momentum.

At high momentum the increasing effect of electromagnetic interactions of the muon in the iron becomes important. Some electrons emerging from these interactions may escape from the bottom of the block and have the possibility of causing one or more extra cells to be allocated. Figure 3.12 shows graphs of the probability of one electron, together with the muon, emerging from an iron block the size of those in MARS, and also the probability of two or more electrons, after Ayre et al. (1971(c)). The experimental points are the measurements made by the above authors with the MARS spectrograph in the earlier photographic run. The solid lines are their theoretical predictions. As has been stated previously, and is apparent from figure 3.12, the probability of single electrons is very nearly constant, ranging from $\sim 6.3\%$ to 10 GeV/c to $\sim 8.9\%$ at 1000 GeV/c,

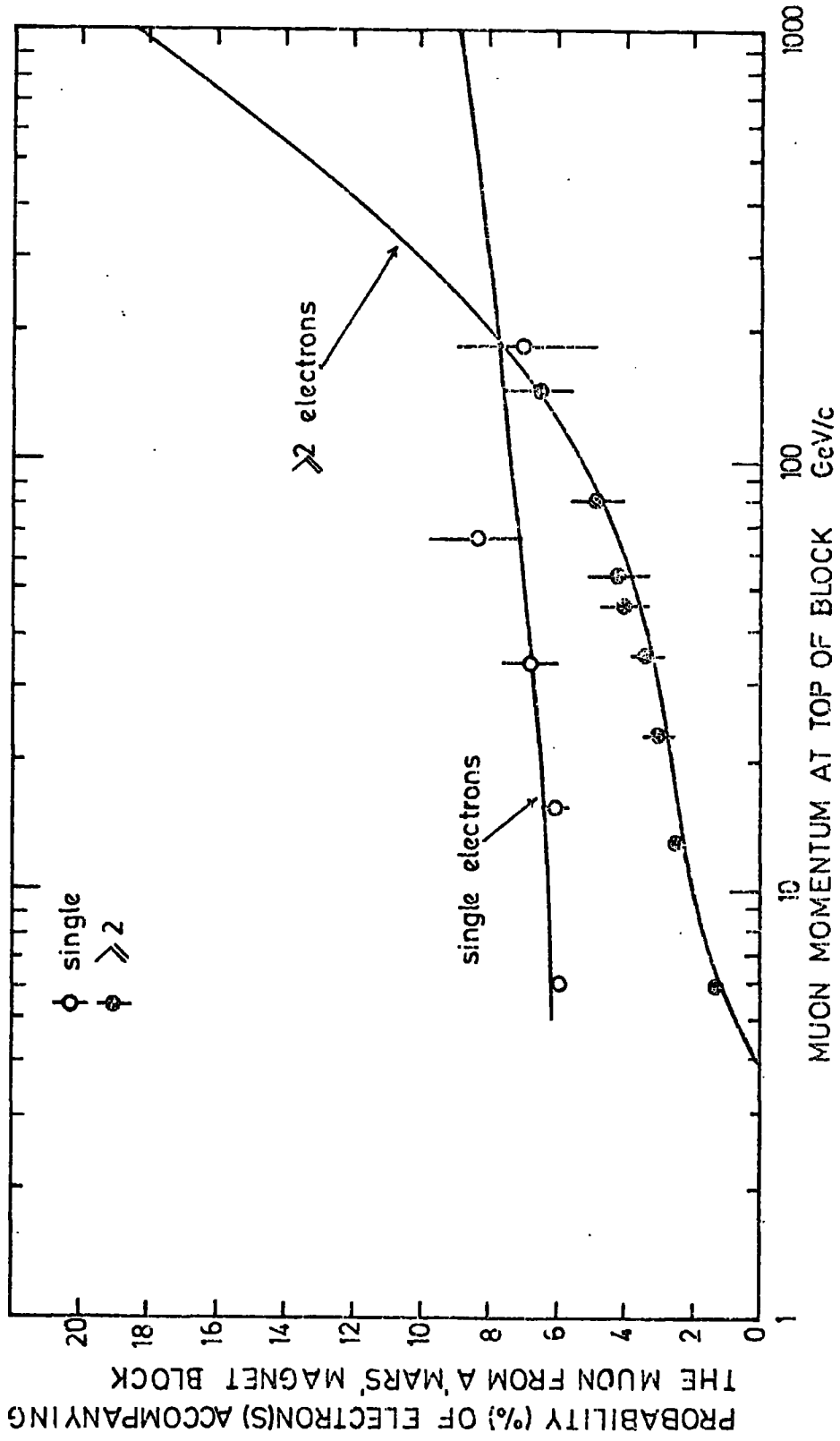


FIGURE 3:12 Probability of Electron(s) accompanying the Muon from a Magnet Block (after Ayre et al., 1971(c)).

whereas the probability of greater than one electron rises rapidly as the energy of the muon increases. This rise is due to the increasing cross-section for pair production and bremsstrahlung at the higher energies, whilst the flatness of the single electrons is due to the knock-on probability (collision loss) being very nearly independent of muon energy.

Even though an electron may accompany the muon from the iron it does not necessarily cause another cell in the momentum selector to be allocated. The electron may be so close to the track of the muon as to be allocated to the same cell, or it may be at such an angle as to produce no extra cell. In order to be able to convert from probabilities of extra particles to probabilities of extra cells, it is necessary to know the angular and lateral distributions of the particles relative to the muon track. This is a very complicated process since the electron suffers considerable multiple coulomb scattering in the iron before emerging. However in the present analysis justifiable assumptions have been made to overcome this difficulty. It is considered that when there are two or more electrons accompanying the muon from one of the magnet blocks, that at least one of these will cause an extra cell to be set. For the single electrons it is difficult to predict theoretically the conversion factor from electrons to triggered cells, though for knock-on electrons alone, including multiple scattering and a momentum selector tray 8 cm. below the iron block it is found, by a Monte Carlo simulation, that 60 - 80 % of the produced knock-on electrons generate extra cells. However since the probability of these single electrons will be assumed to be momentum independent, it is not necessary to know this conversion factor, the correct number will be included with any other momentum independent effects when all the momentum dependent effects have been subtracted from the experimentally measured rates of greater than one cell (table 3.4).

The total contribution of more than one electron to more than one cell is found by integrating their probability curve (figure 3.12) over the momentum spectrum. Account is taken of the different muon energies in

blocks C and A. The results are as follows:

Level 3	:	2.4%
Level 1	:	1.8%

The probability distribution for producing more than one electron is reconsidered later when the total correction factor to the deflection spectrum is calculated.

(iv) Momentum Independent Rejections.

These are inferred by subtracting the weighted momentum dependent effects from the observed frequencies of more than one allocated cell. The situation is summarized in table 3.5.

Level	MOMENTUM DEPENDENT			MOMENTUM INDEPENDENT
	1 Observed % ≥ 2 cells	2 Expected % from large angles	3 Expected % from ≥ 2 electrons	1 - 2 - 3 Remaining %
5	8.3	1.5	0	6.8
3	8.0	0	2.4	5.6
1	10.4	5.1	1.8	3.5

TABLE 3.5

Summary of Categorization of ≥ 2 allocated cells.

The percentages in the final column are taken as being the sum totals of all the momentum independent effects. Whilst it is of no importance as regards the final measured spectrum, it is of interest to examine the origin of these effects. The situation regarding each level is as follows:

(a) Level 5: This has very little absorber above it, and hence is subject to contamination from electrons and other particles which may accompany the muon. Also δ -rays and γ -rays may be produced by interaction of the muon in what little absorber there is in the roof ($\sim 4 \text{ gm cm}^{-2}$), and in the

azimuthal trays supports.

(b) Level 3: A major part of this contamination will be from single electrons produced by the muon interacting in the iron block. Large angled extensive air showers which are able to enter the gap between the magnet blocks will also contribute.

(c) Level 1: The contributions will be the same as in level 3, though since the level is nearer the ground, then the effect of side showers may be somewhat reduced.

(v) The Correction Factor for Rejection of Events.

The situation is summarised in table 3.6. This table assumes that whenever more than one electron accompanies the muon out of a magnet block, at least two cells are set in the shift registers associated with the momentum selector tray at that level. Later it is discussed what happens to the correction factor, and hence to the measured spectrum when this assumption is relaxed. Briefly however, it will have little effect below ~ 100 Gev/c and an increasing effect as the momentum rises.

In calculating the correction factor from the figures shown in table 3.6 it has been assumed that in a given level, momentum dependent, and momentum independent effects do not occur at the same time. In theory some of the effects may happen together but the method of their calculation has assumed this is not true and their combination must also be treated in this fashion. For each level the overall efficiency of producing one cell is calculated by subtracting from unity the sum of the momentum dependent and independent effects. The three efficiencies for the three levels are then multiplied together to give the total correction factor which is shown in the final column of table 3.6.

A correction must also be applied to allow for the tube inefficiencies themselves which in effect contaminate a level by producing no cells. This effect is momentum independent and is taken into account not here but in the category acceptance function which is discussed in the next section.

Incident Momentum p Gev/c	Level 5		Level 3		Level I		Total Correction Factor
	P Independent	P dependent	P independent	P dependent	P independent	F dependent	
20	0.068	—	0.056	0.024	0.035	0.022	0.809
30	0.068	—	0.056	0.028	0.035	0.026	0.802
50	0.068	—	0.056	0.034	0.035	0.033	0.790
70	0.068	—	0.056	0.041	0.035	0.040	0.778
100	0.068	—	0.056	0.050	0.035	0.050	0.762
150	0.068	—	0.056	0.064	0.035	0.064	0.739
200	0.068	—	0.056	0.078	0.035	0.078	0.716
300	0.068	—	0.056	0.100	0.035	0.100	0.680
500	0.068	—	0.056	0.133	0.035	0.133	0.629
700	0.068	—	0.056	0.156	0.035	0.156	0.594
1000	0.068	—	0.056	0.183	0.035	0.183	0.555
5000	0.068	—	0.056	0.270	0.035	0.270	0.437

TABLE 3.6.

The correction factor for event selection (i.e. the amount by which the uncorrected deflection spectrum must be multiplied)

3.4 The Category Acceptance Function

3.4.1 Definition

Reference to the flow diagram of the analysis procedure in figure 3.1 shows that the other main ingredients of the analysis are the shapes of the category acceptance functions which are folded into the corrected deflection distributions (i.e. the deflection spectrum corrected for the instrumental effects), to give the rate of collection of events in each category. This section describes the calculation of the acceptance functions and their importance. To recap, at each of the three levels, the muon's trajectory is allocated to a given cell of width $\frac{1}{2}$ cm.. A category is then allocated based on the relation :

$$N = n_a - 2n_b + n_c \quad (\text{equation 2.3})$$

where the n's represent the allocated cells at the levels. The category acceptance function for a particular category is defined as being the function which describes the probability of different deflections being allocated to that category. Ideally the shape of the functions can be calculated by considering the $\frac{1}{2}$ cm. cells through which the trajectory passes at the measuring levels, all possible trajectories for a given deflection being considered, and will be altered when there is a probability that the trajectory has been allocated to one or more wrong cells at the different levels. There are three reasons for the trajectory being occasionally allocated to the wrong cell :

- (a) The electronic celling is not perfect for trajectories at angles other than 0° to the vertical.
- (b) The flash-tubes are not 100% efficient.
- (c) Knock-on electrons produced in the glass walls of the tubes.

Two approaches to the calculations of the functions are adopted. In the first initially 100% correct celling is assumed and then the effects of the three factors contributing to wrong celling are estimated. In the second method a Monte-Carlo simulation of events using a model of the spectro-

graph and momentum ceiling logic is used.

Due to the shape of the deflection spectrum it is found that the final expected rates of events in the various categories are most sensitive to the shape of the category acceptance functions in the low numbered categories, i.e. for high energies. To a good approximation one finds that the incident angular distributions for these high energies are very nearly the same, being triangular shaped, with a maximum at 0° , and extending from -7° to $+7^\circ$ to the vertical. In all of what follows such an angular distribution has been used.

3.4.2 Method A

(i) Basic Shape.

Disregarding the tube patterns and the electronic ceiling logic, it is possible to calculate the shape of the category acceptance functions by ascertaining through which of the $\frac{1}{2}$ cm. cells at the measuring levels (the level of the middle of the third layer of tubes in the momentum selector trays) the trajectory passes. By considering all possible trajectories for given deflections, the relative numbers allocated to the different categories can be found. Figure 3.13 shows the results when deflections from 0 to +3 cm. are considered with uniform probability, categories 0 to 5 being illustrated. The histograms are the results from this calculation, whilst the solid line is that previously calculated by Nandi (private communication) completely independently. One sees that the categories, although nominally of width $\frac{1}{2}$ cm., do not have a square distribution, but are considerably extended over a 3 cm. range of deflection. This leads to problems particularly if an integral spectrum is to be calculated since the minimum momentum of the categories is very ill-defined.

As previously stated, the cells allocated at the levels are not always correct and the causes of this wrong ceiling are examined in the next three sections.

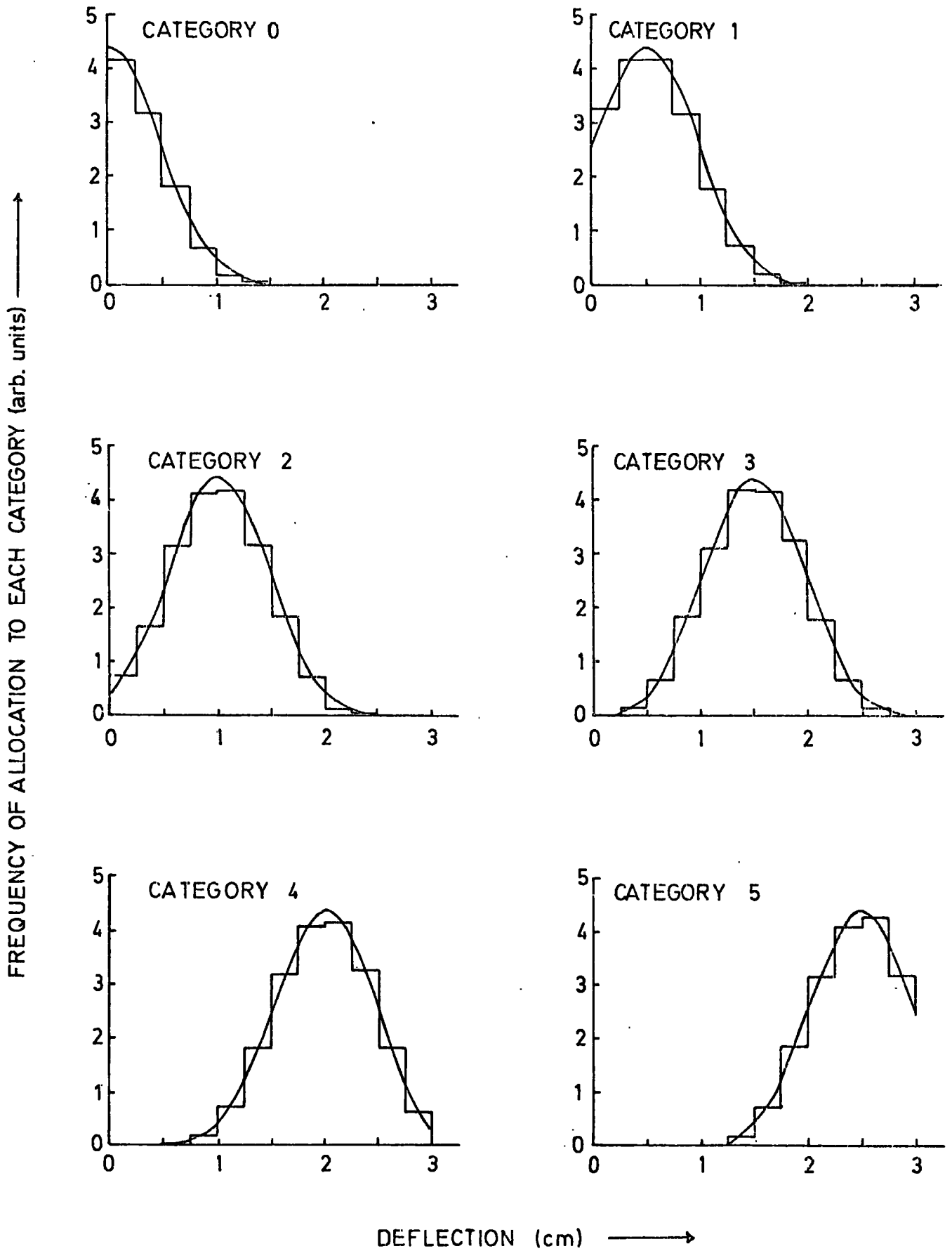


FIGURE 3.13 The Basic Category Acceptance Function Shapes.

(ii) 'Intrinsic' wrong celling.

By intrinsic is meant the wrong celling inherent in the design of the electronics. Obviously it would have been difficult to design a practical system capable of allocating the particle trajectory to its correct cell over the wide range of angles of the trajectories in the trays. By considering the trajectories as different angles, over one tube spacing, and assuming 100% efficient tubes, the results shown in table 3.7 are obtained for the probability of the trajectory being allocated to the correct, or to the adjacent cells (High or Low).

Angle Degrees	Adjacent Cell High %	Correct Cell %	Adjacent Cell Low %
-6	10	80	10
-4	6	87	7
-2	4	93	3
0	0	100	0
2	3	93	4
4	7	87	6
6	5	85	10

TABLE 3.7

Probabilities of Intrinsic Wrong Celling

These are shown graphically as the solid line in figure 3.14. Integrating over the triangular angular acceptance functions of the high momentum categories gives the average probability of the trajectories being allocated to the next higher cell, instead of the correct one, as 3.6%, and to the next lower cell as 3.9%.

(iii) The Effect of Inefficient Flash-Tubes.

When a flash-tube through which the particle has passed does not discharge then there will be an increased probability of the trajectory being allocated to the wrong cell. If η is the tube inefficiency (i.e. the

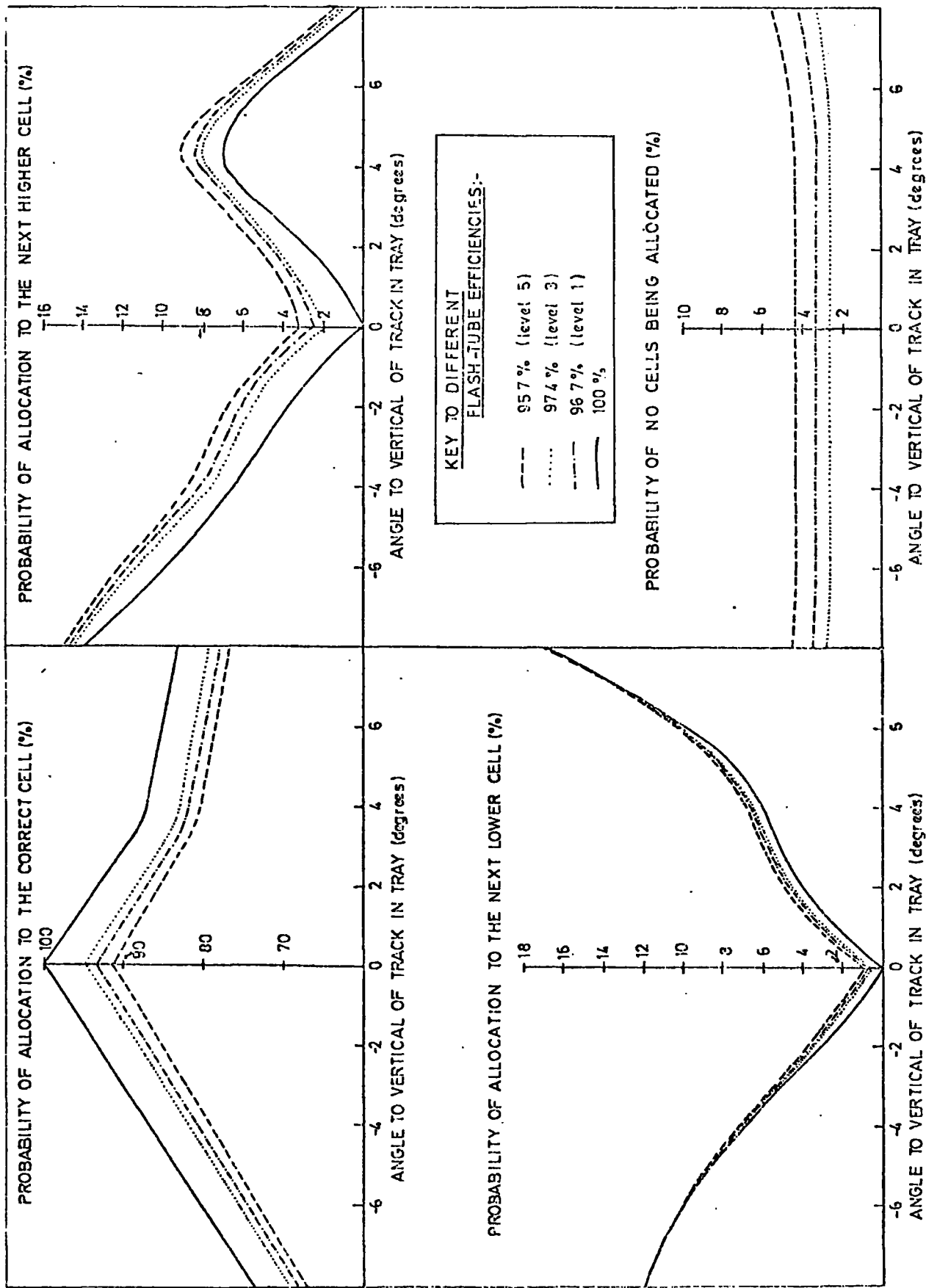


FIGURE 3.14 Probabilities of Allocation to the Correct and Incorrect Cells as a Function of Angle of Track for 100% Efficient Tubes, and for the Efficiencies Estimated in the Three M.S.T.'s.

Angle	Probability of Two Cell Low	Probability of One Cell Low	Probability of Correct Cell	Probability of One Cell High	Probability of Two Cell High	Probability of No Cells
-6	0.10 η	0.10-0.05 η	0.80-1.60 η	0.10+0.35 η	0.20 η	η
-4	0.07 η	0.07+0.04 η	0.87-1.74 η	0.06+0.50 η	0.13 η	η
-2	0.03 η	0.03+0.16 η	0.93-1.86 η	0.04+0.60 η	0.07 η	η
0	0	0.25 η	1.0 -2.0 η	0.75 η	0	η
+2	0	0.04+0.21 η	0.93-1.76 η	0.03+0.52 η	0.03 η	η
+4	0	0.06+0.19 η	0.87-1.54 η	0.07+0.28 η	0.07 η	η
+6	0	0.10+0.10 η	0.85-1.50 η	0.05+0.25 η	0.05 η	1.10 η

TABLE 3.8

Probability of wrong celling including the effects of inefficient flash tubes.

probability of the tube not discharging when a muon has passed through its sensitive volume), then, by considering the tube patterns and celling logic, and assuming that η is small so that there is only a small probability of two inefficiencies occurring in the same track, one finds the resulting probabilities of incorrect celling shown in table 3.8. Figure 3.14 also shows plots of these probabilities, together with those for correct celling and the case of no allocated cells, for the three flash-tube efficiencies (0.957, 0.974, and 0.967) estimated for the tubes in the three momentum selector trays (section 3.3.3.). It is to be noted from table 3.8 that when the tube inefficiencies are introduced, it is possible for the trajectory to be allocated not only to the adjacent cell but also to the next but one cell. However for these small tube inefficiencies (i.e. $\eta < 5\%$) the probabilities of such events occurring are very small, and for simplification in the analysis the probabilities of the cell being incorrectly allocated by two cells will be included in the probabilities of being wrong by one cell. It is considered that this will have a negligible effect upon the final spectrum. The probabilities of the cell allocated being correct, high, and low, are then weighted with the triangular acceptance function and integrated over the angular range of the tracks in a tray. The results for the three measuring levels are shown in table 3.9.

Level	Probability of Being High	Probability of Being Correct	Probability of Being Low
5	0.062	0.848	0.047
3	0.052	0.879	0.043
1	0.056	0.866	0.044

TABLE 3.9.

Probabilities of wrong celling including estimated flash-tube efficiencies and integrated over all angles.

(iv) Knock-on Electrons from Flash-Tubes.

In passing through the glass walls of the flash-tubes the muons may

Angle Degrees	Probability of One Cell Low	Probability of Correct Cell	Probability of One Cell High	Probability of Two allocated Cells
-6	0.50p	1.0-1.25p	0.47p	0.28p
-4	0.55p	1.0-1.26p	0.33p	0.38p
-2	0.50p	1.0-1.09p	0.27p	0.32p
0	0.50p	1.0-0.87p	0.12p	0.25p
+2	0.55p	1.0-1.07p	0.20p	0.32p
+4	0.55p	1.0-1.23p	0.30p	0.38p
+6	0.60p	1.0-1.33p	0.23p	0.50p

TABLE 3.10

Probabilities of wrong calling due to knock-on electrons only.

knock electrons into the gas of a tube and cause it to discharge even though the muon did not pass through its sensitive volume. This has the effect of again causing wrong cells or in some cases two cells to be allocated to the muon's trajectory. Assuming that the probability per layer of an extra tube adjacent to the track discharging is p , then the results shown in table 3.10 for the probabilities of cell allocation at different angles are obtained. It is to be noted that the probabilities in table 3.10 are for the effects of knock-on electrons alone whilst those shown in table 3.8 contain both the effects of inefficient flash-tubes and the inherent wrong celling of the electronic circuitry.

The effect of two cells being allocated is not considered here since it has already been taken into account in the momentum independent part of the correction factor discussed in section 3.3.3.

From the work of Ashton et al. (1973), who have analysed data from a 96 layer array of almost identical flash-tubes, a value for the probability per layer (p) of knock-on electrons discharging adjacent tubes of $\sim 2\%$ is found. Using this value and integrating over the triangular angular acceptance function gives the following :

Probability of setting adjacent high cell = 0.45%

Probability of setting adjacent low cell = 1.05%

Since both the probabilities of wrong celling due to knock-on electrons and due to intrinsic plus inefficient tubes are small, then it suffices simply to add the two together to give the final probabilities of being allocated to either high or low cells. This effectively means that it is assumed that there is no chance of the two occurring together on the same track. The probability of the trajectory being allocated to the correct cell is then simply that value corresponding intrinsic effects plus inefficient tubes minus the sum of the probabilities of high and low celling due to knock-on electrons.

(v) Final Shape.

Tables 3.11, 3.12, and 3.13 illustrate the final results of the probabilities of wrong celling at each level.

Level	Intrinsic	Intrinsic Plus Inefficient Tubes	Knock-on Electrons	Total
5	0.036	0.062	0.004	0.066
3	0.036	0.052	0.004	0.056
1	0.036	0.056	0.004	0.060

TABLE 3.11

Summary of probabilities of allocation to the next higher cell

Level	Intrinsic	Intrinsic Plus Inefficient Tubes	Knock-on Electrons	Total
5	0.038	0.047	0.011	0.058
3	0.038	0.043	0.011	0.054
1	0.038	0.044	0.011	0.055

TABLE 3.12.

Summary of probabilities of allocation to next lower cell

Level	Intrinsic	Intrinsic Plus Inefficient Tubes	Intrinsic Plus Inefficient Tubes Plus K.O. Electrons
5	0.926	0.848	0.833
3	0.926	0.879	0.864
1	0.926	0.866	0.851

TABLE 3.13.

Summary of probabilities of allocation to correct cell

If one assumes that the probabilities at each level are independent of the other two then the probabilities of being allocated to different categories can be calculated by simple consideration of the various combinations of $n_a - 2n_b + n_c$ (equation 2.3). It must be remembered that a given wrong celling in either levels 1 or 5 has the opposite effect on the allocated category as has the same wrong celling in level 3. If H_1 represents the probability

of being high at level 1, C_1 the probability of being allocated to the correct cell, and L_1 the probability of being low, and a similar notation for the other two levels, then the various combinations comprising the different categories are shown in table 3.14.

Error in Category Number.	Combinations of Errors in Celling to Produce Given Error in Category.
-4	$L_5 H_3 L_1$
-3	$C_5 H_3 L_1 + L_5 H_3 C_1$
-2	$H_5 H_3 L_1 + C_5 H_3 C_1 + L_5 H_3 H_1 + L_5 C_3 L_1$
-1	$H_5 H_3 C_1 + C_5 H_3 H_1 + C_5 C_3 L_1 + L_5 C_3 C_1$
0	$H_5 H_3 H_1 + H_5 C_3 L_1 + C_5 C_3 C_1 + L_5 C_3 H_1 + L_5 L_3 L_1$
+1	$H_5 C_3 C_1 + C_5 C_3 H_1 + C_5 L_3 L_1 + L_5 L_3 C_1$
+2	$H_5 C_3 H_1 + H_5 H_3 L_1 + C_5 L_3 C_1 + L_5 L_3 H_1$
+3	$H_5 L_3 C_1 + C_5 L_3 H_1$
+4	$H_5 L_3 H_1$

TABLE 3.14

Relation between wrong celling and category allocations.

Thus it is possible to be in error by as much as four categories.

Using these relations, combined with the probabilities of wrong celling given in tables 3.11, 3.12, and 3.13, gives the results shown in table 3.15. This table shows the category error probabilities, firstly for intrinsic wrong celling alone, then for the addition of inefficient flash-tubes and finally the total results including the effects of knock-on electrons.

Error in Category	Intrinsic	Intrinsic Plus Inefficient Flash -Tubes	Intrinsic plus Inefficient Flash -Tubes Plus K.O. Electrons
-4	0.01	0.01	0.02
-3	0.26	0.41	0.54
-2	3.22	4.02	4.29
-1	6.76	7.39	8.81
0	79.67	65.05	61.90
+1	6.43	9.22	9.63
+2	3.40	3.48	4.21
+3	0.26	0.43	0.57
+4	0.01	0.01	0.02

TABLE 3.15

Probabilities(%) of errors in category allocation for the case of intrinsic wrong celling, intrinsic wrong celling plus flash-tube inefficiencies, and finally for the inclusion of the effects of knock-on electrons.

The probability of being +4 or -4 categories in error is thus very small and has been considered negligible. One fact which emerges from table 3.15 is that the probabilities of being allocated to wrong categories are not symmetric about the correct category. For example, for the total case shown in the last column, there is a 9.7% chance of being allocated to the next higher category than the correct one, but only an 8.8% chance of the next lower category. This is a property of the flash-tube pattern and celling logic, hence when the field is reversed, or alternatively when the sign of the particle is changed, the effect will be the same as completely reversing the tube patterns and hence reversing the assymetry. In the experimental runs approximately equal numbers of particles were recorded in each field direction consequently an averaging of the probabilities of positive and negative category errors is justified.

COMBINED VALUES FOR CATEGORY N

$\Delta = \Delta - \frac{N}{2}$ cm.	N - 3	N - 2	N - 1	N	N + 1	N + 2	N + 3	Intrinsic of tube efficiencies	Plus the effect of knock-ons	Plus the effect of knock-ons
0	0	0.040	0.250	0.440	0.250	0.040	0	.3863	.3305	.3218
2		0.012	0.132	0.404	0.362	0.093	0.005	.3581	.3076	.3001
4		0.002	0.064	0.310	0.430	0.188	0.025	.2860	.2506	.2457
6		0	0.025	0.188	0.430	0.310	0.064	.1903	.1718	.1719
8			0.005	0.093	0.362	0.404	0.132	.1121	.1066	.1095
1.0			0	0.040	0.250	0.440	0.250	.0636	.0642	.0682
1.2				0.012	0.132	0.404	0.362	.0327	.0353	.0391
1.4				0.002	0.064	0.310	0.430	.0173	.0200	.0230
1.6				0	0.025	0.188	0.430	.0091	.0108	.0130
1.8					0.005	0.093	0.362	.0045	.0054	.0066
2.0					0	0.040	0.250	.0021	.0025	.0032
2.2						0.012	0.132	.0008	.0010	.0013
2.4						0.002	0.064	.0003	.0003	.0005
2.6						0	0.025	.0001	.0001	.0001
2.8							0.005	0	0	0
3.0							0			

TABLE 3.16

Illustrating the effect of the three causes of wrong calling to the basic category acceptance shape

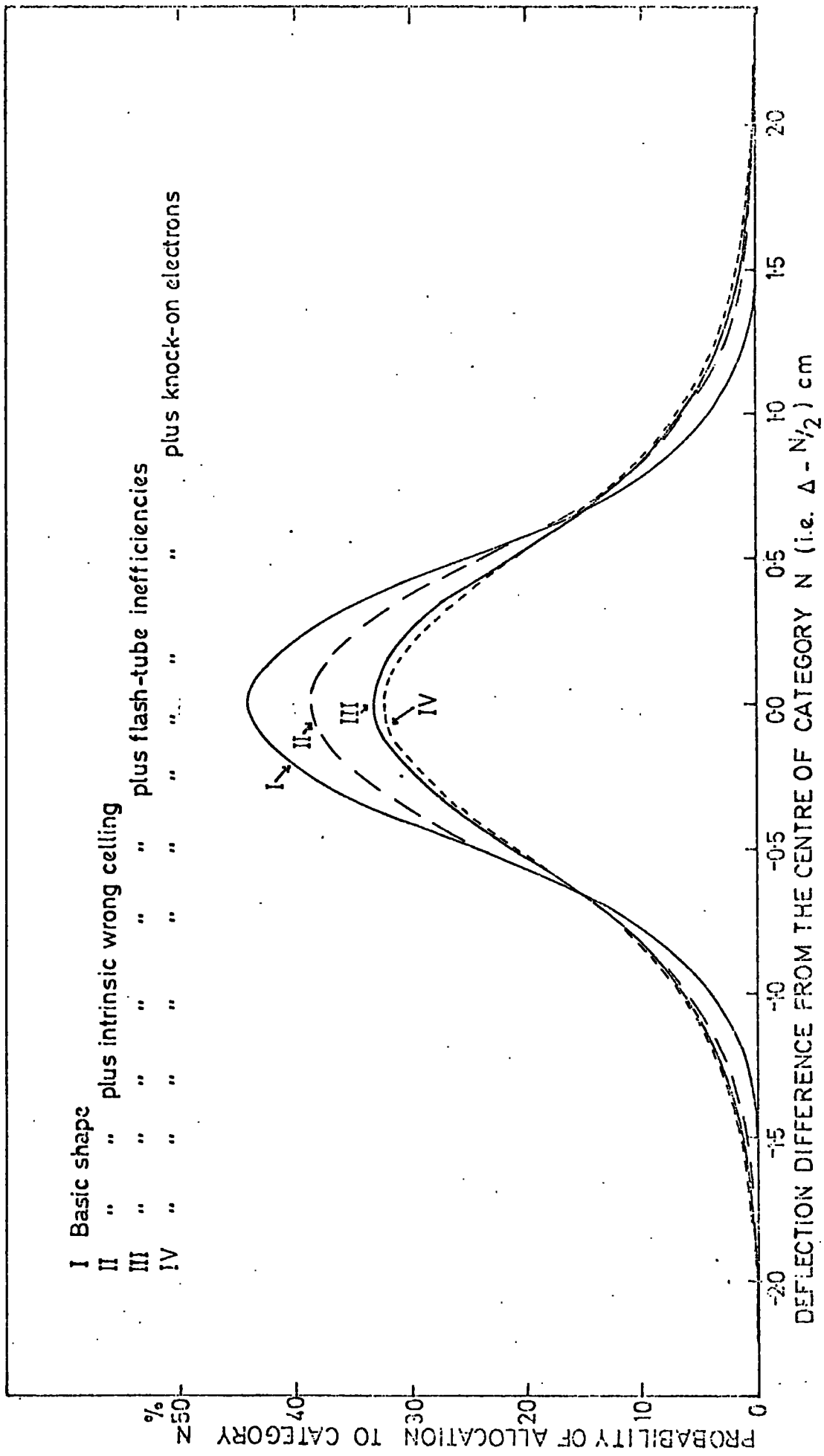


FIGURE 3.15 Illustrating the Category Acceptance Function from Method A.

The method adopted to combine these probabilities with the basic shape derived in section (i) is to add together the basic acceptance functions, at given deflections, for categories $N - 3$ to $N + 3$, each being weighted according to the probabilities of being in error by $+3$ to -3 categories respectively. (i.e. the weight given to $N - 3$ is the probability of an error of $+3$ categories, $N - 2$ that of $+2$ categories, etc). This gives the final category acceptance functions for the central category N , and is illustrated in table 3.16.

In this table N is the category number whose shape is being derived, and Δ the deflection, hence Δ' in the first column represents the difference from the central value of Δ (i.e. $N/2$ cm.) for each category. Columns 2 to 6 show the basic category acceptance functions for the categories $N - 3$ to $N + 3$, all of which contribute to category N due to the probability of wrong categorization, as discussed. The last three columns show the resulting shape of the acceptance functions, firstly when the effects of intrinsic wrong celling alone are considered, then with the addition of inefficient flash-tubes, and finally with the addition of all three factors including the effect of knock-on electrons. The data shown in these three columns, representing the successive addition of the three causes of incorrect celling to the category acceptance function shape, are shown graphically in figure 3.15, where it has been assumed the functions are symmetric about $\Delta' = 0$.

3.4.3 Method E

The second method of calculating the category acceptance function necessitated the setting up of a computer model of the relevant parts of the spectrograph. Such a model involved bending particles in the magnetic field, and projecting them in straight lines across the gaps between the magnet blocks. Models of the momentum selector trays, complete with celling logic were located at their correct positions in the centre and at the extremities of the 'model' spectrograph. Particles of given momenta, and hence known deflection, were fired through the model instrument with the triangular incident angle distribution, and with a random lateral position across one tube spacing

(this is sufficient since the tube pattern and the electronic circuitry repeats every tube spacing). The efficiencies of the flash-tubes estimated in section 3.3.3. were employed, the tubes being assumed to be uniformly efficient across their entire internal diameter.

Initially, for particular momenta, the proportion of events allocated to category zero was calculated. The results of this are shown in figure 3.16 where they are compared with the curve calculated by Method A using the intrinsic plus flash-tube inefficiency wrong celling probabilities. This comparison is made since no account is taken of knock-on electrons from the glass of the flash-tubes.

3.4.4 Comparison of Methods A and B

As can be seen the two methods do not agree, the distribution from Method A being slightly broader. The reason for the disagreement is thought to be in the fact that the probabilities of wrong celling for each level are not independent, as has been assumed in Method A. Figure 3.17 illustrates this none independence. For given angles from -8° to $+8^\circ$ to the vertical 1000 particles of infinite momentum (i.e. having straight line trajectories and hence no deflection) were fired through the model of the spectrograph (multiple scattering of the particles was neglected), and at each level it was ascertained whether or not the correct cell had been allocated by the celling logic. The graphs in figure 3.17 show the number of times wrong celling occurred in each of two levels simultaneously for the same track. The histograms show the results obtained and the solid line is that expected from the individual probabilities of wrong celling at each level assuming complete independence of cell allocation at the two levels. There is little agreement between observation and expectation, indicating that the three levels are not independent. However the situation depicted in Method B is artificial in that everything is precisely defined. In practice this is not the case and it is considered the three levels are far less inter-related than predicted by the Method B. Firstly, as will be shown in the next chapter, the alignment of the trays is only known to within ~ 0.5 mm and this is most likely comparable in size with the extent of any correlations existing in

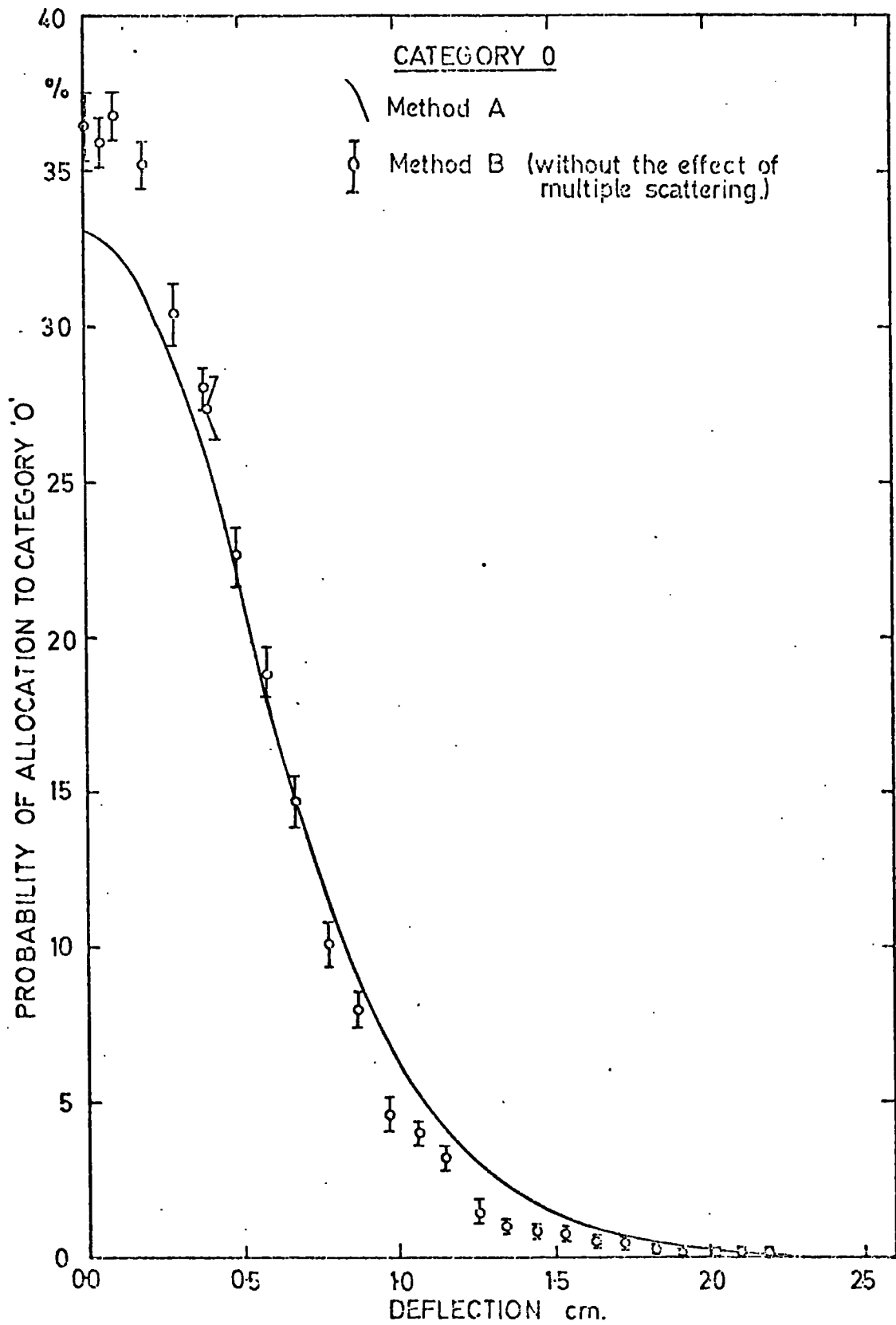


FIGURE 3.16 Comparison between the Category 0 Acceptance Function from Methods A and B.

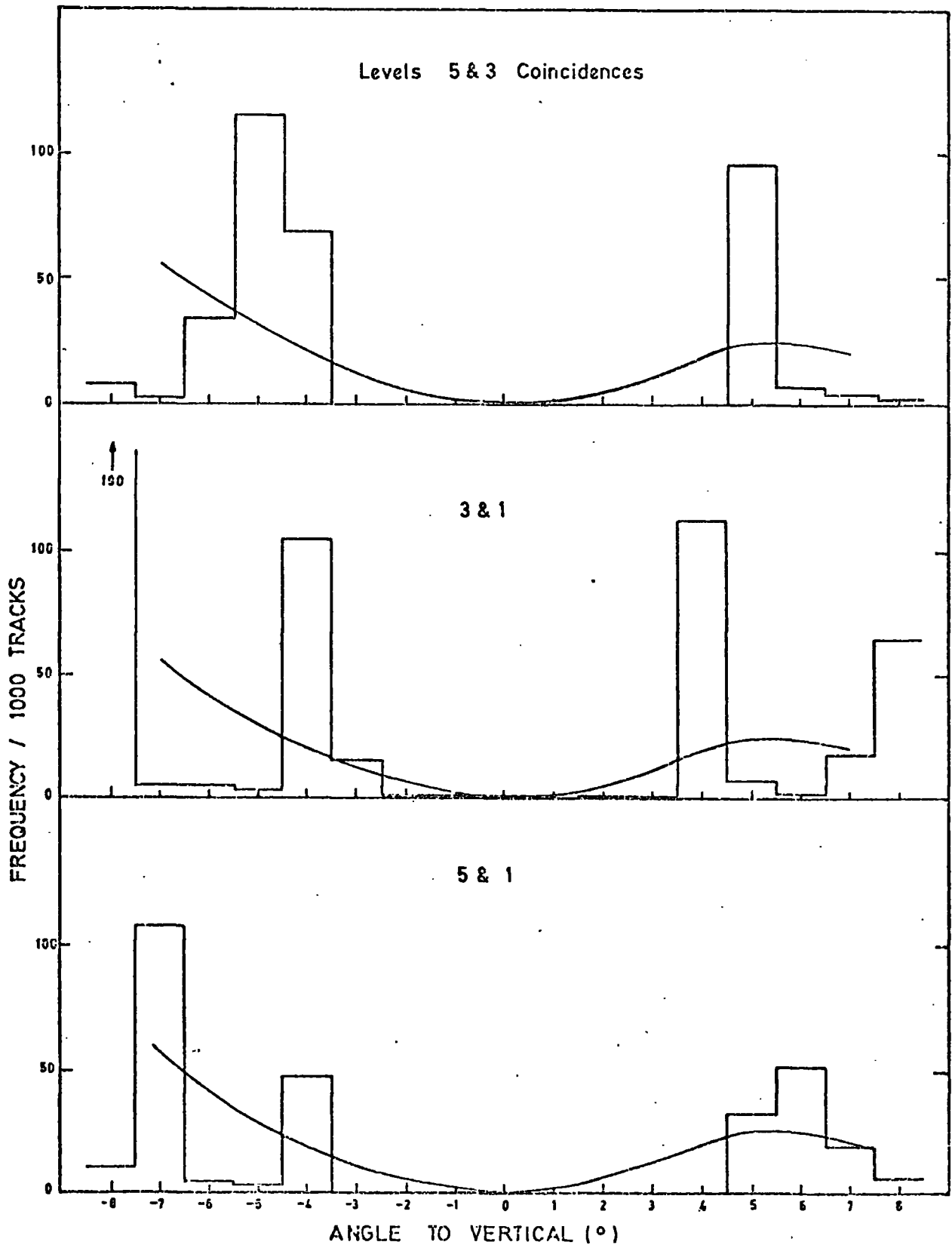


FIGURE 3.17 Coincidences between Wrong Ceiling at the Different Levels calculated in a Monte Carlo Simulation. The Curves are those Expected assuming Complete Independence of the Ceiling at Each Level.

the precisely defined situation of Method B, and secondly, and probably most important, the effect of multiple coulomb scattering of the particles track in the iron will remove the correlations.

To test this assumption the effect of multiple scattering was added to the computer simulation, the particles being given a lateral shift and additional angular deflection according to the equations of Rossi and Greisen (1942), and as outlined in Appendix C. For different momenta the numbers of particles allocated to categories 0 to 4 were counted. Momenta which correspond roughly to a deflection range 0 to 4 cm. were considered. The results are shown in figure 3.18 as the experimental points, the solid line being that calculated using Method A. It can be seen that as the category number increases, then indeed the shape of the category acceptance function calculated by the two methods begin to agree. This agreement at higher deflections is due to the absolute value of the multiple scattering increasing as the deflection increases, and hence any ceiling correlations between the levels being more and more removed.

Since it is believed that in practice each level in the spectrograph is very nearly independent of the others, and since it appears that the only difference between the two methods would occur with the first few categories, and these would be removed due to uncertainties in tray positions, then for the final shape of the category acceptance function, that calculated in Method A with allowance for all three effects of wrong ceiling has been used. It is found that at higher category numbers the shape of the function is not drastically changed, and also in this region the measured spectrum is not as sensitive to the shape, due to the form of the deflection spectrum, as are the lower numbered categories.

3.5 Summary

In this chapter it has been shown how the corrected trial deflection spectrum is calculated, and how the shape of the category acceptance functions are estimated. The next chapter will show how these two are brought together to predict the observed quantities.

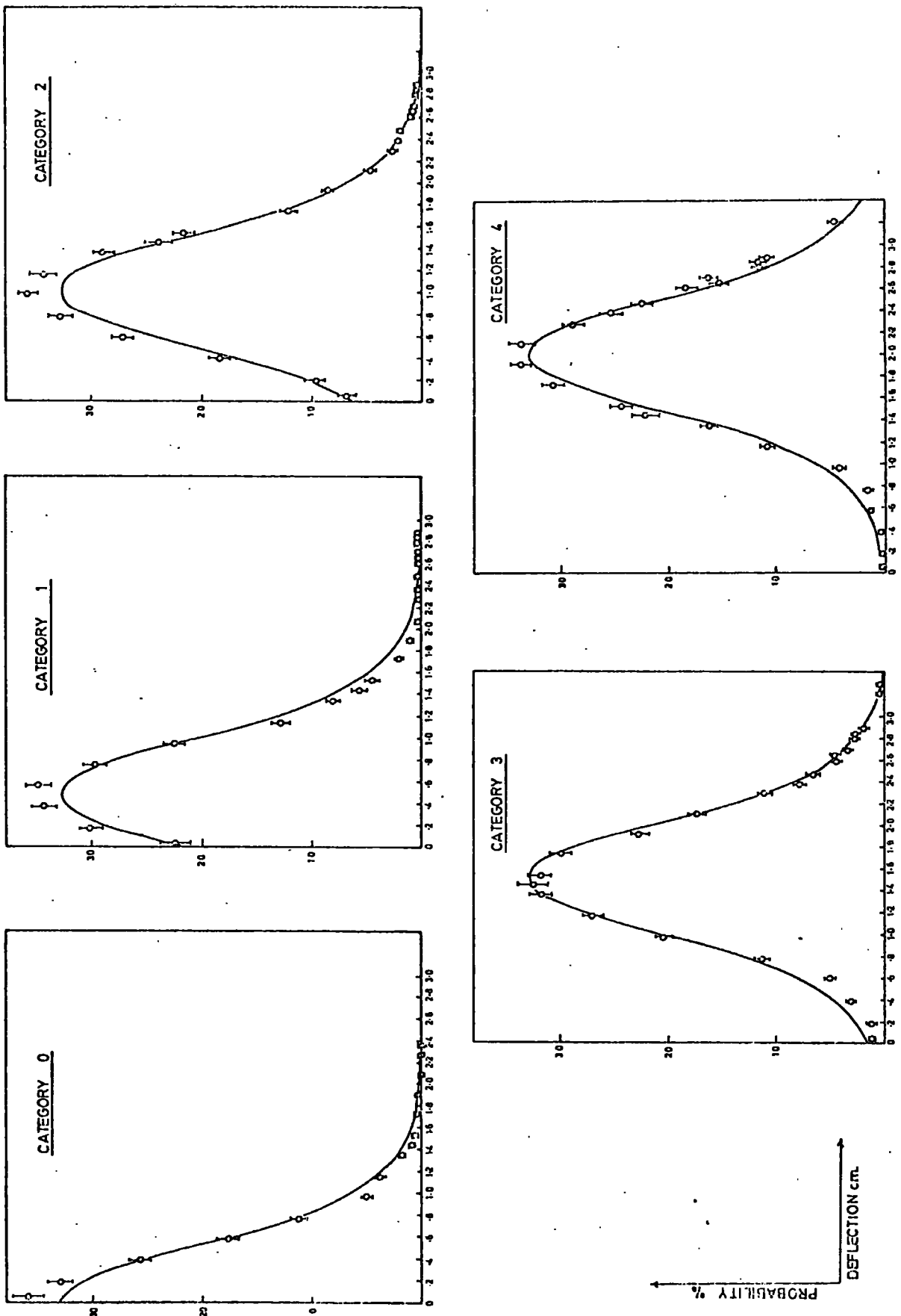


FIGURE 3.18 Comparison between Method A and Method B including the Effects of Multiple Scattering.

CHAPTER 4

THE MOMENTUM SPECTRUM - RESULTS

4.1 Introduction

This chapter is concerned with the prediction of the quantities measured with the spectrograph, taking into account the factors discussed in chapter 3, and their comparison with the experimental data collected. The various sources of error are considered and finally a best estimate of the muon spectrum is presented.

The basic allocation in the device RUDI is into the $\frac{1}{2}$ cm. categories discussed in chapter 3. However as indicated in chapter 2, it is possible to alter the width of the categories such that effectively the contents of adjacent categories are added together in pairs and displayed in this fashion on the FHA. The advantage of this technique is that larger deflections, and hence lower momenta may be studied. The combinations of the cells are shown in chapter 2.

No attempt has been made to analyse the data contained in category 23 with either category configuration (category 23 contains the sum of all the categories ≥ 23). It was considered that due to uncertainties in the performance of the momentum selector tray cell allocation logic for low momentum particles at large angles, and uncertainty in the overall spectrograph acceptance, no useful measurements at the low momenta corresponding to category 23 could be made.

Apart from the experimental runs with the magnetic field on, several runs were made with zero field. The purpose of these is to check the alignment of the flash-tube trays, and this is discussed in section 4.5.1. Sections 4.3 and 4.4 contain the predicted and experimental results with the field on.

4.2 The Deflection Spectrum.

Table 4.1 tabulates the trial deflection spectrum at 1 cm. deflection intervals, together with the corrections as derived in chapter 3. Two points should be noted concerning the mechanics of the calculations: (a) the correction for multiple coulomb scattering given in section 3.3.1 has not been applied to the deflection spectrum directly. As it is small, and varies slowly with deflection, it suffices to apply the correction corresponding to the mean deflection of the category, to the expected rates calculated for that category, as derived in the next section.

(b) in order to give an absolute determination of the spectrum a correction has to be made for the efficiencies of the scintillation counters which provide the main trigger for the system. This efficiency has been measured as described later in chapter 7, in conjunction with the absolute rate experiment, and has been assumed to be independent of the muon's momentum. Allowance for the efficiency is not made in the deflection spectrum but in the effective live time of the experimental runs. The expected rates are thus quoted in terms of units of effective time.

As will become apparent later, the statistical errors on the observed numbers of events in a category can be as small as $\sim 1\%$, hence the calculations have been performed with extreme care, and it is considered that any errors resulting from the mechanics of the calculations will be insignificant.

4.3 Expected Rates and Mean Momenta.

The expected rates for the $\frac{1}{2}$ cm. categories are calculated from the following equation:

$$\text{Rate}_n = \int_{-\infty}^{+\infty} F_n(\Delta) N_c(\Delta) d\Delta \quad 4.1$$

and the mean momentum of the category corresponding to the mean deflection which is calculated from :

$$\bar{\Delta}_n = \frac{\int_{-\infty}^{+\infty} \Delta F_n(\Delta) N_c(\Delta) d\Delta}{\text{Rate}_n} \quad 4.2$$

Deflection $\Delta\text{cm.}$	Momentum $p \text{ GeV/c}$	Intensity $N(p)$ $\text{s}^{-1} \text{cm}^{-2} \text{sr}^{-1}$ $(\text{GeV/c})^{-1}$	$d\Delta/dp$ $\text{cm}(\text{GeV/c})^{-1}$	$N(\Delta)$ $\text{s}^{-1} \text{cm}^{-2} \text{sr}^{-1} \text{cm}^{-1}$	Overall Acceptance $\text{cm}^2 \text{sr}$	Probability of not being rejected	Corrected Deflection spectrum $\text{s}^{-1} \text{cm}^{-1}$
0	∞	0	~	0	408.0	~	0
1	393.5	$3.479 \cdot 10^{-9}$.002566	$1.356 \cdot 10^{-6}$	408.0	.656	$3.629 \cdot 10^{-4}$
2	198.7	$3.423 \cdot 10^{-8}$.01027	$3.333 \cdot 10^{-6}$	408.0	.718	$9.764 \cdot 10^{-4}$
3	133.8	$1.218 \cdot 10^{-7}$.02310	$5.272 \cdot 10^{-6}$	408.0	.747	$1.607 \cdot 10^{-3}$
4	101.3	$2.923 \cdot 10^{-7}$.04107	$7.117 \cdot 10^{-6}$	408.0	.764	$2.218 \cdot 10^{-3}$
5	81.2	$5.727 \cdot 10^{-7}$.06380	$8.976 \cdot 10^{-6}$	407.2	.774	$2.829 \cdot 10^{-3}$
6	68.4	$9.559 \cdot 10^{-7}$.09055	$1.056 \cdot 10^{-5}$	406.8	.781	$3.355 \cdot 10^{-3}$
7	59.2	$1.457 \cdot 10^{-6}$.1259	$1.157 \cdot 10^{-5}$	406.4	.786	$3.696 \cdot 10^{-3}$
8	52.3	$2.080 \cdot 10^{-6}$.1644	$1.265 \cdot 10^{-5}$	405.6	.790	$4.053 \cdot 10^{-3}$
9	47.0	$2.813 \cdot 10^{-6}$.2081	$1.352 \cdot 10^{-5}$	404.7	.792	$4.333 \cdot 10^{-3}$
10	42.8	$3.657 \cdot 10^{-6}$.2574	$1.421 \cdot 10^{-5}$	403.9	.794	$4.557 \cdot 10^{-3}$
11	39.11	$4.689 \cdot 10^{-6}$.3109	$1.508 \cdot 10^{-5}$	402.9	.797	$4.842 \cdot 10^{-3}$
12	36.19	$5.810 \cdot 10^{-6}$.3695	$1.572 \cdot 10^{-5}$	401.9	.799	$5.048 \cdot 10^{-3}$
13	33.67	$7.068 \cdot 10^{-6}$.4340	$1.629 \cdot 10^{-5}$	400.7	.800	$5.222 \cdot 10^{-3}$
14	31.57	$8.397 \cdot 10^{-6}$.5040	$1.666 \cdot 10^{-5}$	399.4	.802	$5.337 \cdot 10^{-3}$
15	29.70	$9.856 \cdot 10^{-6}$.5790	$1.702 \cdot 10^{-5}$	398.0	.803	$5.439 \cdot 10^{-3}$
16	28.09	$1.141 \cdot 10^{-5}$.6600	$1.729 \cdot 10^{-5}$	396.6	.804	$5.513 \cdot 10^{-3}$
17	26.65	$1.310 \cdot 10^{-5}$.7440	$1.758 \cdot 10^{-5}$	395.1	.805	$5.591 \cdot 10^{-3}$
18	25.41	$1.484 \cdot 10^{-5}$.8395	$1.768 \cdot 10^{-5}$	393.7	.806	$5.610 \cdot 10^{-3}$
19	24.30	$1.662 \cdot 10^{-5}$.9325	$1.782 \cdot 10^{-5}$	392.1	.806	$5.632 \cdot 10^{-3}$
20	23.31	$1.844 \cdot 10^{-5}$	1.0331	$1.785 \cdot 10^{-5}$	390.5	.807	$5.625 \cdot 10^{-3}$
21	22.36	$2.053 \cdot 10^{-5}$	1.140	$1.800 \cdot 10^{-5}$	388.8	.807	$5.648 \cdot 10^{-3}$
22	21.57	$2.258 \cdot 10^{-5}$	1.256	$1.798 \cdot 10^{-5}$	386.8	.808	$5.657 \cdot 10^{-3}$
23	20.72	$2.479 \cdot 10^{-5}$	1.372	$1.807 \cdot 10^{-5}$	384.7	.803	$5.617 \cdot 10^{-3}$
24	20.05	$2.686 \cdot 10^{-5}$	1.500	$1.791 \cdot 10^{-5}$	383.9	.808	$5.556 \cdot 10^{-3}$

Table 4.1

Illustrating the Calculation of the Corrected Deflection Spectrum

Category No.	$\frac{1}{2}$ cm. categories			1 cm. categories		
	mean deflection cm	mean momentum GeV/c	Rate per effective hour	mean deflection cm	mean momentum GeV/c	Rate per effective hour
0	0.89	442.	0.1230	1.05	376.	0.5020
1	1.10	358.	0.3782	1.68	236.	1.913
2	1.44	274.	0.7217	2.50	260.	3.968
3	1.82	214.	1.191	3.41	118.	6.140
4	2.25	177.	1.721	4.35	93.0	8.158
5	2.69	145.	2.267	5.33	76.6	9.391
6	3.15	128.	2.811	6.30	65.3	11.53
7	3.62	112.	3.331	7.29	57.0	12.81
8	4.10	98.3	3.830	8.28	50.7	13.90
9	4.58	88.3	4.328	9.27	45.8	14.86
10	5.07	80.0	4.790	10.27	41.7	15.67
11	5.56	73.7	5.210	11.27	38.3	16.41
12	6.05	67.9	5.591	12.26	35.3	17.03
13	6.54	63.0	5.937	13.26	33.1	17.51
14	7.04	58.9	6.255	14.26	31.0	17.90
15	7.53	55.2	6.557	15.26	29.3	18.18
16	8.03	52.1	6.828	16.25	27.7	18.38
17	8.53	49.3	7.085	17.25	26.3	18.52
18	9.02	47.1	7.313	18.25	25.1	18.61
19	9.52	44.8	7.535	19.25	24.1	18.69
20	10.02	43.8	7.745	20.25	23.1	18.69
21	10.52	40.8	7.939	21.25	22.1	18.64
22	11.02	39.3	8.122	22.25	21.3	18.54

Table 4.2.

The mean momenta and expected rates for the categories

where $F_n(\Delta)$ is the category acceptance function as given in section 3.4, and $N_c(\Delta)$ the corrected deflection spectrum given in the previous section, 4.2. For the 1 cm. categories the expected rates and mean momenta are calculated by combining the appropriate two $\frac{1}{2}$ cm. categories. Table 4.2 shows the mean deflections and the corresponding mean momenta of the categories and also the final expected rates for each category. Results are given both for the $\frac{1}{2}$ and 1 cm. categories. The rates are quoted as per effective hour and have been corrected for multiple scattering in the manner described.

It is to be noted that the exact values of the mean momenta are not critical so long as the shape of the spectrum with respect to the trial spectrum does not vary rapidly over the extent of the relevant category.

4.4 Full Field Runs

4.4.1 Introduction

The spectrograph was operated for the purpose of this experiment for a period of 8 months from April to November 1972. During this time data was collected both in the $\frac{1}{2}$ cm. and 1 cm. categories, a total of over 10^6 events being recorded. Operation was not continuous, being divided into a series of 'runs', each run being approximately 12 hours in duration, and generally taking place overnight. After each run the magnetic field was reversed to minimise any instrumental biases. Roughly equal numbers of particles were recorded in each field direction. Table 4.3 shows a rough breakdown of the numbers of particles collected, and the relevant times. It can be seen that the total running time was 3182.3 hours, which due to a paralysis of ~3.5 seconds between events, resulted in a live time of 1507.8 hours. It is also apparent from the table that the great proportion of data, ~87% for the $\frac{1}{2}$ cm. categories and ~73% for the 1 cm. categories, lies in category 23. This leaves a total of 105523 particles in the $\frac{1}{2}$ cm. and 91911 in the 1 cm. categories which can be analysed. The division of that data into categories 0 - 22 for both types of category is shown in table 4.4 where positive and negative muons, and both field directions, are

	$\frac{1}{2}$ CM. CATEGORIES			1 CM. CATEGORIES				
	Positive Field Categories 0 - 22	Total Stored	Negative Field Categories 0 - 22	Total Stored	Positive Field Categories 0 - 22	Total Stored	Negative Field Categories 0 - 22	Total Stored
μ^+	29830	215744	29236	222104	25697	66136	26154	68617
μ^-	23357	174978	23100	166142	20148	53275	19912	50795
Total	53187	390722	52336	388246	45845	119411	46066	119412
Running time (hrs)	1232.9		1215.4		370.5			369.5
Live time (hrs)	579.9		577.2		175.2			175.5

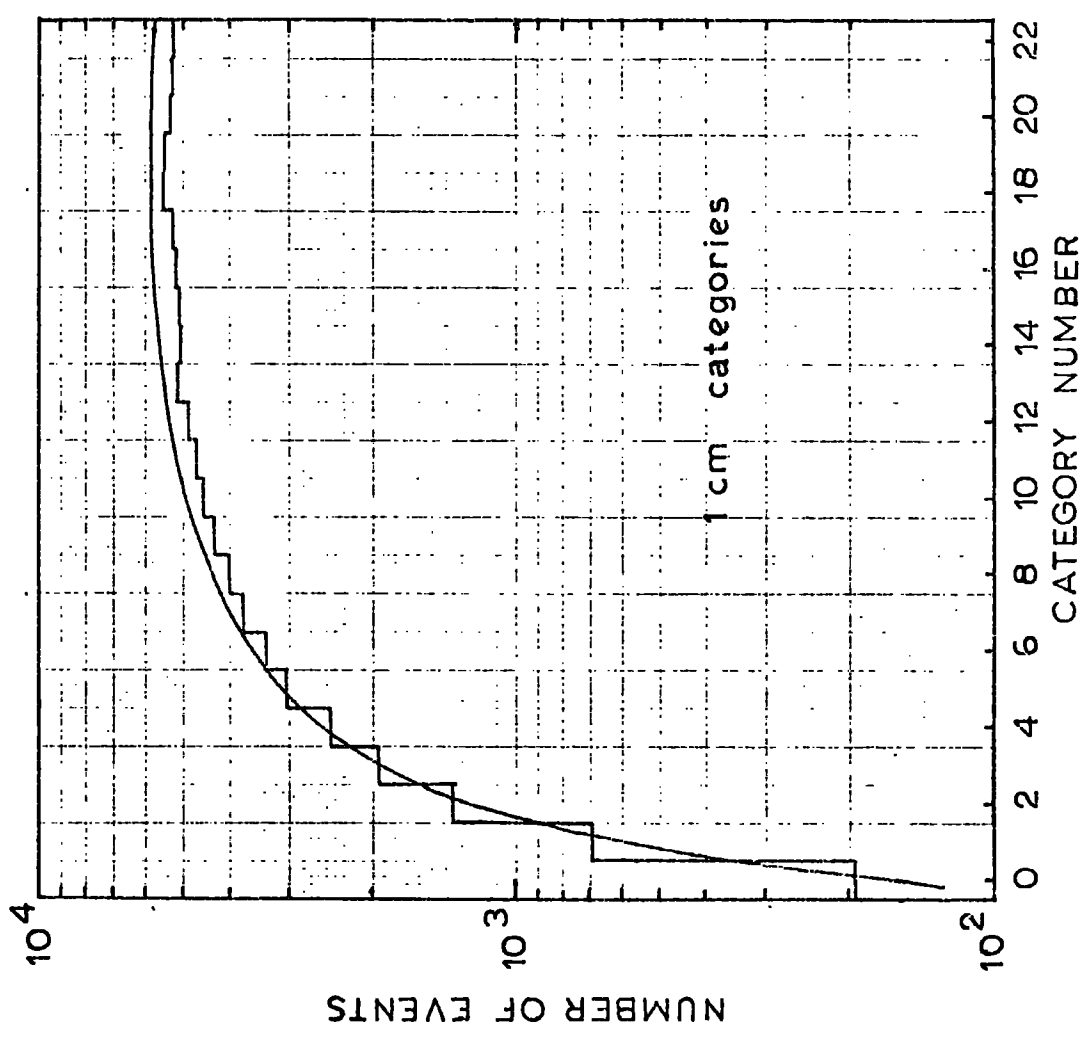
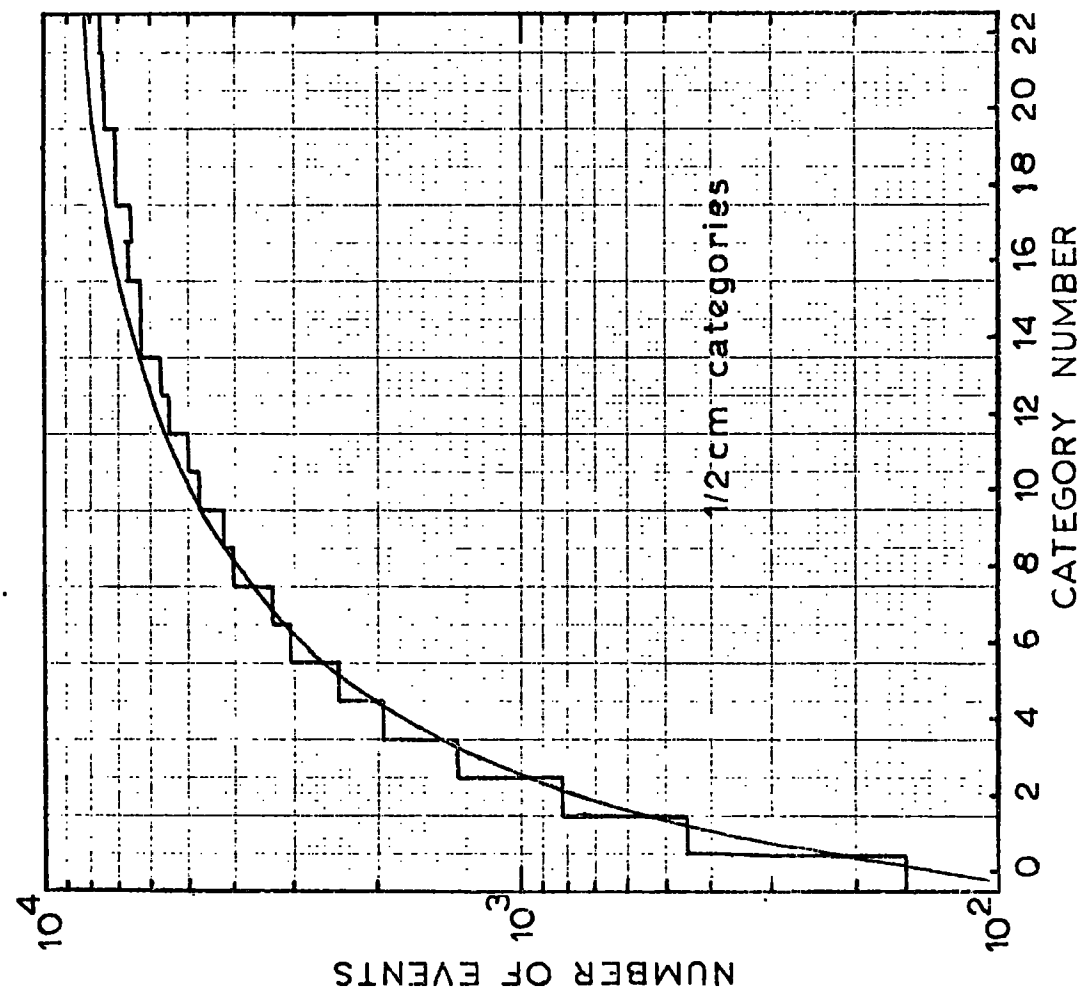
Table 4.3

Summary of the data collected

	$\frac{1}{2}$ CM. CATEGORIES				1 CM. CATEGORIES			
	Positive Field		Negative Field		Positive Field		Negative Field	
	μ^+	μ^-	μ^+	μ^-	μ^+	μ^-	μ^+	μ^-
0	31	45	41	41	55	45	43	51
1	152	82	124	92	198	144	200	156
2	222	176	244	176	384	301	376	307
3	398	277	369	314	538	416	563	451
4	543	424	525	451	658	545	689	550
5	680	522	664	538	841	628	886	677
6	852	658	857	670	978	753	941	710
7	950	749	883	726	1046	834	1058	832
8	1096	883	1149	920	1100	836	1207	863
9	1153	905	1150	990	1245	978	1153	925
10	1363	1090	1277	1045	1205	1035	1353	981
11	1405	1071	1408	1116	1293	1035	1330	1042
12	1615	1236	1443	1172	1432	1088	1337	1042
13	1576	1280	1548	1274	1445	1096	1493	1123
14	1784	1433	1737	1326	1480	1114	1403	1080
15	1808	1402	1686	1374	1418	1123	1453	1110
16	1973	1467	1926	1398	1412	1173	1460	1154
17	1860	1458	1834	1462	1486	1159	1465	1131
18	1931	1597	1977	1602	1506	1170	1600	1193
19	1985	1618	2003	1556	1527	1189	1543	1186
20	2066	1682	2137	1607	1476	1192	1542	1095
21	2160	1660	2106	1636	1486	1153	1543	1114
22	2227	1642	2148	1614	1488	1141	1507	1139
TOTAL	29830	23357	29236	23100	25647	20148	26154	19912

Table 4.4

The data from categories 0-22 for both
signs of muon and field direction



FIGURES 4.1 & 4.2 The Total Observed Numbers of Events in the 1/2 cm. and the 1cm. Categories, (Histograms). The Curves represent those Expected.

indicated separately. Each of these numbers is the total of the 8 angular ranges into which RUDI allocates the events. These angular-range divisions provide a useful check that the instrument is working correctly. The original data was examined carefully for any obvious errors due to instrumental malfunction and any such data were rejected.

Figures 4.1 and 4.2 show the measured total category distributions for the $\frac{1}{2}$ cm. and 1 cm. categories respectively. Also shown on these diagrams is a line drawn through the expected values. For the $\frac{1}{2}$ cm. categories it is seen that there appears to be some evidence of grouping of adjacent categories, particularly in the middle region. This is considered to be due to some instrumental edge effect, (at present unknown), and is not important since it is believed that the mean values of the adjacent categories will be correct. In the 1 cm. distribution it is seen that the grouping disappears lending support to the correctness of the mean values of the $\frac{1}{2}$ cm. distribution. Any fluctuations in the 1 cm. distribution can be shown to be statistical and only one frequency value is outside 2 standard deviations from a smooth line drawn through the data, approximately $2/3$ lying within 1 standard deviation.

4.4.2 Comparison of the Observed data with Expectation

The total live time for the $\frac{1}{2}$ cm. categories was 1156.9 hours and for the 1 cm., 350.7 hours. When combined with the scintillation counter efficiency of 0.894, as derived in chapter 7, these give effective times of 1034.3 and 313.5 hours respectively. These times were measured with an electronic scaler counting mains frequency at 50 Hz, and are considered accurate to a fraction of a percent. Table 4.5 is a comparison of the observed numbers of events with those expected in the above effective times, the latter being calculated from the rates given in table 4.2. The comparison is also shown in figure 4.1 and 4.2.

It is seen that in both cases the observed numbers lie above expectations in the low category numbers (high energy), and level off at nearly 10% below expectation at high category numbers. The implications of this are

Category No.	$\frac{1}{2}$ cm. Categories			1 cm. Categories		
	Expected No.	Observed No.	Obs/Exp	Expected No.	Observed No.	Obs/Exp
0	128	158	1.234	157	194	1.236
1	391	450	1.151	599	689	1.165
2	746	818	1.097	1248	1368	1.096
3	1231	1358	1.103	1923	1968	1.023
4	1778	1943	1.093	2555	2451	0.959
5	2342	2404	1.026	3129	3032	0.969
6	2905	3037	1.045	3611	3362	0.937
7	3442	3308	0.961	4012	3770	0.940
8	3958	4048	1.023	4353	4006	0.920
9	4472	4198	0.939	4654	4301	0.924
10	4950	4775	0.965	4908	4574	0.932
11	5383	5000	0.929	5140	4700	0.914
12	5777	5466	0.946	5334	4899	0.918
13	6135	5678	0.926	5484	5157	0.940
14	6463	6280	0.972	5606	5077	0.906
15	6775	6270	0.925	5694	5104	0.896
16	7055	6764	0.959	5757	5199	0.903
17	7321	6614	0.903	5800	5241	0.904
18	7557	7107	0.940	5829	5469	0.938
19	7786	7162	0.920	5854	5445	0.930
20	8003	7492	0.936	5854	5305	0.905
21	8203	7562	0.922	5838	5296	0.907
22	8392	7631	0.909	5807	5275	0.908

Table 4.5

Comparison of Observed to Expected Numbers

Category No.	Mean Momentum p GeV/c	$p^3 N(p)_{\text{TRIAL}} s^{-1} \text{cm}^{-2} \text{sr}^{-1} (\text{GeV}/c)^2$	$N(p)_{\text{TRIAL}} s^{-1} \text{cm}^{-2} \text{sr}^{-1} (\text{GeV}/c)^4$	$\frac{\text{observed}}{\text{Expected}}$	$N(p)_{\text{MEAS}} s^{-1} \text{cm}^{-2} \text{sr}^{-1} (\text{GeV}/c)^4$	$N(p)_{\text{MEAS}} \text{ for } 90\% \text{ burst correction}$	% error
0	442.	.2003	$2.320 \cdot 10^{-9}$	1.234	$2.863 \cdot 10^{-9}$	$2.764 \cdot 10^{-9}$	8.0
1	358.	.2192	$4.777 \cdot 10^{-9}$	1.151	$5.498 \cdot 10^{-9}$	$5.328 \cdot 10^{-9}$	4.7
2	274.	.2425	$1.179 \cdot 10^{-8}$	1.097	$1.293 \cdot 10^{-8}$	$1.260 \cdot 10^{-8}$	3.5
3	214.	.2627	$2.681 \cdot 10^{-8}$	1.103	$2.957 \cdot 10^{-8}$	$2.893 \cdot 10^{-8}$	2.7
4	177.	.2764	$4.984 \cdot 10^{-8}$	1.093	$5.448 \cdot 10^{-8}$	$5.352 \cdot 10^{-8}$	2.3
5	145.	.2893	$9.490 \cdot 10^{-8}$	1.026	$9.737 \cdot 10^{-8}$	$9.603 \cdot 10^{-8}$	2.0
6	128.	.2955	$1.409 \cdot 10^{-7}$	1.045	$1.472 \cdot 10^{-7}$	$1.454 \cdot 10^{-7}$	1.8
7	112.	.3004	$2.138 \cdot 10^{-7}$	0.961	$2.055 \cdot 10^{-7}$	$2.037 \cdot 10^{-7}$	1.7
8	98.3	.3043	$3.204 \cdot 10^{-7}$	1.023	$3.278 \cdot 10^{-7}$	$3.252 \cdot 10^{-7}$	1.6
9	88.3	.3060	$4.445 \cdot 10^{-7}$	0.939	$4.174 \cdot 10^{-7}$	$4.149 \cdot 10^{-7}$	1.5
10	80.0	.3068	$5.992 \cdot 10^{-7}$	0.965	$5.782 \cdot 10^{-7}$	$5.753 \cdot 10^{-7}$	1.4
11	73.7	.3065	$7.656 \cdot 10^{-7}$	0.929	$7.112 \cdot 10^{-7}$	$7.084 \cdot 10^{-7}$	1.4
12	67.9	.3059	$9.772 \cdot 10^{-7}$	0.946	$9.244 \cdot 10^{-7}$	$9.216 \cdot 10^{-7}$	1.4
13	63.0	.3041	$1.216 \cdot 10^{-6}$	0.926	$1.126 \cdot 10^{-6}$	$1.123 \cdot 10^{-6}$	1.3
14	58.9	.3020	$1.478 \cdot 10^{-6}$	0.972	$1.437 \cdot 10^{-6}$	$1.434 \cdot 10^{-6}$	1.3
15	55.2	.2998	$1.782 \cdot 10^{-6}$	0.925	$1.648 \cdot 10^{-6}$	$1.646 \cdot 10^{-6}$	1.3
16	52.1	.2972	$2.102 \cdot 10^{-6}$	0.959	$2.016 \cdot 10^{-6}$	$2.014 \cdot 10^{-6}$	1.2
17	49.3	.2944	$2.457 \cdot 10^{-6}$	0.903	$2.219 \cdot 10^{-6}$	$2.217 \cdot 10^{-6}$	1.2
18	47.1	.2922	$2.795 \cdot 10^{-6}$	0.940	$2.628 \cdot 10^{-6}$	$2.628 \cdot 10^{-6}$	1.2
19	44.8	.2895	$3.220 \cdot 10^{-6}$	0.920	$2.962 \cdot 10^{-6}$	$2.962 \cdot 10^{-6}$	1.2
20	42.8	.2865	$3.654 \cdot 10^{-6}$	0.936	$3.420 \cdot 10^{-6}$	$3.420 \cdot 10^{-6}$	1.2
21	40.8	.2835	$4.174 \cdot 10^{-6}$	0.922	$3.848 \cdot 10^{-6}$	$3.848 \cdot 10^{-6}$	1.1
22	39.3	.2810	$4.629 \cdot 10^{-6}$	0.909	$4.208 \cdot 10^{-6}$	$4.208 \cdot 10^{-6}$	1.1

TABLE 4.6

The Measured Spectrum of the π^+ cm. Categories.

Category No.	Mean Momentum p GeV/c	$p^3 N(p)_{\text{TRIAL}}$ $s^{-1} \text{cm}^{-2} \text{s}^{-1} (\text{GeV}/c)^2$	$K(p)_{\text{TRIAL}}$ $s^{-1} \text{cm}^{-2} \text{s}^{-1} (\text{GeV}/c)^{-1}$	Observed Expected	$N(p)_{\text{HEAS}}$ $s^{-1} \text{cm}^{-2} \text{s}^{-1} (\text{GeV}/c)^{-1}$	$N(p)_{\text{HEAS}}$ for 90% burst correction	% error
0	367.	.2152	$4.048 \cdot 10^{-9}$	1.236	$5003 \cdot 10^{-9}$	$4.843 \cdot 10^{-9}$	7.2
1	236.	.2508	$1.908 \cdot 10^{-8}$	1.165	$2.223 \cdot 10^{-8}$	$2.171 \cdot 10^{-8}$	3.8
2	160.	.2832	$6.914 \cdot 10^{-8}$	1.096	$7.578 \cdot 10^{-8}$	$7.459 \cdot 10^{-8}$	2.7
3	118.	.2988	$1.819 \cdot 10^{-7}$	1.023	$1.861 \cdot 10^{-7}$	$1.842 \cdot 10^{-8}$	2.3
4	93.0	.3054	$3.797 \cdot 10^{-7}$	0.959	$3.641 \cdot 10^{-7}$	$3.616 \cdot 10^{-7}$	2.0
5	76.6	.3066	$6.822 \cdot 10^{-7}$	0.969	$6.611 \cdot 10^{-7}$	$6.585 \cdot 10^{-7}$	1.8
6	65.3	.3050	$1.095 \cdot 10^{-6}$	0.937	$1.026 \cdot 10^{-6}$	$1.023 \cdot 10^{-6}$	1.7
7	57.0	.3009	$1.625 \cdot 10^{-6}$	0.940	$1.528 \cdot 10^{-6}$	$1.525 \cdot 10^{-6}$	1.6
8	50.7	.2959	$2.270 \cdot 10^{-6}$	0.920	$2.088 \cdot 10^{-6}$	$2.086 \cdot 10^{-6}$	1.6
9	45.8	.2908	$3.027 \cdot 10^{-6}$	0.924	$2.797 \cdot 10^{-6}$	$2.797 \cdot 10^{-6}$	1.5
10	41.7	.2850	$3.930 \cdot 10^{-6}$	0.932	$3.663 \cdot 10^{-6}$	$3.663 \cdot 10^{-6}$	1.5
11	38.3	.2795	$4.975 \cdot 10^{-6}$	0.914	$4.547 \cdot 10^{-6}$	$4.547 \cdot 10^{-6}$	1.5
12	35.3	.2733	$6.213 \cdot 10^{-6}$	0.918	$5.704 \cdot 10^{-6}$	$5.704 \cdot 10^{-6}$	1.4
13	33.1	.2680	$7.390 \cdot 10^{-6}$	0.940	$6.947 \cdot 10^{-6}$	$6.947 \cdot 10^{-6}$	1.4
14	31.0	.2620	$8.795 \cdot 10^{-6}$	0.906	$7.968 \cdot 10^{-6}$	$7.968 \cdot 10^{-6}$	1.4
15	29.3	.2563	$1.019 \cdot 10^{-5}$	0.896	$9.130 \cdot 10^{-6}$	$9.130 \cdot 10^{-6}$	1.4
16	27.7	.2513	$1.182 \cdot 10^{-5}$	0.903	$1.067 \cdot 10^{-5}$	$1.067 \cdot 10^{-5}$	1.4
17	26.3	.2463	$1.354 \cdot 10^{-5}$	0.904	$1.224 \cdot 10^{-5}$	$1.224 \cdot 10^{-5}$	1.4
18	25.1	.2415	$1.527 \cdot 10^{-5}$	0.938	$1.432 \cdot 10^{-5}$	$1.432 \cdot 10^{-5}$	1.4
19	24.1	.2370	$1.693 \cdot 10^{-5}$	0.930	$1.574 \cdot 10^{-5}$	$1.574 \cdot 10^{-5}$	1.4
20	23.1	.2323	$1.885 \cdot 10^{-5}$	0.906	$1.708 \cdot 10^{-5}$	$1.708 \cdot 10^{-5}$	1.4
21	22.1	.2272	$2.105 \cdot 10^{-5}$	0.907	$1.909 \cdot 10^{-5}$	$1.909 \cdot 10^{-5}$	1.4
22	21.3	.2230	$2.308 \cdot 10^{-5}$	0.908	$2.096 \cdot 10^{-5}$	$2096 \cdot 10^{-5}$	1.4

TABLE 4.7

The Measured Spectrum in the lcm. Categories.

discussed in chapter 5.

4.4.3 The Measured Spectrum.

The values of the experimentally measured spectrum are obtained by multiplying the values of the trial spectrum, at the mean momenta of the categories, by the ratio of the observed to expected numbers in that category. It was found to be more satisfactory to read off the values of the trial spectrum in the form $p^3 N(p)$ against p , p being the muon momentum, since this varies much less rapidly than $N(p)$ alone. Table 4.6 shows the results of this procedure for the $\frac{1}{2}$ cm. categories and table 4.7 the same for the 1 cm.. The errors quoted are purely statistical. Columns 7 of these tables show the results obtained when only 90% of events accompanied by two or more electrons from a magnet block are assumed to cause event rejection by setting off more than one cell at the levels of the trays in the momentum selector. This is discussed in the next section.

4.4.4 The Effect of Varying the Burst Correction

In section 3.3.3 it was assumed that if a muon leaves a magnet block accompanied by more than one electron, due to electromagnetic interactions of the muon in the block, then there is a 100% chance of more than one cell being set in the tray of the momentum selector, and this could lead to the rejection of the event. This section examines the effect upon the overall correction factor, and hence upon the measured spectrum, of relaxing this condition. Reducing the effect of the bursts will have the effect of decreasing the correction factor particularly in the high energy region where it has the greatest effect. There will also be some second order effect upon the momentum independent corrections since these were estimated by subtracting the overall burst correction from the observed rejection rates. Figure 4.3 shows the effect of reducing this burst correction to 90% and 80%. Table 4.8 shows the result of applying these corrections to the deflection spectrum given in section 4.2 and including the category acceptance functions, given in terms of the amount by which the expected rates in each category have to be increased.

AMOUNT (%) BY WHICH THE CORRECTED DEFLECTION SPECTRUM (TABLE 4.1) HAS TO BE INCREASED TO ALLOW FOR VARIOUS DEGREES OF BURST CORRECTION.

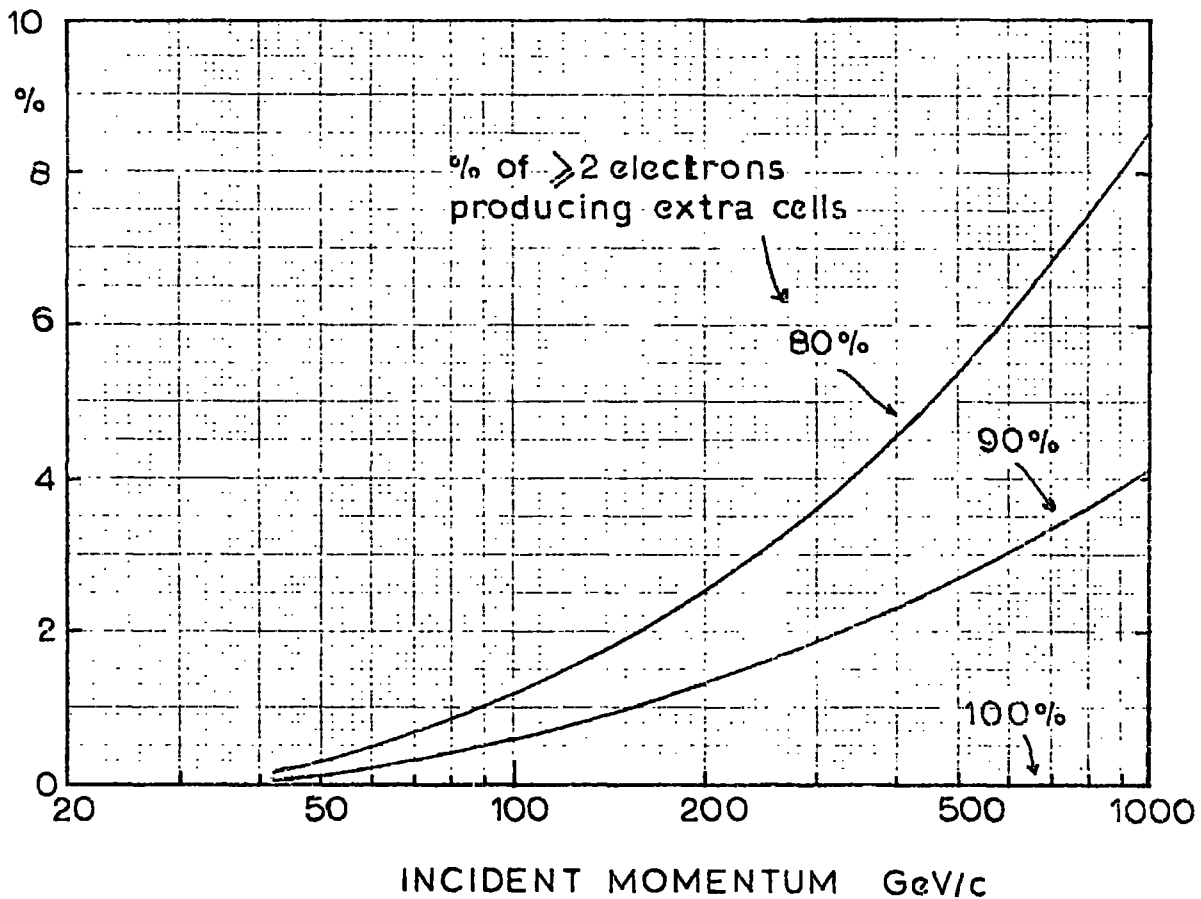


FIGURE 4.3 The Effect of Reducing the Burst Correction, (i.e. Reducing the Number of Electrons which set Extra Cells.).

Category No.	No. of ≥ 2 electrons producing extra cells.			
	$\frac{1}{2}$ cm. categories		1 cm. categories	
	90%	80%	90%	80%
0	1.036	1.055	1.033	1.051
1	1.032	1.048	1.024	1.035
2	1.026	1.039	1.016	1.023
3	1.022	1.032	1.010	1.016
4	1.018	1.026	1.007	1.011
5	1.014	1.021	1.004	1.008
6	1.012	1.018	1.003	1.006
7	1.009	1.015	1.002	1.004
8	1.008	1.013	1.001	1.003
9	1.006	1.010	1.000	1.002
10	1.005	1.009	1.000	1.002
11	1.004	1.008	1.000	1.001
12	1.003	1.006	1.000	1.001
13	1.003	1.006	1.000	1.000
14	1.002	1.005	1.000	1.000
15	1.001	1.004	1.000	1.000
16	1.001	1.003	1.000	1.000
17	1.001	1.003	1.000	1.000
18	1.000	1.002	1.000	1.000
19	1.000	1.002	1.000	1.000
20	1.000	1.002	1.000	1.000
21	1.000	1.002	1.000	1.000
22	1.000	1.001	1.000	1.000

Table 4.8

The effect of varying the amount of ≥ 2 electrons
producing extra cells.

In order to ascertain a correct value for the magnitude of the burst correction, photographic records of events which has been taken in a previous experiment to investigate electromagnetic interactions using the measuring trays (Hamdan , 1972) were studied. Events which had been assumed by the above author to contain two electrons were selected and the discharged tube patterns in the trays examined. A tracing of a momentum selector tray tube pattern, to the same scale as the measuring trays, was superimposed at random upon the tube configurations, and an estimate made of the momentum tray tubes which would have discharged, and hence of the cells which would have been allocated. Thirty-four such events were studied, the tube patterns being superimposed at six random positions on each. The frequency of extra cells being allocated was found to be $78 \pm 5\%$. Allowance must also be made for the variation of the ratio of 2 generated electrons to ≥ 3 electrons with momentum. This ratio has been given by Hansen (private communication) and varies from ~ 0.55 at 400 GeV/c to ~ 0.96 at 20 GeV/c. Using the reasonable estimate of the probability of ≥ 3 electrons producing an extra cell of 100%, it is found that the overall probability of producing at least one extra cell due to ≥ 2 electrons is 92% at 400 GeV/c and 89% at 20 GeV/c, with an error of $\pm 5\%$. Hence throughout the calculations a value of $90 \pm 5\%$ is used as indicated in the previous section 4.4.3.

4.5 Sources of Error.

4.5.1. Tray Alignment

(i) Theoretical Calculations.

As with all spectrograph measurements, and particularly in this case where the instrument is completely automated, it is very important that the errors in the alignment of the trays be small. It is not as important that the trays be vertically beneath each other but they are required to lie in a straight line with respect to one another. If this was not so, the effect would be to displace the category acceptance functions relative to the deflection spectrum causing either an increase or decrease in the measured rates depending upon the direction of the displacement, the sign

Category	0.0 cm.	0.10 cm.			0.20 cm.		
	displacement	displacement			displacement		
No.	\pm mean	+	-	mean	+	-	mean
Expected Rate in each Category (Arbitrary Units).							
0	0.230	0.235	0.235	0.235	0.250	0.250	0.250
1	0.352	0.403	0.309	0.356	0.462	0.275	0.368
2	0.674	0.756	0.598	0.677	0.841	0.527	0.684
3	1.115	1.211	1.021	1.116	1.309	0.929	1.119
4	1.611	1.713	1.509	1.611	1.816	1.408	1.612
5	2.126	2.230	2.023	2.126	2.333	1.919	2.126
6	2.642	2.744	2.539	2.642	2.845	2.436	2.640
7	3.147	3.246	3.047	3.146	3.345	2.946	3.146
8	3.636	3.732	3.540	3.636	3.827	3.443	3.635
9	4.107	4.199	4.014	4.106	4.289	3.921	4.105
10	4.557	4.644	4.469	4.556	4.731	4.380	4.556

Table 4.9

The effect of a displacement in the deflection spectrum on the expected values of the rates

Category	Amount of Displacement (cm.)					
No.	0.00	0.05	0.10	0.15	0.20	0.25
0	1.000	1.006	1.022	1.050	1.088	1.137
1	1.000	1.003	1.011	1.026	1.046	1.072
2	1.000	1.001	1.003	1.008	1.014	1.022
3	1.000	1.000	1.001	1.002	1.004	1.006
4	1.000	1.000	1.000	1.001	1.001	1.001
5	1.000	1.000	1.000	1.000	1.000	1.000
6	1.000	1.000	1.000	1.000	1.000	1.000
7	1.000	1.000	1.000	1.000	1.000	1.000
8	1.000	1.000	1.000	1.000	1.000	1.000
9	1.000	1.000	1.000	1.000	1.000	1.000
10	1.000	1.000	1.000	1.000	1.000	1.000

Table 4.10

The effect of a displacement in the deflection spectrum on the overall spectrum measurements.

of the muon, and the direction of the magnetic field. Due to the steepness of the deflection spectrum in the high energy region it is there that there will be the most pronounced effect. Table 4.9 shows the calculated effect of displacing the deflection spectrum and category acceptance function relative to each other by given amounts. The distances quoted are the amount by which the deflection spectrum was displaced, which is effectively twice the amount of misalignment of the trays since the deflection is given by $a - 2b + c$ as shown in chapter 2. The positive and negative signs refer to opposite directions of displacement of the category acceptance function relative to the deflection spectrum, each representing the situation for a given sign of particle in a particular field direction. All values are in arbitrary units, the value for zero displacement being given for comparison.

From the point of view of the spectrum measurement, it is the mean values which are important since both signs of particle and both field directions are combined together. Table 4.10 gives the effect of various displacements upon the overall spectrum measurements, where it is seen that it is only in the first four categories that there is any noticeable effect.

ii Experimental Observations.

The initial flash tube tray alignment was made using vertical plumb lines and cathetometers. Measurements were then made on the zero-field deflection spectrum (for the method of reducing the field to zero see chapter 7). If the momentum selector trays were exactly aligned, then the measured spectrum would be symmetric and centred on zero deflection. The distributions are in fact the sum of the multiple scattering distributions of the different momentum muons and it is believed that there is no difference between the scattering of those having positive or negative charge. Any misalignment of the trays will be reflected in a displacement of the mean from zero.

Consider the figure 4.4, n_3 is the number of particles observed in category zero, n_1 the total number with negative deflections, and n_2 with positive deflections. It is assumed that the distribution in category zero is flat as indicated on the diagram. The point of zero deflection is 0 and C is the median of the distribution, that is the value of Δ at which

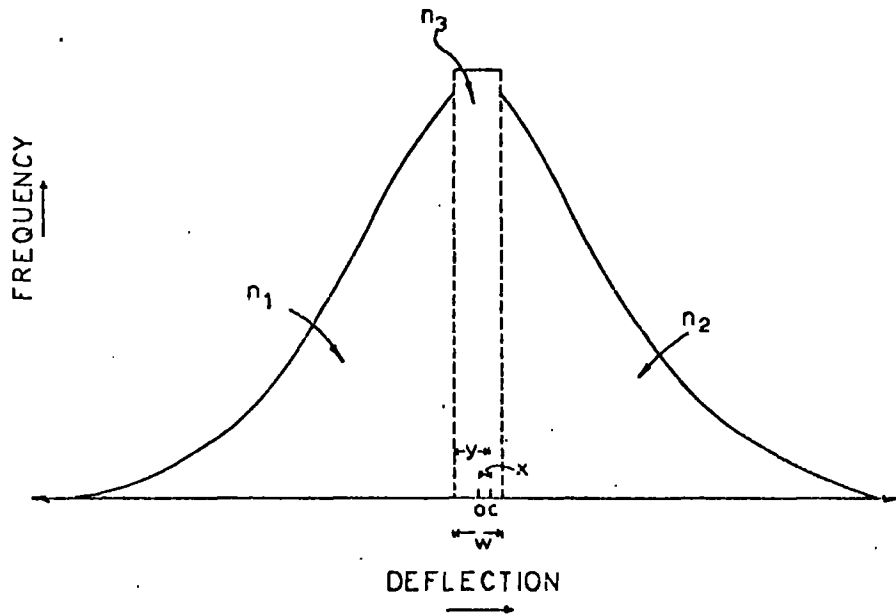


FIGURE 4.4 The Notation used in Calculating the Tray Misalignment from the Zero-Field RUDI Distributions.

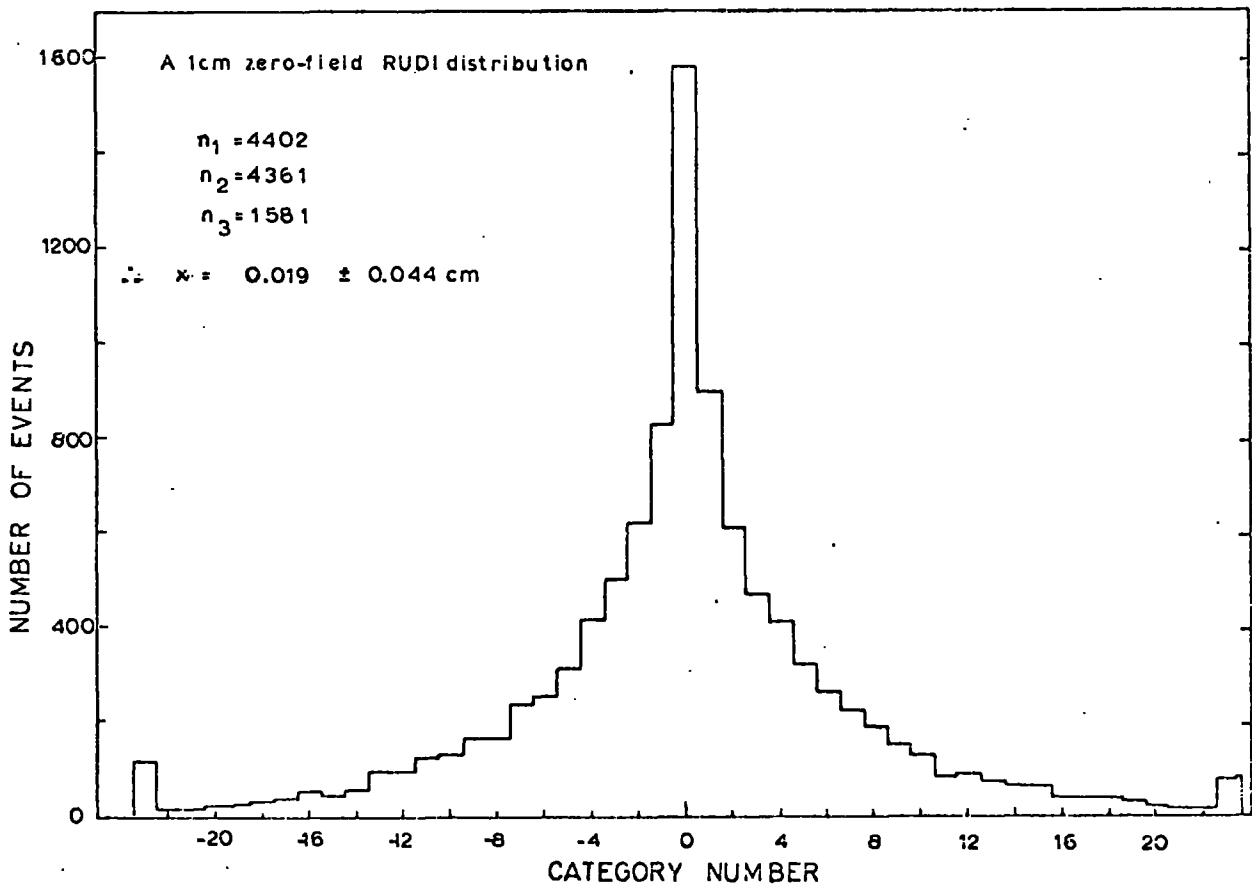


FIGURE 4.5 A Typical Zero-Field Distribution.

equal numbers lie on either side. Let y be the distance from C to the lower edge of category zero and x be the distance from C to O . The cell width, w , is either $\frac{1}{2}$ cm. for the $\frac{1}{2}$ cm. cells, or $1\frac{1}{2}$ cm. for the 1 cm. cells, since the latter's category zero contains three $\frac{1}{2}$ cm. cells ($\pm 1, 0$). Finally n_y is the number of particles in the distance y assuming the flat distribution. Then since C is the median we have:

$$n_1 + n_y = n_2 + n_3 - n_y$$

therefore
$$n_y = \frac{n_2 - n_1 + n_3}{2} \quad 4.3$$

Now
$$y = \frac{n_y}{n_3} w = \frac{n_2 - n_1 + n_3}{2} \cdot \frac{w}{n_3} = \frac{n_2 - n_1}{2 n_3} \cdot w + \frac{w}{2}$$

therefore
$$x = y - \frac{w}{2} = \frac{n_2 - n_1}{2 n_3} \cdot w \quad 4.4$$

The distance x is twice the amount of misalignment of the trays. After the first few zero-field runs the middle tray was moved by the distances ($x/2$) until finally the zero-field runs were consistent with the misalignment being small. The results of the final five zero-field runs, with 1 cm. categories, before the field was turned on, are shown in table 4.11. A typical zero-field distribution is shown in figure 4.5.

n_1	n_2	n_3	$\frac{x}{\text{cm.}}$	$\frac{\alpha x}{\text{cm.}}$
3953	3837	1409	-0.062	0.046
4507	4695	1646	+0.086	0.044
4836	4905	1689	+0.031	0.044
4402	4361	1581	-0.019	0.044
2403	2494	933	+0.073	0.056
TOTAL				
20101	20292	7258	+0.020	0.021

Table 4.11

The results from the initial zero-field runs

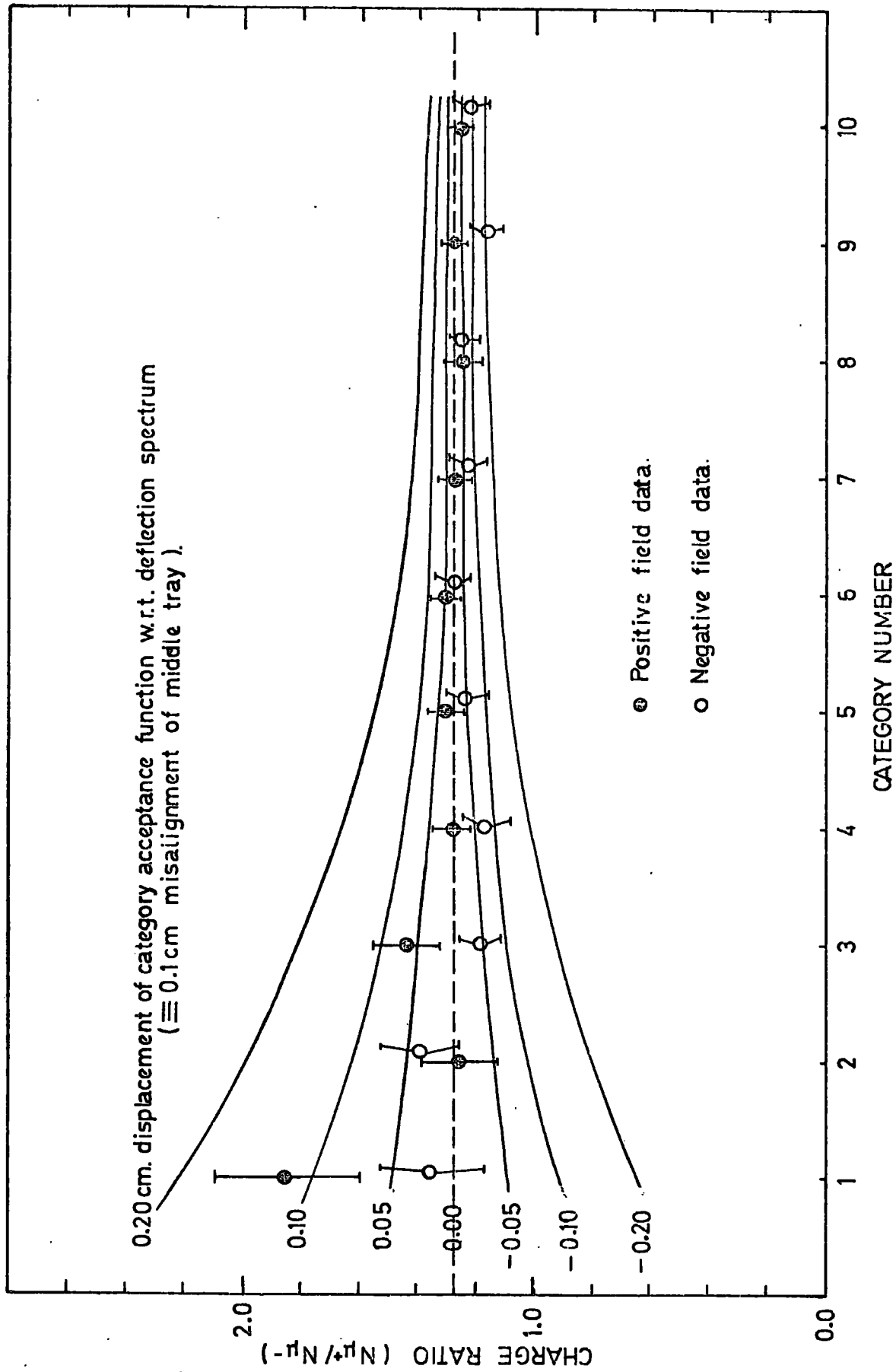


FIGURE 4.6 The Effect of Tray Misalignment on the Charge Ratio.

The errors on x are calculated in the usual statistical way and are given by :

$$\alpha_x^2 = \frac{1}{4 n_3^2} \left[(n_2 + n_1) + \frac{(n_2 - n_1)^2}{n_3} \right] \cdot w^2 \quad 4.5$$

These are the values quoted in the final column of table 4.11.

At the end of all the full-field runs, the magnetic field was again reduced to zero, and x redetermined. This value of x was found to be -0.032 ± 0.031 cm. The conclusion that is drawn from these values is that the trays are aligned to within 0.05 cm., and that no appreciable movement occurred during the operation of the spectrograph. Considering the figures, in table 4.10, giving the effect of misalignment on the spectrum measurement, it is seen that any such effect, corresponding to the x values deduced above, is negligible.

Further support for the satisfactory alignment of the trays may be obtained by examination of the charge ratio of the muons recorded during the full-field runs, particularly in the lower category numbers. Figure 4.6 shows the expected effects of various tray misalignments on the charge ratio, where an assumed value of the true ratio of 1.23 is taken. Also shown for comparison are the experimentally observed values from the $\frac{1}{2}$ cm. category runs. As can be seen the results are consistent with the trays being aligned to within 0.05 cm.

4.5.2 Other Sources of Error

So far two sources of error have been discussed, the effect of varying the amount of burst correction, and the effect of a misalignment of the trays. A best estimate of the former has been taken, whilst the latter has been shown to be negligible. Other factors which will have an effect on the spectrum, particularly its absolute height are, the magnitude of the magnetic field, the efficiency of the flash-tubes, the values of the overall acceptance, and the efficiency of the scintillation counters. Each of these is now considered in turn.

It was shown in section 2.3 that the best estimate of the magnitude of the field was $16.3 \text{ kG} \pm 1\%$. The effect of this 1% variation on the calculated deflection spectrum is estimated as follows:

Over a limited range of deflection the relation between momentum and deflection can be written as :

$$(p - \alpha) \Delta = C \quad 4.6$$

where α is a constant, representing half the energy loss of the muon through the magnet, and C is a constant proportional to the magnitude of the field. From this we have :

$$\frac{dp}{d\Delta} = - \frac{C}{\Delta^2} \quad 4.7$$

Now if we represent the differential momentum spectrum, again over a limited region, by :

$$N(p) = A p^{-\gamma} \quad 4.8$$

then we have:

$$N(\Delta) = N(p) \cdot \frac{dp}{d\Delta} = A p^{-\gamma} \cdot \frac{C}{\Delta^2}$$

$$\text{therefore } N(\Delta) = A \left(\frac{C}{\Delta} + \alpha \right)^{-\gamma} \cdot \frac{C}{\Delta^2} \quad 4.9$$

From the trial spectrum, γ is found to be ~ 2.5 at 20 GeV/c and ~ 3.5 at 500 GeV/c. Putting in reasonable values ($\sim 4 \text{ GeV}$) for the energy loss α , and varying C by $\pm 1\%$, the effect on $N(\Delta)$ is shown in table 4.12.

$\Delta \text{ cm}$	$p \text{ GeV/c}$	γ	$\delta N\%$	$N(\Delta) \%$
24	20	2.5	1.0	1.0
5.86	70	3.0	1.0	1.9
0.78	500	3.5	1.0	2.5

Table 4.12

The effect of a 1% error in the field on the calculated deflection spectrum.

These figures are consistent with the fact that at higher energies, when energy loss is negligible, $N(\Delta)$ varies as $C^{-\gamma+1}$.

(b) The efficiency of the flash tubes:

In section 3.3.3 the efficiencies of the individual flash-tube trays were calculated with their corresponding errors. Combining these we find that the overall flash tube efficiency is $90.0 \pm 0.5\%$.

(c) Overall acceptance:

In Appendix B it is shown that the acceptance corresponding to muons of infinite momentum is $408 \pm 2 \text{ cm}^2\text{sr}$, the error arising because of the uncertainty in the effective separation of the scintillation counters due to their finite thickness. Since in the momentum range of the measured spectrum, the minimum value of the relative acceptance is ~ 0.93 then it is considered that the errors on these values will be small. Consequently the error quoted on the overall acceptance will be 0.5% , coming from the infinite momentum value alone.

(d) The efficiency of the scintillation counters:

The calculation of the efficiencies of the scintillation counters is shown in chapter 7. The overall value is found to be 0.894 ± 0.002 , i.e. the uncertainty in the efficiency is 0.2% .

4.5.3 Combination of all non-statistical (systematic) errors.

Table 4.13 and figure 4.7 show the various sources of error, the total error being obtained by summing the individual errors in quadrature. The effect of a 5% variation in the burst correction is also included, and it is seen that this, together with the effect of the error on the magnetic field, constitute the only errors affecting the relative shape of the spectrum. The sum of these in quadrature is also indicated. It is to be noted that most of the error arises from the error in the magnetic field. These errors must be added directly to the statistical errors since they reflect uncertainties in the absolute height of the spectrum, and are not random errors. When considering the shape of the spectrum it is necessary only to consider the amount by which these errors vary with momentum over

Momentum GeV/c.	Error (%) affecting the shape of the spectrum.		Error (%) not affecting the shape of the spectrum.		Total	Error due to magnetic field burst correction	Error in overall acceptance	Error in flash tube efficiency	Error in scintillation counter efficiency	Overall Total
	Error due to magnetic field	Error due to burst correction	Error in overall acceptance	Error in flash tube efficiency						
20	1.00	0.00	0.50	0.50	1.00				0.20	1.24
30	1.38	0.00	0.50	0.50	1.38				0.20	1.56
50	1.72	0.10	0.50	0.50	1.72				0.20	1.87
70	1.90	0.19	0.50	0.50	1.91				0.20	2.04
100	2.05	0.30	0.50	0.50	2.07				0.20	2.19
150	2.19	0.45	0.50	0.50	2.24				0.20	2.36
200	2.27	0.58	0.50	0.50	2.34				0.20	2.45
300	2.37	0.82	0.50	0.50	2.51				0.20	2.61
400	2.44	1.07	0.50	0.50	2.66				0.20	2.76
500	2.50	1.30	0.50	0.50	2.82				0.20	2.91

Table 4.13

Summary of the non-statistical (systematic) errors

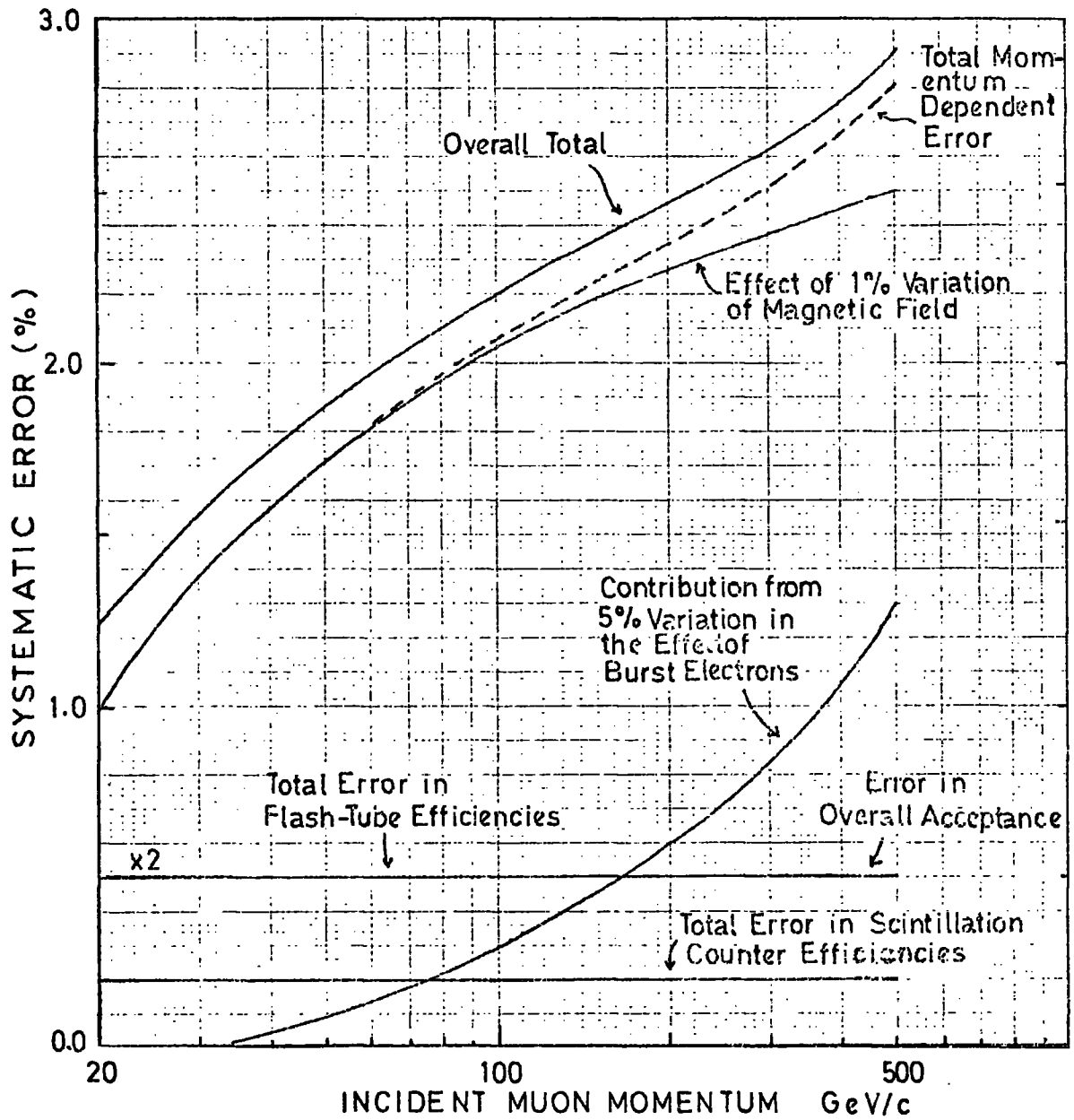


FIGURE 4-7 Summary of the Systematic Errors.

the region of interest. The total uncertainty in the absolute height is thus seen to vary from $\sim 1.2\%$ at 20 GeV/c to $\sim 2.9\%$ at 500 GeV/c, whilst the errors on the shape, which are assumed to be 0% at 20 GeV/c, vary from $\sim 0.9\%$ at 70 GeV/c to $\sim 1.8\%$ at 500 GeV/c. These values are noted to be comparable with the statistical errors, and therefore must be taken into account.

4.6 The Maximum Detectable Momentum

The usual definition of the maximum detectable momentum (m.d.m.) is that momentum at which the error on the measurement of momentum is equal to the momentum itself. More frequently one is dealing with deflections rather than momentum directly, and hence a quantity, the minimum detectable deflection can be likewise defined. What has usually been done, with many previous spectrographs, is to add the m.d.m. correction in quadrature with the multiple scattering correction to define an error on the momentum as δp given by

$$\delta p = p \sqrt{c^2 + (p/P_{\text{mdm}})^2} \quad 4.10$$

where c is the scattering correction, and P_{mdm} is the m.d.m. of the instrument. By working with the category acceptance functions, as discussed, account has effectively been taken of the location errors, which are the main contributory factors to the m.d.m. correction, consequently no addition has been made to the scattering correction as in equation 4.10.

However in order to assess the working of the system one may define a quantity, which can be likened to the m.d.m. in that it gives a measure of the extent of the uncertainty in momentum measurement. This is the RMS value of the category zero acceptance function, which is found to be 0.586 cm. This corresponds to a momentum of 670 GeV/c. Hence, it is possible to define the m.d.m. as 670 GeV/c, although no correction, as such, need be applied to allow for it.

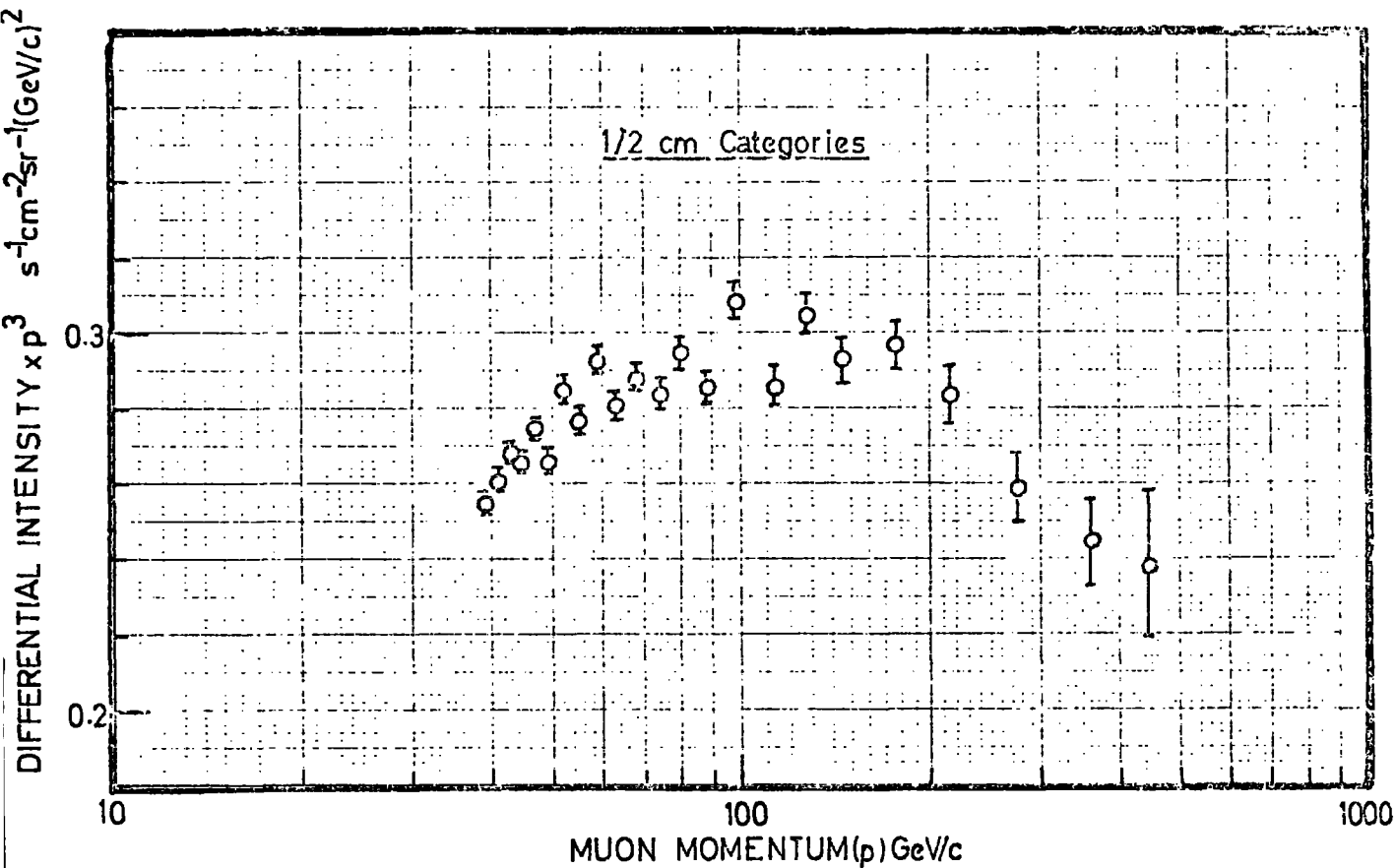


FIGURE 4.8 The Measured Momentum Spectrum from the $1/2$ cm. Categories.

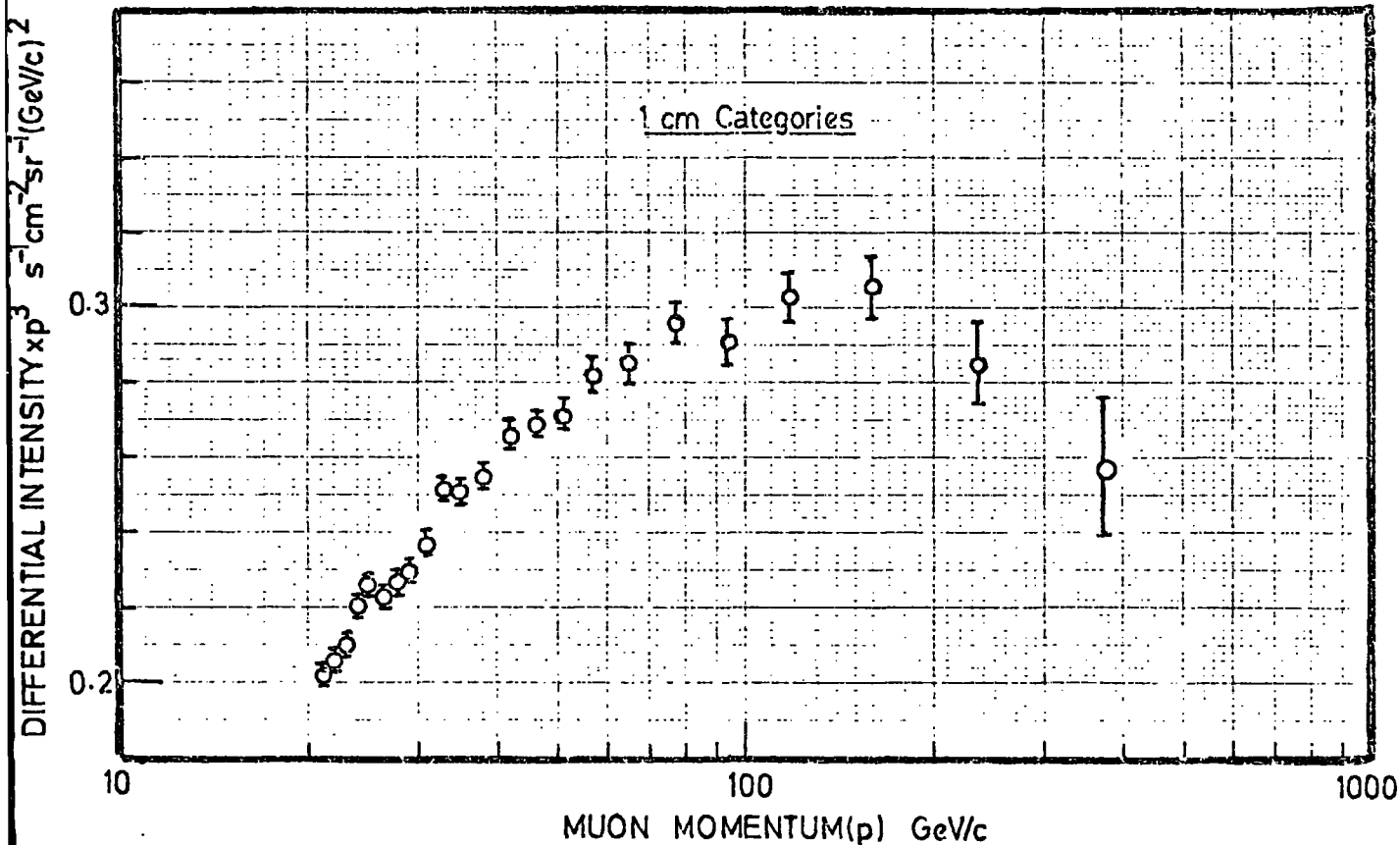


FIGURE 4.9 The Measured Momentum Spectrum from the 1cm. Categories.

4.7 The Best Estimate of the Spectrum

Figures 4.8 and 4.9 show the final results from the $\frac{1}{2}$ cm. and 1 cm. categories respectively, in the form $p^3N(p)$. Due to the obvious systematic variation of alternate points in the $\frac{1}{2}$ cm. distribution, and to the closeness of the points in the lower energy region, all the data have been combined to produce a best estimate of the spectrum from 20 GeV/c to 500 GeV/c. The grouping together was made over three separate regions as follows:

(a) $p < 40$ GeV/c.

In this region the data, all except the point indicated, come from the 1 cm. results. The grouping is shown in table 4.14. The mean values of $N(p)$ and $p^3N(p)$ were found by weighting with the square of the statistical errors, that is by the numbers of events, and the mean value of momentum p is found from the mean values of $N(p)$ and $p^3N(p)$. This method gives the most satisfactory results because of the steepness of the $N(p)$ spectrum which makes an accurate value of the mean momentum difficult to calculate.

(b) 40 GeV/c $< p < 200$ GeV/c.

In this region there is complete overlap of the $\frac{1}{2}$ cm. and 1 cm. data, hence the $\frac{1}{2}$ cm. data has been added together to give equivalent 1 cm. categories and combined with the corresponding 1 cm. category. Table 4.15 shows the results of this procedure. Values of the ratio of observed to expected numbers were obtained in the same manner as before, and the values of the trial spectrum, assuming an effective 90% burst correction, multiplied by this ratio are plotted at the mean momenta of the 1 cm. categories.

(c) $p > 200$ GeV/c.

As in (b) there is an overlap of data. In order to maximise the number of points in this region the data have not been combined into 1 cm. categories but in a manner similar to that in (a). Table 4.16 shows the results of these calculations.

Also shown in tables 4.14, 4.15, and 4.16, are the statistical errors based on the number of events recorded, together with the non-statistical (systematic) errors which affect the shape of the spectrum. The total error shown is the sum of these individual errors.

Momentum (p) GeV/c	Differential intensity $N(p)$ $s^{-1} cm^{-2} sr^{-1}$ (GeV/c) ⁻¹	$p^3 N(p)$ $s^{-1} cm^{-2} sr^{-1}$ (GeV/c) ²	Number of Events	Mean value of $p^3 N(p)$ $s^{-1} cm^{-2} sr^{-1}$ (GeV/c) ²	Mean value of $N(p)$ $s^{-1} cm^{-2} sr^{-1}$ (GeV/c) ⁻¹	Mean Momentum GeV/c	Statistical	E R R O R (%)	
								Non-statistical affecting shape	Total affecting shape
21.3	$2.096 \cdot 10^{-5}$	0.2025	5275	0.2043	$2.002 \cdot 10^{-5}$	21.69	0.97	0.10	1.07
22.1	$1.909 \cdot 10^{-5}$	0.2061	5296						
23.1	$1.708 \cdot 10^{-5}$	0.2105	5305	0.2155	$1.640 \cdot 10^{-5}$	23.60	0.96	0.18	1.14
24.1	$1.574 \cdot 10^{-5}$	0.2203	5445						
25.1	$1.432 \cdot 10^{-5}$	0.2264	5469	0.2246	$1.330 \cdot 10^{-5}$	25.66	0.97	0.26	1.23
26.3	$1.224 \cdot 10^{-5}$	0.2227	5241						
27.7	$1.067 \cdot 10^{-5}$	0.2268	5199	0.2282	$9.907 \cdot 10^{-6}$	28.45	0.99	0.34	1.33
29.3	$9.130 \cdot 10^{-6}$	0.2297	5104						
31.0	$7.968 \cdot 10^{-6}$	0.2374	5077	0.2374	$7.968 \cdot 10^{-6}$	31.0	1.40	0.41	1.81
33.1	$6.947 \cdot 10^{-6}$	0.2519	5157	0.2519	$6.947 \cdot 10^{-6}$	33.1	1.39	0.45	1.84
35.3	$5.704 \cdot 10^{-6}$	0.2509	4899	0.2509	$5.704 \cdot 10^{-6}$	35.3	1.43	0.50	1.93
38.3	$4.547 \cdot 10^{-6}$	0.2555	4700						
*39.3	$4.208 \cdot 10^{-6}$	0.2554	7631	0.2554	$4.337 \cdot 10^{-6}$	38.91	0.90	0.56	1.46

* indicates the only $\frac{1}{2}$ cm. category.

Table 4.14 Combination of data for $p < 40$ GeV/c.

Numbers in relevant categories		Total Expected	Observed / Expected	N(p) TRIAL assuming 90% of burst correction	N(p) meas. $s^{-1} cm^{-2} sr^{-1} (GeV/c)^{-1}$	$p^3 N(p) meas. s^{-1} cm^{-2} sr^{-1} (GeV/c)^2$	Mean Momentum of the 1 cm. category GeV/c	Error %		
1/2 cm. Observed	1 cm. Observed							Statistical	Non-statistical affecting the shape	Total affecting the shape
1943 2404	1368 5715	5372	1.064	$6.805 \cdot 10^{-8}$	$7.241 \cdot 10^{-8}$	0.2966	160.0	1.32	1.25	2.57
3037 3305	1968 8313	8275	1.005	$1.801 \cdot 10^{-7}$	$1.810 \cdot 10^{-7}$	0.2974	118.0	1.10	1.14	2.24
4048 4198	2451 10697	10995	0.973	$3.771 \cdot 10^{-7}$	$3.669 \cdot 10^{-7}$	0.2951	93.0	0.97	1.04	2.01
4775 5000	3032 12807	13466	0.951	$6.795 \cdot 10^{-7}$	$6.462 \cdot 10^{-7}$	0.2904	76.6	0.88	0.95	1.83
5466 5678	3382 14526	15540	0.935	$1.092 \cdot 10^{-6}$	$1.021 \cdot 10^{-6}$	0.2843	65.3	0.83	0.86	1.69
6280 6270	3770 16320	17295	0.945	$1.622 \cdot 10^{-6}$	$1.533 \cdot 10^{-6}$	0.2839	57.0	0.78	0.79	1.57
6764 6614	4006 17384	18734	0.928	$2.268 \cdot 10^{-6}$	$2.105 \cdot 10^{-6}$	0.2743	50.7	0.76	0.72	1.48
7107 7162	4301 18570	20028	0.927	$3.027 \cdot 10^{-6}$	$2.806 \cdot 10^{-6}$	0.2696	45.8	0.73	0.66	1.39
7492 7562	4574 19628	21120	0.929	$3.930 \cdot 10^{-6}$	$3.651 \cdot 10^{-6}$	0.2647	41.7	0.71	0.61	1.32

Table 4.15 Combination of data for $(40 < p < 200) GeV/c$

Momentum (p) GeV/c	Differential intensity $N(p)$ $s^{-1} cm^{-2} sr^{-1} (GeV/c)^{-1}$	$p^3 N(p)$ $s^{-1} cm^{-2} sr^{-1} (GeV/c)^2$	Number of Events	Mean value of $p^3 N(p)$ $s^{-1} cm^{-2} sr^{-1} (GeV/c)^2$	Mean value of $N(p)$ $s^{-1} cm^{-2} sr^{-1} (GeV/c)^{-1}$	Mean Momentum GeV/c	Statistical Error	Non-statistical affecting shape	Total affecting shape
214.	$2.893 \cdot 10^{-8}$	0.2835	1358	0.2841	$2.643 \cdot 10^{-8}$	220.6	2.20	1.37	3.57
236.	$2.171 \cdot 10^{-8}$	0.2854	698						
274.	$1.260 \cdot 10^{-8}$	0.2592	818	0.2592	$1.260 \cdot 10^{-8}$	274.0	3.50	1.46	4.96
358.	$5.328 \cdot 10^{-9}$	0.2445	450	0.2484	$5.182 \cdot 10^{-9}$	363.6	3.94	1.60	5.54
376.	$4.843 \cdot 10^{-9}$	0.2574	194						
442.	$2.764 \cdot 10^{-9}$	0.2386	158	0.2386	$2.764 \cdot 10^{-9}$	442.0	7.96	1.72	9.68

Table 4.16

Combination of data for $p > 200$ GeV/c.

Figures 4.10 and 4.11 show plots of the best estimate of the measured spectrum in the form $N(p)$ and $p^3 N(p)$ respectively. The merit of the latter, when considering the details of the spectrum, is immediately obvious from these figures. Errors on the experimental points are shown as statistical, and extended to show the systematic errors affecting the shape (assuming 0° at 20 GeV/c. The curves drawn through the data represent a fit of the form :

$$p^3 N(p) = a_0 + a_1(\ln p) + a_2 (\ln p)^2 + a_3 (\ln p)^3 \quad 4.11$$

The method of fitting used a least squares technique, the coefficients, a , being as follows :

$$\left. \begin{array}{l} a_0 = -52.36 \\ a_1 = 36.59 \\ a_2 = -4.45 \\ a_3 = 0.08 \end{array} \right] \times 10^{-2}$$

This provides a practical formula for the computation of the spectrum over the region 20 - 500 GeV/c, and is further useful in that it can be integrated simply to give a form :

$$p^2 N(>p) = b_0 + b_1 (\ln p) + b_2 (\ln p)^2 + b_3 (\ln p)^3 \quad 4.12$$

where the coefficients b can be shown to be related to the a 's as follows:

$$\left. \begin{array}{l} b_0 = a_1 - 2a_0 \\ b_1 = 2a_2 - 2a_1 \\ b_2 = 3a_3 - 2a_2 \\ b_3 = -2a_3 \end{array} \right] \quad 4.13$$

putting in the values for the a 's and solving the above equations we find:

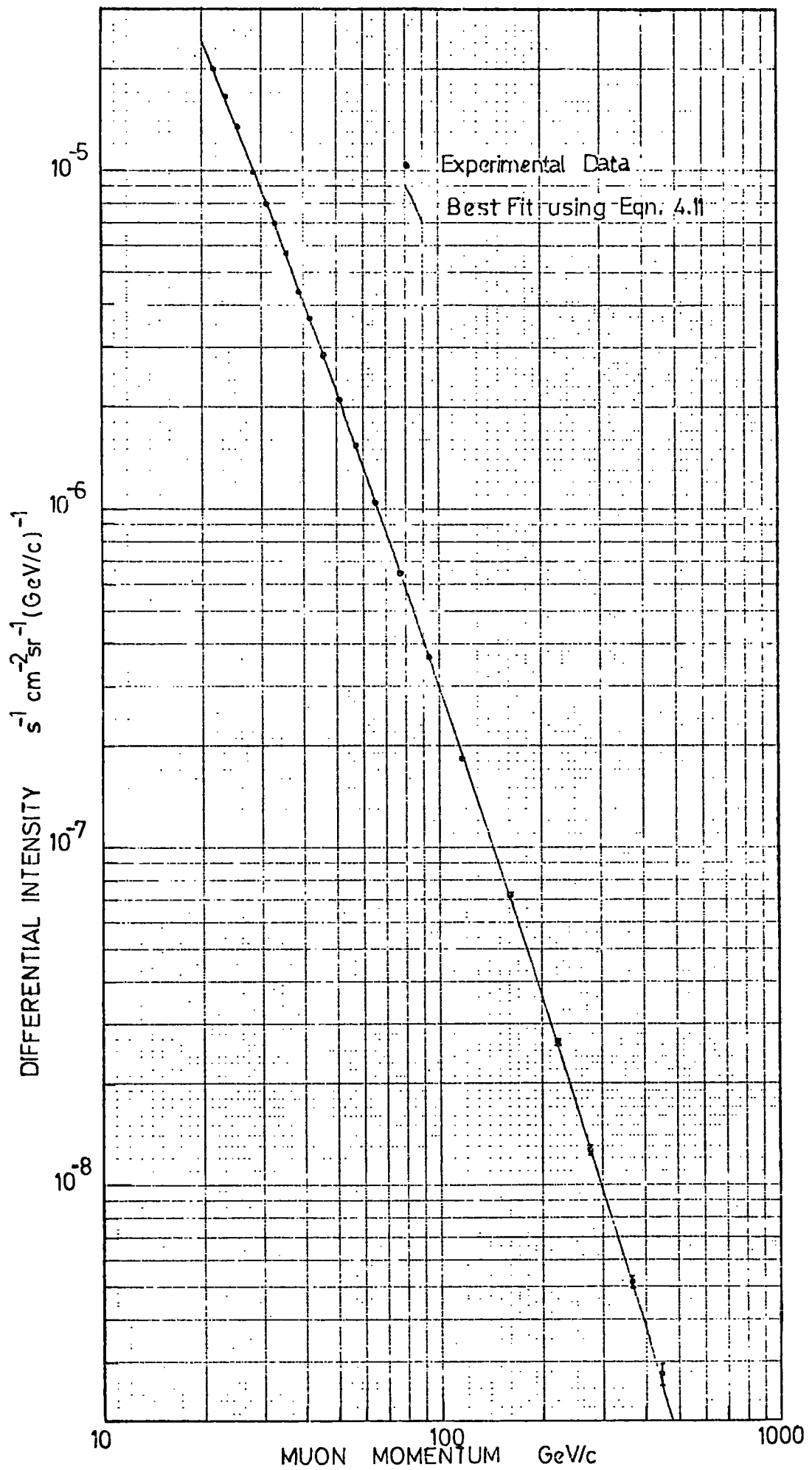


FIGURE 4.10 The Combined Best Estimate of the Spectrum.

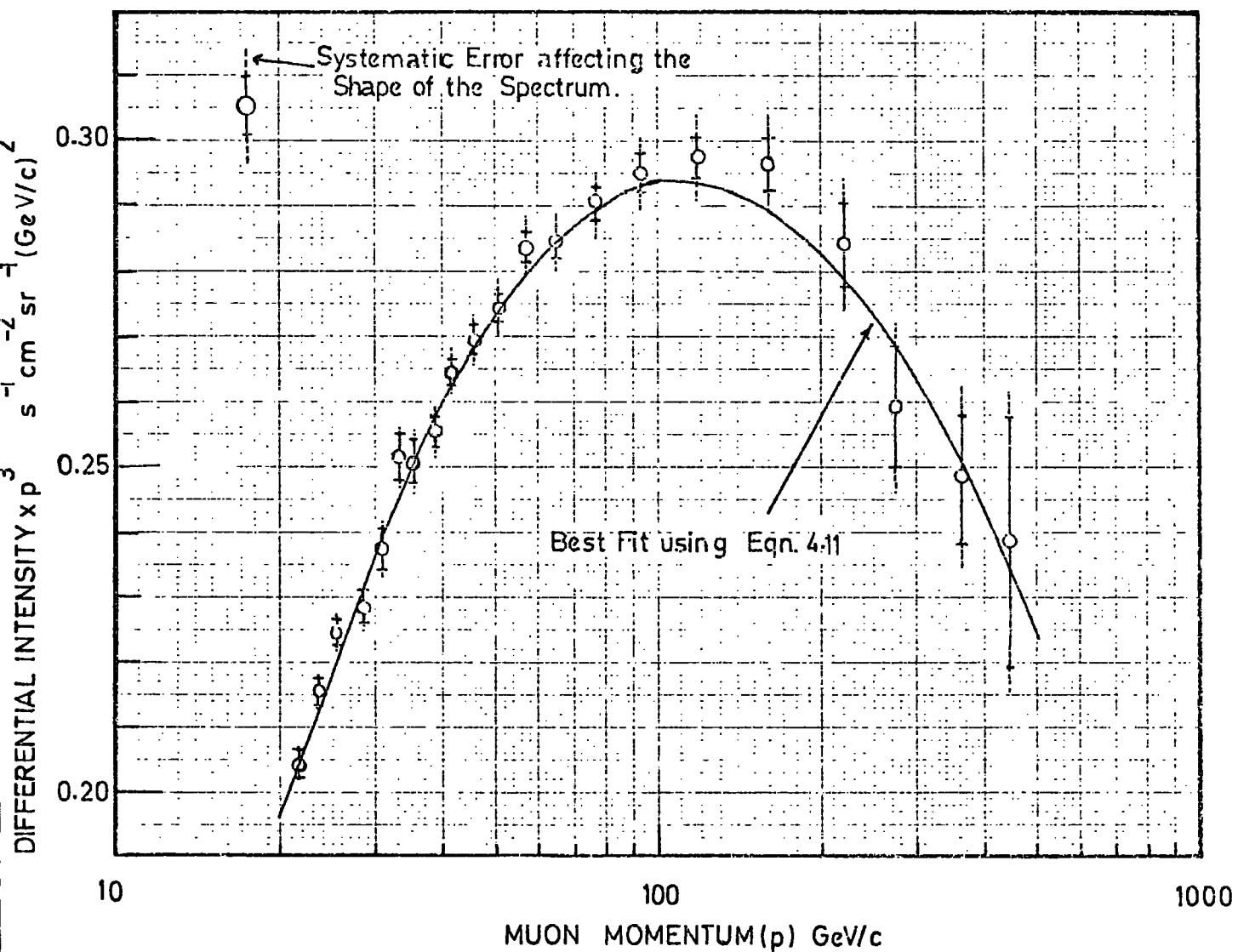


FIGURE 4-11 As in Figure 4-10 but plotted as $p^3 N(p)$ to Increase Readability.

$$\left. \begin{array}{l} b_0 = 18.11 \\ b_1 = -16.13 \\ b_2 = 2.16 \\ b_3 = -0.04 \end{array} \right] \times 10^{-2}$$

When using this integral expression it must be remembered that the original fit (equation 4.11) was only made up to 500 GeV/c and consequently there are no constraints on the fitted spectrum above this value. In the next chapter a best estimate of the integral intensity above 500 GeV/c is calculated using an extrapolation of a phenomenological model of muon production and propagation through the atmosphere. Table 4.17 shows values of the measured differential and integral spectrum in the region 20 - 500 GeV/c, calculated using equations 4.11 and 4.12, and using the estimate of the integral intensity above 500 GeV/c given in the next chapter.

Momentum GeV/c	Differential Spectrum $s^{-1} cm^{-2} sr^{-1} (GeV/c)^{-1}$	Integral Spectrum $s^{-1} cm^{-2} sr^{-1}$
20	$2.43 \cdot 10^{-5}$	$2.96 \cdot 10^{-4}$
30	$8.80 \cdot 10^{-6}$	$1.48 \cdot 10^{-4}$
40	$4.06 \cdot 10^{-6}$	$8.67 \cdot 10^{-5}$
50	$2.20 \cdot 10^{-6}$	$5.70 \cdot 10^{-5}$
60	$1.31 \cdot 10^{-6}$	$4.02 \cdot 10^{-5}$
70	$8.43 \cdot 10^{-7}$	$2.94 \cdot 10^{-5}$
80	$5.71 \cdot 10^{-7}$	$2.26 \cdot 10^{-5}$
90	$4.04 \cdot 10^{-7}$	$1.78 \cdot 10^{-5}$
100	$2.96 \cdot 10^{-7}$	$1.42 \cdot 10^{-5}$
150	$8.68 \cdot 10^{-8}$	$6.00 \cdot 10^{-6}$
200	$3.56 \cdot 10^{-8}$	$3.18 \cdot 10^{-6}$
300	$9.77 \cdot 10^{-9}$	$1.26 \cdot 10^{-6}$
400	$3.80 \cdot 10^{-9}$	$6.46 \cdot 10^{-7}$
500	$1.79 \cdot 10^{-10}$	$3.74 \cdot 10^{-7}$

Table 4.17

Values of the measured differential and
integral spectra at standard momenta

CHAPTER 5

DERIVATION OF THE PION AND KAON PRODUCTION SPECTRA

5.1 Introduction

As briefly outlined in the first chapter, the vast majority of muons observed at sea level are the decay products of the secondary particles of the nuclear interactions of the primary cosmic ray nucleons with the atmospheric nuclei. Other sources such as the interaction of the secondaries themselves with nuclei in the atmosphere can be considered negligible. The present chapter deals with the calculation of the production spectrum of these secondary particles, assumed to be pions and kaons, from the measurements made on the muon spectrum.

The relationship between the muon spectrum, and the parent particle spectrum has been extensively covered in many publications (e.g. Smith and Duller, 1959; Bull et al., 1965), most of which base their derivations on the work of Barrett et al. (1952). In general the diffusion equation of the muon parents in the atmosphere is used, together with several simplifying assumptions, to predict the production spectrum of the muons, and hence via their decay and energy loss, their sea level spectrum. It has usually been the case that for vertical measurements pions have been taken to be the only source of muons, and kaons as another source have only been considered when comparison have been made with large angled spectra where their effect is more pronounced. In fact this method has been used to estimate the K/π ratio at production, (Ashton et al., 1966). It is well established from accelerator data that kaons are produced along with pions to the extent of about 15% in nuclear interactions, and hence will contribute, via the dominant $K_{\mu 2}$ decay mode ($K \rightarrow \mu + \nu$; branching ratio $\sim 58\%$), $\sim 9\%$ of the muon intensity in the vertical direction at 20 GeV increasing to $\sim 12\%$ at 1000 GeV. The good agreement obtained by many workers using an all pion source of muons in the theoretical model is thought to be due to the lack of good statistics in the >100 GeV region together with the slow variation of the effect of

kaons for moderate energies, (≤ 100 GeV). In the present experiment the statistics are good, and hence it is believed that the inclusion of kaons is a necessity. Initially however pions will be considered as the only source of muons, and later the effect of kaons will be included. No other sources of muons, (e.g. direct production) will be assumed.

5.2 Theoretical Model

5.2.1 Introduction

Following the treatment of Bull et al. (1965), starting with the diffusion equation of pions in the atmosphere, the spectrum of muons at production is calculated, and this is then extrapolated to sea level. Finally the effect of kaons on the muon intensity is considered.

In the model several simplifying assumptions are made as follows:

- (a) the muon parent production spectrum is assumed to follow a power law given by $AE^{-\gamma}$ where A is a constant, E the particles energy, and the constant γ is taken to be the same for both pions and kaons.
- (b) a constant production depth in the atmosphere for muons is taken (100 gm cm^{-2}).
- (c) all particles are assumed to travel in a vertical direction with no transverse component of momentum.
- (d) initially the atmosphere is assumed to be isothermal, and then a correction is applied to correct for this assumption.
- (e) the interaction lengths for protons and pions are assumed to be equal (120 gm cm^{-2}).
- (f) a constant energy relation between the muons and their parents is taken.

At the relevant steps in the calculation where the above assumptions are made, they are indicated and where necessary elaborated upon.

5.2.2 The Pion Spectrum in the Atmosphere

The diffusion equation expressing the differential flux of pions travelling in a vertical direction at a depth y (gm cm^{-2}) is written as follows:

$$\frac{dN_{\pi}}{dy} = \frac{A_{\pi}^3 \pi^{-y}}{\lambda_p} \exp\left(\frac{-y}{\lambda_p}\right) - \frac{N_{\pi}}{\lambda_{\pi}} - \frac{m_{\pi} c^2 N_{\pi}}{\rho(y) \tau_{\pi} c E_{\pi}} \quad 5.1$$

The first term on the RHS represents the production of pions in nuclear collisions between the primaries and the atmospheric nuclei, assuming an exponential decrease of nucleons characterised by an absorption length λ_p . The second term represents the interaction, and consequent loss of pions, with an interaction length λ_{π} . The decrease in the number of pions due to their decay into muons is given by the third term, where m_{π} and τ_{π} are the rest mass and lifetime respectively of pions, E_{π} their energy and $\rho(y)$ the atmospheric density at a depth y . The form of this final term comes about by considering the mean distance travelled before decay ($E_{\pi} \tau_{\pi} c / m_{\pi} c^2$), the air density being included since y is effectively the air pressure (gm cm^{-2}).

In an isothermal atmosphere the air density can be related to the depth by the relation:

$$\rho(y) = \rho(0) \frac{y}{y_0} \quad 5.2$$

where $\rho(0)$ and y_0 are the density and depth of the atmosphere at sea level, (taken to be $0.00124 \text{ gm cm}^{-3}$ and 1033 gm cm^{-2} respectively). Smith and Duller introduce a factor b ($= 0.771$) to allow for the non-isothermal nature of the atmosphere defining b as follows :

$$\frac{b y_0}{\rho(0)} = \frac{R T_e}{Mg} \quad 5.3$$

where R is the gas constant ($8.314 \text{ joules (gm mole)}^{-1}$), T_e the effective temperature of the atmosphere ($\sim 219^{\circ}\text{K}$), M the average molecular weight of the air (28.97), and g the acceleration due to gravity ($981.3 \text{ cm sec}^{-2}$).

Thus they define the density at a depth y as :

$$\rho(y) = \rho(0) \frac{y}{by_0} \quad 5.4$$

Substituting for $\rho(y)$ in the diffusion equation (5.1) we have:

$$\frac{dN_{\pi}}{dy} = A_{\pi} E_{\pi}^{-y} \exp\left(\frac{-y}{\lambda_{\pi}}\right) - \frac{E_{\pi}}{\lambda_{\pi}} - \frac{m_{\pi} c^2 N_{\pi} b y_0}{\rho(0) y \tau_{\pi} c E_{\pi}} \quad 5.5$$

The solution of this equation (5.5) is given by Bull et al. (1965) as:

$$N_{\pi} = A_{\pi} E_{\pi}^{-y} \exp\left(\frac{-y}{\lambda_{\pi}}\right) \sum_{n=0}^{\infty} \left(\frac{y}{\lambda}\right)^n \left\{ n! \left(1 + n + \frac{m_{\pi} c^2 y_0 b}{\tau_{\pi} c \rho(0) E_{\pi}} \right) \right\}^{-1} \quad 5.6$$

with $\frac{1}{\lambda} = \frac{1}{\lambda_{\pi}} - \frac{1}{\lambda_{\rho}}$

and represents the flux of pions of energy E_{π} travelling in a vertical direction at a depth y .

5.2.3 The Muon Production Spectrum

As in any two bodied decay, the energy of a daughter particle (in this case a muon) has a uniform probability distribution ranging from some minimum to a maximum value. In the case of pion decay the muon can have energy between E_{π} and $(m_{\mu}^2/m_{\pi}^2)E_{\pi}$ where m_{μ} and m_{π} are the masses of the muon and the pion respectively. In the present treatment it will be assumed that the muon takes a constant fraction (r_{π}) of the pion's energy, which is given by :

$$r_{\pi} = \frac{m_{\mu}}{m_{\pi}} = 0.76 \quad 5.7$$

(N.B. this is only an approximation to the mean of the energy distribution, and a value defined in a likewise manner for kaons (r_{κ}) would be 0.21, which is not close to the centre of the muon energy distribution from kaons, which ranges from $0.05E_{\kappa}$ to E_{κ} . A more reasonable value for the mean of this distribution is $r_{\kappa} = 0.52$, which has been used for the inclusion of kaons at a later stage).

Again considering pions as the only source, the production spectrum of muons of energy E'_{μ} , can be written as :

$$M_{\mu}(E'_{\mu}) = \int_0^{y_0} N_{\pi}(E_{\pi}, y) \frac{dt}{dy} \frac{dy}{\tau} \quad 5.8$$

where τ is the dilated lifetime of the pion $\frac{E_{\pi}}{m_{\pi}c^2} \tau_{\pi}$, and E'_{μ} and E_{π} are related by the factor r_{π} . Since the pion can be assumed to be travelling at the speed of light (c) then we have:

$$dt = \frac{dy}{\rho(y)c} \quad 5.9$$

and so

$$M_{\mu}(E'_{\mu}) = A_{\pi} \int_0^{\frac{m_{\pi}c^2 y_0}{E_{\pi}}} \frac{dy}{\lambda_{\pi}} \exp\left(\frac{-y}{\lambda_{\pi}}\right) \sum_{n=0}^{\infty} \left(\frac{y}{\lambda}\right)^n \left\{ n! \left(1 + n + \frac{m_{\pi}c^2 y_0 b}{\tau_{\pi} c \rho(0) E_{\pi}} \right) \right\}^{-1} \frac{m_{\pi}c^2}{E_{\pi} \tau_{\pi}} \frac{dy}{\rho(y)c} \quad 5.10$$

where the upper limit of the integration has been extended from y_0 to ∞ with negligible difference.

Following Bull et al. (1965) we make the substitution of j_{π} for $\frac{m_{\pi}c^2 y_0}{\tau_{\pi} c \rho(0)}$ and perform the integration with the result:

$$M_{\mu}(E'_{\mu}) = \frac{A_{\pi} E_{\pi}^{-(\gamma+1)} b j_{\pi} \lambda_{\pi}}{\lambda_{\pi}} \sum_{n=0}^{\infty} \left(\frac{\lambda_{\pi} - \lambda_{\pi}}{\lambda_{\pi}}\right)^n \left(n+1 + \frac{b j_{\pi}}{E_{\pi}}\right)^{-1} \quad 5.11$$

The assumption is now made that λ_{π} and λ_{μ} are equal, and consequently the only remaining term in 5.11 is that with $n = 0$. Thus the muon production spectrum can be written as :

$$M_{\mu}(E'_{\mu}) = \frac{A_{\pi} E_{\pi}^{-(\gamma+1)} b j_{\pi}}{1 + \frac{b j_{\pi}}{E_{\pi}}} \quad 5.12$$

remembering that $E'_{\mu} = r_{\pi} E_{\pi}$ and hence $dE'_{\mu} = r_{\pi} dE_{\pi}$ it follows that:

$$M_{\mu}(E'_{\mu}) dE'_{\mu} = \frac{A_{\pi} E_{\pi}^{-\gamma} r_{\pi}^{\gamma-1} r_{\pi} b j_{\pi}}{E_{\mu} + r_{\pi} b j_{\pi}} dE'_{\mu} \quad 5.13$$

and putting B_{π} for $r_{\pi} b j_{\pi}$ gives the muon spectrum at production as:

$$M_{\mu}(E'_{\mu})dE'_{\mu} = \frac{A_{\pi}E_{\mu}^{\gamma} r_{\pi}^{\gamma-1} B_{\pi}}{E'_{\mu} + B_{\pi}} \quad 5.14$$

Putting in values for m_{π} (0.140 GeV/c²) and τ_{π} (2.60x10⁻⁸ sec) one finds that $B_{\pi} \sim 90$ GeV which is close enough approximation considering all the assumptions which have been made in the derivation.

5.2.4 The Muon Spectrum at Sea Level

During its traversal of the atmosphere from production to sea level, the muon loses energy, mainly by ionization, and suffers the probability of decay into an electron. The expression for the rate of energy loss used is taken from Maeda, (1964) and is given by :

$$-\frac{dE}{dx} = (2.5 + 0.0025 E) \text{ MeV gm}^{-1} \text{ cm}^2 \quad 5.15$$

The decay of the muon is represented by its survival probability from point of production to sea level. This is calculated following Rossi (1952), giving the probability of a muon produced at a depth y surviving to sea level (y_0) as:

$$P_{\mu}(Ey_0, y) = \left(\frac{y}{y_0}\right) \cdot \frac{Ey_0}{Ey} \left(\frac{m_{\mu} c^2}{\rho(y)\tau_{\mu}cE_{top}}\right) \quad 5.16$$

where E_{y_0} , E_y , and E_{top} are the energy of the muon at sea level, at a depth y , and at the top of the atmosphere respectively. Again substituting for $\rho(y)$ from equation 5.4, and writing the rate of energy loss as ϵ we have:

$$P_{\mu}(Ey_0, y) = \frac{y}{y_0} \cdot \left(\frac{Ey_0}{Ey_0 + \epsilon(y_0 - y)}\right) \left(\frac{by_0 m_{\mu} c^2}{\rho(0)\tau_{\mu}c(\epsilon y_0 + \epsilon y)}\right) \quad 5.17$$

Making the approximation that there is a single height of production (100 gm cm⁻²) and taking the latest values for the constants in 5.17 we find :

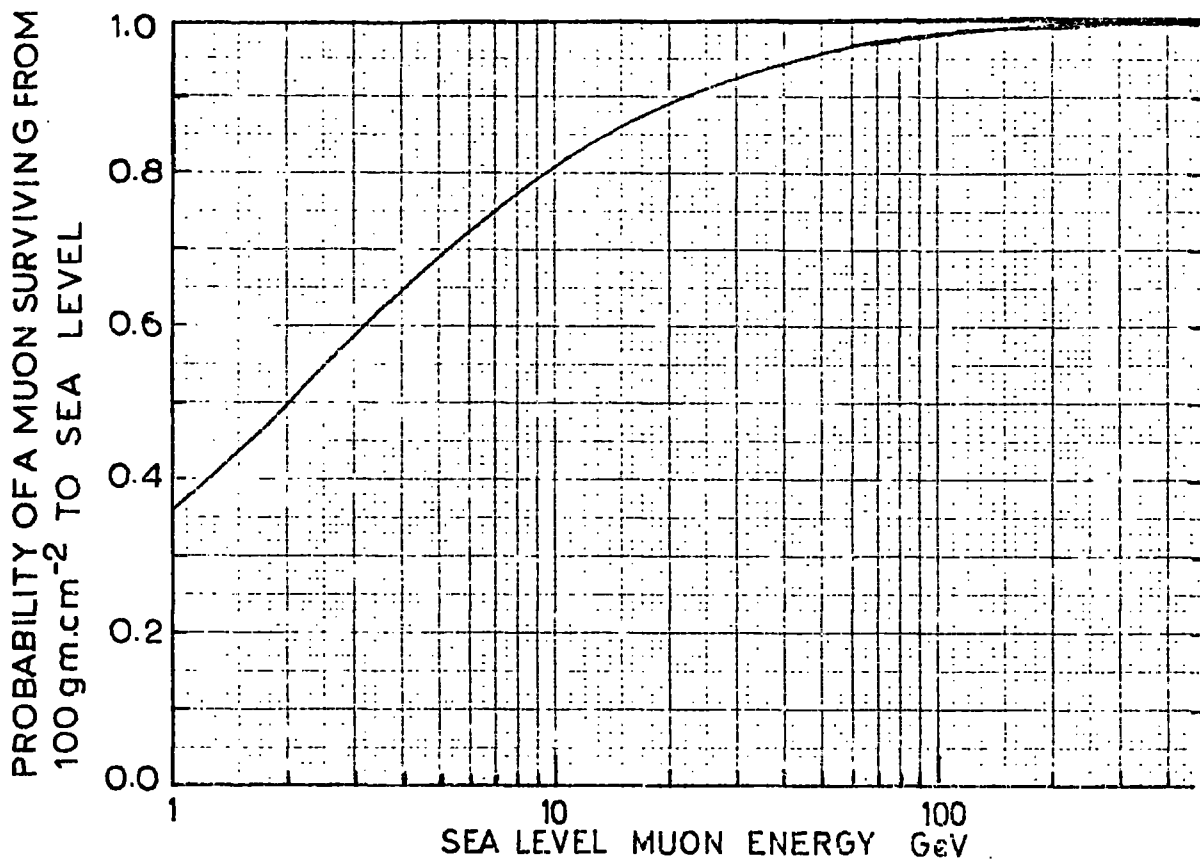


FIGURE 5.1 The Muon Survival Probability.

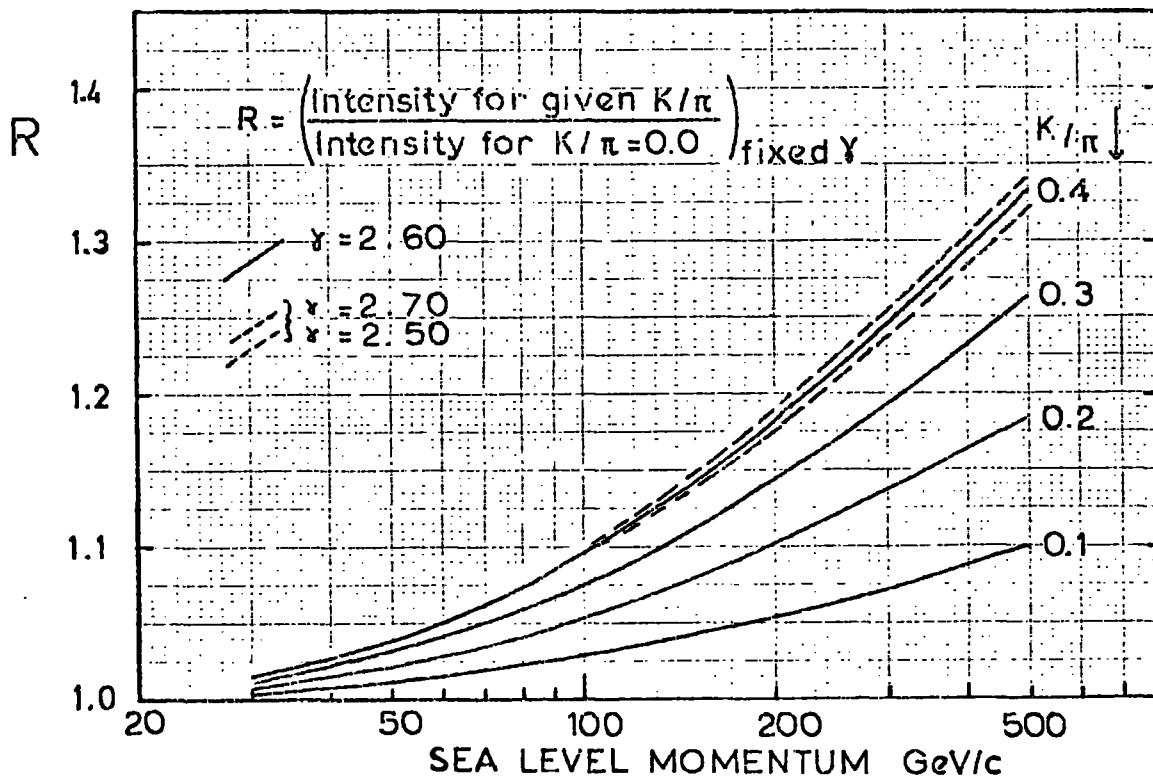


FIGURE 5.2 The Effect of Kaons on the Muon Spectrum.

$$P_{\mu}(E_{y_0}) = \left(\frac{100}{1033} \cdot \frac{E_{y_0}}{E_{y_0} + 933\epsilon} \right)^{\left(\frac{1.027}{E_{y_0} + 1033\epsilon} \right)} \quad 5.18$$

This expression has been used throughout to calculate the survival probability, and is shown graphically in figure 5.1.

Thus incorporating the survival probability, and ionization loss with the muon production spectrum, the muon spectrum at sea level due to pion decay alone is given by :

$$N_{\mu}(E_{\mu}) dE_{\mu} = A_{\pi} P_{\mu} (E_{\mu} + \Delta E_{\mu})^{-\gamma} \frac{r_{\pi}^{\gamma-1} B_{\pi}}{(E_{\mu} + \Delta E_{\mu} + B_{\pi})} \quad 5.19$$

where ΔE_{μ} is the energy loss from production (i.e. $E'_{\mu} = E_{\mu} + \Delta E_{\mu}$)

5.2.5 The Effect of Including Kaon Decay.

The derivation given above can be generalized to any muon producer via decay. The most likely such muon parent is the kaon, producing muons via the dominant $K_{\mu 2}$ decay mode. Including this decay mode in the expression for the muon spectrum at sea level gives:

$$N_{\mu}(E_{\mu}) dE_{\mu} = A P_{\mu}(E_{\mu} + \Delta E_{\mu}) \left[\frac{r_{\pi}^{\gamma-1} B_{\pi}}{(E'_{\mu} + \Delta E_{\mu} + B_{\pi})} + \frac{K r_k^{\gamma-1} B_k}{(E_{\mu} + \Delta E_{\mu} + B_k)} \right] \quad 5.20$$

where r_k (0.52) is defined as in section 5.2.3 and K is the K/π ratio at production. B_k is defined in a likewise manner to B_{π} , and is found to have a value ~ 450 GeV, (with $m_k = 0.494$ GeV/c² and $\tau_k = 1.24 \cdot 10^{-8}$ sec).

Including the effect of kaon production is found to increase the muon intensity at higher energies above that expected from the same value of γ and pion production alone. Figure 5.2 shows the enhancement as a function of momentum when the two cases are normalized to each other at 20 GeV/c. Values are shown for four different K/π ratios from 0.1 to 0.4. It can be seen that for $K/\pi \sim 15\%$ as suggested by the recent accelerator results, the enhancement is $\sim 4\%$ at 100 GeV/c, reaching $\sim 14\%$ at 500 GeV/c. (The distinction between energy and momentum is considered negligible at the high energy in the present situation).

5.3 Comparison of the Predicted and Measured Muon Spectrum

5.3.1 Method of Comparison

Using the equation 5.20 it is possible to compare the predictions for various values of γ , A , and K using a simple χ^2 test. Normally χ^2 is used with frequency distributions and is given by :

$$\chi^2 = \sum \frac{(N_{\text{obs}} - N_{\text{exp}})^2}{N_{\text{exp}}} \quad 5.21$$

Essentially χ^2 is a measure of how good the experimental points are compared with the experimental errors assuming the theoretical distribution is a true representation of the situation. In the present application a more general form is used, viz:

$$\chi^2 = \sum \left(\frac{I_o - I_e}{\delta I_o} \right)^2 \quad 5.22$$

where I_o is the observed intensity with a standard error δI_o and I_e the expected intensity.

The method used was to fix γ and K , and vary A until the minimum value of χ^2 was obtained. This procedure was repeated for different values of γ and the variation of the minimum χ^2 with γ found. The best fit γ is then that value corresponding to the minimum of the minimum χ^2 (hereinafter called simply the minimum χ^2). Figure 5.3(a) shows the $\chi^2 - \gamma$ plot obtained with $K = 0.0$ and will be discussed in more detail in the next section.

Initially an all pion source is considered, and then the effects of kaon production are estimated.

5.3.2 All Pion Source

Table 5.1 shows the values of χ^2 obtained for various values of γ with $K/\pi = 0.0$. Column 2 shows the results when no allowance for the systematic errors is made, and columns 3 and 4 show the effect of displacing the measured values to the upper and lower limits respectively, of the systematic errors which affect the shape of the spectrum, (mainly the effect of the error in

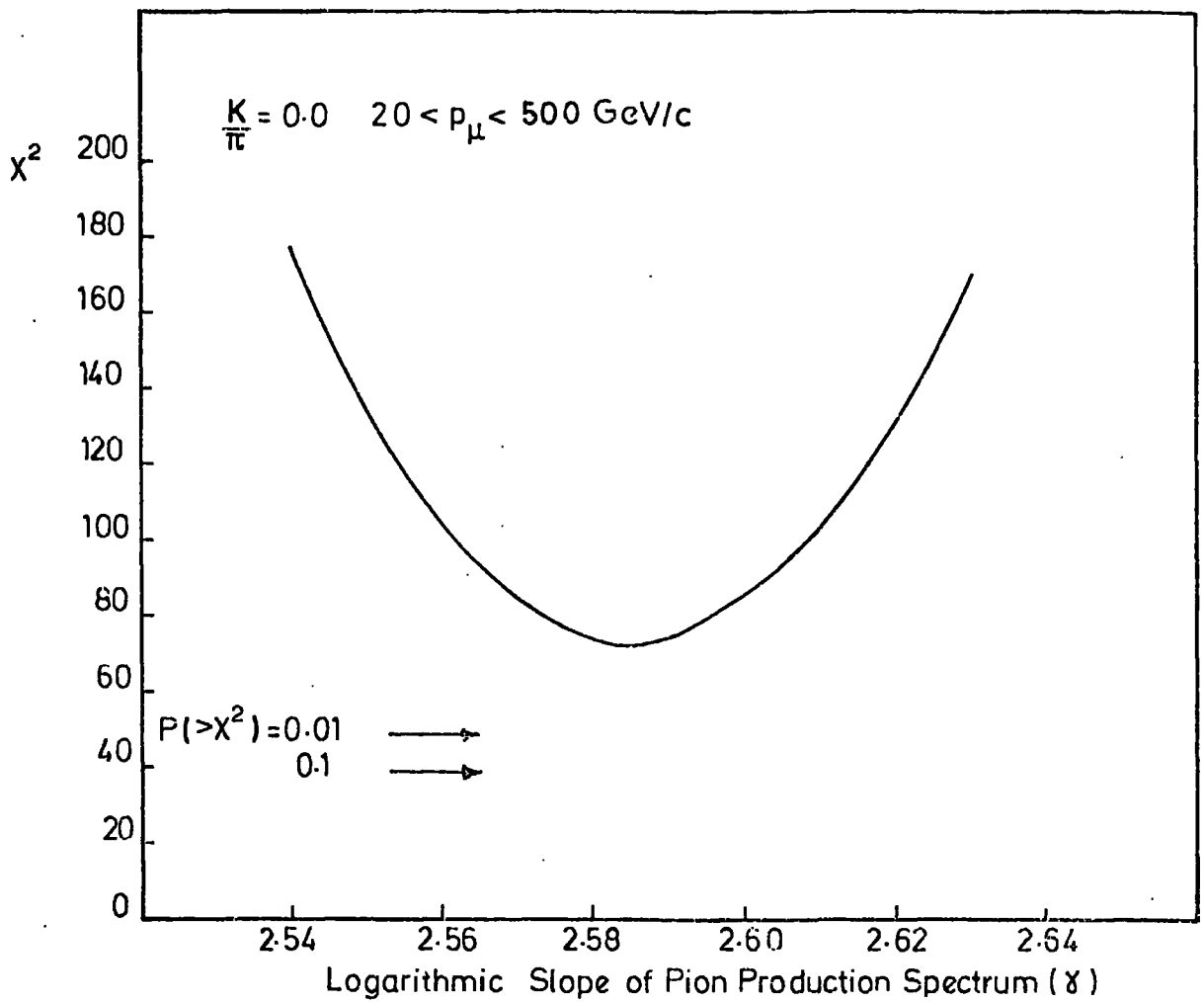


FIGURE 5.3(a) χ^2 - γ Plot for the Whole Momentum Range.

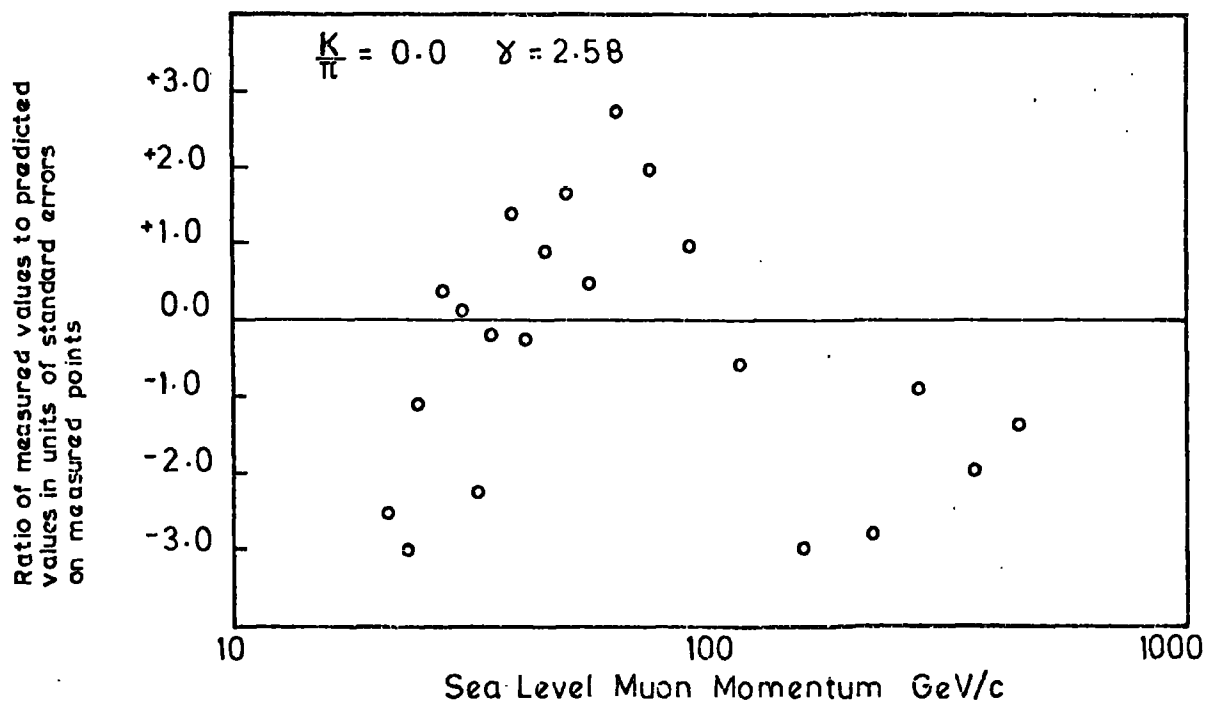


FIGURE 5.3(b) Distribution of Experimental Points around the BestFit Curve for the Whole Momentum Range.

γ	Values of χ^2		
	no systematic errors.	upper limit to systematic errors affecting shape.	lower limit to systematic errors affecting shape.
2.54	174.2	146.0	204.9
2.55	134.6	111.0	160.1
2.56	103.9	87.0	125.3
2.57	83.9	73.2	98.8
2.58	74.2	69.4	82.9
2.59	74.7	75.7	77.4
2.60	85.3	92.1	81.2
2.61	103.4	116.4	93.8
2.62	131.9	150.4	116.6
2.63	171.4	195.3	150.2

Table 5.1
Minimum values of χ^2 corresponding to different values of γ in equation 5.20 with $K/\pi = 0.0$

the magnetic field). As can be seen there are no significant differences between the three sets of χ^2 except a slight shift in the γ -axis. In all cases in computing the values of χ^2 only the statistical errors have been used in the denominator of the expression (5.22). The values of χ^2 neglecting systematic errors are shown in figure 5.3.(a). In the method of calculating χ^2 the variation of A was simply to give the minimum value of χ^2 and does not reduce the number of degrees of freedom which is consequently the same as the number of data points being considered. For the figures shown in table 5.1 all 21 data points have been used i.e. the full momentum range from 20 GeV/c to 500 GeV/c. Examination of the χ^2 tables for 21 degrees of freedom shows that for 1% significance $\chi^2 = 38.9$, and for 0.1%, $\chi^2 = 46.8$. These values are indicated in figure 5.3(a) showing that the best fit obtained with $K/\pi = 0.0$, and all the data from 20 GeV/c to 500 GeV/c sea level muon momentum, is very poor indeed. This is emphasised in figure 5.3(b) which shows the ratio of the experimental values to those calculated, with $K/\pi = 0.0$ and the minimum value of γ ($= 2.58$) expressed in units of

standard errors of the experimental points. Whilst no points actually lie outside three standard errors, it is seen that there is a systematic variation, the experimental values being lower at the ends of the energy range, and higher in the middle. The conclusion is that a model with $K/\pi = 0.0$ and a constant value of γ gives a poor fit to the experimental data.

For the case of a single source of muons (e.g. pions) it is possible to work directly from the muon spectrum at sea level to the parent production spectrum. This is not possible for two different parents (e.g. pions and kaons) since the energies of the parents which produce a given muon energy are different and the problem becomes a function of γ through the $r^{\gamma-1}$ term of equation 5.20. For the case of an all pion source however, the intensity of pions at production, corresponding to each of the experimentally determined muon intensities (given in section 4.7), has been calculated and the results are illustrated as the experimental points in figure 5.4. The procedure for calculating the points is the inverse of equation 5.19, and is shown in table 5.2., based on the relation:

$$N_{\pi}(E_{\pi}) dE_{\pi} = N_{\mu}(E_{\mu}) \left(\frac{B_{\pi} + E_{\mu}}{B_{\pi}} \right) \frac{r_{\pi}}{P_{\mu}} dE_{\mu} \quad 5.23$$

where the notation is as in section 5.2.

Examination of this calculated pion production spectrum shows that on a log-log plot the data follow roughly a straight line up to $E_{\pi} \sim 100$ GeV, indicating a constant value of γ , then suffer an increase in intensity indicating a reduction of the slope, γ . Consideration of the two regions separately, using the χ^2 method gives a best fit γ of 2.63 ($\chi^2 = 15.4$; significance level $\sim 35\%$) for $E_{\pi} < 100$ GeV, and a γ of 2.51 ($\chi^2 = 2.4$; significance level $\sim 90\%$) for $E_{\pi} > 100$ GeV. These two best fit lines are shown as the solid lines in figure 5.4, whilst the broken line shows the best fit with γ a constant 2.58 over the whole energy range. It is obvious that the two- γ case gives a much better fit to the experimental data, which is reinforced by the values of χ^2 found. If the 20% significance level is arbitrarily taken for the limits of the errors, then we can say that for a

Sea Level Muon Energy GeV	Sea Level Muon Energy at Production GeV	Muon Energy at Production E'_μ	Equivalent pion energy $E_\pi = E'_\mu / r_\pi$	Survival Probability P_μ	$\frac{E_\pi}{E'_\mu + E_\pi}$	Muon intensity at sea level $s^{-1} cm^{-2} sr^{-1} (GeV)^{-1}$ $N(E_\mu)$	$N(E_\pi)$ (from $eqn. 5.22$) $s^{-1} cm^{-2} sr^{-1}$ (GeV) ⁻¹	Error %
21.69	24.07	31.66	0.902	0.789	2.002×10^{-5}	2.138×10^{-5}	0.97	
23.60	25.99	34.20	0.909	0.776	1.640×10^{-5}	1.767×10^{-5}	0.96	
25.66	28.05	36.91	0.916	0.762	1.330×10^{-5}	1.448×10^{-5}	0.97	
28.45	30.85	40.59	0.923	0.745	9.907×10^{-6}	1.095×10^{-5}	0.99	
31.0	33.40	43.95	0.929	0.729	7.968×10^{-6}	8.937×10^{-6}	1.40	
33.1	35.51	46.72	0.933	0.717	6.947×10^{-6}	7.889×10^{-6}	1.39	
35.3	37.71	49.62	0.937	0.705	5.704×10^{-6}	6.565×10^{-6}	1.43	
38.91	41.33	54.38	0.943	0.685	4.337×10^{-6}	5.102×10^{-6}	0.90	
41.7	44.1	58.0	0.946	0.671	3.651×10^{-6}	4.370×10^{-6}	0.71	
45.8	48.2	63.4	0.951	0.651	2.806×10^{-6}	3.445×10^{-6}	0.73	
50.7	53.2	70.0	0.955	0.628	2.107×10^{-6}	2.667×10^{-6}	0.76	
57.0	59.5	78.3	0.960	0.602	1.532×10^{-6}	2.015×10^{-6}	0.78	
65.3	67.8	89.2	0.965	0.570	1.021×10^{-6}	1.410×10^{-6}	0.83	
76.6	79.1	104.1	0.970	0.532	6.461×10^{-7}	9.514×10^{-7}	0.88	
93.0	95.5	125.7	0.975	0.485	3.668×10^{-7}	5.893×10^{-7}	0.97	
118.0	120.6	158.7	0.980	0.427	1.809×10^{-7}	3.284×10^{-7}	1.10	
160.0	162.7	214.1	0.985	0.356	7.241×10^{-8}	1.568×10^{-7}	1.32	
220.6	223.4	293.9	0.989	0.287	2.648×10^{-8}	7.083×10^{-8}	2.20	
274.0	277.0	364.5	0.991	0.245	1.260×10^{-8}	3.940×10^{-8}	3.50	
363.3	366.5	482.2	0.993	0.197	5.182×10^{-9}	2.011×10^{-8}	3.94	
442.0	445.4	586.1	0.995	0.168	2.764×10^{-9}	1.256×10^{-8}	7.96	

Table 5.2. The calculation of pion production spectrum "point by point" assuming an all pion source

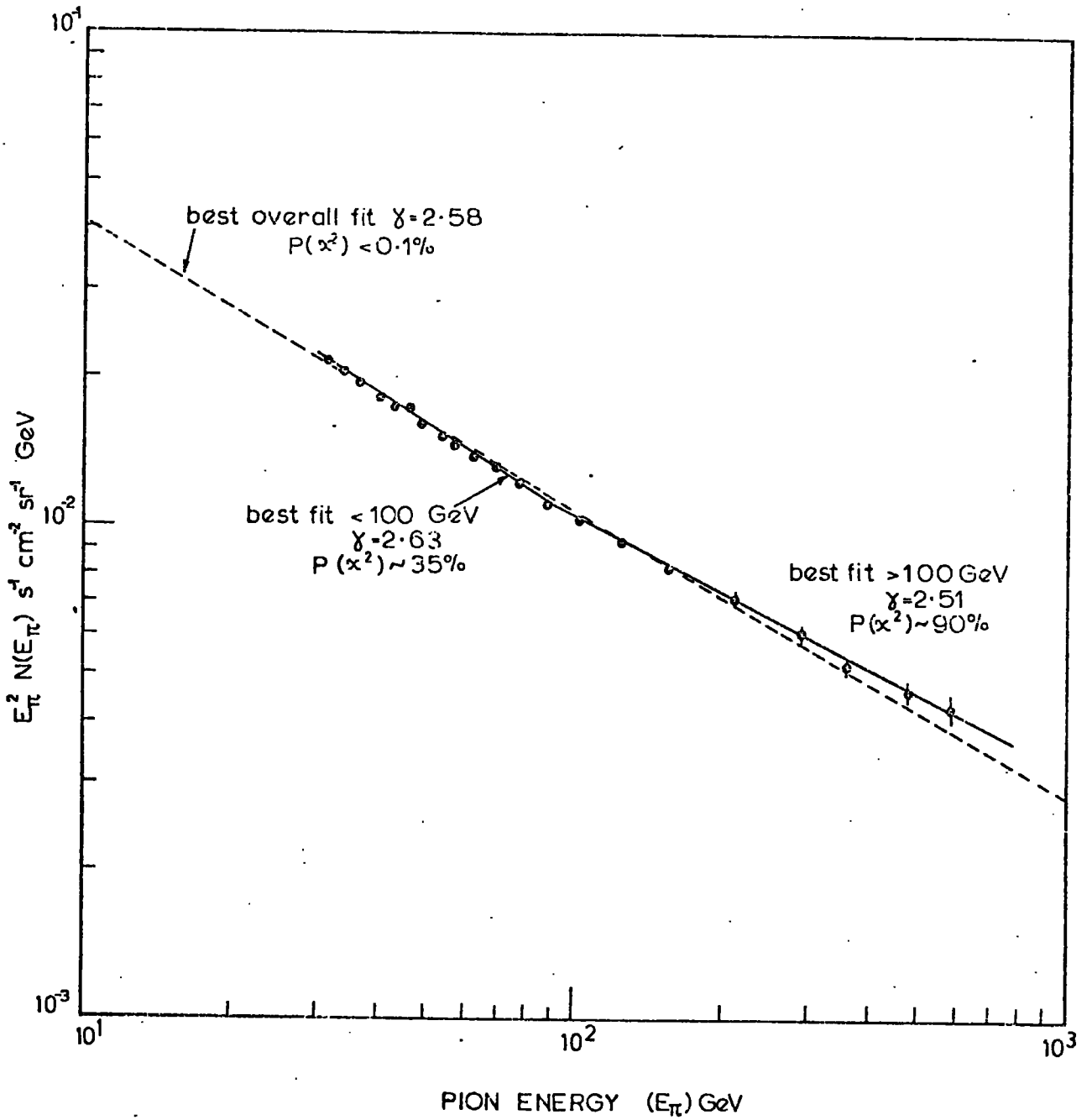


FIGURE 5.4 Point-by-Point Calculation of the Pion Production Spectrum.

K/ π ratio of 0.0 then :

$$N_{\pi}(E_{\pi}) \propto E_{\pi}^{-2.63 \pm 0.02} \quad 30 \text{ GeV} < E_{\pi} < 100 \text{ GeV}$$

$$N_{\pi}(E_{\pi}) \propto E_{\pi}^{-2.51 \pm 0.04} \quad 100 \text{ GeV} < E_{\pi} < 700 \text{ GeV}$$

5.3.3 Inclusion of Kaons.

It is well established, both in accelerator measurements and in cosmic ray spectra measurements at large angles, that kaons are certainly produced in nuclear interactions, and consequently must constitute a part of the parentage of the sea level muons, the extent of which has been illustrated in figure 5.2. In this section the effect of including kaons will be considered to see if this is a possible explanation of the anomalous results found in the previous section. (i.e. the apparent non-constancy of γ in the all pion case.)

Again the χ^2 test was used to compare prediction with observation to investigate the relationship of the best values of K/ π and γ . The results of this analysis are shown in table 5.3 and in figure 5.5. As before in addition to considering the data over the entire momentum range with a constant γ , two momentum regions have been taken, (i.e. $p_{\mu} < 70 \text{ GeV/c}$, and $p_{\mu} > 70 \text{ GeV/c}$), the division being made at approximately 100 GeV pion energy. The figures in brackets are the χ^2 obtained.

$\frac{K}{\pi}$ ratio	Values of γ corresponding to minimum χ^2		
	($20 < p_{\mu} < 500$) GeV/c 21 points	($20 < p_{\mu} < 70$) GeV/c 13 points	($70 < p_{\mu} < 500$) GeV/c 8 points
0.0	2.585 (74.2)	2.625 (15.4)	2.515 (2.4)
0.1	2.605 (55.8)	2.640 (14.4)	2.545 (2.5)
0.2	2.625 (46.3)	2.655 (14.0)	2.575 (2.9)
0.3	2.640 (36.9)	2.665 (14.1)	2.600 (2.9)
0.4	2.655 (32.8)	2.675 (14.1)	2.620 (3.1)
0.5	2.665 (29.2)	2.685 (14.3)	2.635 (3.3)
0.6	2.680 (25.3)	2.695 (14.9)	2.655 (3.3)

Table 5.3.

Values of γ corresponding to the best fits with different K/ π ratios. () indicate the corresponding values of χ^2 .

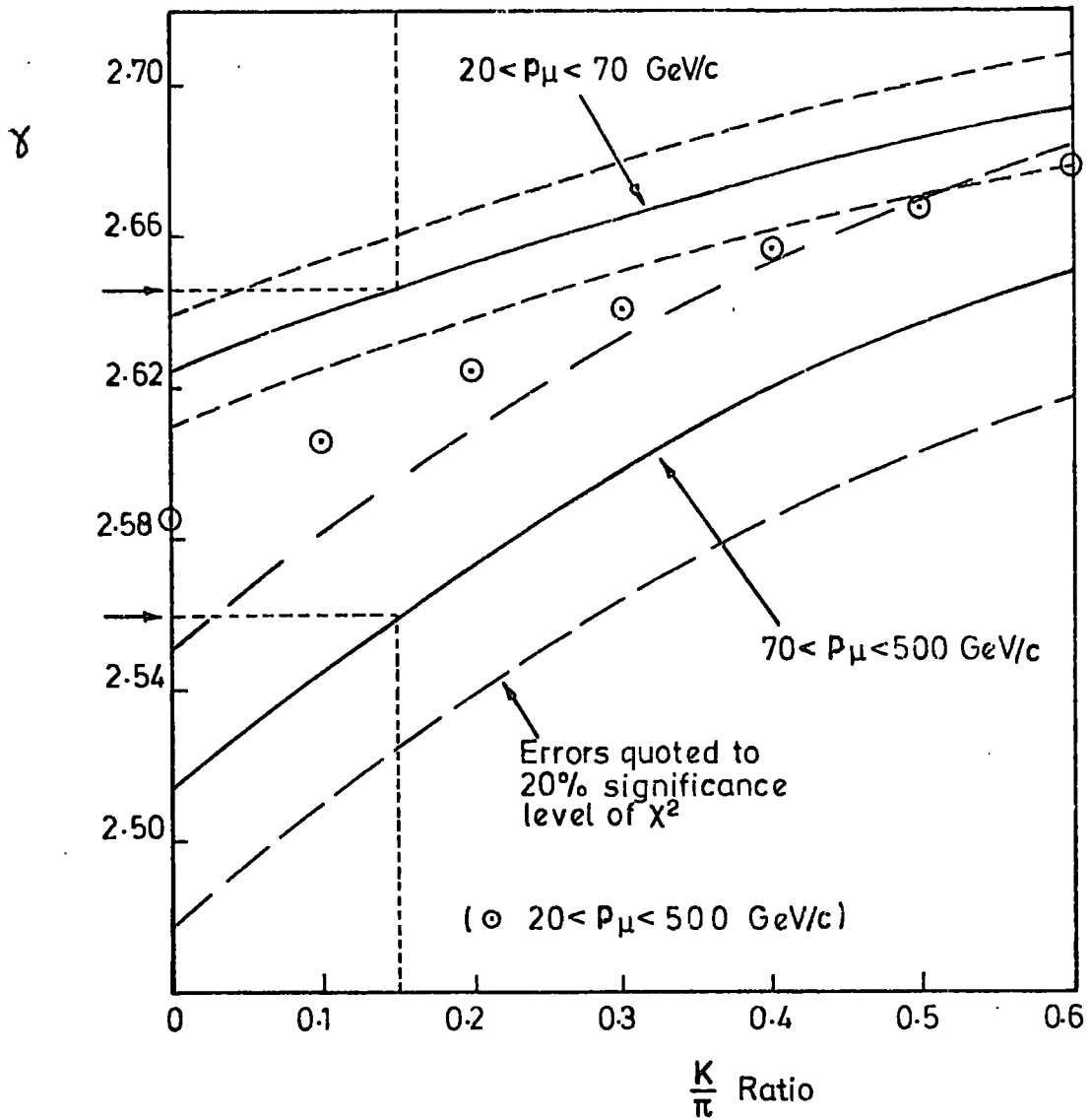


FIGURE 5.5 Variation of the Best Fit γ with K/π for the Different Momentum Ranges.

Consider first the entire momentum range. In this case we have 21 degrees of freedom and the value of χ^2 for 20% significance is 26.2, and for 5% is 32.7. Thus it appears that it would require a K/π ratio of ~ 0.60 to produce a constant value γ with 20% significance and a value of 0.40 to produce 5% significance. These values are well above the accelerator measured value of 0.15, which gives a $< 0.1\%$ significance level.

Relaxing the condition of a single value of γ over the entire momentum range one sees that for $p_\mu < 70$ GeV/c the values of χ^2 are quite constant at around the 35% significance level, with a slight minimum at $K/\pi \sim 0.2$. (This is probably fortuitous as it is felt that it would be unlikely that the K/π ratio could be determined so precisely in this low energy region.)

For $p_\mu > 70$ GeV/c again the χ^2 fits are seen to be very good, having $\sim 90\%$ significance level.

It is interesting to note that the degree of significance has risen markedly in the higher energy region. Apart from the obvious reason that the theoretical prediction may be a better representation at higher energies, the most likely reason is that there is some constant random error in the experimental data which naturally has more effect when the statistical errors are small, that is in the lower energy region. Such an effect, if random, will be unimportant except in the estimation of the errors in γ , which will artificially be made smaller if the χ^2 are made larger in the manner suggested. (i.e. assuming the errors are simply taken at some arbitrary significance level, in this case 20%).

If one assumes the value of the K/π ratio to be the 15% given by the accelerator experiments, then the values of γ giving the best fit for the two momentum regions can be read from figure 5.5 (indicated by the dashed lines) as 2.56 and 2.645 for the regions greater than and less than 70 GeV/c respectively.

Figure 5.6. shows plots of the χ^2 obtained for $K/\pi = 0.15$ as a function of γ . Also shown are those obtained when the experimental data are displaced to the upper and lower limits of the systematic errors which affect the shape of the spectrum. Taking these into account the uncertainties

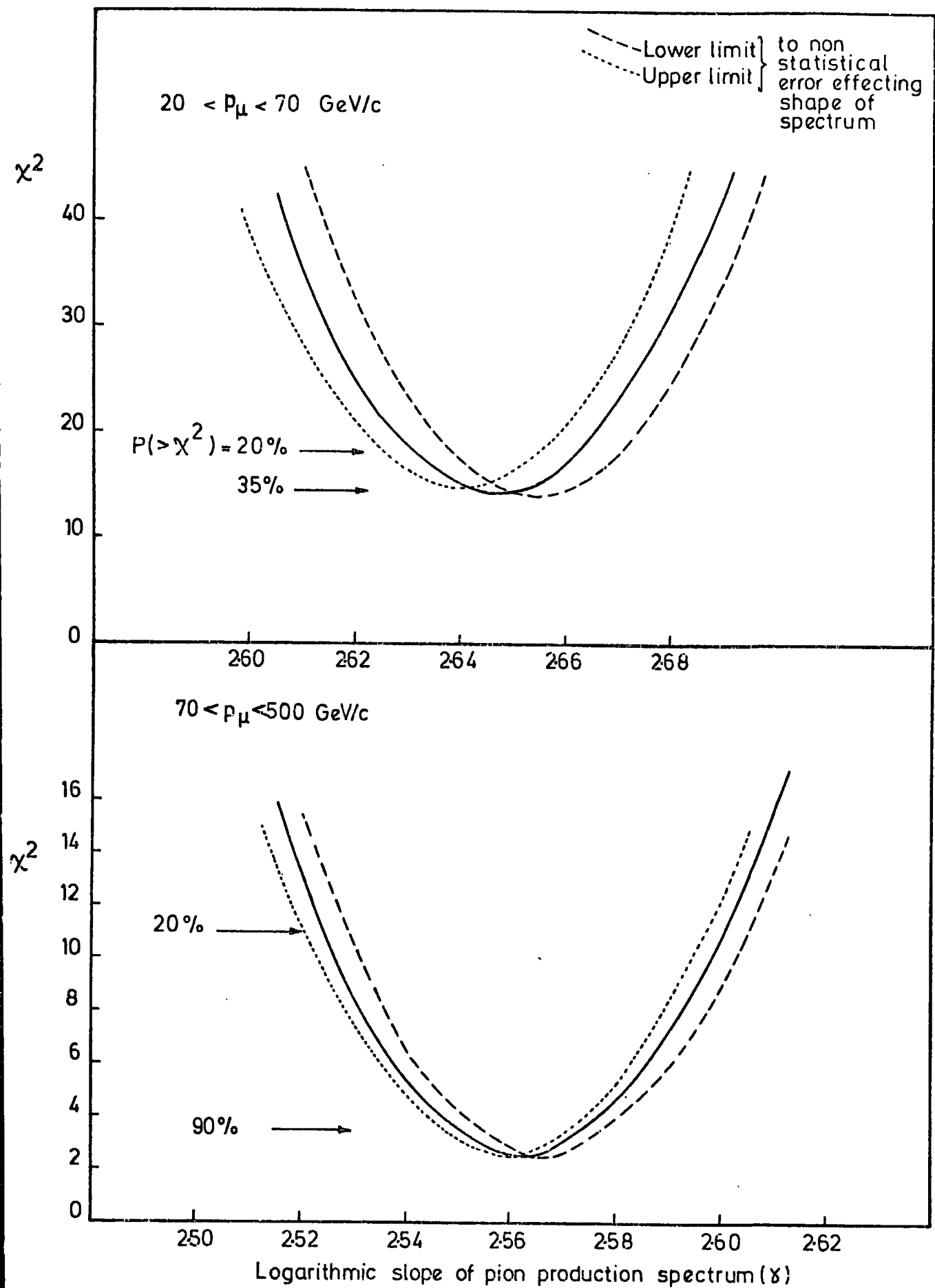


FIGURE 5.6 χ^2 - γ Plot for the Two Momentum Ranges ($K/\pi = 0.15$).

on the γ values for the two momentum regions are 0.020 and 0.040 respectively, (at 20% significance). Thus we have the following situation for the muon parent production spectrum, assuming 15% kaons.

$$N(E) \propto E^{-2.645 \pm 0.02} \quad 20 \text{ GeV/c} < p_{\mu} < 70 \text{ GeV/c}$$

$$N(E) \propto E^{-2.56 \pm 0.04} \quad 70 \text{ GeV/c} < p_{\mu} < 500 \text{ GeV/c}$$

which is taken to be the best representation of the experimental data.

5.4 The Integral Intensity above 500 GeV/c

Using the present experimental arrangement it is difficult to measure the integral spectrum due to the extent of the category acceptance functions and the consequential ill definition of the minimum momentum of the categories. As remarked at the end of chapter 4, it is possible to integrate the logarithmic polynomial expansion fitted to the experimental data in the aforementioned chapter, but this will only be correct over the range of the data points, i.e. up to 500 GeV/c. Consequently there will be an uncertainty as to the actual values above this momentum. To overcome this to some extent the best fit expression derived in the previous section can be used. The procedure is to use equation 5.20 with $K = 0.15$ and $\gamma = 2.56$, and fix A by making the value at 500 GeV/c agree with that of the best fit from chapter 4 (i.e. $1.79 \times 10^{-9} \text{ s}^{-1} \text{ cm}^{-2} \text{ sr}^{-1} (\text{GeV/c})^{-1}$). Having obtained the value of A , equation 5.20 can be integrated numerically, using Simpson's rule, from 500 GeV/c to effectively infinity. Using this method one finds $A = 0.1187$ and the intensity above 500 GeV/c = $3.74 \times 10^{-7} \text{ s}^{-1} \text{ cm}^{-2} \text{ sr}^{-1}$.

Table 5.4 shows how the values of this intensity would vary for different values of γ , in each case normalizing to the differential intensity 500 GeV/c.

Examination of this table shows that the integral intensity only varies by $\pm 7\%$ around $\gamma = 2.60$ for γ from 2.50 to 2.70. Consequently even if γ had been incorrectly determined in the previous section, the integral intensities given in table 4 would only be in error slightly (i.e. not more than a few %).

γ	$N(> 500 \text{ GeV/c})$ $\text{s}^{-1} \text{cm}^{-2} \text{sr}^{-1}$
2.50	$3.83 \cdot 10^{-7}$
2.55	$3.75 \cdot 10^{-7}$
2.60	$3.67 \cdot 10^{-7}$
2.65	$3.60 \cdot 10^{-7}$
2.70	$3.57 \cdot 10^{-7}$

Table 5.4.

Values of the integral intensity above 500 GeV/c obtained by normalizing the theoretical model (eqn. 5.20) to the differential intensity at 500 GeV/c and fixing the K/ π ratio to 0.15.

5.5 Conclusion.

In this chapter it has been shown how using a simple model of muon production and propagation through the atmosphere, the muon's parents' production spectrum can be calculated. It has been found that a power law production spectrum with a constant power (γ) over the entire energy range, including kaon production as well as pion production, does not represent the situation at all satisfactorily. In order to obtain significant values of χ^2 the K/ π ratio at production is required to be ~60%, or at least rise to these values at high energy, which in the light of other evidence seems highly unlikely. The only solution to the problem is to allow γ to vary with energy, and in particular two values of γ , 2.645 below and 2.56 above 70 GeV/c are found to be in good agreement with the experimental data assuming a value of 15% kaon production in interactions. It must be stressed however that the taking of two values of γ is only a first approximation, and that most likely if the shape does vary then it will do so smoothly. The values obtained here, particularly in the high energy region where the change is most likely taking place, are average values.

CHAPTER 6

COMPARISON WITH OTHER RESULTS

6.1 Introduction

This chapter attempts to compare the present results on the muon spectrum with those obtained by other workers, primarily those of other spectrograph measurements in a comparable energy range.

Methods of measuring the muon sea level spectrum fall into two classes: (a) direct determinations, and (b) indirect determinations. In class (a) are the measurements made at the surface of the earth with range spectrographs, and magnetic spectrographs similar to MARS. The indirect measurements of class (b) fall into three types, firstly measurements of the intensity of muons at various depths underground, secondly measurements on the electromagnetic bursts produced in local absorbers, and thirdly via measurements made on the γ -ray flux at various depths in the atmosphere. The calculation of the muon sea level spectrum from indirect measurements suffers the disadvantage that it relies upon assumptions made about not too well founded physical theories, namely those of nuclear, and electromagnetic interactions. Direct measurements on the other hand, although being somewhat limited in the energy range so far attained, are inherently more reliable in that the assumptions made are generally of a more well founded nature, i.e. the motion of charged particles in magnetic fields, and energy loss relations in well defined substances such as lead or iron. So far direct measurements have been made up to ~ 1000 GeV, whilst particles having a sea level energy $\sim 10^5$ GeV have been detected indirectly.

Most of the comparisons made in the present chapter will be with those of other direct measurements in an effort to see how justified are the conclusions reached in chapter 5 about the possible change in slope of the pion production spectrum. A short discussion is also given of some indirect measurements at higher energies than measured in the present experiment to see how the present results fit in with the overall picture of the muon spectrum.

6.2 Direct Determinations of the Muon Spectrum.

6.2.1 Introduction

It is not the purpose here to give a complete survey of all measurements to date of the muon spectrum. This has been done for many of the earlier experiments in reviews by several authors (Rossi, 1948; Fowler and Wolfendale, 1961). Also many of these early measurements have been shown to be in error and have been superseded by more precise experimental data, and more refined experimental techniques. Notable omissions are the work of the Manchester group in the 1950's (Owen and Wilson, 1955; Holmes et al., 1961), who measured the spectrum from a few GeV to 1000 GeV, but which was shown to be in error particularly in the high energy region possibly because their m.d.m. (~ 240 GeV/c) was exceeded by a large factor, and also possibly due to the difficulty in making precise measurements in cloud chambers due to the turbulence set up in the gas. Other measurements such as the work of Caro et al. (1951) in Melbourne (Australia), and that of the Cornell group (Pak et al., 1961; and Pine et al., 1959) have also been omitted.

The starting point will be taken in the early 1960's with the construction of the first muon spectrograph in Durham. Since then measurements have been made at a variety of places worldwide, notably at Nottingham (U.K.), Keil (W. Germany), and Dagapur (India). Recently some of the large spectrographs set up initially to examine the Utah effect have begun to produce results, in particular that at San Deigo (California, U.S.A.) and at College Station (Texas, U.S.A.).

To re-iterate what was mentioned in the first chapter, in recent years attention has been concentrated upon the absolute height of the muon spectrum, prompted initially by the work of Allkofer et al. (1970), who estimated that the Rossi point at 1 GeV/c (differential intensity $2.45 \times 10^{-3} \text{ s}^{-1} \text{ cm}^{-2} \text{ sr}^{-1} (\text{GeV}/c)^{-1}$) was probably underestimated by $\sim 20\%$. Since then a number of experiments have been performed in this energy region most of which confirm to some degree the findings of Allkofer et al..

Because of the difficulty in assigning an absolute height to the measured muon momentum spectra, due generally to ill defined rejection criteria, it had become customary for workers to normalise their data to some standard value which is most frequently the aforementioned Rossi point, (or some point on a spectrum which itself had been normalised to the Rossi point). Consequently a renormalisation of the spectra of many workers has been made, and frequently in the following comparisons the spectra have been normalised at different momentum values. When such a procedure has been used then the new normalisation point will be specified.

In order to compare the results of other workers with the present work, it is first necessary to define a standard comparison spectrum which represents a smooth fit to the experimental data. This is discussed in the next section.

6.2.2 The Standard Comparison Spectrum

Between 20 GeV/c and 500 GeV/c, the spectrum used is the logarithmic polynomial expansion given in chapter 4. This is found to be a very good fit to all the present experimental points over the entire momentum range. Above 500 GeV/c the spectrum has been extrapolated using the phenomenological model of muon production and propagation through the atmosphere given in chapter 5. The spectrum has been assumed to continue with the same value of γ (2.56) and the K/π ratio has again been taken to be 0.15. In order to determine the constant A (eqn.5.20) the model has been normalised to the value given by the polynomial fit at 500 GeV/c ($1.786 \times 10^{-9} \text{ s}^{-1} \text{ cm}^{-2} \text{ sr}^{-1} (\text{GeV}/c)^{-1}$). This procedure assigns a value to A of 0.1187. It can be justifiably assumed that if the experimental results up to 500 GeV/c are correct then such an extrapolation at least up to ~ 800 GeV/c is reasonable. Below 20 GeV/c again an extrapolation has been used with the same model but with $\gamma = 2.645$ and $A = 0.1815$, the best fit values found for a K/π ratio of 0.15 in the lower energy regions. It is interesting that such an extrapolation is only good down to ~ 7 GeV/c, below this value the intensities given are lower than those given in other experiments, in particular at 1 GeV/c

by Allkofer et al. (1970).

De et al. (1973) have examined the differential momentum spectrum in the region below 10 GeV/c, and taking into account the most recent absolute measurements have produced a mathematical expression, for the best fit, of the form :

$$I(p)dp = 3.08 \cdot 10^{-3} p^{\alpha_1 + \alpha_2 \ln p} dp \quad 6.1$$

where $\alpha_1 = -0.5483$ and $\alpha_2 = -0.3977$.

This is referred to by the above authors as their form fit, and as shown by Allkofer and Jokisch (1972) is a much better fit to the data, of the Kiel group (Allkofer et al., 1971) and that of Bateman et al. (1971), then had previously been taken (e.g. the ACD spectrum of the Kiel Group). This will be returned to later, however that is important for the present is the fact that this form fit joins on very well with the extrapolation of the present MARS spectrum below 20 GeV/c, with only a very slight discontinuity in slope at around 7 GeV/c. Hence in comparing with the data of other workers below 7 GeV/c this form fit has been used, the discontinuity at 7 GeV/c manifesting itself in some of the comparisons as a slight enhancement of the intensity (~few %).

Table 6.1 shows the values of the comparison spectrum which is taken at the best representation of the present experimental results. Both the differential and integral intensities are given, the latter being calculated simply by integrating the best fit differential spectrum. Figure 6.1 shows graphically these best fit spectra.

6.2.3 The Earlier Durham Measurements

Results were reported by Gardener et al. (1962), and by Hayman and Wolfendale (1962), on the spectrum measurements made in the region 0.4 to 10 GeV/c, and 5 to 1000 GeV/c respectively, using the then newly constructed cosmic ray muon spectrograph in Durham. The instrument was of an air gap magnet type utilizing geiger tubes for muon detection and low momentum measurements, and later neon flash-tubes to increase the resolution, using the geiger tubes as an automatic momentum selector. The m.d.m. of

Momentum GeV/c	Differential Intensities $s^{-1} cm^{-2} sr^{-1}$ (GeV/c) $^{-1}$	Integral Intensities $s^{-1} cm^{-2} sr^{-1}$		
1	3.08×10^{-3}	7.09×10^{-3}	Form fit of De et al., 1972	
1.5	2.31×10^{-3}	5.75×10^{-3}		
2	1.74×10^{-3}	4.75×10^{-2}		
3	1.04×10^{-3}	3.40×10^{-3}		
5	4.55×10^{-4}	2.00×10^{-3}		
7	2.35×10^{-4}	1.34×10^{-3}		Extrapolation of present work below 20 GeV/c.
10	1.16×10^{-4}	8.47×10^{-4}		
15	4.81×10^{-5}	4.69×10^{-4}		
20	2.43×10^{-5}	2.96×10^{-4}		
30	8.80×10^{-6}	1.48×10^{-4}		
50	2.20×10^{-6}	5.70×10^{-5}	Best fit logarithmic polynomial expansion to the present experimental results.	
70	8.43×10^{-7}	2.94×10^{-5}		
100	2.96×10^{-7}	1.42×10^{-5}		
150	8.68×10^{-8}	6.00×10^{-6}		
200	3.56×10^{-8}	3.18×10^{-6}		
300	9.77×10^{-9}	1.26×10^{-6}	Extrapolation of present work above 500 GeV/c.	
500	1.79×10^{-9}	3.74×10^{-7}		
700	5.76×10^{-10}	1.67×10^{-7}		
1000	1.72×10^{-10}	7.00×10^{-8}		

Table 6.1

Values of the Best Estimate of the Spectrum
used for Comparisons with other data.

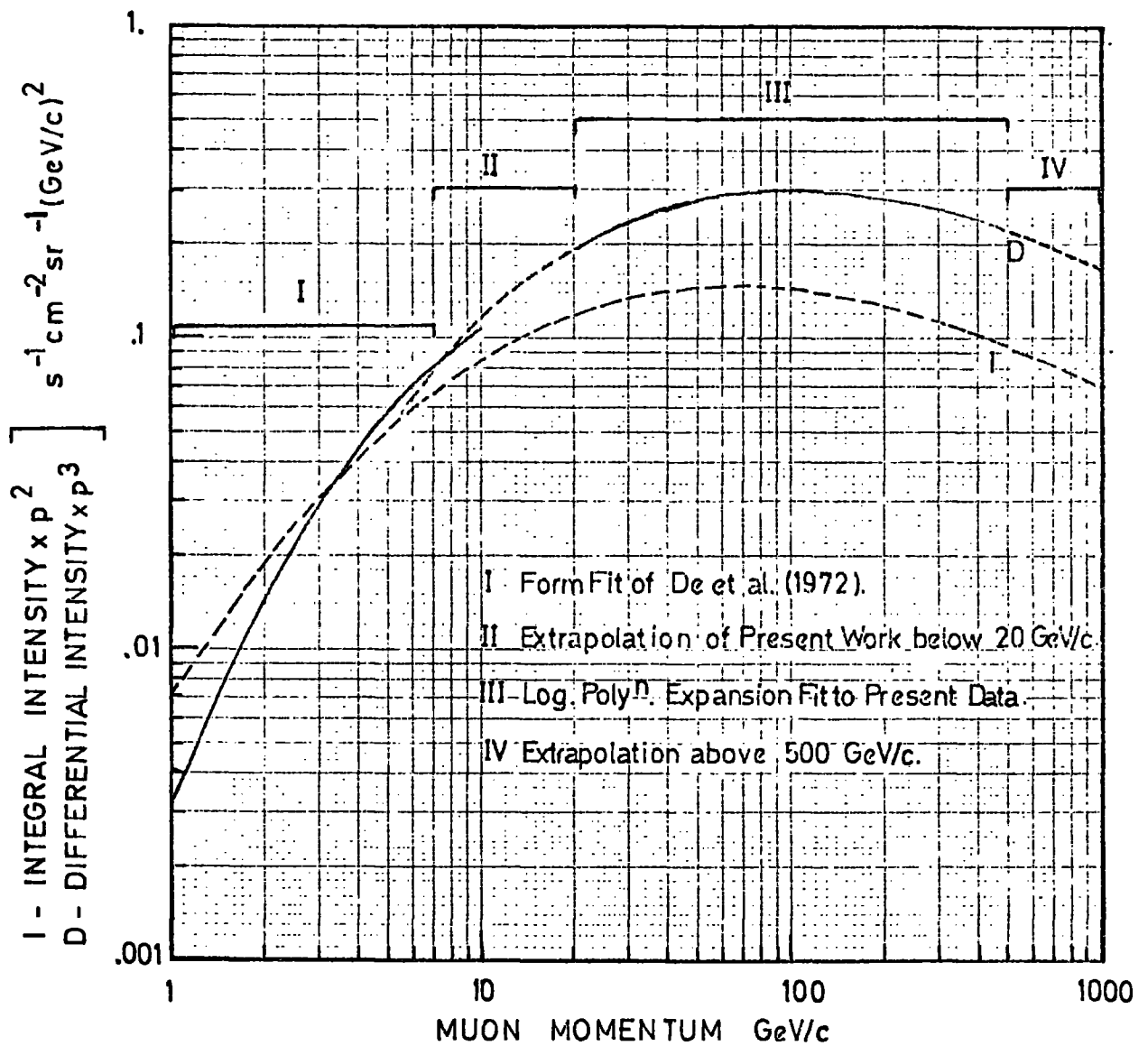


FIGURE 6.1 The Best Estimate Muon Spectrum including the Present Results (the Standard Comparison Spectrum).

each arrangement was quoted as 26 GeV/c and 657 GeV/c respectively.

The results of Gardener et al., based upon 191000 events recorded automatically with the geiger tubes, are shown in figure 6.2(a) together with those of Hayman and Wolfendale using the increased resolution of the flash-tubes, who measured 14556 events, 4520 corresponding to a momentum >20 GeV/c. The results from both these experiments were combined together by Hayman and Wolfendale to give a best estimate of the spectrum from 0.4 to 1000 GeV/c, shown as the HW spectrum in figure 6.2(a). This fitted curve was based upon a model of muon production and propagation through the atmosphere identical to that discussed in chapter 5, the authors having assumed that all the muons came from pions. The best fit value of Y was found to be 2.64 ± 0.05 in the region >10 GeV/c with a 50% significance level, (the errors quoted to the 16% level), using a standard χ^2 test. For momenta <10 GeV/c, Y was found, by Gardener et al., to decrease from a constant 2.65 above 5 GeV/c to 1.93 at 1 GeV/c.

Subsequently an instrumental bias was found in the HW spectrum, and Osborne et al. (1964) produced a spectrum, combining the corrected HW spectrum with the muon spectrum deduced from the measurements of Duthie et al. (1962) on the intensity of γ -rays in the atmosphere. The γ -rays were taken as the decay products of the π^0 's produced along with the charged pions in the nuclear interactions of the primaries in the atmosphere, and with the assumption of charge independence (i.e. equal numbers of all three charged states of the pion, π^0) in nuclear interactions, the pion production spectrum, and hence the muon sea level spectrum was deduced. The spectrum of Osborne et al., referred to as the OPW spectrum, is also shown in figure 6.2.(a) where the effect of the correction to the HW spectrum can easily be seen. All the results in figure 6.2.(a), with the exception of the comparison spectrum, which is also shown, have been renormalized to the Allkofer value at 1 GeV/c; their previous normalization having been to the Rossi point.

Finally the Durham spectrograph was modified by Aurela (1965) with the

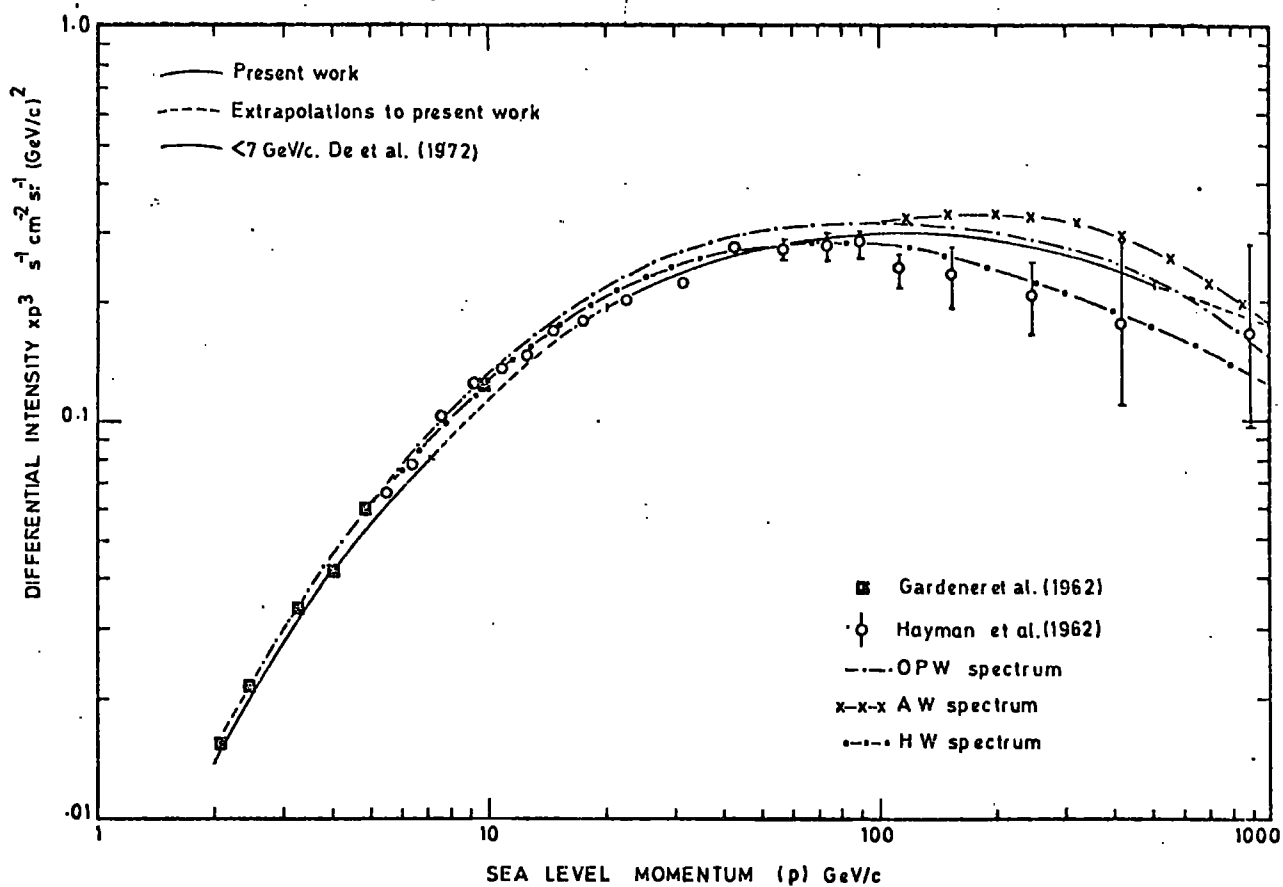


FIGURE 6.2(a) Previous Durham Spectra.

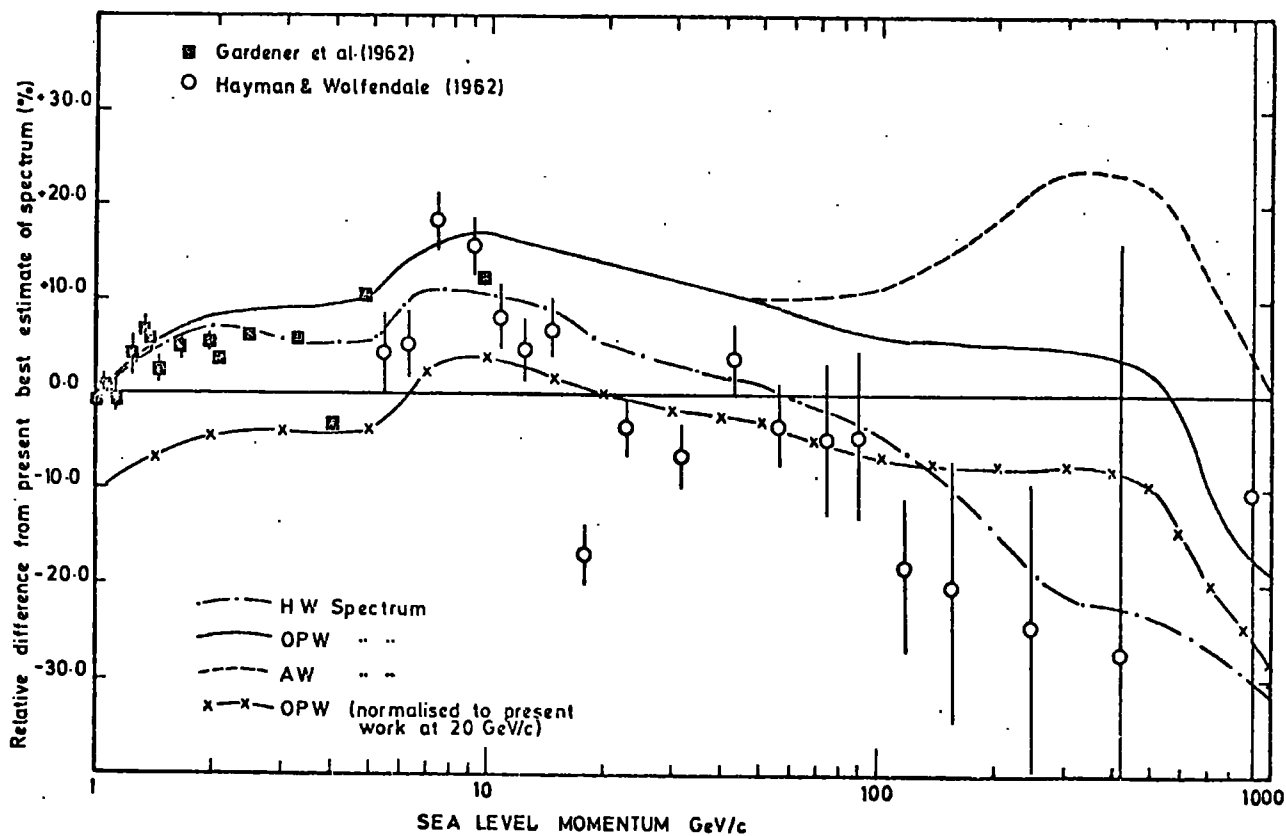


FIGURE 6.2(b) Comparison between the Previous Durham Spectra and the Present Best Estimate.

inclusion of an iron plug in the magnet to increase the magnetic flux, and hence the resolution of the instrument. These results together with the OPW spectrum and the underground measurements of Achar et al. (1965) were combined by Aurela and Wolfendale (1967) to give the AW spectrum also shown in figure 6.2.(a), which as can be seen differs only from the OPW spectrum in the higher momentum regions (>100 GeV/c). This excess is thought to be in error due to the normalisation of the various components making up the spectrum, particularly the underground measurements. Consequently the best estimate of the muon spectrum previously produced by the Durham group is considered to be the OPW spectrum.

Figure 6.2.(b) shows the relative difference of the various spectra from the present best estimate, normalisation, apart from that stated to the contrary, is to the 1 GeV/c point of Allkofer et al. The experimental points are again those of Gardener et al. and Hayman and Wolfendale. The sudden change in slope at around 7 GeV/c is artificial and can be attributed to the slight discontinuity of the comparison spectrum. The HW spectrum is generally steeper than the OPW and AW, due to the instrumental bias found in these measurements. Considering the OPW spectrum one sees that the general trend is that above 10 GeV/c it is slightly steeper than the present spectrum and if normalised to the Allkofer point at 1 GeV/c predicts higher intensities up to several hundred GeV/c, at which point the relative difference falls dramatically, presumably due to the extrapolation of the present spectrum at the high energy end. The AW spectrum is in agreement with the OPW up to ~ 100 GeV/c at which point it rises considerably and is thought to be incorrect in the way described. If the OPW spectrum is normalised to the present best fit at 20 GeV/c, then it is seen that for the region 20 GeV/c to 500 GeV/c over which the present experimental data were collected, the discrepancy between the OPW and the present data is everywhere small rising to only 10% at 500 GeV/c. The flattening in the curve at around 100 GeV/c indicates a flattening of the muon spectrum to very nearly the same shape as the present results, though in the region below this momentum the spectrum is obviously steeper.

6.2.4. The Work of the Nottingham Group

A major step forward in spectrum measurements was the inclusion of large solid iron magnets instead of air gap magnets. Apart from increasing the resolution, and the rate of collection of data, by allowing a large uniform magnetic field be sustained over a large volume, the iron also acts to filter off other less penetrating particles which could possibly be mistaken for muons in the air gap types of spectrograph. One of the early solid iron instruments was that constructed at Nottingham, results from which were initially reported by Bull et al. (1965).

The spectrograph used geiger tubes for triggering and hence acceptance defining devices, and optical neon flash-tubes for trajectory location, there being two sets of each type of detector both above and below the magnet. The m.d.m. was quoted as 360 GeV/c.

Subsequent to the initial measurements of Bull et al., more data was collected first by Eaber et al. (1968), and then by Appleton et al. (1971). The results of the analyses of both these groups of authors are shown of figure 6.3.(a) where they have been normalised at 20 GeV/c to the present results, the best fit curve of which is also shown. Using an all pion muon production model Eaber et al. find a best fit value of 2.65 ± 0.03 for γ , whilst in their initial analysis using fairly large deflection ranges, Appleton et al. find a γ value of 2.73 ± 0.02 . There seems to be no reason for this difference other than statistical. The latter value is based upon more particles including, however, those in the former experiment. Appleton et al. then further divide their highest momentum categories into smaller deflection ranges, and attempt to find a best fit with the inclusion of either kaons or the X-particle (direct muon production, i.e. the Utah effect.), as muon producers. Using a standard χ^2 test they find a best fit with $\gamma = 2.745$ and a K/π ratio of 20%, the same value of γ being found for the best fit with 5% direct production. The values of the best fit curves of both Eaber et al. and Appleton et al., again normalised to 20 GeV/c are shown in figure 6.3.(a), whilst figure 6.3.(b) shows the ratio of these Nottingham spectra to the best estimate from the present

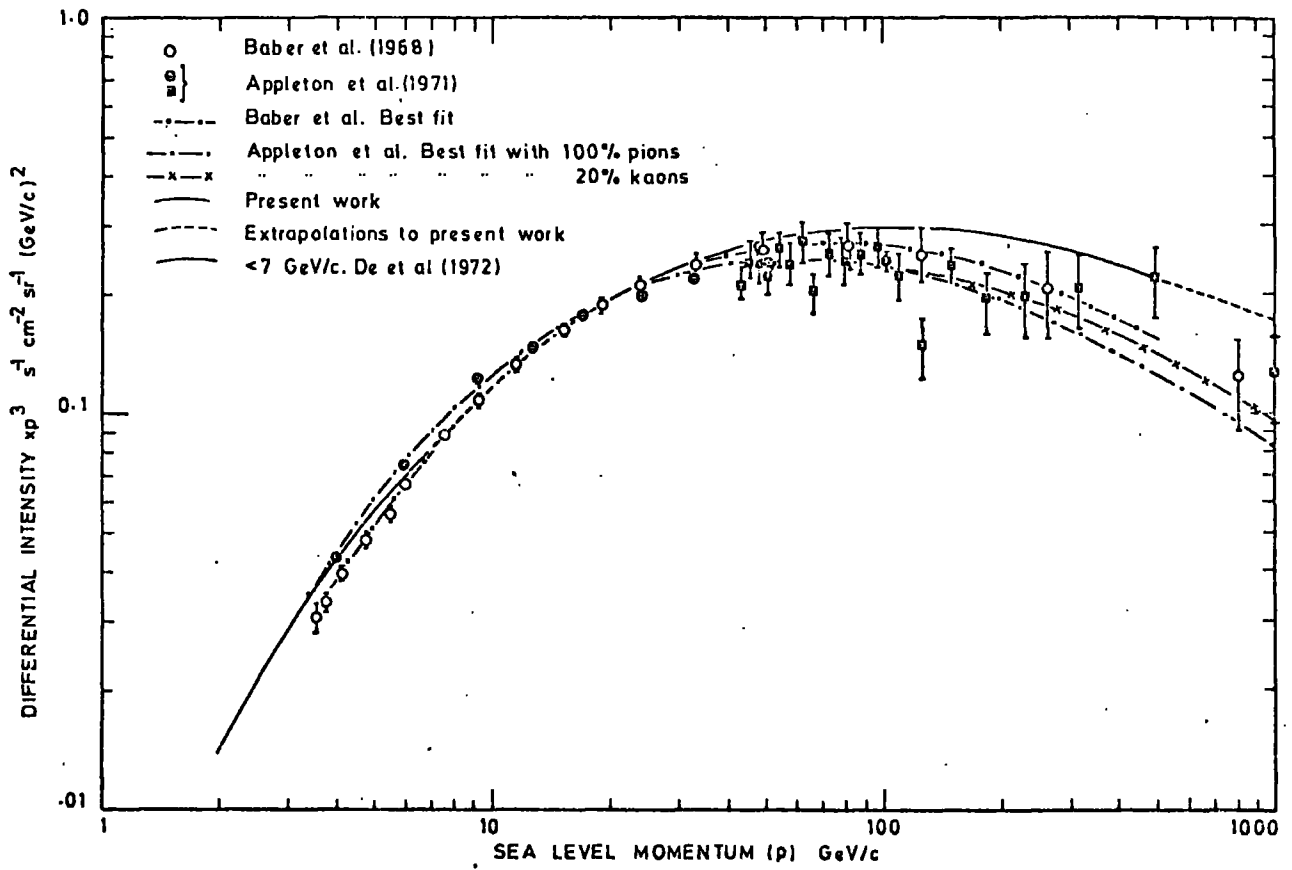


FIGURE 6.3(a) The Nottingham Spectra.

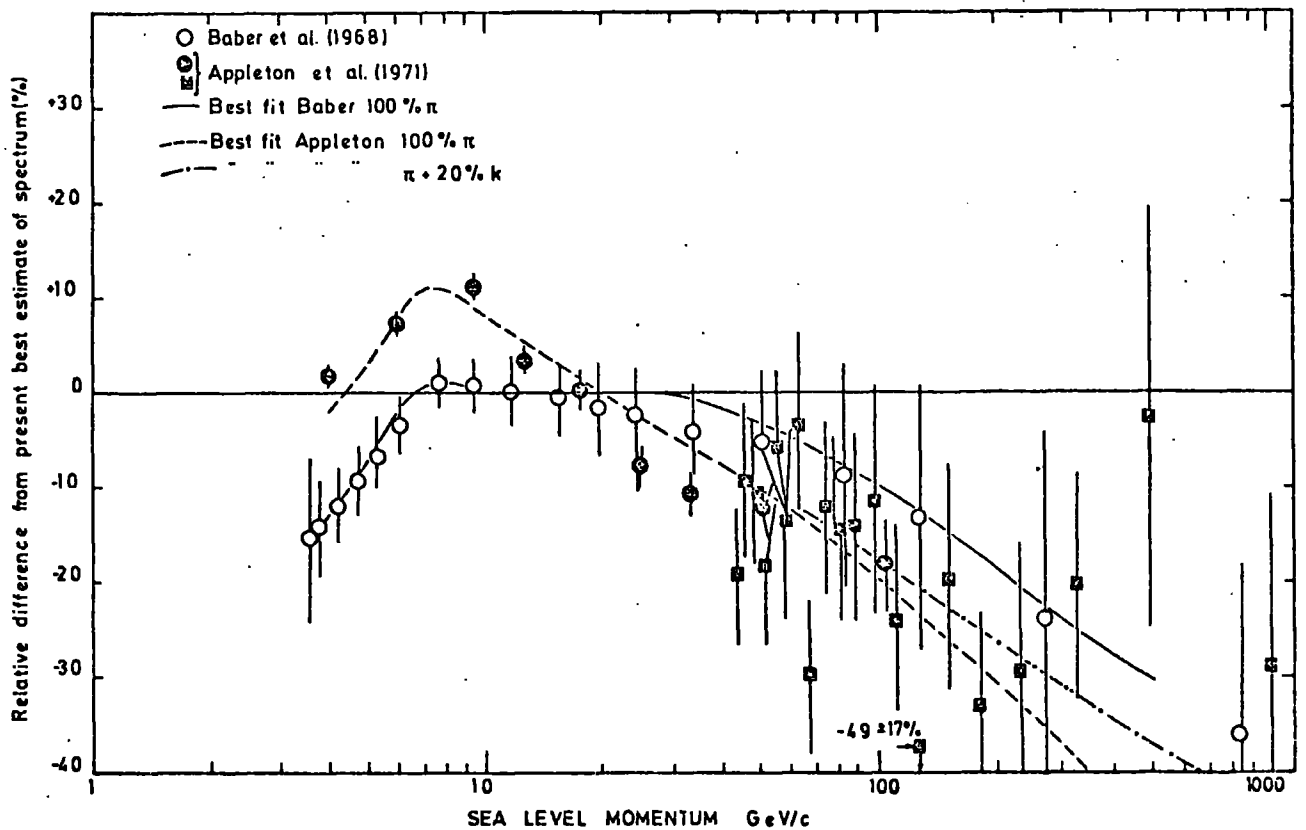


FIGURE 6.3(b) Comparison between the Nottingham Spectra and the Present Best Estimate.

results. As in the earlier Durham work, the spectra are obviously steeper, though in the Nottingham case this is even more pronounced, the best fit curve of the latest result being ~ 30 to 40% lower at ~ 500 GeV/c. A possible source of such a difference could be in the neglect of any momentum dependent effects contributing to event rejection in the analysis procedure. For example, as in the present analysis (chapter 3), the probability of the muon being accompanied by electrons from the iron block is strongly dependent upon momentum, and since the Nottingham spectrograph has only two flash-tube trays below the magnet, any such events producing extra tracks are very likely to have been rejected. Another possible momentum dependent effect is the probability of a muon being accompanied by an air shower which again would cause the event to be rejected. However in most other spectrograph measurements, including the present MARS one, such a momentum dependent effect has also been neglected, and consequently it is difficult to see how this will effect the relative difference between the two measurements of the muon spectrum, unless such an effect is a function of the spectrograph itself, i.e. dependent upon the size of the spectrograph and the details of its construction. If this is the case then it will be very difficult to compare the results of different spectrographs of vastly different sizes, to any degree of precision.

The general conclusion is that the Nottingham results seem to give a greatly steeper spectrum over the whole energy region, than the present results. It is interesting to note that Appleton et al. make the remark that their experimental points lie consistently above the best fit line (even with the inclusion of the other sources of muons), at the higher energies. This, they conclude, could be due to additional contributions from kaons or direct production, poor statistical accuracy, or inadequacies in the theoretical model expressing the muon production. However it is, to some extent, the same effect as in the present experimental data, and also could possibly be due to a flattening in the production spectrum of the muons' parents.

6.2.5 The Spectrum of the Kiel Group

As well as the absolute rate experiments performed by the workers at Kiel, the vertical muon momentum spectrum has also been measured, over a wide range of energies, in a series of experiments using three different spectrographs. The results from all three instruments, combined with their absolute intensity point at 1.11 GeV/c, have been collected together by Allkofer et al. (1971) to produce a best estimate of the spectrum from 0.2 GeV/c to 1000 GeV/c.

The experiments consisted of measurements with two air gap magnet spectrographs in the region 0.2 to 10 GeV/c and one solid iron magnetic spectrograph measuring momenta >10 GeV/c. The spectrum measured with the latter was absolute, whilst the former were not and were normalised to the absolute intensity point at 1.11 GeV/c. The results from these experiments, as presented by Allkofer et al. (1971) at the Hobart Cosmic Ray Conference, are shown in figure 6.4, along with other recent measurements to be described later. To produce their best fit spectrum the usual theoretical model, identical with that outlined in chapter 5, was used and a best fit value of γ of 2.63 and a K/π ratio of 0.0 was found. This is shown as the ACD (Allkofer, Carstensen, and Dau) spectrum in figure 6.4. Close examination of this spectrum over the entire energy region shows that it is a fairly good fit in the lower energy region (below that shown on figure 6.4), but begins to fail at the higher energies, presumably due to the constant γ being taken over such a wide momentum range. Further examination of the Kiel data shows that the results of their high energy experiment (10 to 1000 GeV/c; shown as crosses), and low energy experiments (open circles and triangles) are in disagreement in the region of 10 GeV/c. In fact the low energy data lies below the ACD spectrum in the region 2 to 10 GeV/c, and that at high energy lies above the ACD spectrum in the region 10 - 20 GeV/c, but becomes lower as the momentum increases. As a result of this discrepancy the high energy results are examined in more detail below.

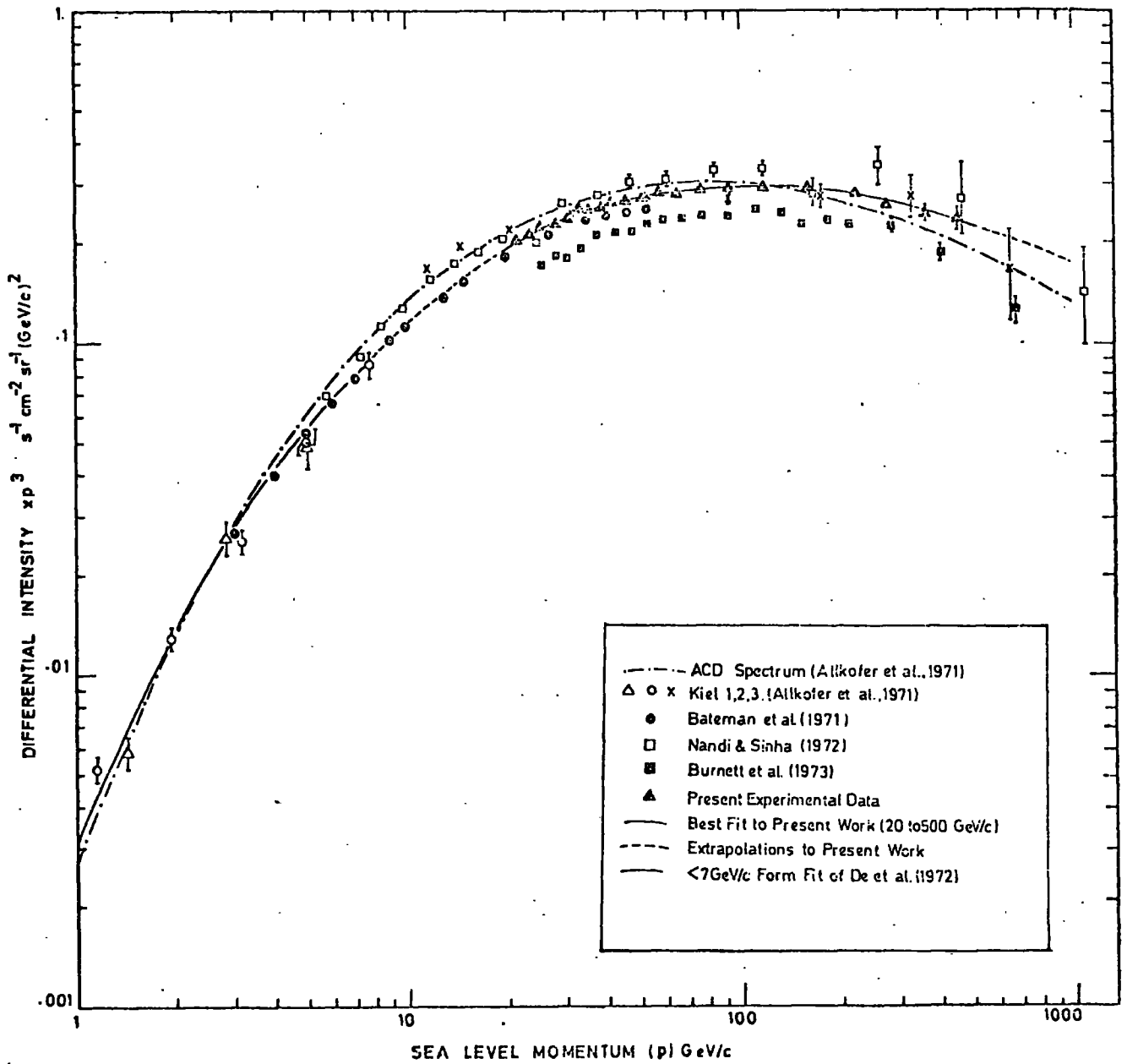


FIGURE 6.4 Recent Measurements of the Muon Spectrum.

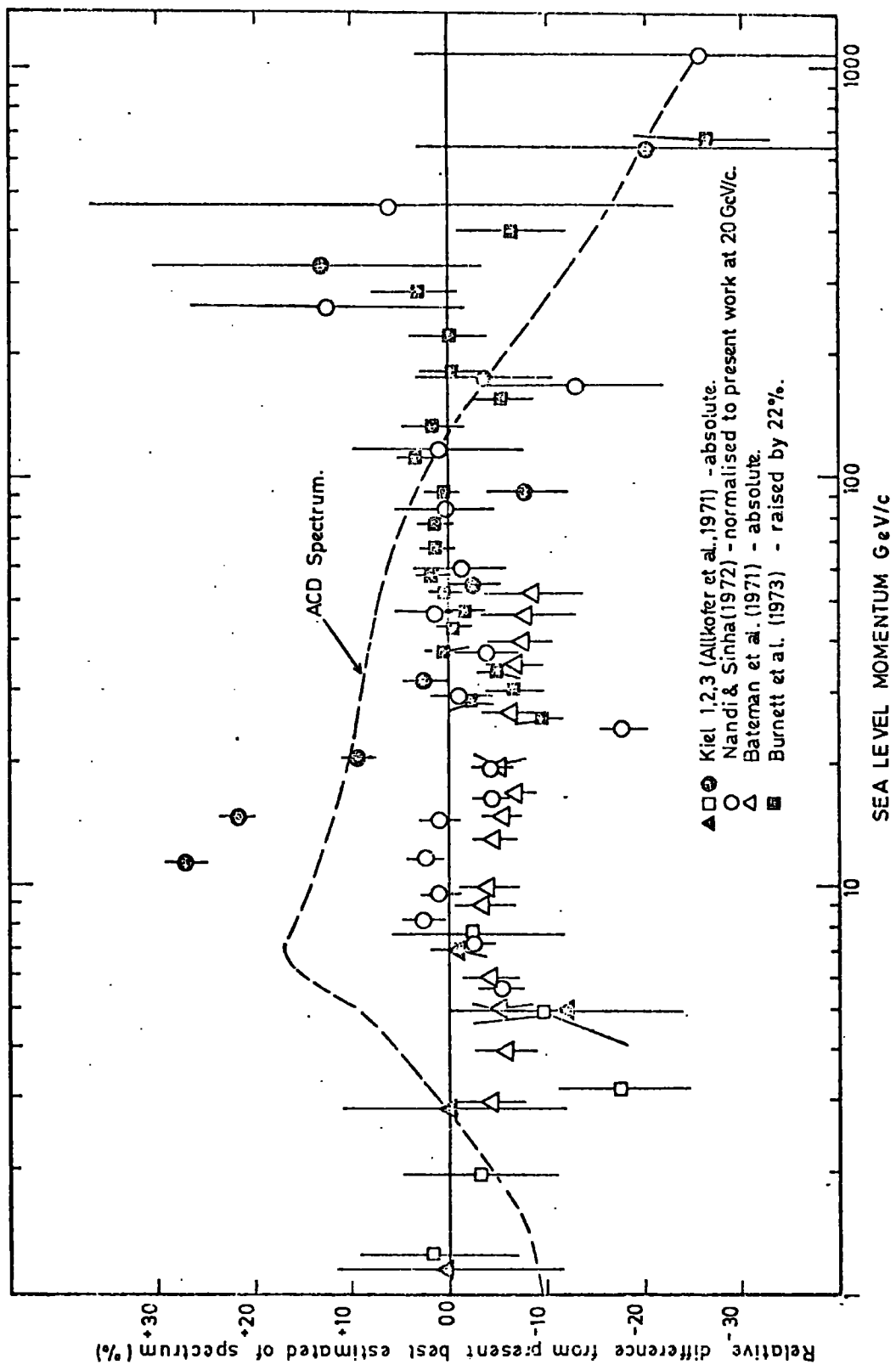


FIGURE 6.5 Comparison between Recent Measurements and the Present Best Estimate of the Muon Spectrum.

The HERMES spectrograph (as it is known) consists of a large solid iron magnet with particle detectors above and below. The whole instrument is located on a frame which can be rotated to investigate the spectrum at inclined angles. Triggering is by means of four scintillation counters, two above and two below the magnet. Six double gap optical spark chambers constitute the trajectory location elements, three being situated between each of the pairs of scintillation counters. The spectrograph is sited beneath a thick concrete roof ($\sim 800 \text{ gm cm}^{-2}$) of irregular but known shape. The procedure of the analysis was to fit straight line tracks to the sparks in the two sets of these spark chambers whenever possible, and calculate the muon's momentum from the amount of angular deflection. The position of emergence of the muon track from the iron block is then computed from a knowledge of the incident position, angle, and momentum, and compared with that observed. If there is agreement within three times the standard deviation expected from multiple scattering, then the event is accepted. The sea level momentum is then calculated by projecting back through the concrete roof.

No momentum dependent corrections have been included to allow for the electromagnetic interactions of the muon in the iron, or in the concrete roof, which would have caused a particle to be accompanied by burst electrons. This would be a difficult correction to make as such events are not automatically rejected, and was neglected by the workers on the grounds that such an effect would be expected to be small, and the statistical errors are so large that it is not justified. However there may be some effect causing a depression at the high energy end.

A more serious effect which may have some bearing on the 'highness' of the lower energy points may be caused by the criteria used to select events, i.e. comparing the point of emergence from the magnet with that expected. In the Diplomarbeit of Fänders (1971), who was responsible for the selection, the events are grouped according to the number of spark chambers, either above or below the magnet, which had sparks in them,

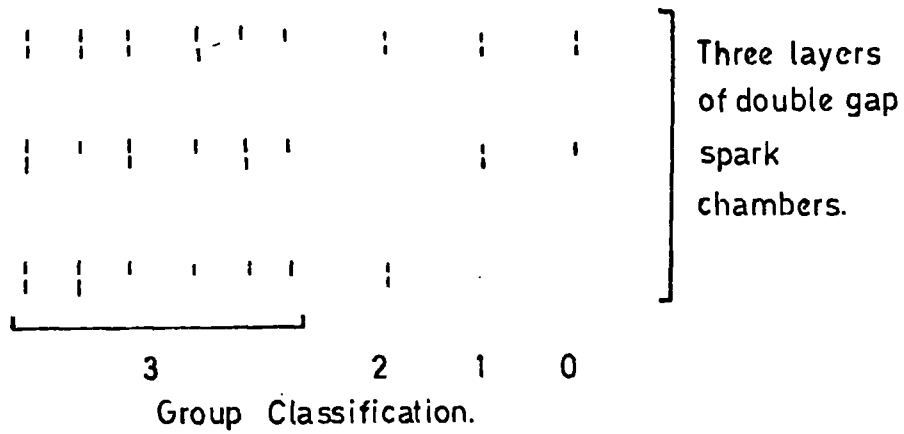


FIGURE 6.6(a) Classification of the Tracks observed with the Spark Chambers in the Kiel High Energy Spectrum Measurements.

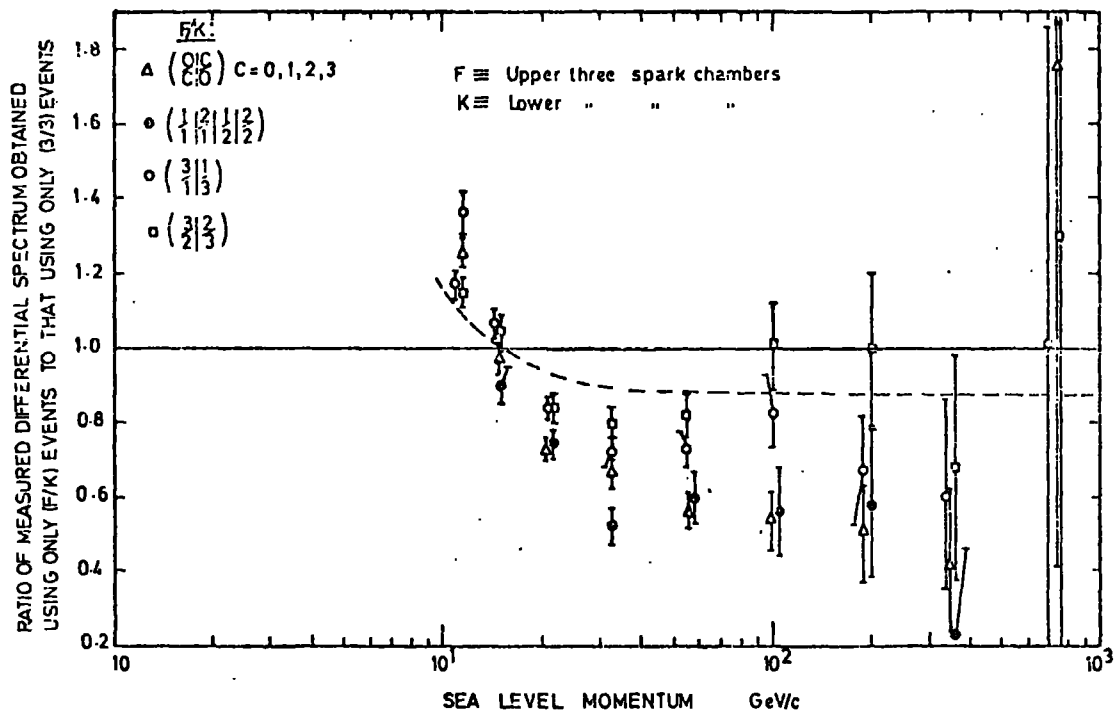


FIGURE 6.6(b) Comparison between the Spectra calculated using Different Combinations of the Tracks shown in Figure 6.6(a) above (after Fährders, 1971).

the groups being labelled 3 to 0 as shown in figure 6.6(a). If the fitting criteria were correct, and only muon tracks were being accepted then one would expect the same shape for the spectrum obtained by considering any of the groups of tracks. However, as shown in figure 6.6.(b), reproduced from the work of Fährnders, this is not the case. The differential spectra obtained from the different combinations of groups above and below the magnet are plotted relative to that obtained only considering group 3 events in both the upper and lower levels of spark chambers.

Figure 6.6(b) shows that whenever the track of the muon is not defined by all three spark chambers then a momentum dependent effect is introduced. A possible explanation for this is that when there are only two spark chambers operative in defining the muon's track, then there is a greater chance that any spurious sparks will lie within the scattering criteria at lower momenta, since the absolute size of the acceptable channels increase as the momentum decreases. Since there are approximately equal numbers of $\binom{3}{3}$ events and other events in the data making up the final spectrum, one might expect the total effect to be roughly as shown in the dashed line in figure 6.6.(b). It is interesting to note that such a rise is exactly what is observed in figures 6.4 and 6.5 which show the relative difference of recent results from the present best estimate of the spectrum, and in fact these lower momentum points (10 GeV/c to 20 GeV/c) may be ~20% too high.

Considering the overall picture of the spectrum from the Kiel group it appears that between 1 and 10 GeV/c the spectrum is more accurately given by the form fit of De et al., than the ACD spectrum, and above 10 GeV/c, remembering that there may be a momentum bias, there is fairly good agreement, within the experimental errors, with the present results. The ACD spectrum is 10% too high in the region ~20 GeV/c and, being steeper than the present spectrum, falls to ~20% below the present work at 500 GeV/c.

6.2.6 The Dagapur Spectrum

Nandi and Sinha (1972) have reported a measurement of the vertical muon

spectrum in the range 5 to 1200 GeV/c, made using a solid iron magnet spectrograph incorporating geiger and flash-tube detectors, having an m.d.m. of 985 GeV/c. A best fit γ of 2.61 was found for an all pion production spectrum with 32% significance. The results are shown in figures 6.4 and 6.5, where it is seen that there is fairly good agreement with the present results with regard to the shape although the results of Nandi and Sinha are $\sim 10\%$ higher in figure 6.7 where they have been normalised to the Allkofer et al. (1970) intensity at 1 GeV/c, the normalisation being made by extrapolating the best fit curve from 5 GeV/c down to 1 GeV/c. This indicates that either the extrapolation is not valid, or that there exists a difference in shape between the two spectra in the region < 5 GeV/c. Figure 6.5 shows the comparison when normalisation is made to the present results at 20 GeV/c, and as noted there is good agreement up to ~ 1000 GeV/c, within the errors, which at this momentum become very large.

6.2.7 Spectrum Measurements Presented at the Denver Conference.

Apart from the preliminary results of the work constituting the main bulk of this thesis, two other direct measurements of the vertical sea level spectrum were reported; from the AMH spectrograph at College Station, Texas, and the UCSD spectrograph at San Diego, California.

(a) The AMH Results.

Results up to ~ 50 GeV/c had been previously reported from this group by Bateman et al. (1971) who measured the absolute spectrum in the region 3 to 53 GeV/c. Again the spectrograph is a solid iron magnet type, with scintillation counter, and optical spark chamber particle detectors. The results are shown in figures 6.4 and 6.5 where they are seen to agree very well in shape with the present best estimate of the spectrum; this is as expected below 7 GeV/c, since the form fit of De et al., which is taken as the best estimate below this momentum, was based partly upon these results. The absolute height is seen to be $\sim 5\%$ below that estimated in the present work.

Extended measurements have been presented by the same group (Abdel-Monem et al., 1973) at the Denver Conference, and on fitting a standard theoretical

model to the data assuming an all pion source, the group find a best fit γ of 2.67. Closer examination of the data presented, in figure 6.7, reveals that the measured points are much lower in intensity above 20 GeV/c, than their best fit, which presumably is weighted by the small errors on the low momentum points. Because of this apparent inconsistency, and the lack of agreement with the other results, this data will not be considered any further.

(b) The UCSD Spectrograph.

Burnett et al. (1973) have reported recent results from the spectrograph at San Diego. The instrument is a large solid iron magnet spectrograph capable of being rotated to different zenith angles. The m.d.m. is quoted as 2500 GeV/c and the overall acceptance as $1550 \text{ cm}^2 \text{ sr}$, consequently it is one of the largest so far operational and compares in size with MARS. The particle detection elements are scintillation counters and spark chambers with digitised magnetostrictive read-outs, resulting in the ability to analyse a large amount of data ($\sim 2 \times 10^6$ events in the above publication). Measurements were made at various zenith angles, and a method presented enabling the data from the different angles to be combined together to give an estimate of the vertical spectrum. The method is based upon a theoretical model of muon production and propagation similar to that given in chapter 5, and assumes a constant value of γ , and an all pion source. Using their method, Burnett et al. deduce that the best fit γ is 2.715 ± 0.015 , and present a spectrum in terms of the parameter $k (= 1/E)$. Since the publication at the Denver Conference the results have been raised by 15%, and are shown converted to a differential momentum spectrum in figures 6.4 and 6.5. (in the former they have the same normalisation as given by the authors, raised by 15%, whilst in the latter they have been raised by a further 22% to bring them closer to the present results). It can be seen that they represent, apart from the present MARS results, the most statistically accurate data in the region above 100 GeV/c, so far reported, and indeed are very compatible in shape with the present results, the absolute normalisation however, even

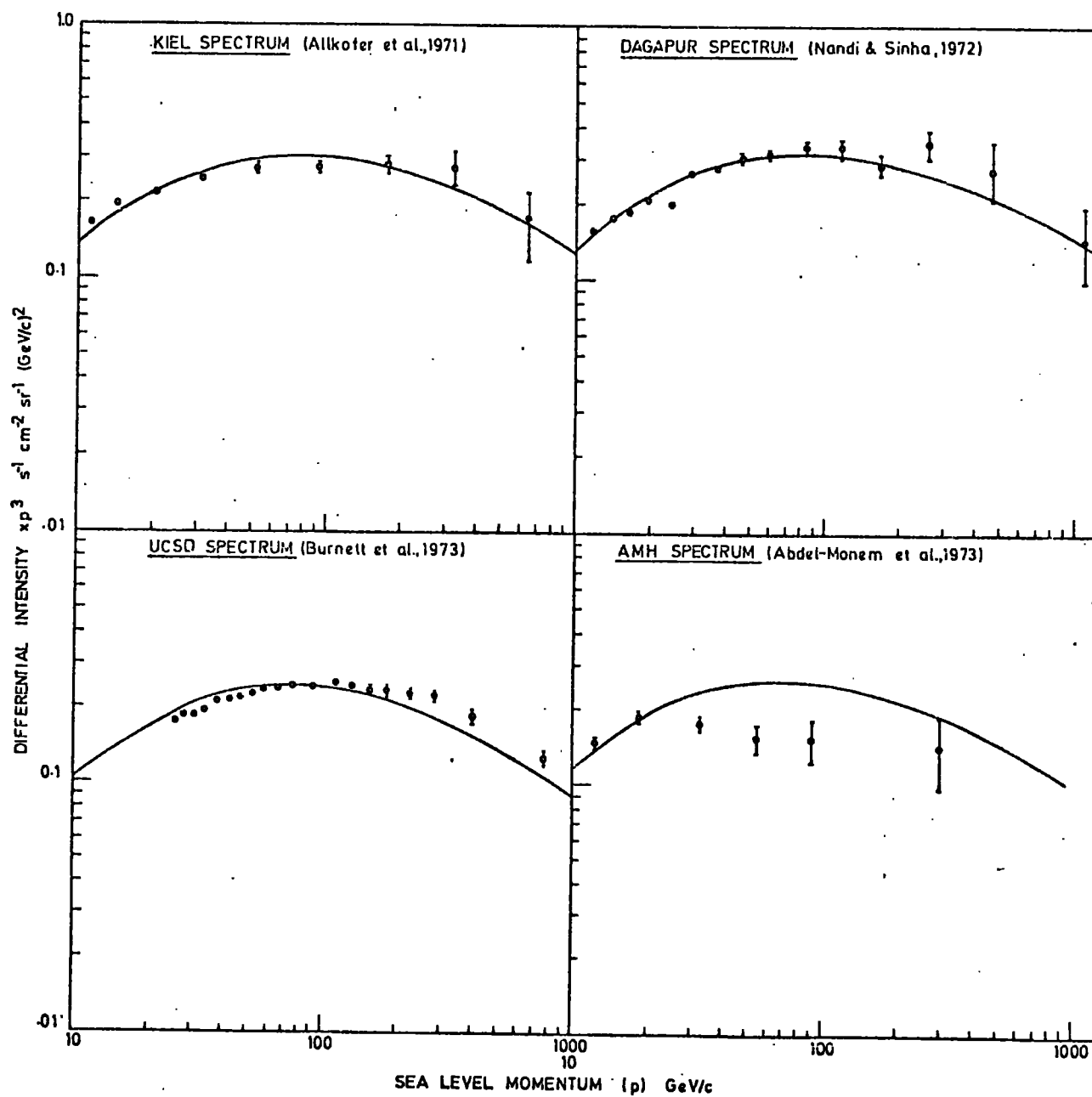


FIGURE 6.7 Comparisons of the Experimental Data Points and the Best Fit Curves obtained in the Four Most Recent Spectrum Measurements.

with the increase of 15% being 22% lower. It is not clear at the present time what are the full implications of the procedure of combining together the data from different zenith angles in the way the authors describe; a point which is further emphasized by the fact that the spectrum of actual combined experimental data points appears much flatter, particularly at the higher momenta, than the best fit with $\gamma = 2.715$ (see figure 6.7). It is encouraging however that the shape deduced agrees so well with that of the present experiment.

6.2.8 Conclusion from the Direct Measurements

Examination of figures 6.4 and 6.5 shows that in the recent measurements made of the muon spectrum up to 1000 GeV/c there is no evidence to suggest that the results found in the present experiment are incorrect to any large degree, though in the majority of cases the experimental errors are so large as to prohibit any firm conclusions. The reasons for discrepancies with the earlier measurements (e.g. Durham and Nottingham), which generally give steeper spectra at higher energies, may be put down to poor statistical accuracy, and possibly instrumental biases in these experiments.

The ACD spectrum of Allkofer et al. seems to be in error by $\sim 10\%$ in the region 10 to 100 GeV/c, (the peaking at 7 GeV/c is artificially caused by the discontinuity in the comparison spectrum). The sudden downward 'kink' in the comparison with the ACD spectrum in figure 6.5 is a reflection of the fact that at around this energy the comparison spectrum changes slope dramatically, and further emphasises the conclusions reached at the end of chapter 5.

As an argument against the constant γ pion spectrum fitted by most workers to their data, figure 6.7 shows the results of the four most recent experiments, indicating both the experimental points and the best fit spectra quoted by the authors, (that of the AMH spectrograph is shown for completeness). In each case there is evidence, though not conclusive, that towards the high energy end, the spectrum is becoming flatter than that corresponding to a constant value of γ .

6.3 Indirect Determinations of the Muon Spectrum.

As indicated at the beginning of this chapter, apart from the direct measurements of the sea level muon spectrum, there are three main methods for its deduction indirectly. The last of these methods, based upon measurements of the γ -ray flux in the atmosphere, has been used by Osborne et al. (1964) to produce the OPW spectrum, (from the measurements of Duthie et al. 1962), and will not be discussed any further. The other methods involve the observation of either the muon intensities underground or underwater, or the examination of electromagnetic bursts produced by muons in absorbing materials. Initially the basis of these methods will be outlined, and then the results from two recent surveys will be compared with the present results.

Underground measurements of muon intensities are converted to sea level spectra by the use of range-energy relations, calculated from the theories of electromagnetic interactions, (ionization, bremsstrahlung, and pair production), and nuclear interactions of the muon in the particular material traversed by the muon from sea level to the detector. Two problems arise in the interpretation of such results, in the calculation of the equivalent sea level energy, and in the determination of the intensity. Since the energy deduced at sea level is dependent upon the amount of energy lost in the muons travel, the accuracy of the energy determination is governed by the accuracy to which the energy loss processes can be formulated mathematically, and by the accuracy of the knowledge of the amount and type of material traversed, and to this latter end extensive geological surveys are necessary. The main source of error in the energy loss theory is in the nuclear interactions which become important at high energy. The situation is further complicated by the fact that the energy losses due to bremsstrahlung (radiation loss) are not continuous, and the muon has the infrequent probability of losing a large part of its energy in a single collision, resulting in the range of the muon fluctuating. This becomes important at high energies (large depths) where the spectrum is very steep, and causes an effective increase in the intensity. Therefore a correction

has to be made to the intensity to allow for these fluctuations, which is generally calculated using Monte Carlo techniques (e.g. Hayman et al., 1963; Menon and Ramana Murthy, 1967), and which, together with the range-energy relation, plays an important part in the interpretation of the results.

With regard to the burst experiments the situation is somewhat similar in that the reliability of the electromagnetic theory, particularly that of bremsstrahlung, is directly related to the accuracy of energy measurements. Also of importance is the sensitivity of the detectors from which the burst size has to be determined, and obviously a wrong estimate of any of these effects could lead to a wrong energy determination. In the main, three types of detector have been used : plastic scintillation counters, ionization chambers, and X-ray emulsions, the latter two mainly being exploited by workers in the U.S.S.R.. They are generally built into 'sandwich' like constructions, the detectors being interleaved with absorbing material (usually lead) and the development of the cascade of electrons, produced by the muons, studied. The energy of the muon is deduced from the size of the shower. Recently there has been controversy about the differences in the results from the ionization chamber experiments and those using X-ray emulsions. Experiments with the former (e.g. Erlykin et al., 1971) give a much flatter spectrum above a few hundred GeV than that expected theoretically, and which had been observed with the X-ray emulsion technique. Recently Erlykin et al. (1973) have suggested a solution in the possible existence of an anomalous interaction which produces electron-photon cascades having a wider angular distribution than predicted by conventional theory, and which are detected by the ionization calorimeters but not by the X-ray emulsion techniques.

Figure 6.8 shows the results given in two recent surveys of indirect measurements. The experimental points above 1000 GeV/c are the data given by Ng et al. (1973(a) and 1973(b), internal communication), who used the most recent data, combined with a recalculation of the range-energy relation and fluctuation problem, to produce a best fit line, using the standard

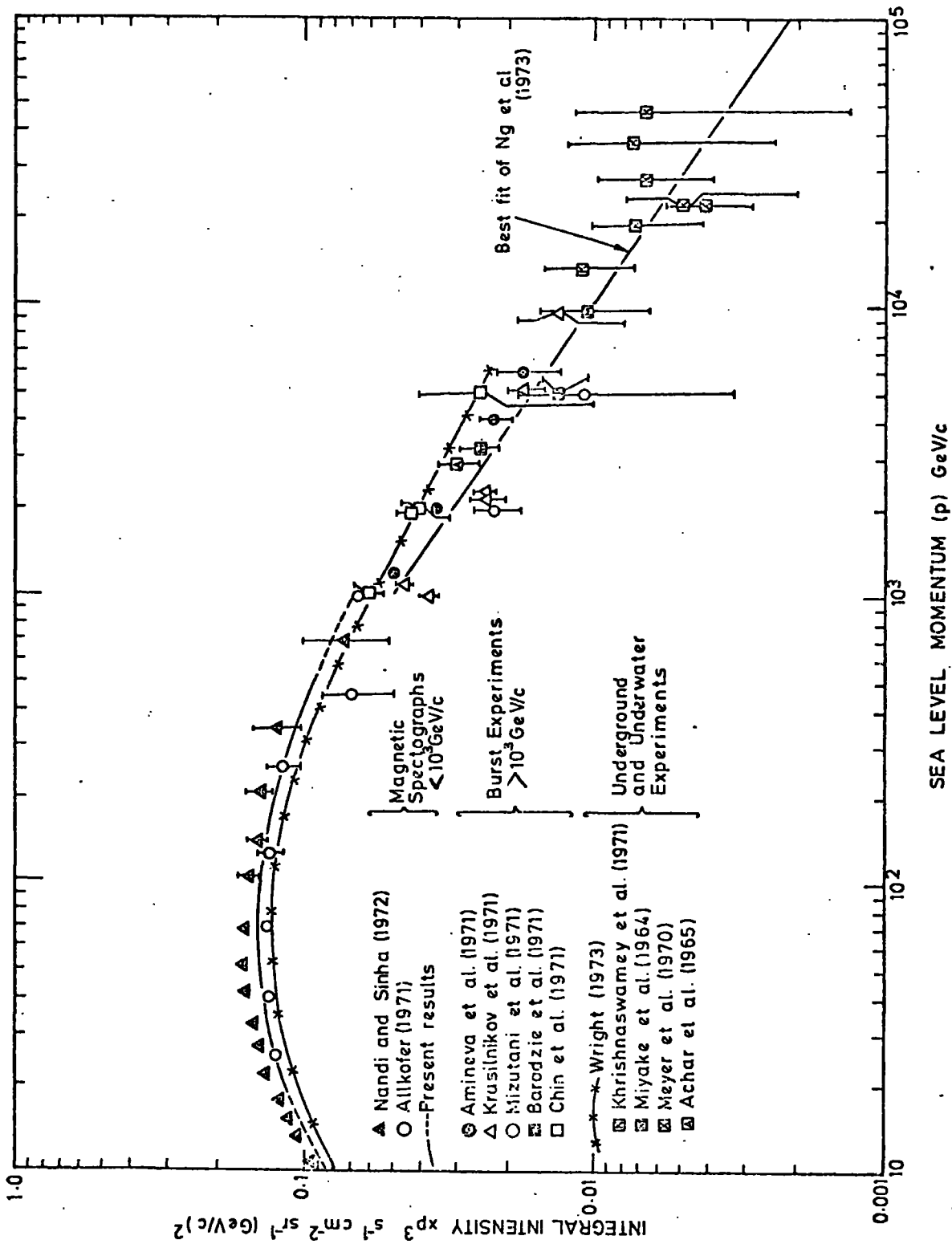


FIGURE 6.8 High Energy Indirect Measurements of the Muon Spectrum (also shown for Comparison are the Present Work and that of Other Direct Measurements).

model with all pion production, having $\gamma = 2.70 \pm 0.03$ from 10^3 GeV to 10^5 GeV. Also shown is a survey by Wright (1973 (a) private communication) based on underground and underwater data, and a reassessment of the range-energy relation for different types of material (Wright, 1973(b)). Shown for comparison in figure 6.8 are the results of the present experiment, those of Allkofer et al. (1971), and those of Nandi and Sinha (1972), all normalised as in the original publications.

As can be seen there is agreement in shape between the present results and those of Wright over the energy range of the present experiment. Above 500 GeV both an extrapolation of present results and the data of Wright seems to be giving too high intensities compared with the experimental points at these energies. Examination of the available data above 1000 GeV shows that it is possible that the present results (< 500 GeV) could be correct, and would imply that the muon spectrum, and hence the pion spectrum would have to decrease in slope again somewhere in the region 1000 to 10000 GeV.

6.4 Summary

Comparison with other direct measurements shows that there is no evidence to suggest that the present results, and their interpretation in terms of a decrease in the value of γ of the parent production spectra, are incorrect. This seems to be further supported by the fact that many other experiments seem also to show the same tendency of an increase in muon intensity at high energies above that expected on a constant model although the implications have not been pursued. When one considers also the indirect measurements it is clear that if they are correct, then the spectrum cannot continue with this lower value of γ , and a rise in its value, and hence a relative decrease in the muon intensity above ~ 1000 GeV would be implied.

It is interesting to note that in a recent paper by Wdowczyk and Wolfendale (1973) a decrease in the slope of the primary spectrum above ~ 1000 GeV (to an integral slope of 1.44) was proposed to accommodate the recent direct

measurements on the primary spectrum of Ryan et al. (1971) which if extrapolated to the energies of air shower measurements would result in too low an intensity. If one assumes the theory of scaling to be true, then the slope of the pion spectrum would reflect the slope of the primary spectrum and taking an approximate figure of 10:1 for the ratio between the primaries and the eventual resultant muons (a ratio suggested by the fact that the mean value of the energy of the pions, which are important in cosmic ray studies, from the I.S.R. data is 0.16 of the energy of the primaries), then the theory of the above authors would predict an increase in the muon intensity at ~ 100 GeV similar to that which has been observed in the present work. Whilst at the present time there is no conclusive evidence in favour of a flattening of the primary spectrum, the present results suggest that the possibility of the spectrum becoming less steep in the region of 1000 GeV cannot be ruled out.

As regards the absolute normalisation of the muon spectrum it is seen that there is still some disagreement, presumably reflecting the difficulty of its measurement, and recent results are seen to vary considerably. However the present result is satisfactorily consistent with the mean of the recent observations, and the agreement in intensity between the present work and the spectrum of De et al. supports the view of the present work that it is accurate to within a few percent. In the next chapter an experiment is described to measure the integral absolute rate above the cut-off momentum imposed by the iron in the spectrograph (~ 7 GeV/c) which as will be seen lends support to the correctness of the present estimate of the height of the spectrum.

THE ABSOLUTE RATE EXPERIMENT

7.1 Introduction

The MARS spectrograph, as well as being operated as a magnet spectrograph, can also be used as a range spectrograph to measure the integral muon intensity above the effective cut-off momentum defined by the quantity of absorbing material in the muon beam. The results of such an experiment were reported at the Hobart Cosmic Ray Conference (Ayre et al., 1971(b)), and were found to be in disagreement with several other results, notably those of Allkofer et al. (1971). The MARS intensities were found to be 11.5% and 10.9% lower than those predicted by the ACD spectrum at momenta of 3.48 and 7.12 GeV/c respectively, and in view of the grossness of these discrepancies it was decided to repeat the experiment at the high momentum value. The results of this 'repeat' experiment are given in this chapter, and they have also been presented at the Denver Conference (Ayre et al., 1973).

For the purpose of this experiment MARS essentially consists of four large solid iron blocks, and three scintillation counters, (as shown in figure 2.1). The experimental procedure is to reduce the magnetic field in the blocks to zero, and count the rate of 3-fold coincidences between the scintillation counters. From this information, after applying several corrections to be described in the following sections, the rate above the effective cut-off momentum (~ 7 GeV/c) of the whole instrument can be calculated. (The lower momentum value (3.48 GeV/c) in the previous experiment came from considering only particles penetrating the top two iron blocks. Since there were similar discrepancies between the initial MARS measurements and the measurements of other workers at both momenta it was only felt necessary to repeat the experiment at one value of momentum, the higher being the easier as this did not involve moving the scintillation counters from the position they occupied during the spectrum measurements.)

7.2 Reduction of the Magnetic Field to Zero

The reduction of the magnetic field to zero involved the standard method of successively reversing the field whilst gradually reducing the energising current to zero. The procedure of reversing the field was to switch the current off, wait ~ 30 seconds, and then switch the current on again in the opposite direction with a slightly reduced value, (the 30 seconds delay was necessary to allow the large inductive effects of the magnet coils to die away before attempting to reverse the field which otherwise could result in damage to the instrument, and possibly to the operator). Table 7.1 shows the current steps used in this reduction method together with the values of the field at the end of the first four current ranges, which have been calculated from measurements of $\int V dt$, made using a large loop of wire around one arm of a magnet block.

Current Reduction Range (amps)	Approximate Reduction Step Length (amps)	Magnetic Field at end of Reduction Range (kG)	3-fold Coincidence rate (min^{-1})
50	\sim	16.3	17.68 ± 0.28
50-9.95	0.5	11.5	21.25 ± 0.17
9.95-6.05	0.5	8.5	23.53 ± 0.27
6.05-4.10	0.2	5.7	25.49 ± 0.15
4.10-2.00	0.1	2.3	28.11 ± 0.18
2.00-1.00	0.1	—	—
1.00-0.30	0.05	—	—
0.30-0.20	0.02	—	—
0.20-0.10	0.01	—	—
0.10-0.05	0.005	—	—
0.05-0.02	0.002	—	—
0.02-0.00	0.001	0.	28.34 ± 0.17

Table 7.1

Summary of the Procedure of Reducing the Field to Zero

The small current reduction steps used, particularly at low currents, are important since, in order to reach a zero-field condition, the field must actually be reversed in each cycle, and if at any stage there is not complete reversal then there will be a remnant field. Also given in table 7.1 are

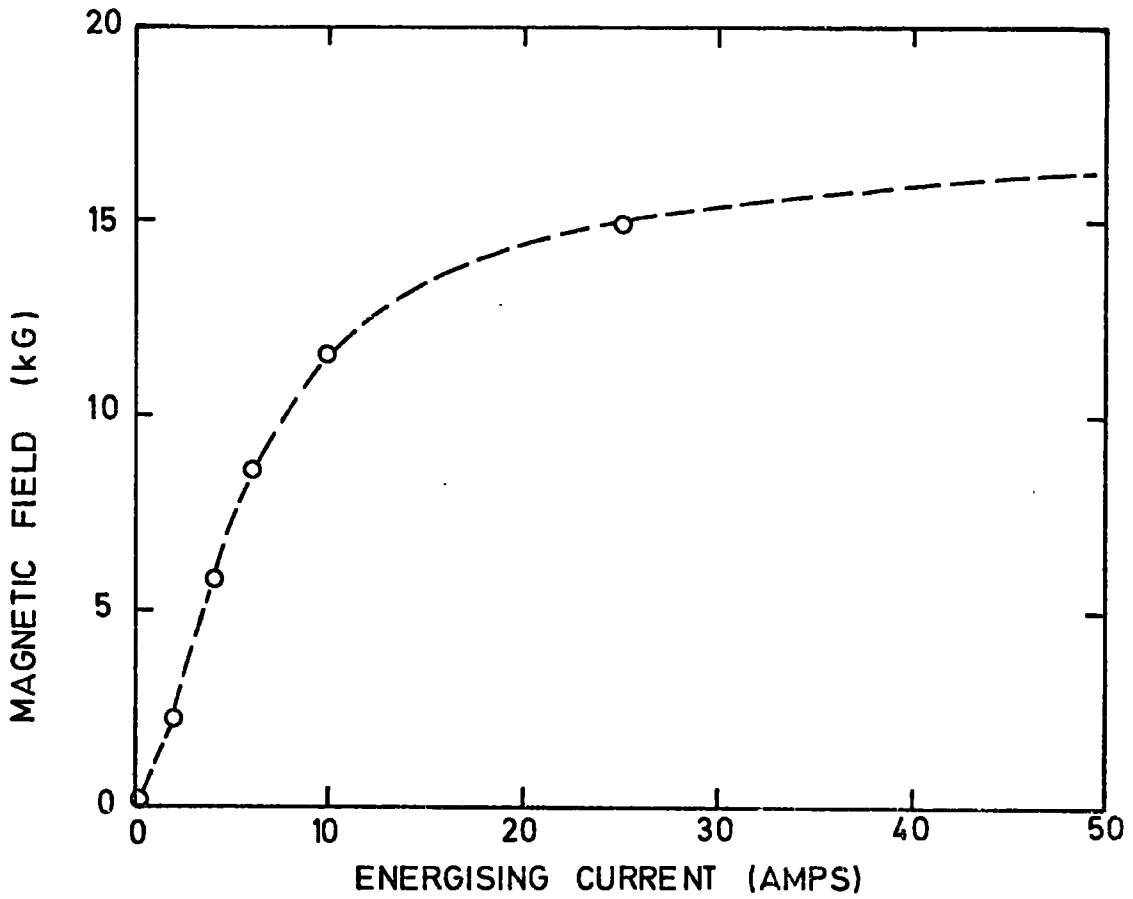


FIGURE 7.1 The Measured Field as a Function of Energising Current

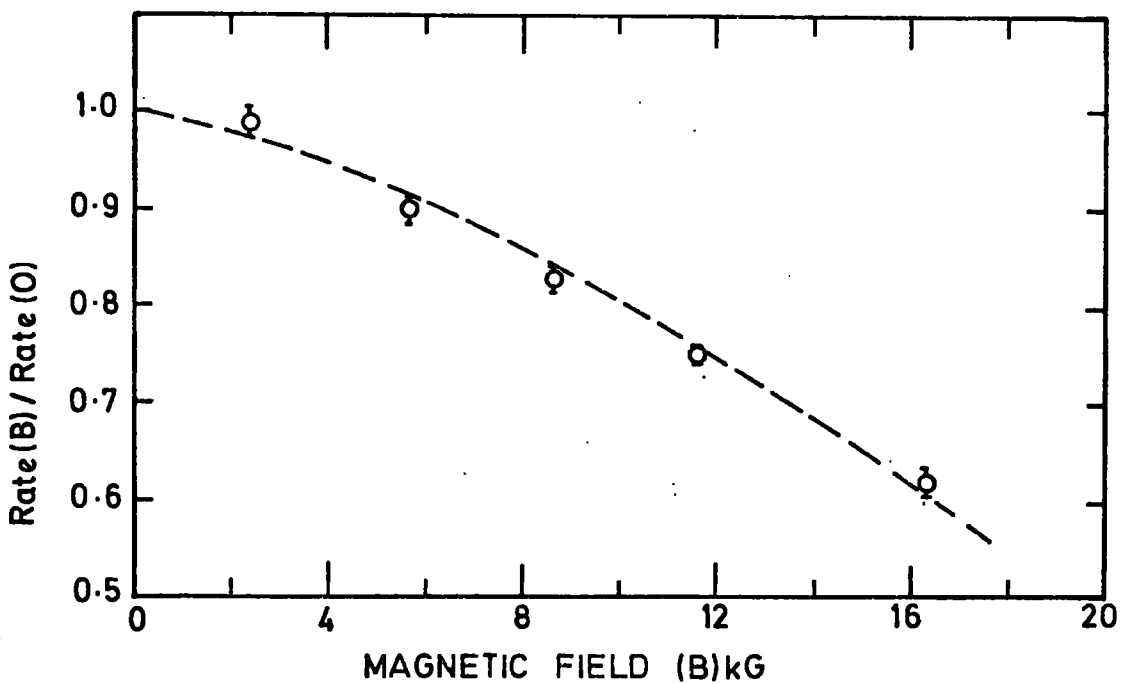


FIGURE 7.2 The Observed 3-Fold Rates as a Function of Magnetic Field

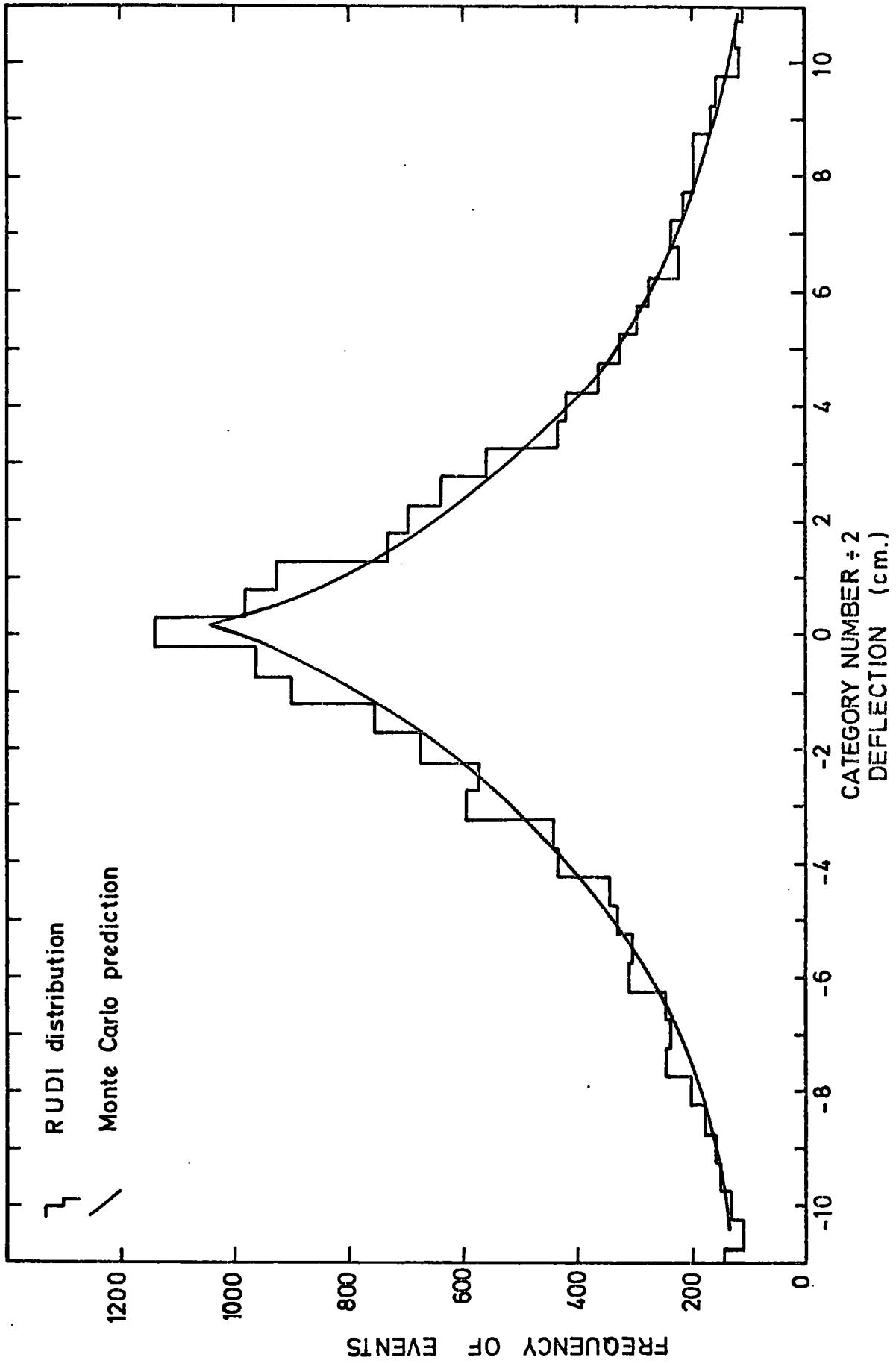


FIGURE 7.3 The RUDI Distributions from the first Two Runs after the Field has been reduced to "Zero"

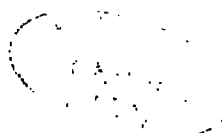
the 3-fold coincidence rates between the three scintillation counters which, as expected, are seen to rise as the field decreases due to the reducing loss of low momentum particles which are normally bent out of the acceptance volume of the instrument. Figure 7.1 shows the measured field as a function of energising current, the point at 25 amps being obtained simply by reducing the current in one cycle from 50 to 25 amps, in a separate measurement. The dashed line is a fit by eye to the measured points. Figure 7.2 shows the measured 3-fold rates, plotted relative to the zero-field rate, as a function of magnetic field. The dashed line in this case is a theoretical estimate based on calculations of the acceptance of the three scintillation counters at reduced values of the field using the methods given in Appendix B, and integrating over the incident momentum spectrum. It can be seen that there is good agreement with expectation, which lends support both to the method of calculating the acceptances, and to the measurements of the magnetic fields. Examination of figure 7.2 shows that even with a field of $\sim 2\text{kG}$ the rate is only $\sim 2\%$ below that of the zero-field rate. It is considered that the final field is much less than 2 kG and very close to true zero, consequently the true zero-field rate will be measured to within a fraction of a percent. Support for the field being zero is obtained from the RUDI distributions of the data from the momentum selector trays. The sum of the first two of these distributions, after the field had been completely reduced, is shown in figure 7.3, which also shows a theoretical estimation based upon a Monte Carlo simulation of particles through the spectrograph with their correct input momentum spectrum, and including the effects of multiple scattering. Clearly there is good agreement, and the fact that there is no apparent division into positive and negative charges, which would manifest itself as splitting of the peak of the distribution, leads to the conclusion that the field is very small, and hence the observed rates are the true zero-field rates.

7.3 Measurement of the Efficiency of the Scintillation Counters

One of the key parameters in the measurement of an absolute value of

the intensity is the exact efficiency of detection of events, in this case a knowledge of the scintillation counter efficiencies. In the previous experiment these efficiencies were calculated by examining the pulse height distributions from the counters, and estimating how many real events were being rejected by the discriminators, through which the pulses from the counters were passed before being put into coincidence. In the present experiment a more direct method has been adopted namely using an extra small scintillation counter in such a position that the particles passing through the small counter and the other two main counters would also pass through the counter under test. The dimensions of the small scintillation counter were 55 x 68 cm. compared with 176 x 75 cm. for the main counters, and consequently it was possible to study three regions along the length of each counter, known as the north, centre, and south regions. The positions used for the small scintillation counter were directly below the upper and middle counters for measurements on the upper and middle levels respectively, and above the lowest counter for measurements at this level, the reason for this latter being that there is no space below the lowest counter, and care was taken to arrange the position of the small counter such that particles could not pass through the small counter and the other two counters, and miss the lowest one.

The experimental arrangement is shown in figure 7.4, in this case for the examination of the centre region of the middle scintillation counter. As can be seen, the 3-fold coincidence rate between the other two counters (the upper and lower) and the small counter, together with the total 4-fold coincidence rate is measured. The inefficiency of the region under test is then given by the difference in these coincidence rates, since each particle producing a 3-fold coincidence must also have passed through the fourth counter. The discriminator settings used in this part of the experiment were the same as those used in the actual final measurement of the main 3-fold rate. Table 7.2 shows the results of this procedure for all three regions of each scintillation counter.



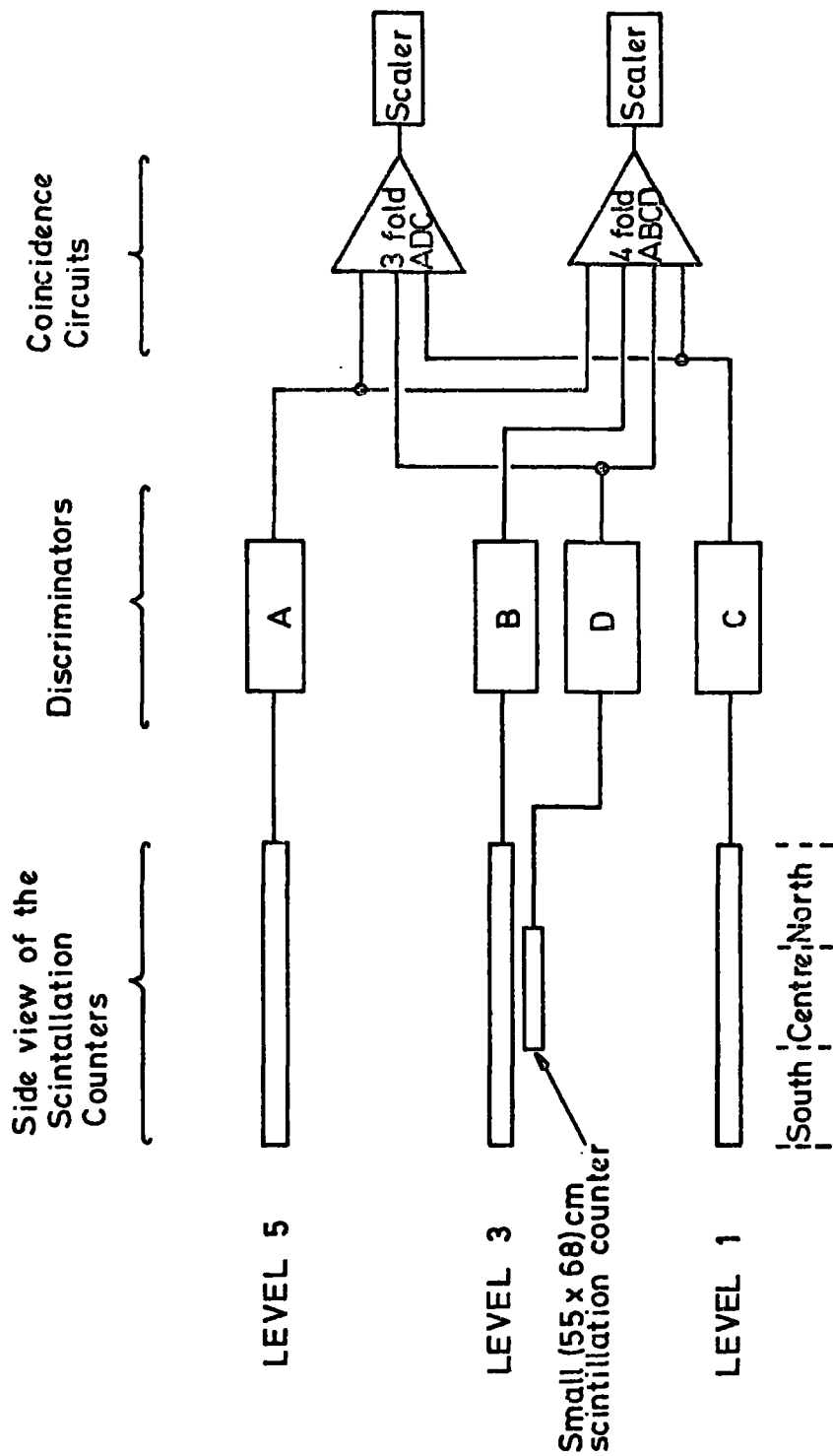


FIGURE 7.4 The Experimental Arrangement for Measuring the Scintillation Counter Efficiencies

S.C. Region and Level	Running Time (min)	No. of 3-fold coincidences	No. of 4-fold coincidences	3-fold Rate (min^{-1})	4-fold Rate (min^{-1})	Efficiency (%)	Average Efficiency (%) per Level
Top South	1100	10476	9713	9.52±0.09	8.83±0.09	92.72±0.15	
Top Centre	2566	24436	21631	9.52±0.06	8.43±0.06	88.52±0.20	91.90±0.14
Top North	923	8680	8199	9.40±0.10	8.88±0.10	94.47±0.25	
Mid South	1347	8416	8339	6.25±0.07	6.19±0.07	99.09±0.10	
Mid Centre	3137	39003	38717	12.43±0.06	12.34±0.06	99.27±0.04	99.22±0.05
Mid North	935	5857	5811	6.26±0.08	6.21±0.08	99.21±0.12	
Lower South	1330	11364	11160	8.54±0.08	8.39±0.08	98.20±0.12	
Lower Centre	1792	15751	15405	8.79±0.07	8.60±0.07	97.77±0.14	98.02±0.08
Lower North	954	8425	8263	8.83±0.10	8.66±0.10	98.08±0.15	

Table 7.2

Summarising the Calculation of the Scintillation Counter Efficiencies

Combining the three average efficiencies at each level one finds that the overall efficiency of the scintillation counter system is (0.894 ± 0.002) , most of the inefficiency arising from the top counter.

7.4 Measurement of the 3-fold Coincidence Rate

Measurement of the 3-fold rate between the three main spectrograph scintillation counters was made using the spectrograph coincidence unit (as described by Ayre, 1971) and a scaler capable of counting rates far in excess of those observed in the present experiment ($\sim 2 \text{ s}^{-1}$). In short, pulses from the photomultipliers attached to the scintillators (shown schematically in figure 2.4) are amplified and passed through discriminators, the outputs of which are fed into a three-fold coincidence gate.

Data was collected during the months of January and February 1973, and together with the 3-fold coincidence rates, the atmospheric pressure, recorded on a barograph, was measured. For the timing of the runs a mains regulated digital clock was used, which is very accurate over the periods used in the experiment. Table 7.3 summarises the data collected. Figure 7.5 shows the observed 3-fold coincidence rates as a function of pressure, and also the results of combining the points in pressure ranges of 5 mm Hg. In the paper presented at the Denver Conference (Ayre et al., 1973) the rate was quoted as $28.35 \pm 0.20 \text{ min}^{-1}$ at 760 mm Hg, and was estimated from the raw experimental data, the error being a conservative estimate considering the size of the errors and the spread of the data. In the present work the mean value of the rate, at the mean pressure is taken, being $23.57 \pm 0.04 \text{ min}^{-1}$ at 754 mm Hg. Examination of figure 7.5 also shows that there is a strong dependence of the rate upon pressure, and assuming a linear relationship between the two, the pressure coefficient is seen to be $\sim -0.1\%$ per mm Hg.

7.5 Absorbing Material in the Muon Beam

The greatest proportion of the absorbing material ($\sim 99\%$) is the iron

Date of Run	Running Time (min)	No. of 3-fold Coincidence	Mean Pressure (mm Hg)	3-fold Coincidence Rate (min ⁻¹)
Jan. 15	1080	31265	742	28.95±0.16
16	301	8769	747	29.13±0.31
16/17	843	24475	751	29.03±0.19
17/18	828	23570	759	28.47±0.19
18	495	14061	760	28.41±0.24
18/19	860	24574	758	28.57±0.18
19/20	1043	30043	748	28.80±0.17
20/22	2750	79419	745	28.88±0.10
22	423	12056	760	28.50±0.26
22/23	935	26307	761	28.14±0.17
23/24	1330	37659	764	28.32±0.15
28/29	1246	35382	757	28.40±0.15
29/30	923	26168	754	28.35±0.18
Feb. 3/5	2520	71137	764	28.23±0.11
5/6	941	26773	760	28.45±0.17
6/7	956	27225	754	28.48±0.17
7/8	973	27679	748	28.45±0.17
9/12	3881	111255	750	28.67±0.09

Table 7.3

Summary of the 3-fold Coincidence Rate Data Collected

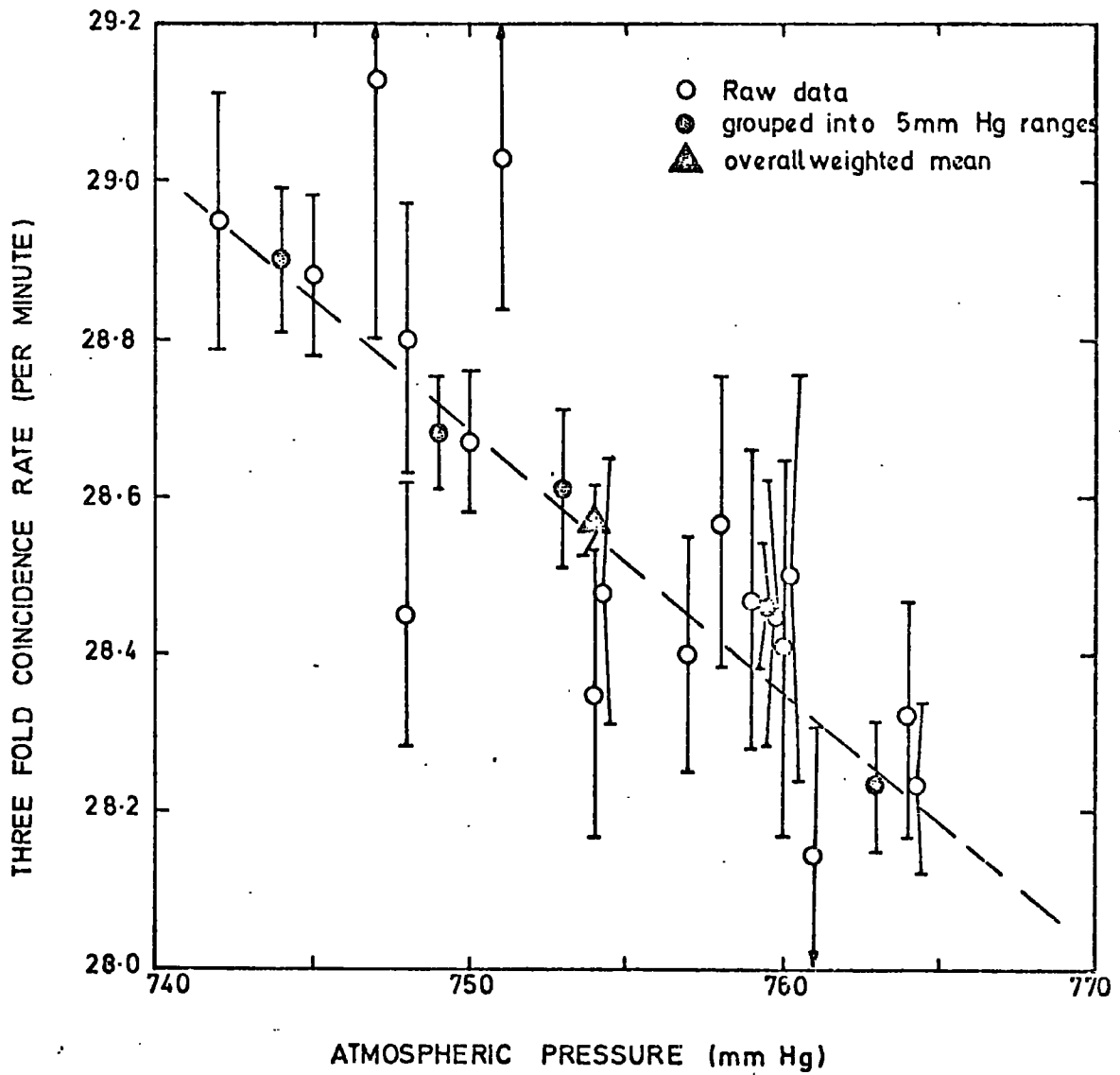


FIGURE 7.5 The 3-Fold Rates as a Function of Atmospheric Pressure

of the magnets. This is found from the dimensions and weights of the individual plates comprising the magnet blocks to amount to a total of $3875 \pm 20 \text{ gm cm}^{-2}$ the error coming from the quoted tolerance by the supplier on each plate. This figure is consistent with the fact that the height of the magnet blocks decrease from 125.0 cm for the upper to 123.2 cm for the lower. The total figure above, assuming a density of iron of 7.90 gm cm^{-3} , gives a block height of 122.6 cm which is close to that of the lower block, which is therefore virtually fully compressed by the mass above it.

Other absorbing materials present are the scintillation counters, the copper coils of the magnet windings, and the momentum selector trays. The amounts of absorber contained in these have been calculated from their dimensions and respective densities, and table 7.4 summarises the total amount of absorber present.

Element	Material	Thickness (gm cm^{-2})
Magnet Blocks	Fe	3875 ± 20
Scintillation Counters	Al Nel02A	13
Magnet Coils	Cu	22
Momentum Selector Trays	Al Glass	17
TOTAL		3927 ± 20

Table 7.4

The Various Contributions to the Total Amount of Absorbers

The energy loss curves of Sternheimer (1956) for ionisation loss, and Hayman and Wolfendale (1963), converted from rock to iron, for pair production, bremsstrahlung, and nuclear losses, have been used to convert the total amount of absorber into a momentum threshold. (The distinction between momentum and energy at these energies is neglected.) Figure 7.6 shows the range-momentum relation calculated from above sources, in the

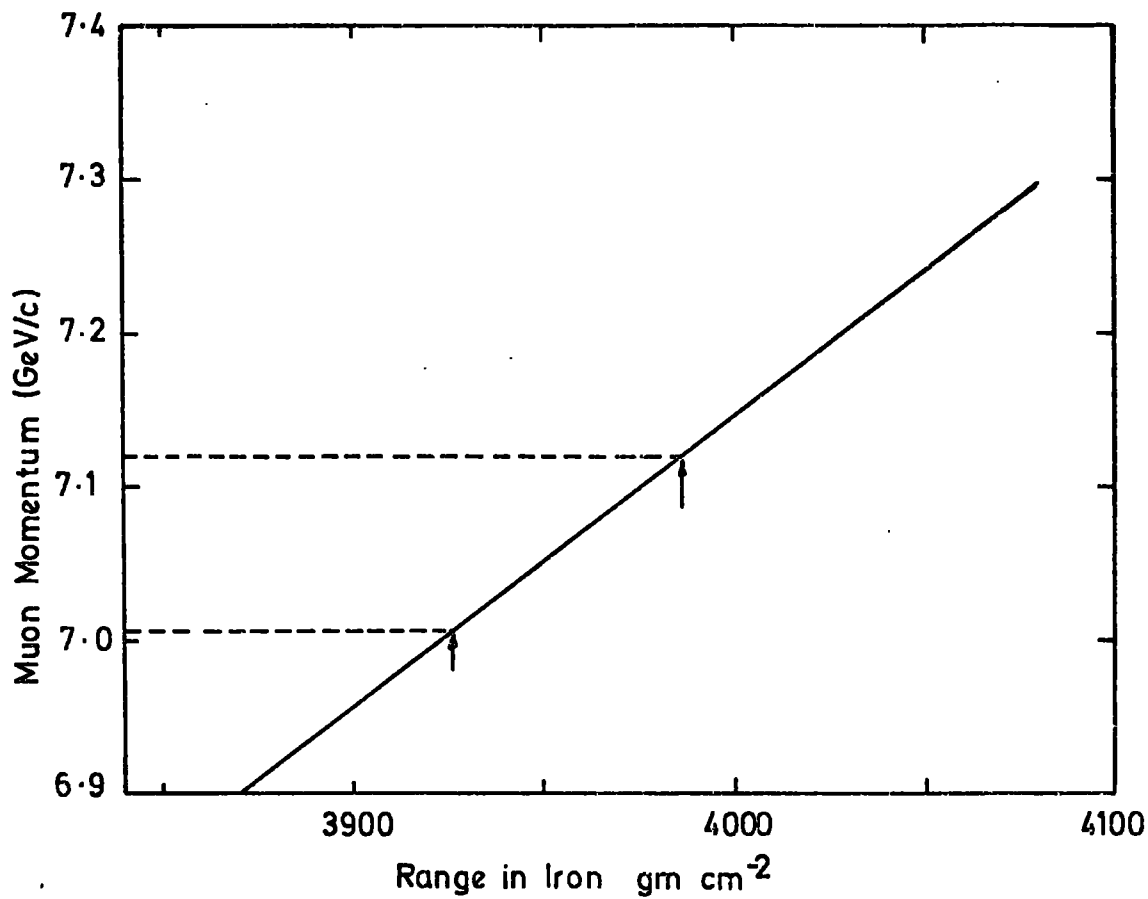


FIGURE 7.6 The Range - Momentum Relation in Iron

region of 4000 gm. cm^{-2} . Neglecting the effect of fluctuations in energy loss, which will be insignificant at these energies, and assuming that the range-momentum relation is the same for other types of absorbing material as it is for iron, which again will introduce negligible error, the cut-off momentum for 3875 gm cm^{-2} is 7.01 GeV/c , shown by the arrow in figure 7.6. The second arrow is shown at the effective amount of absorbing material after correction for instrumental effects as discussed in the next section.

7.6 Corrections due to Instrumental Effects

7.6.1 Multiple Coulomb Scattering

Multiple coulomb scattering causes two effects:

- (a) it causes the particle to execute a 'zig-zag' motion in the iron, increasing the effective path length, and hence increasing the effective cut-off momentum.
- (b) particles can be scattered in or out of the geometrical acceptance of the scintillation counters hence necessitating a correction to the measured 3-fold rate.

Each of these is considered in turn.

(a) 'Zig-Zag' Motion.

This has been studied by Koenig (1946) who gives an expression for the effective increase in path length of particle of momentum p_0 just penetrating an absorber as :

$$\Delta R = \int_0^{p_0} \frac{\mathfrak{D}_m^2}{2} \frac{dR}{d(p/\mu)} d(p/\mu) \quad 7.1$$

$$\text{where } \mathfrak{D}_m^2 = K \times [R(p_0) - R(p)] \cdot \frac{\log_e \left(\frac{1+y}{1+y_0} \cdot \frac{p_0}{p} \right)}{y_0 + \frac{1}{y_0} - (y + \frac{1}{y})}$$

$$y = \left[\frac{p^2}{\mu^2} + 1 \right]^{\frac{1}{2}}, \text{ and } K = 16\pi \frac{\mu_e^2}{\mu^2} \cdot N r_0^2 \frac{Z^2}{A} \log_e \left(\frac{183}{Z} \right)$$

In this expression R is the range as a function of momentum p , μ and μ_e are the masses of the muon and electron respectively, N is Avagadro's number, r_0 is the classical electron radius, and Z and A are the atomic number and atomic mass of the absorbing material. Substituting numerical values for the constants, and using the range-momentum relation given in the previous section one finds that for a 7 GeV/c muon just able to penetrate an iron absorber, the increase in path length is 0.8%. Thus the amount of absorber must be increased by this amount to allow for the effect.

(b) Scattering In and Out of the Acceptance

Particles which, in the absence of multiple scattering (i.e. straight line trajectories) would be accepted by the three scintillation counters have a probability of being scattered out and missing either the middle and/or the lower scintillation counters. Conversely, particles which would have been outside the geometry defined by the counters can be scattered in. The net result of this competition between scattering in and scattering out necessitates a correction to the observed 3-fold rate.

In order to calculate the scattering effects, initially a two dimensional computer model of the three scintillation counters and the magnet blocks was set up. Particles incident in the vertical direction were considered and were followed through step by step including the effects of energy loss and of multiple scattering, as outlined in Appendix C. Two distributions were calculated from these simulations at given momenta:

- (i) the lateral distribution at the lower level around the point at which the particles would have been incident without the effect of scattering.
- (ii) the lateral distribution at the middle level around the line joining the outer two co-ordinates (upper and lower levels) of each individual track in the simulation.

Both these distributions are found to be gaussian with standard deviations σ_m and σ_l respectively, shown in figure 7.7 as functions of incident momentum. The experimental points are the results of the computer simulations, and the dashed lines represent those expected from simply

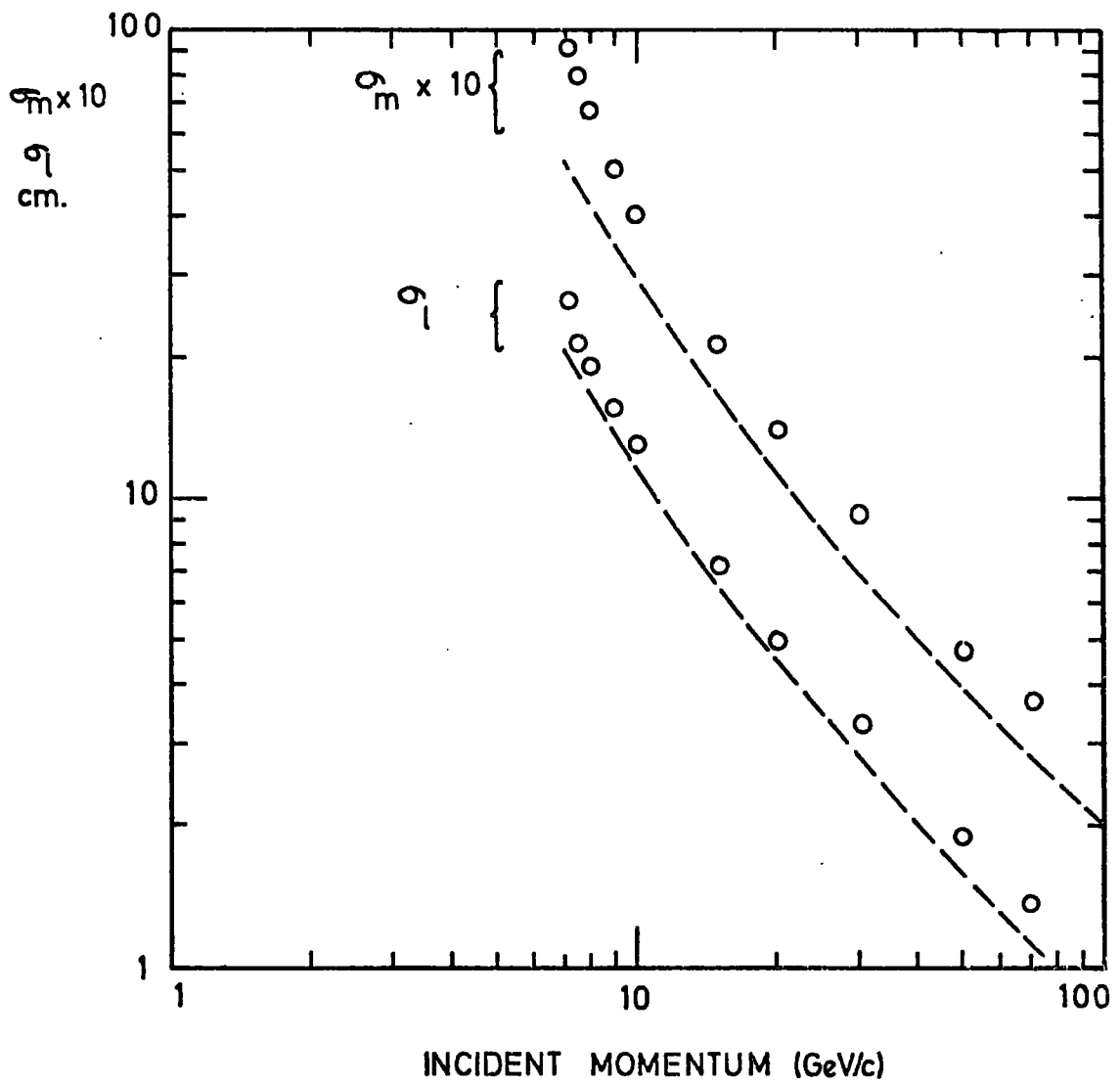


FIGURE 7.7 The Scattering Standard Deviations (σ_m & σ_l) as a Function of Momentum

considering the iron alone, taking a mean value for the momenta in the spectrograph, and using the expression given by Rossi and Greisen (1942) for the standard deviations. As would be expected, the effect of the gaps between the magnet blocks is to broaden the distributions. Neglecting the effect of the increase in path length, these distributions may be considered applicable to all angles of incidence. Two planes perpendicular to each other were considered and the scattering in each taken to be independent. The front plane is defined as that plane at right angles to the flash tubes, (i.e. a scintillation counter width of 75 cm), and the side plane is parallel to the flash tubes, (i.e. a counter width of 176 cm). In order to compute the probability of being accepted by the scintillation counters, for a given angle, a treble integration has to be performed over the respective widths of the three counters. This can be expressed, for the front plane as :

$$P(\theta, \vartheta) = \frac{1}{2\pi\sigma_m\sigma_l} \cdot \frac{1}{75} \int_0^{75} \int_0^{75} \int_0^{75} \exp\left\{-\frac{1}{2}\left(\frac{x_1-x_3}{\sigma_l}\right)^2\right\} \exp\left\{-\frac{1}{2}\left(\frac{x_2 - \left[\frac{x_1-x_3}{2}\right]}{\sigma_m}\right)^2\right\} dx_1 dx_2 dx_3 \quad 7.2.$$

where x_3 , x_2 , and x_1 are the co-ordinates at the top, middle, and lower levels respectively. A similar expression exists for the side plane, but with the 75's replaced by 176's, the standard deviations, σ_m and σ_l , however, remaining the same.

Solving the integral 7.2 numerically gives the probabilities of particles of a given momentum being accepted as a function of angle. Figures 7.8 and 7.9 show the results for momenta of 7.5 and 10 GeV/c for both the front and side planes. Also shown are the probabilities expected for particles with infinite momentum, (i.e. having no multiple scattering), and as would be expected the scattering is much more evident in the front plane, as the dimensions are smaller whilst the scattering deviations are constant in both planes. Integration of these curves over the incident angle, ϑ , and comparison with that expected from infinite momentum, gives the net probability of being 'lost' due to multiple scattering as shown in figure 7.10, where again the effect is much greater in the front than in the side

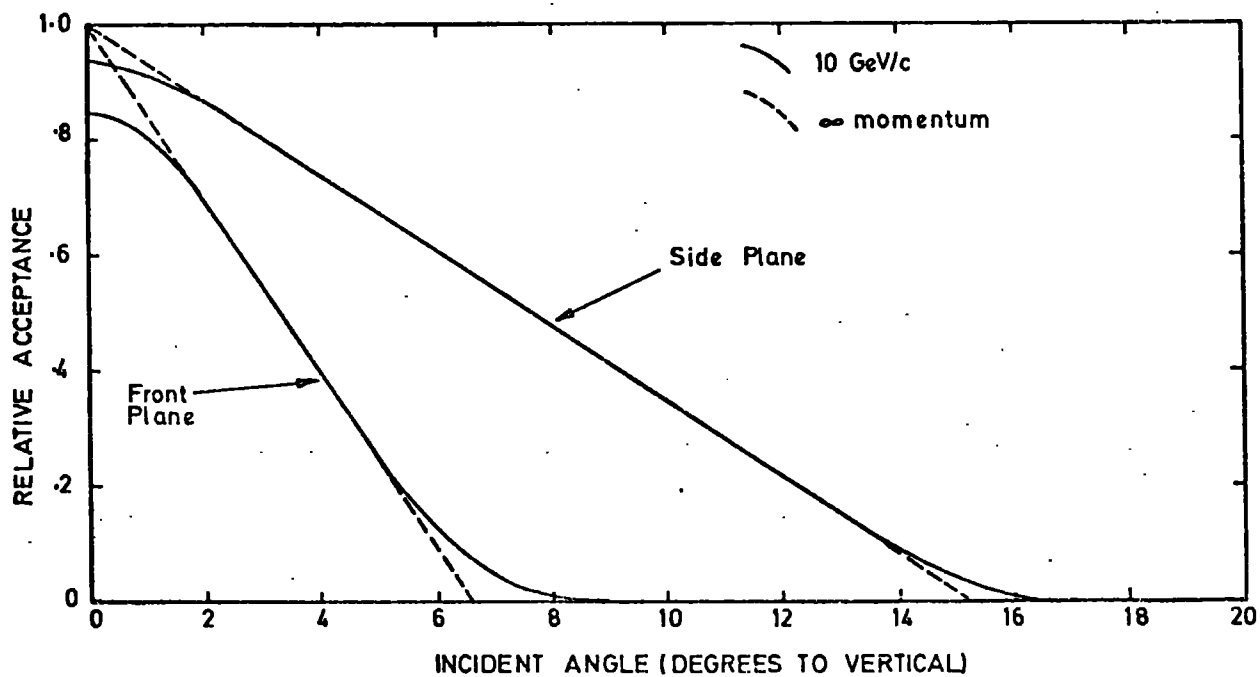
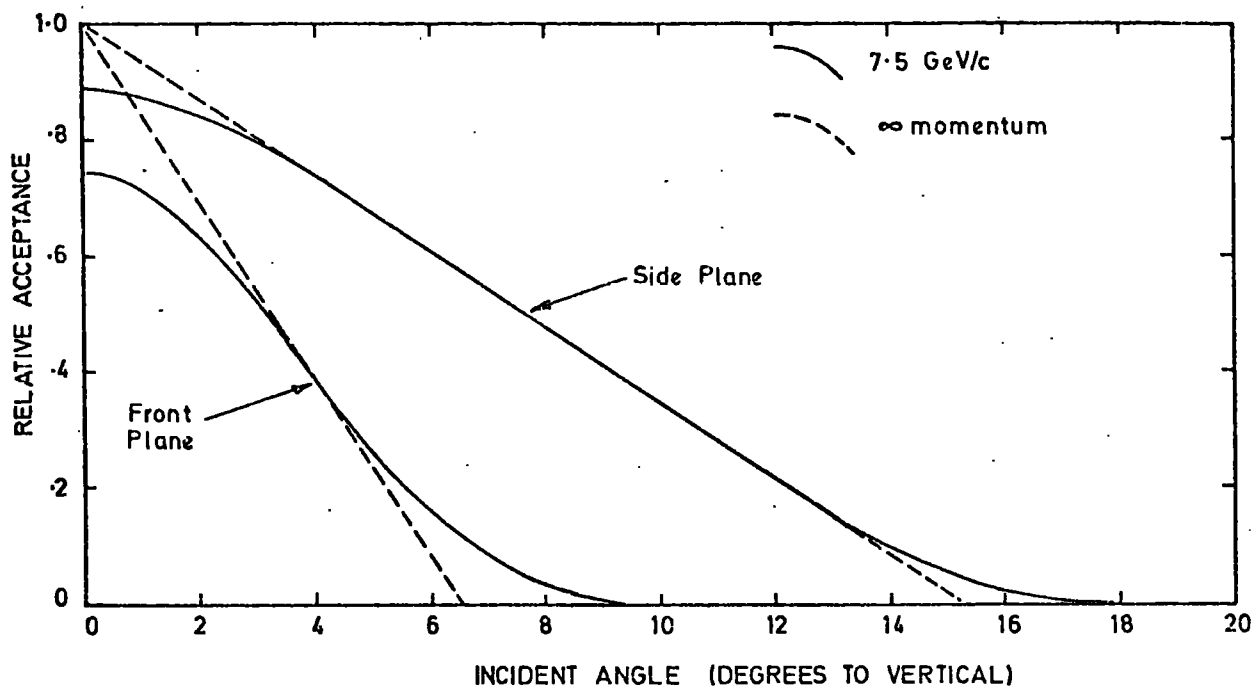


FIGURE 7.8 & 7.9 The Relative Acceptance as a Function of Incident Angle with the Inclusion of Multiple Scattering (7.5 & 10.0 GeV/c Incident Momentum).

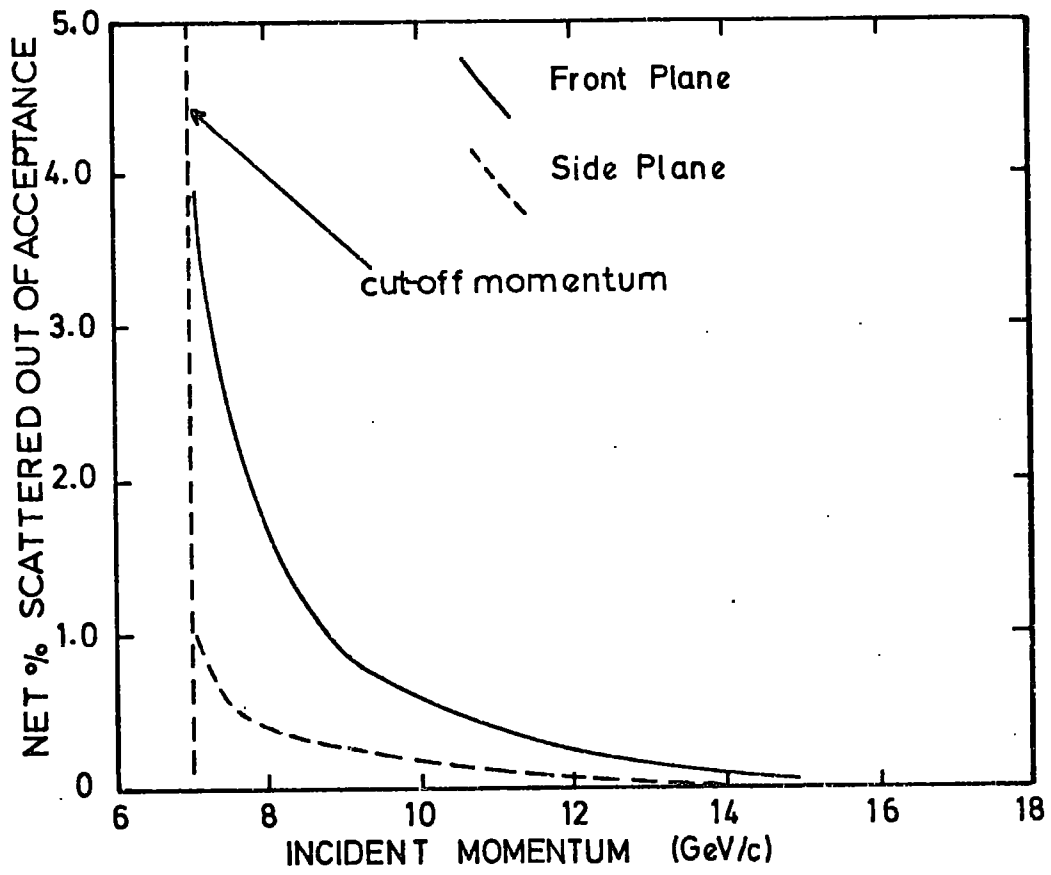


FIGURE 7.10 The Overall Probabilities of Being "Lost" due to Multiple Scattering.

plane. Averaging over the incident momentum spectrum gives an average net loss in the front plane of 0.75% and in the side plane of 0.20%, this amounting to a total net loss due to scattering of 0.95%. It is to be noted that this is very small, considering the large amount of iron in the spectrograph, which is due to an almost equal number of events being scattered in and out of the acceptance.

7.6.2 Non-Vertical Angles of Incidence

Particles traversing the spectrograph with non-vertical angles of incidence pass through a greater thickness of absorber than calculated in section 7.5 and hence have a higher cut-off momentum. The situation is shown in figure 7.11 (a), and considering first the front plane, the path length at an angle ϑ_1 , to the vertical is given by $h/\cos\vartheta_1$, where h is the vertical separation between the scintillation counters. Integrating over all angles of incidence weighted by their relative acceptance probabilities as given in Appendix B, and letting w_1 be the width of the scintillators we find:

$$\begin{aligned} \text{Mean Path Length} &= \frac{\int_0^{\vartheta_{1\max}} \frac{h}{\cos\vartheta} (w_1 \cos\vartheta - h \sin\vartheta) d\vartheta}{\int_0^{\vartheta_{1\max}} (w_1 \cos\vartheta - h \sin\vartheta) d\vartheta} \\ \text{in front plane.} & \\ &= \frac{w_1 \vartheta_{1\max} + h \log_e(\cos\vartheta_{1\max})}{w_1 \sin\vartheta_{1\max} - h(1 - \cos\vartheta_{1\max})} \end{aligned} \quad 7.3$$

$$\text{where } \vartheta_{1\max} = \tan^{-1} \left(\frac{w_1}{h} \right)$$

Substitution of numerical values for w_1 (= 75 cm.) and h (= 649.6 cm.) gives the mean path length as 1.001xh, and a similar calculation for the side plane gives the mean path length as 1.006xh. The combination of the two mean path lengths in the front and side planes is illustrated in figure 7.11 (b), where it can be shown that the overall mean path length \bar{d} is given by:

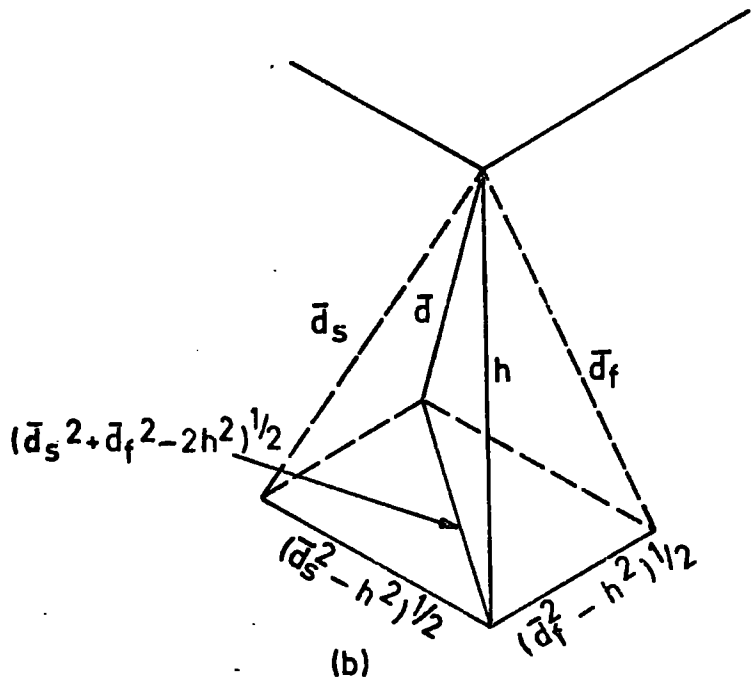
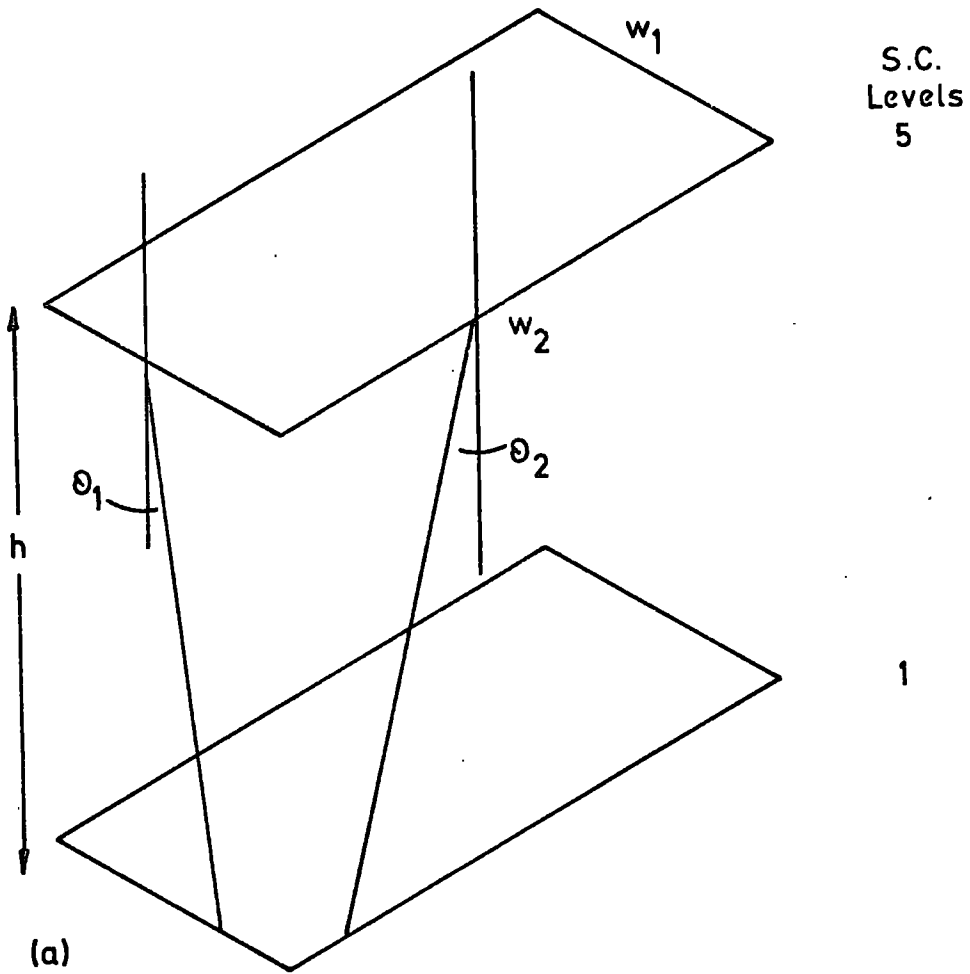


FIGURE 7.11 The Notation used in Calculating the Mean Path Length due to Non-Vertical Angles of Incidence.

$$\bar{d}^2 = \bar{d}_s^2 + \bar{d}_f^2 - h^2$$

7.4

Putting the values for the mean path lengths in the front (\bar{d}_f) and side (\bar{d}_s) planes we see that the mean path length is $1.007xh$ i.e. an increase of 0.7%. Consequently the amount of absorbing material must be increased by this amount.

7.6.3 Air Shower Triggers.

Large air showers can cause pulses in all three scintillation counters, hence simulating the passage of a muon. Typical events photographed using the flash tubes in the measuring trays have been scanned and it is seen that the rate of occurrence of such showers is $\sim 1\%$. The error on this is considered to be quite large ($\sim 0.5\%$) due to the objective nature of assessing whether such events were accompanied by muons which would have triggered the apparatus, or whether or not the shower itself would have actually caused triggering. A downward correction of $1.0 \pm 0.5\%$ has therefore to be applied to the observed 3-fold rate.

7.6.4. Short Pulses in the Coincidence Unit

The pulses which are actually put in coincidence in the coincidence gate are only $\sim 0.1 \mu s$ in length, consequently there is some loss of events due to variations in the arrival times of these pulses at the gate. This was tested using a separate coincidence circuit employing $2 \mu s$ pulses at coincidence and the rate with this was found to be 1.06% higher than with the main coincidence unit. For this reason an upward correction of this magnitude must be applied to all the rates measured with the main coincidence unit.

7.6.5 Random Coincidences

The counting rates of the individual scintillation counters is $\sim 340 \text{ sec}^{-1}$, and the resolution of the coincidence arrangement is $\sim 0.1 \mu s$, which gives a random 3-fold coincidence rate of $\sim 10^{-6} \text{ sec}^{-1}$ which has consequently been neglected.

7.6.6 Summary of All Corrections

	Correction to Observed Rate %	Correction to Absorber Thickness %
Multiple Scattering	+ 0.95	+ 0.6
Non-Vertical Incidence	—	+ 0.7
E.A.S. Triggers	- 1.00	—
Coincidence Unit	+ 1.06	—
TOTALS	+ 1.01	+ 1.50

Table 7.5Summary of all Corrections.

Table 7.5 summarises all the corrections which have to be made to the rate and to the absorber thickness. The total rate after correction for the above effects is thus 28.86 min^{-1} and the effective amount of absorber is 3933 gm cm^{-2} which from figure 7.6 is seen to correspond to a mean cut-off momentum of 7.12 GeV/c , as shown by the second arrow in that figure.

7.7 The Final Rate

Combining the observed rate, corrected as above, with the scintillation counter efficiency of 0.894, and the overall acceptance of $408 \text{ cm}^2 \text{ sr}$ as given in Appendix B, the measured muon rate above 7.12 GeV/c is $(1.319 \pm 0.011) \times 10^{-3} \text{ s}^{-1} \text{ cm}^{-2} \text{ sr}^{-1}$, where the error is a combination of all the sources of error and amounts to 0.8%. This is for a mean pressure of 754 mm Hg .

7.8 Discussion

It can be seen that the present result agrees very well with the previous MARS result $(1.31 \pm 0.02 \times 10^{-3} \text{ s}^{-1} \text{ cm}^{-2} \text{ sr}^{-1})$ at the same value of momentum, and hence suggests that both of the previous results were correct. Figure 7.12 shows a summary of recent absolute intensity measurements between 1 GeV/c and 10 GeV/c . The points of the Nottingham workers (Crookes and

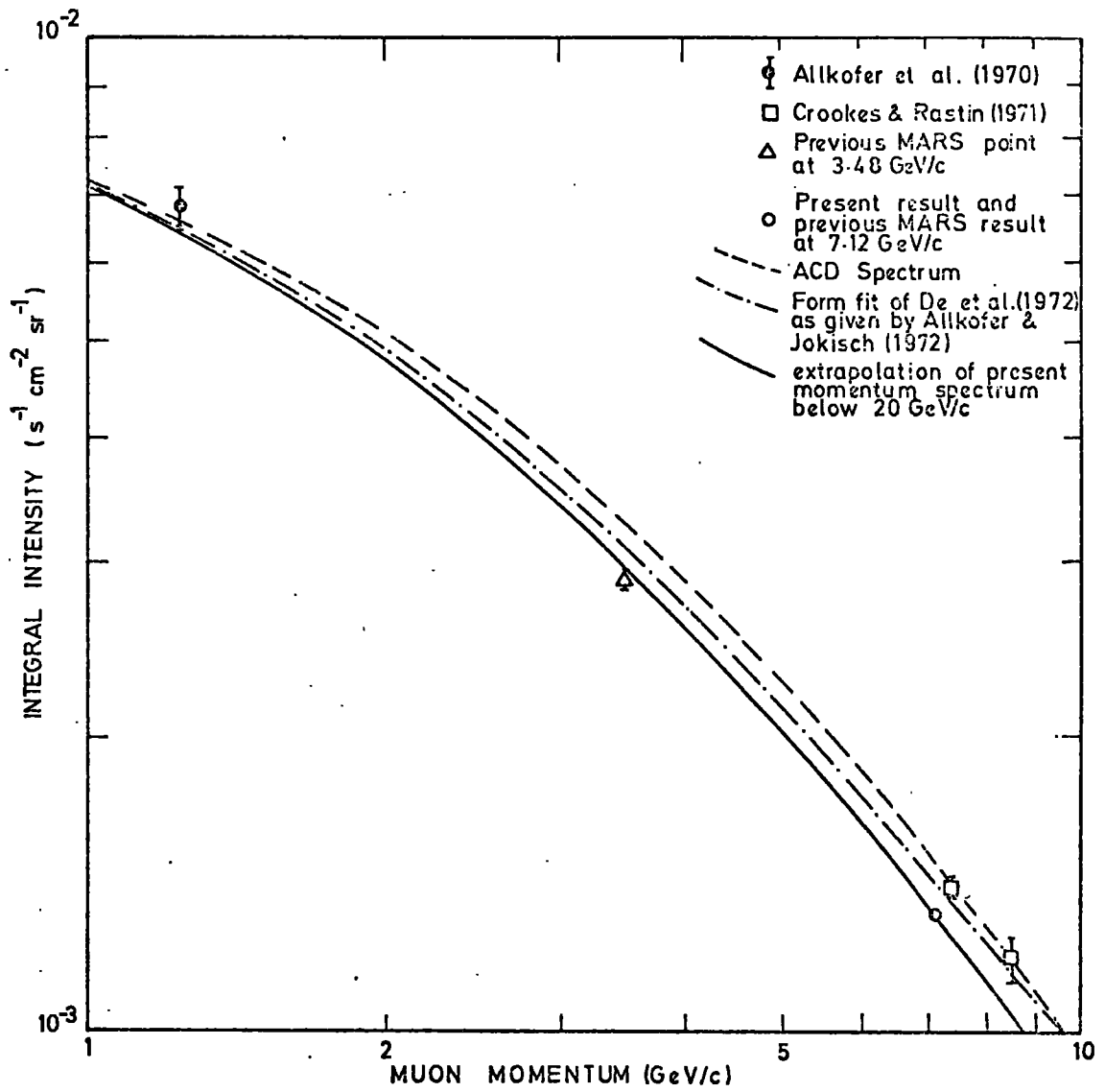


FIGURE 7.12 Recent Absolute Determinations of the Integral Spectrum between 1 & 10 GeV/c.

Rastin, 1971) and the Kiel point (Allkofer et al., 1970) have been taken from the summary by Allkofer and Jokisch (1972), as also has the integral form fit spectra of De et al. (1972). Also shown are the previous two MARS points and the present results (the two 7.12 GeV/c measurements being shown at the same point as they were in agreement), together with the ACD spectrum (Allkofer et al., 1971) and the extrapolation of the present measurement of the spectrum as given in chapter 5 of this thesis. As can be seen all the results agree fairly well in the region of 1 GeV/c where the value of the intensity has been confirmed in several other experiments below this momentum (e.g. Ashton et al., 1972). Above 1 GeV/c there is divergence of the results, the ACD spectrum giving the highest intensities and the extrapolation from the present work the lowest. The form fit of De et al., as quoted by Allkofer and Jokisch, lies in between the two spectra. In fact the extrapolation of the present work was also based on this form fit, which was originally made by De et al. to recent absolute differential points, and gave a differential intensity 10% less than the ACD spectrum at 10 GeV/c. In producing their integral from fit, Allkofer and Jokisch have taken the ACD spectrum to be correct above 10 GeV/c, whereas in the present work the intensity above 10 GeV/c is 10% less than the ACD spectrum, hence the divergence of the two integral spectra calculated basically from the same source.

As can be seen the present results agree very well with the extrapolation of the MARS spectrum which also agrees with the established values at 1 GeV/c. The Nottingham results however support the ACD spectrum, but could possibly be in error as they were underground measurements, and hence rely on an accurate knowledge of the terrain above the detector. Clearly more measurements are needed in this region before any firm conclusions can be made. However considering the present work alone there is a consistent picture of the spectrum from -1 GeV/c to nearly 1000 GeV/c in which the measurements of the differential spectrum above 20 GeV/c and the absolute intensity at 7.12 GeV/c are in good agreement. As a final remark the only common factors

between the two present experiments, are the overall acceptance ($408 \pm 2 \text{ cm}^2 \text{ sr}$) and the scintillation counter efficiencies (0.894 ± 0.002), and it is thought that these quantities are known sufficiently well to say that the absolute height of the spectrum, bearing in mind the consistency between the two results, is correct to within a few percent.

CHAPTER 8

CONCLUSIONS AND FUTURE WORK

8.1 Conclusions

The final conclusions are fundamentally the same as those reached at the end of chapter 6. The present measurements of the muon differential spectrum in the range 20 GeV/c to 500 GeV/c agree reasonably well with the measurements of other recent experiments (see figure 6.5), though many of the earlier results (e.g. Hayman and Wolfendale, 1962; Appleton et al., 1971) give a steeper spectrum, possibly due to instrumental biases in these data.

An attempt to fit an all pion production model, with a constant exponent pion production spectrum, as outlined in chapter 5 proved unsuccessful, and a simple χ^2 test showed the significance of such a fit to be less than 0.1%. Even with the inclusion of kaons as a second source of muons, the fits obtained are poor (unless a very high K/ π ratio, ~ 0.6 , is taken). It is found that at the higher momenta ($p_\mu > 70 \text{ GeV/c}$), the observed muon intensities are higher than those predicted by a fit to the lower momenta data using the model with a constant exponent (γ), and consequently the best representation of the present results is obtained when γ is allowed to increase with momentum. In particular a model containing two values of γ is found to fit the data reasonably well, assuming a K/ π ratio of 0.15 as indicated by the I.S.R. measurements at CERN, namely with $\gamma = 2.645$ for a muon momentum less than 70 GeV/c and $\gamma = 2.56$ for muons in excess of this momentum. This appears contrary to the findings of many other workers (e.g. Allkofer et al., 1971; Handi and Sinha, 1972) who fit a constant γ , all pion production model to their measurements. Closer examination of their actual data reveals that their experimental points tend to lie above the fitted curves at high momenta, and hence support the idea of a decrease in the slope of the production spectra, (see figure 6.7). It is considered that the reason these workers were able to fit

such a model to their data is that their statistical accuracy at the higher momenta was very poor, and hence the fits are heavily weighted by the low momentum points.

With regard to measurements made at very high energies (indirect measurements), it is found that the extrapolation of the present work above 500 GeV, whilst agreeing in shape with a recent survey of underground, and underwater measurements by Wright (1973), gives higher intensities, above a muon energy of 1000 GeV, than the data given in a second survey of all indirect measurements above 300 GeV by Ng et al. (1973). If the spectrum given by the present work is correct then it is reasonable to assume that its extrapolation up to at least ~ 800 GeV is valid, but at energies much in excess of this, the indications are that γ must increase again, hence producing the relative decrease in the muon intensity necessary for agreement with the high energy indirect measurements of the muon spectrum.

As pointed out in chapter 6, a decrease in the slope of the primary spectrum has recently been suggested by Wdowczyk and Wolfendale (1973) in an attempt to give agreement between the recent primary spectrum measurements of Ryan et al. (1972) and the E.A.S. measurements in excess of 10^{15} eV. The former if extrapolated from 10^{12} eV to 10^{15} eV gives too low intensities, and hence it is proposed that the primary spectrum slope decreases to a differential value of 2.44 to allow for this. If the theory of scaling is valid, then the slope of the pion production spectrum should follow that of the primary spectrum, and consequently should decrease above 10^{12} eV and remain at this value to $\sim 10^{15}$ eV. The decrease in the slope of the pion production spectrum at $\sim 10^{12}$ eV is consistent with the present results, but its constancy at the lower value is inconsistent with the indications, from indirect measurements of the muon spectrum, that it should increase again above $\sim 10^{13}$ eV. This would imply the breakdown of the theory of scaling, and the present results would indicate that such a breakdown is occurring at proton energies in excess of $\sim 10^{13}$ eV. However it is by no means certain that such a decrease in slope of the primary spectrum

exists, indeed the measurements of the PHOTON satellites (Grigorov et al., 1971) suggest that the slope remains constant (~ 2.7) for energies up to $\sim 10^{14}$ eV. All that can be remarked is that the present results tend to support the idea of a decrease in the slope.

As regards the absolute height of the spectrum, there seems to be disagreement among many experiments. The work of the Kiel group (Altkofer et al., 1971) gives a spectrum (the ACD spectrum) which is $\sim 10\%$ higher than the present work at 20 GeV/c, the difference decreasing with increasing momentum and is 20% below that of the present work at 500 GeV/c. The ACD spectrum, however, is a composite based upon the results from three magnet spectrographs and one range spectrograph, and as explained in chapter 6, it is considered that in the region above 1 GeV/c, it may be too high, and possibly a bias exists in the high momentum spectrograph data due to the track fitting criteria used. Consequently it is believed that the present results are in agreement with the data from the Kiel experiments, but not with the ACD spectrum above 1 GeV/c. The spectrum of Burnett et al. (1973) gives intensities $\sim 22\%$ lower than those of the present work, however due to the nature of the derivation of this spectrum, (combining data from different zenith angles), it is uncertain as to the validity of the results, though they do agree in shape very well with the present results.

Further support that the present results are correct is afforded by their extrapolation below 20 GeV/c where they are found to join quite well with the form fit of De et al. (1972) at ~ 7 GeV/c, and the integration of this composite spectrum is seen to agree with the absolute rate intensities given in chapter 7, and also with the previous absolute rate measurements with the MARS spectrograph.

The total systematic error on the spectrum measurements is seen, from chapter 4, to range from $\sim 1.2\%$ at 20 GeV/c to $\sim 2.9\%$ at 500 GeV/c, consequently it is considered that the spectrum given in chapter 6 as the comparison spectrum, which includes the present work, when allowance is made for both statistical and systematic errors, is correct to $\sim 2\%$ at 20 GeV/c and $\sim 10\%$

at 500 GeV/c, and can reasonably be extended above this energy to ~800 GeV/c using the model given in chapter 5.

8.2. Future Work

Clearly the spectrum measurements should be extended to higher momenta. This is being done at present with the high resolution system of MARS using the small diameter flash tubes in the measuring trays, and storing the data on the 1130 computer, as outlined in chapter 2. This system has an m.d.m. in excess of 5000 GeV/c, and will overlap the present measured spectrum in the region 200 to 500 GeV/c, and consequently any change in the slope of the pion production spectrum should be apparent. The present work will be useful in that it will provide a normalisation for this high energy spectrum which may otherwise be difficult to fix due to rejection criteria in the computer analysis programmes.

APPENDIX A

THE TRAJECTORY OF MUONS THROUGH THE MAGNET BLOCKS

A charged particle moving in a magnetic field B (gauss), is subject to a force at right angles to its direction of motion, causing it, in the absence of energy loss, to move in a circular orbit. If p (eV/c) is the momentum of the particle (of single charge) then the radius of curvature of this orbit, r (cm), is given by :

$$r = \frac{p}{300 B} \quad \text{A.1.}$$

For the present situation with $B = 16.3$ kG, and changing p to MeV/c we have:

$$r = 0.2045 p \quad \text{A.2.}$$

This equation has been used throughout the present work to calculate radius of curvature of the particles in the magnetic field.

Consider figure A.1., which represents a layer of magnetised iron of thickness h , in which the muon will be assumed to have a constant momentum, the radius of curvature, r , hence being defined by equation A.2. If θ is the incident angle at point A, and α the change in angle at point B, as in figure A.1., then we have :

$$\text{Chord AB} = 2 r \sin \frac{\alpha}{2} \quad \text{A.3.}$$

and also

$$h = \text{Chord AB} \times \cos \left(\theta - \frac{\alpha}{2} \right) \quad \text{A.4.}$$

Eliminating (chord AB) between these two equations gives :

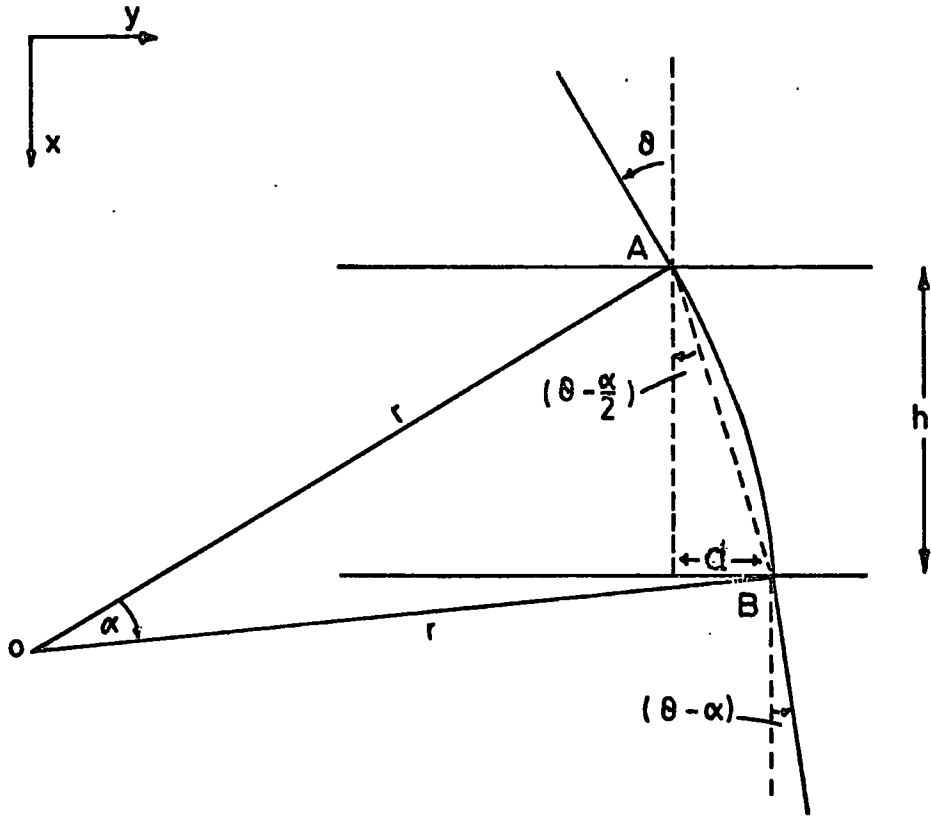


FIGURE A.1 The Trajectory of a Muon in a Layer of Magnetised Iron.

$$\frac{h}{2r} = \sin \frac{\alpha}{2} \cos \left(\vartheta - \frac{\alpha}{2} \right) \quad \text{A.5.}$$

which can be solved for α giving:

$$\alpha = \sin^{-1} \left(\frac{h}{r} - \sin \vartheta \right) + \vartheta \quad \text{A.6.}$$

Similarly for the opposite sign of bending α can be shown to be given by :

$$\alpha = \sin^{-1} \left(\frac{h}{r} + \sin \vartheta \right) - \vartheta \quad \text{A.7.}$$

The lateral displacement d from point A to point B is therefore given by :

$$d = h \tan \left(\vartheta - \frac{\alpha}{2} \right) \quad \text{A.8.}$$

If the muon suffered no energy loss then the width h could be taken as the full width of the blocks, and the position and angle of emergence from the block could be calculated from the above equations, and a knowledge of the incident angle and position. To allow for energy loss the block is divided into a number of layers (usually ~ 50) and the momentum assumed to be constant in each. The particle is then traced through the block layer by layer at each step applying the above equations to find the angles and positions after each layer and subtracting the relevant amount of energy loss depending upon the momentum of the particle (see figure 3.2.). This method has been used extensively to investigate the instrumental biases in the spectrograph, and to calculate the relationship between momentum and deflection.

APPENDIX B

CALCULATION OF THE SPECTROGRAPH ACCEPTANCE

By definition, the acceptance of the spectrograph is that quantity by which the vertical intensity has to be multiplied in order to give the rate of passage of muons through the three scintillation counters. Due to bending of the particles in the magnetic field this quantity is a function of momentum, and consequently its determination is divided into two parts. In the first case particles with an assumed infinite momentum are considered (which therefore, neglecting multiple scattering, travel in straight lines), and in the second, bending of the particles in the plane perpendicular to the magnetic field lines is considered and the acceptance relative to that with infinite momentum calculated. In the calculation of both these effects the variation of muons intensity with zenith angle has been neglected. Shown in figure B.1 is the muon intensity as a function of zenith angle for a number of different momenta (Coates, 1967). As can be seen for momenta >20 GeV/c, which are important for the momentum spectrum measurements, the variation is not more than $\sim 1\%$ at 6° , the mean angle of incidence. Even for the absolute rate experiment in which the lowest momentum is ~ 7 GeV/c, the variation with zenith angle is still small at these near vertical angles, and its omission introduces negligible error into the results. The effect of multiple scattering on the acceptance, which has been shown to be small in chapter 7 with zero field in the magnet blocks, is also neglected in the acceptance calculations.

(a) Infinite Momentum Acceptance.

Consider figure B.2(a) which shows the passage of a muon through the upper and lower scintillation counters, A and B being the points of intersection with each respectively. The two counters have been assumed to be represented by planes, the actual separation of which is ill-defined due to the finite thickness of the scintillators, and introduces an error into the acceptance which is discussed later.

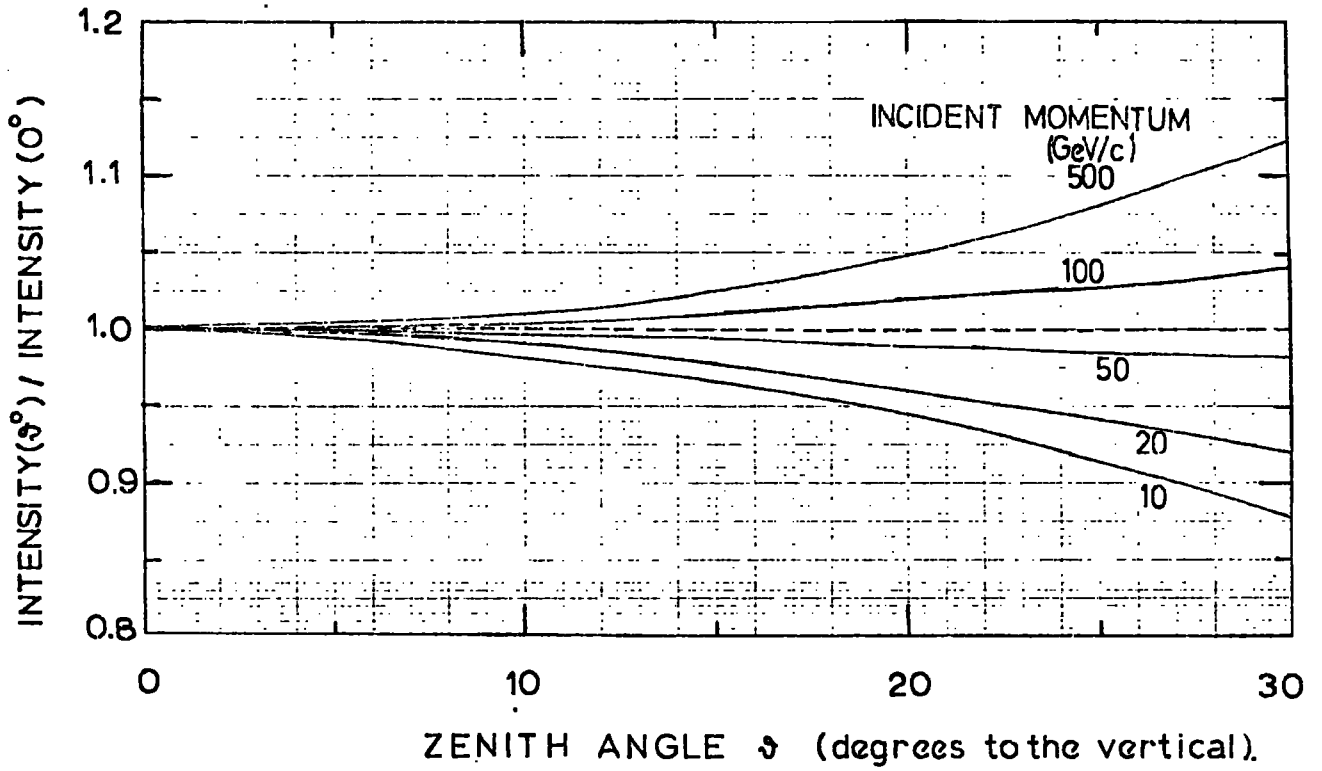


FIGURE B.1 Variation of Muon Intensity with Zenith Angle
(after Coates, 1967)

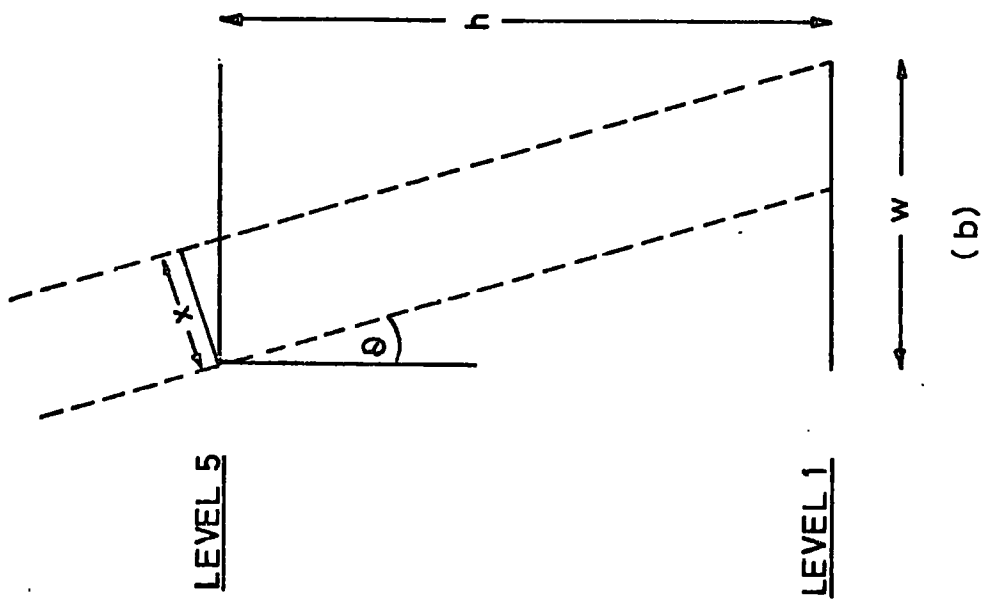
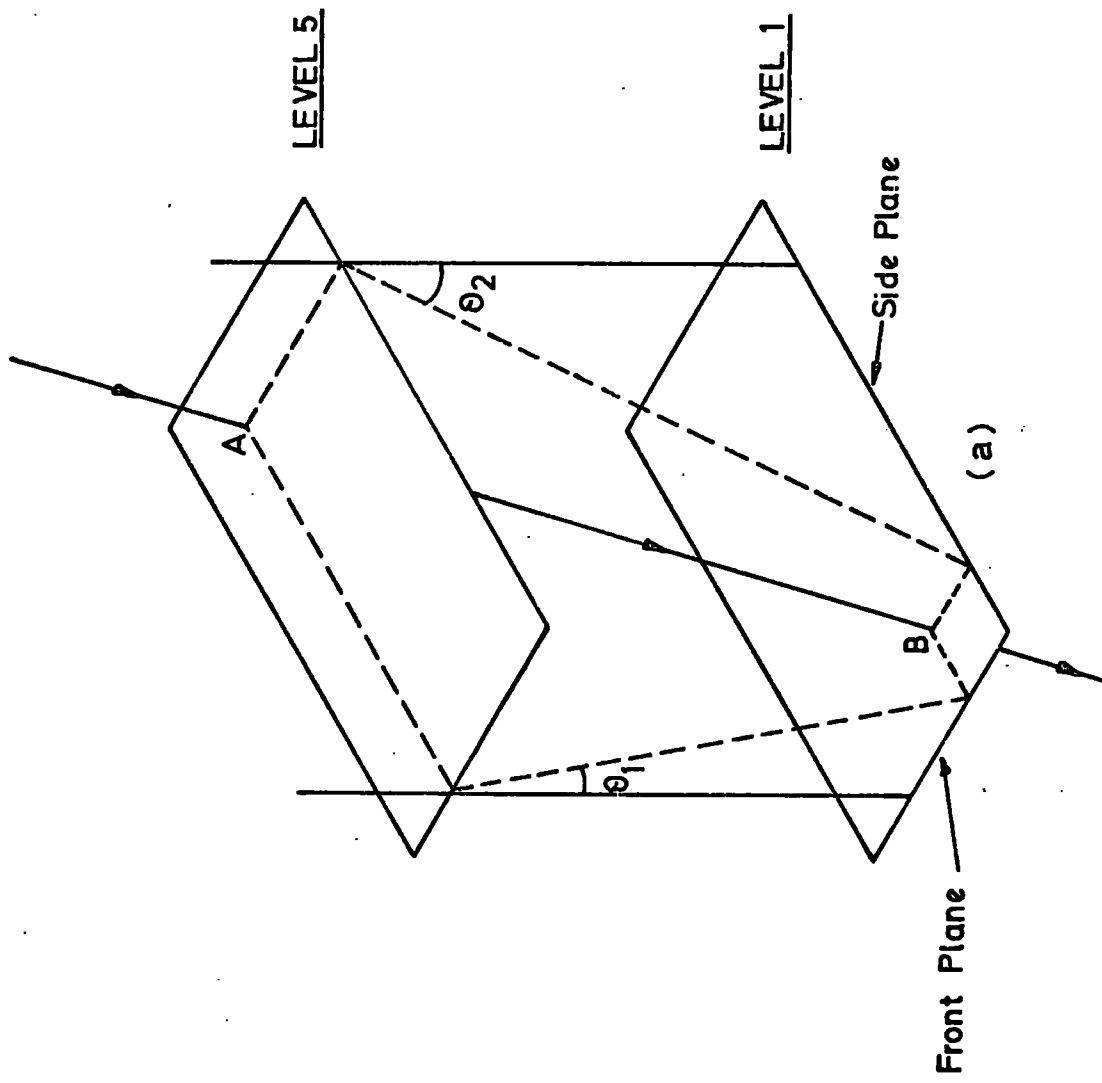


FIGURE B.2 Illustrating the Notation used in Calculating the Infinite Momentum Acceptance.

For the purpose of calculating the acceptance the muon trajectory is divided into the two planes at right angles to each other as shown in figure B.2 (a), and since the two are independent they can be considered separately. ϑ_1 and ϑ_2 are defined as the projected angles the track makes to the vertical in the front and side planes respectively, the latter being in the direction of the magnetic field lines, and the former perpendicular to this.

Figure B.2(b) shows a two dimensional picture of either of the two planes. The acceptance at an angle ϑ is then represented by the distance x , and from simple geometrical considerations can be shown to be given by :

$$x = w \cos \vartheta - h \sin \vartheta \quad \text{B.1.}$$

thus the two dimensional acceptance can be written as:

$$A_2 = 2 \int_0^{\vartheta_{\max}} (w \cos \vartheta - h \sin \vartheta) d\vartheta \quad \text{B.2.}$$

where $\vartheta_{\max} = \tan^{-1} \left(\frac{w}{h} \right)$ and the factor two arises since the integration is taken from 0 to ϑ_{\max} instead of $-\vartheta_{\max}$ to $+\vartheta_{\max}$. Evaluating this integral and substituting for ϑ_{\max} gives:

$$A_2 = 2 \left[(h^2 + w^2)^{\frac{1}{2}} - h \right] \quad \text{B.3.}$$

Assuming that both planes are independent, then the total three dimensional acceptance can be written, using the subscripts 1 and 2 to refer to the two planes, as

$$A_3 = 4 \int_0^{\vartheta_1^{\max}} A_1(\vartheta_1) d\vartheta_1 \int_0^{\vartheta_2^{\max}} A_2(\vartheta_2) d\vartheta_2 \quad \text{B.4.}$$

which reduces to :

$$A_3 = 4 \left[(h^2 + w_1^2)^{\frac{1}{2}} - h \right] \cdot \left[(h^2 + w_2^2)^{\frac{1}{2}} - h \right] \quad \text{B.5.}$$

Due to the finite thickness of the scintillators, the distance h in the above equations is not well defined. Clearly it is not the centre to centre distance between the scintillators, since particles at large angles

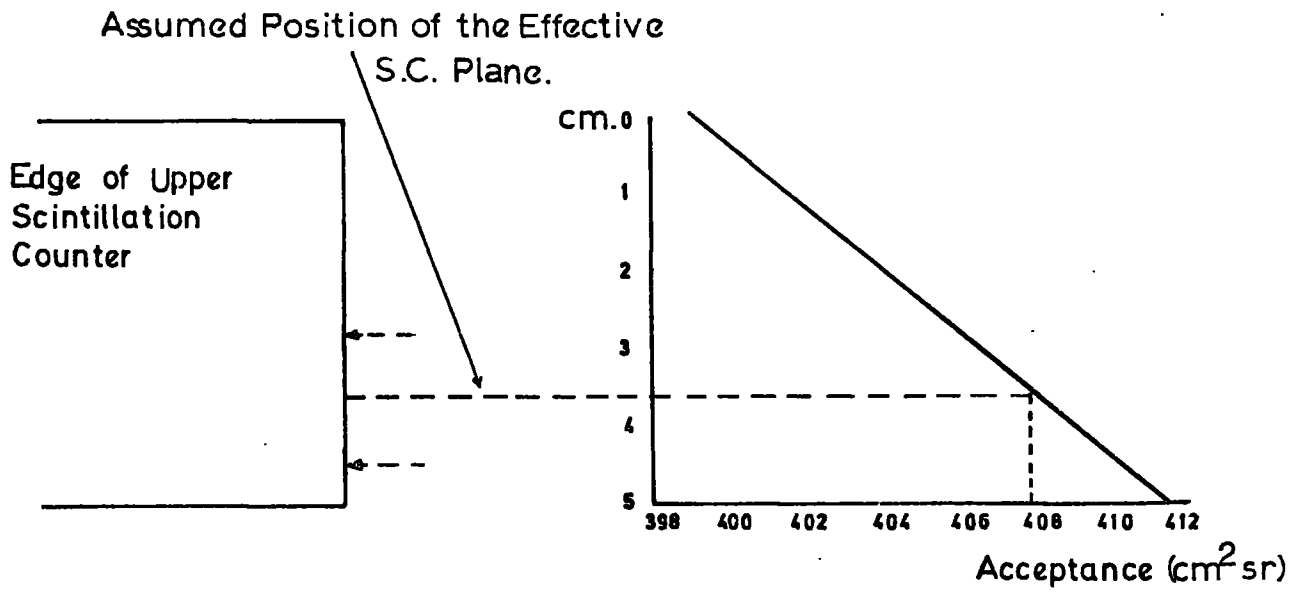


FIGURE B.3 The Infinite Momentum for Different Positions of the Effective Scintillation Counter Plane.

could pass through the corners and still trigger the counter.

Equally well the separation is not that of the inside edges as the particles must pass through a finite distance of scintillator. Figure B.3 summarises the situation, showing the acceptance calculated from equation B.5 for different positions of the effective plane, the inverse being taken for the lower scintillator (i.e. distances above the centre plane). Examination of this figure, together with a reasonable estimate of how much scintillator has to be traversed before triggering the counter, leads to the value of $408 \pm 2 \text{ cm}^2 \text{ sr}$ for the infinite momentum acceptance, the errors being given by the positions of the arrows in figure B.3 and represent an estimate of the error on the position of the effective plane.

(b) Relative Acceptance.

In order to calculate the relative acceptance one only needs to consider the plane perpendicular to the magnetic field lines in which the particle is bent. The procedure was to use a computer simulation of events incorporating the methods outlined in Appendix A. Particles of a given incidence angle and momentum were considered, and the extent of lateral movement possible for the trajectory to remain within each of the three scintillators, and within the magnet blocks, was ascertained. Thus effectively a channel is defined in which the particle can pass and trigger all three scintillation counters. The projection of the width of this channel on the plane normal to the direction of incidence of the particle is a measure of the relative acceptance for that particular angle and momentum. Figure B.4 summarises the situation for a trajectory bounded by the edges of the middle and the lower scintillators. The distance x divided by the width of the scintillator (75 cm.), is the relative acceptance. Repeating this procedure for different angles and momenta enables the relative acceptance integrated over all angles, as a function of momentum to be determined. Table B.1 gives the relative values obtained for particular momenta, and these are plotted in figure B.5.

Incident Momentum GeV/c	Relative Acceptance	Incident Momentum GeV/c	Relative Acceptance
7.8	0.014	12.5	0.764
8	0.055	15	0.862
8.5	0.177	20	0.935
9	0.298	40	0.987
9.5	0.408	80	0.996
10	0.500	100	1.000

Table P.1.

The relative acceptance for various values of momentum

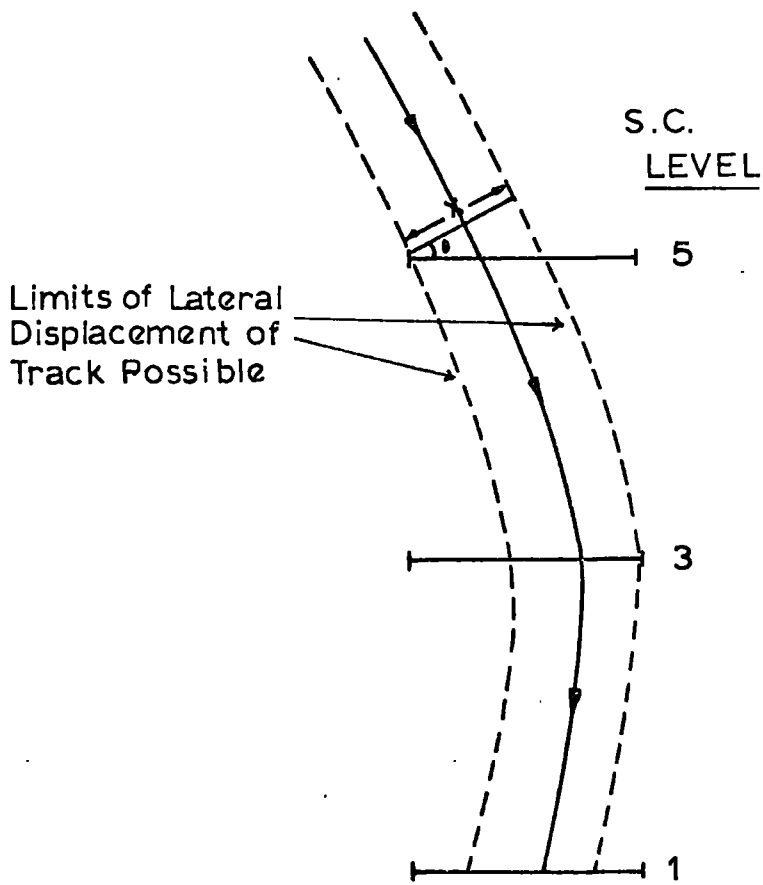


FIGURE B.4 A Typical Curved Trajectory of a Muon through the Spectrograph.
The Distance x is Proportional to the Acceptance.

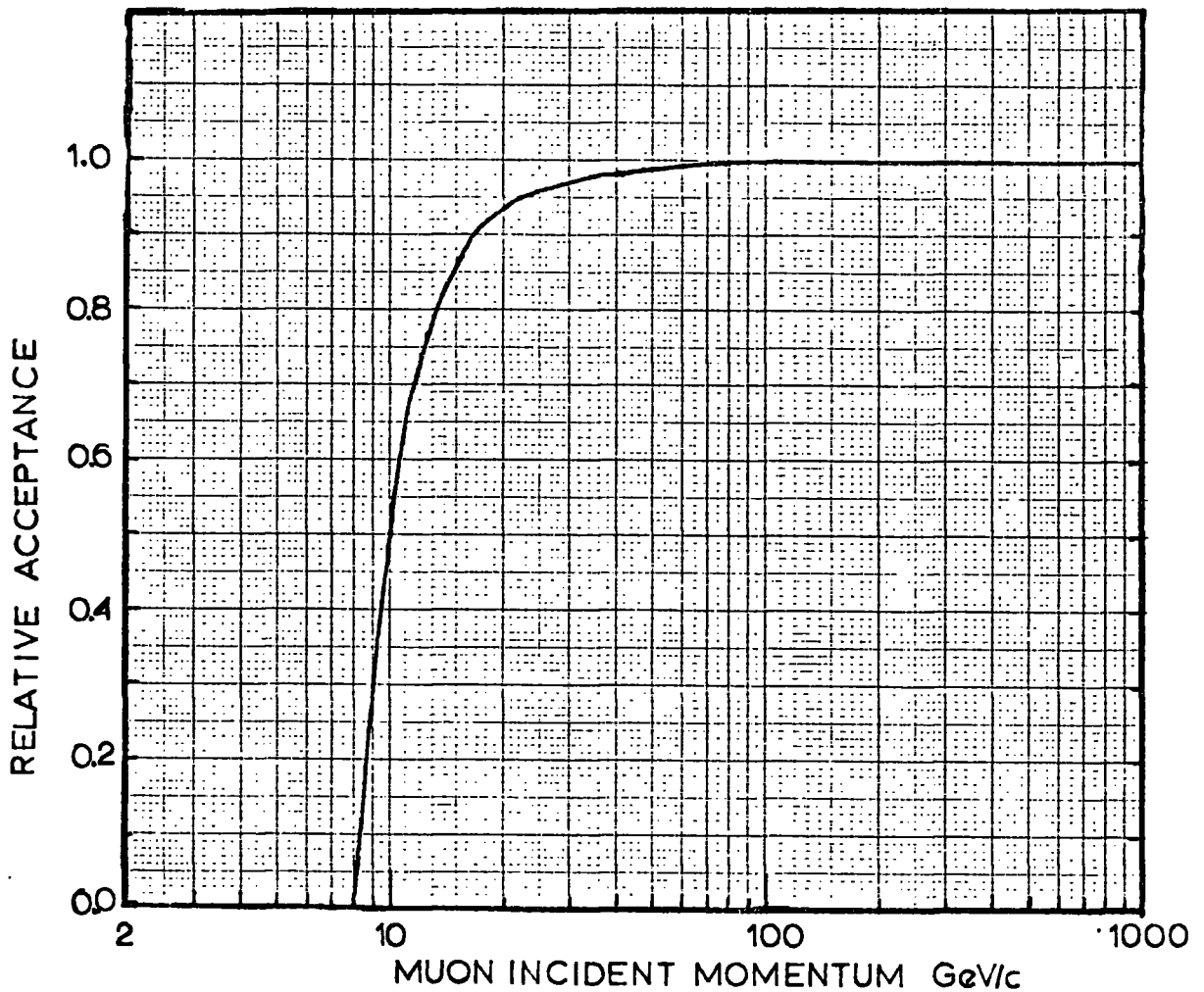


FIGURE B.5 The Overall Relative Acceptance.

APPENDIX C

MULTIPLE COULOMB SCATTERING IN THE IRON -

In its passage through the iron the muon is scattered many times by the iron atoms causing its path to deviate from a straight line. The probability of a particle which suffers no energy loss being scattered into a projected angle ϑ to $\vartheta + d\vartheta$, and a projected lateral displacement y to $y + dy$ is given, by Rossi and Greisen (1942), as:

$$F(t, y, \vartheta) = \frac{\sqrt{3}}{2\pi} \frac{\omega^2}{t^2} \exp \left[-\omega^2 \left(\frac{\vartheta^2}{t} - \frac{3y\vartheta}{t^2} + \frac{3y^2}{t^3} \right) \right] \quad \text{C.1.}$$

where t is the distance travelled in the iron (radiation lengths) and $\omega = (2p\beta/E_s)$, p being the muon's momentum, and E_s a constant having the value 21.2 MeV/c. Integration of equation C.1. with respect to both ϑ and y separately shows that the resultant distributions in y and ϑ respectively are gaussian with means of zero. However if a particular value of y (or ϑ) is taken then the resultant distribution in ϑ (or y) is not gaussian about a mean of zero and may be examined, for example for the case of a fixed value of y , by writing equation C.1. as follows:

$$F(t, y, \vartheta) = C \exp \left[-\frac{\omega^2}{t} \left((\vartheta - \alpha)^2 + \gamma^2 \right) \right] \quad \text{C.2.}$$

where C , α , and γ are constants. Expanding equation C.2. and equating the coefficients of ϑ to those in equation C.1. we find :

$$\alpha = \frac{3y}{2t} \quad \text{C.3.}$$

$$\gamma = \frac{\sqrt{3}}{2} \frac{y}{t}$$

Clearly then the resultant distribution is gaussian in ϑ about the mean value $\vartheta = 3y/2t$, and has a standard deviation, σ_{ϑ_y} , given by :

$$\sigma_{\delta y}^2 = \frac{E_s^2 t}{8 p^2 \beta^2} \quad \text{C.4.}$$

It is interesting to note that this standard deviation is exactly half that found when the sum over all values of y is taken (see Rossi and Greisen).

The treatment in the present work used Monte Carlo simulations of muons through the spectrograph based upon equations C.2, C.3, and C.4. In order to take account of the loss of energy of the muon in the iron blocks, they are divided into several layers (~50) and the energy is assumed constant in each layer, the correct amount of energy being subtracted between each. At the top of each layer the incident angle and position are known, and the increments in these caused by multiple scattering in the layer are calculated from the above equations and added to give the outgoing angle and position. The procedure for calculating the increments in the layers, was initially to select a lateral displacement (y) from a gaussian distribution with a standard deviation, σ_y , given by Rossi and Greisen as:

$$\sigma_y^2 = \frac{E_s^2 t^3}{6 p^2 \beta^2} \quad \text{C.5.}$$

which is the total overall possible scattered angles, then using this value of y to select an angle δ from another gaussian distribution having a standard deviation $\sigma_{\delta y}$ and a mean value of $3y/2t$ as given in equations C.4 and C.3 respectively. In this way particles can be followed through the spectrograph and the co-ordinates found at the measuring levels. Clearly the method can also be extended to also include magnetic bending by adding, as well as the scattering increments, also the magnetic deflection increments as given in Appendix A, at each step. This method has been used to calculate the effect of scattering upon the deflections observed for different momenta. Events of given momenta were simulated in the spectrograph in the manner described, and the distributions in deflection (as defined in chapter 2) were calculated. These distributions were found

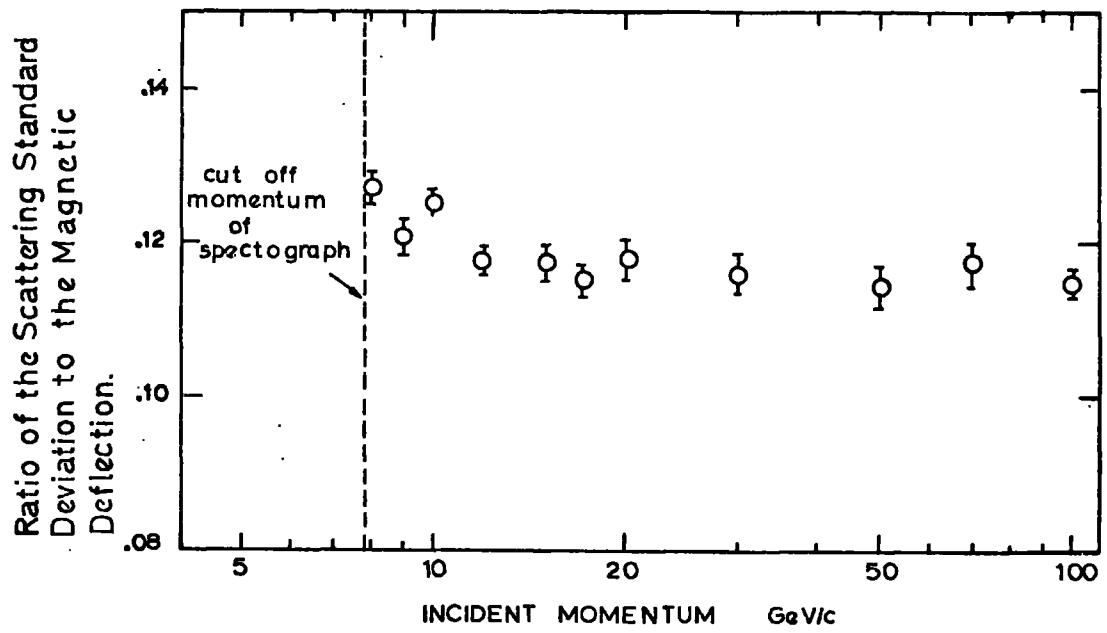


FIGURE C.1 The Effect of Multiple Scattering on the Deflection.

to be very closely gaussian centred upon the mean value observed without scattering. Figure C.1 shows values of the ratios of the scattering standard deviations to the magnetic deflections without scattering, where it can be seen that the ratio is very nearly independent of momentum, and has a value $12'$ at the mean momentum (~ 15 GeV/c) of the incident spectrum. Consequently the value of $12'$ has been used in the present work in calculating the effect on the spectrum in section 3.3.1. It is to be noted that the magnetic deflections used in calculating the data shown in figure C.1 were those corresponding to $(b-a) = 0$ whenever possible as explained in section 2.3.2., since these were the values used in the momentum deflection relation given in section 3.2.1. At the very low momenta (< 10 GeV/c) it is found that the case with $(b-a) = 0$ is not accepted by the spectrograph, and consequently the values of magnetic deflection used were those corresponding to the maximum in the variation^{of} acceptance with incidence angle. This however introduces negligible errors since at these low momenta, the variation of deflection with incident angle is very small.

ACKNOWLEDGMENTS

The author wishes to thank Professor G.D. Rochester, F.R.S., for the provision of the facilities for this work, and for his interest in the experiment.

He wishes to express his sincere gratitude for the help and guidance throughout this work given by his supervisor, Dr. M.C. Thompson, and also to Professor A.W. Wolfendale for many useful and helpful discussions.

Members of the MARS, both past and present, in particular Dr. C.A. Ayre, Dr. S.C. Wells, Mr. J.S. Hansen, and Mr. C.J. Hume, are thanked for their help, both in discussion and in the running of the apparatus.

The members of the Technical Staff of the Physics Department who have been active in this work, are thanked, particularly Mr. K. Tindale, the group's technician, and Mrs. A. Gregory for her help in the drawing of the diagrams for this thesis.

The Staff of the University Computer Unit are also thanked for the provision of their computing facilities.

The author is grateful to Mrs. S. Jobling for her conscientious and rapid typing of this thesis.

Finally the Science Research Council is thanked for providing a Research Studentship.

REFERENCES

- Abdel-Monem, M.S., Benbrook, J.R., Osborne, A.R., Sheldon, W.R., Duller, N.M., and Green, P.J., 1973, P.I.C.C.R., Denver, 2, 1811.
- Achar, C.V., Narasimham, V.S., Ramana Murthy, P.V., Creed, D.R., Pattison, J.M.B., and Wolfendale, A.W., 1965, Proc. Phys. Soc., 86, 1305.
- Allkofer, O.C., Dau, W.D., and Jokisch, H., 1970, Proc. 6th Interamerican Seminar on Cosmic Rays, La Paz, 937.
- Allkofer, O.C., Carstensen, K., and Dau, W.D., 1971, P.I.C.C.R., Hobart, 4, 1314.
- Allkofer, O.C., and Jokisch, H., 1972, Nuovo Cim., 15A, 371.
- Amineva, T.P., Cherdyntseva, K.V., Khristiansen, G.B., Dubrovina, S.A., Ivanenko, I.P., Ivannova, M.A., Kalmykov, N.N., Mandritskaya, K.V., Mursina, E.A., Nikol'sky, S.I., Osipova, E.A., Rakobolskaya, I.V., Sokolskaya, N.V., Varkovitskaya, A.Ya., and Zatsepin, G.T., 1971, P.I.C.C.R., Hobart, 6, 2387.
- Anderson, C.D., 1932, Science, 76, 238.
- Appleton, I.C., Hogue, M.T., and Rastin, B.C., 1971, Nucl. Phys., B26, 365.
- Ashton, F., Kamiya, Y., Mackeown, P.K., Osborne, J.L., Pattison, J.M.B., Ramana Murthy, P.V., and Wolfendale, A.W., 1966, Proc. Phys. Soc., 87, 79.
- Ashton, F., Tsuji, K., and Wolfendale, A.W., 1972, Nuovo Cim., 9B, 344.
- Ashton, F., Cooper, D.A., Parvaresh, A., and Saleh, A.J., 1973, P.I.C.C.R. Denver, 4, 2997.
- Aurela, A.M., 1965, Ph.D. Thesis, University of Durham.
- Aurela, A.M., and Wolfendale, A.W., 1967, Ann. Acad. Sci. Fenn., A6, 226.
- Ayre, C.A., and Thompson, M.G., 1969, Nucl. Inst. and Meth., 69, 106.
- Ayre, C.A., 1971, Ph.D. Thesis, University of Durham.
- Ayre, C.A., Hamdan, M.A., Hume, C.J., Thompson, M.G., Wells, S.C., Whalley, M.R., and Wolfendale, A.W., 1971(a), P.I.C.C.R., Hobart, 4, 1364.
- Ayre, C.A., Hamdan, M.A., Holroyd, F.W., Hume, C.J., Nandi, B.C., Thompson, M.G., Wells, S.C., Whalley, M.R., and Wolfendale, A.W., 1971(b), P.I.C.C.R., Hobart, 4, 1309.
- Ayre, C.A., Grupen, C., Hamdan, M.A., Hume, C.J., Thompson, M.G., Wells, S.C., and Wolfendale, A.W., 1971(c), P.I.C.C.R., Hobart, 4, 1447.
- Ayre, C.A., Hamdan, M.A., Hume, C.J., Stubbs, F.W., Thompson, M.G., Wells, S.C., and Whalley, M.R., 1972(a), Nucl. Inst. and Meth., 102, 12.
- Ayre, C.A., Hamdan, M.A., Hume, C.J., Nandi, B.C., Thompson, M.G., Wells, S.C., and Whalley, M.R., 1972(b), Nucl. Inst. and Meth., 102, 29.
- Ayre, C.A., Thompson, M.G., Whalley, M.R., and Young, E.C., 1972(c), Nucl. Inst. and Meth., 103, 49.

- Ayre, C.A., Baxendale, J.M., Daniel, B.J., Hume, C.J., Thompson, H.G., Whalley, M.R., and Wolfendale, A.W., 1973, P.I.C.C.R., Denver, 3, 1754.
- Baber, S.R., Nash, W.F., and Rastin, B.C., 1968, Nucl. Phys., B4, 539.
- Baradzei, L.T., Kanevskaya, E.A., Smorodin, Yu. A., and Solviev, M.V., 1971, P.I.C.C.R., Hobart, 6, 2397.
- Barrett, P.H., Bollinger, L.M., Cocconi, G., Eisenberg, Y., and Greisen, K., 1952, Rev. Mod. Phys., 24, 133.
- Bateman, B.J., Cantrell, W.G., Durda, D.R., Duller, H.M., Green, P.J., Jelinek, A.V., Nagy, T.A., and Sheldon, W.R., 1971, Phys. Lett., 36B, 144.
- de Beer, J.F., Holyoak, B., Wdowczyk, J., and Wolfendale, A.W., 1966, Proc. Phys. Soc., 89, 567.
- Bergeson, H.E., Keuffel, J.W., Larson, M.O., Martin, E.R., Masen, G.W., and Sternerson, R.D., 1968, Canad. J. Phys., 46, S399.
- Bertin, A., Capiluppi, P., D'Agostino-Bruno, M., Ellis, R.J., Giacomelli, G., Rossi, A.M., Vannini, G., Bussiere, A., and Poe, R.T., 1972, Phys. Lett., 41B, 201.
- Bothe, W., and Kolhorster, W., 1929, Zeits. Phys., 56, 751.
- Bull, R.M., Nash, W.F., and Rastin, B.C., 1965, Nuovo Cim., 40A, 365.
- Burnett, T.H., Masek, G.E., Maung, T., Miller, E.S., Ruderman, H., and Vernon, W., 1973, P.I.C.C.R., Denver, 3, 1764.
- Caro, D.E., Parry, J.K., and Rathgeber, H.D., 1951, Aust. J. Sci. Res., A4, 16.
- Chin, S., Hanayama, Y., Hara, T., Higashi, S., Kitamura, T., Miono, S., Nakagawa, M., Ozaki, S., Takahashi, T., Tsuji, K., Watase, V., Kobayakawa, K., and Shibata, H., 1969, P.I.C.C.R., Budapest, 4, 65.
- Coates, R.B., 1967, Ph.D. Thesis, University of Durham.
- Cocconi, G., Koester, L.J., and Perkins, D.H., 1961, Lawrence Radiation Lab. High Energy Physics Study Seminars No. 28 pt.2.
- Conversi, M., and Gozzini, A., 1955, Nuovo Cim, 2, 189.
- Crookes, J.N., and Rastin, B.C., 1971, P.I.C.C.R., Hobart, 4, 1369.
- De, A.K., Ghosh, P., Mitra, S., Bhattacharya, P.C., and Das, A.K., 1972, J. Phys. A : Gen.Phys., 5, 1236.
- Duthie, J., Fowler, P.H., Kaddoura, A., Perkins, D.H., and Pinkau, K., 1962, Nuovo Cim, 24, 122.
- Erlykin, A.D., Kulichenko, A.K., Machavariani, S.K., Maznichenko, S.S., and Meshkov, E.A., 1971, P.I.C.C.R., Hobart, 6, 2142.
- Erlykin, A.D., Kulichenko, A.K., Machavariani, S.K., and Nikdsky, S.I., 1973, P.I.C.C.R., Denver, 3, 1803.

- Fähnders, E., 1971, Diplomarbeit, University of Kiel, W. Germany.
- Feynman, R.P., 1969, Phys. Rev. Lett., 23, 1415.
- Fowler, G.N., and Wolfendale, A.W., 1961, Handb. der Phys., 46, 272.
- Fowler, P.H., Adams, R.A., Cowen, V.G., and Kidd, J.M., 1967, Proc. Roy. Soc. (London), 301A, 39.
- Gardener, M., Jones, D.G., Taylor, F.E., and Wolfendale, A.W., 1962, Proc. Phys. Soc., 80, 697.
- Greisen K., 1965, P.I.C.C.R., London, 2, 609.
- Greisen K., 1966, Phys. Rev. Lett., 16, 748.
- Grigorov, N.L., Mamontova, N.A., Rapoport, I.D., Savenko, I.A., Akimov, V.V., and Nesterov, V.E., 1971, P.I.C.C.R., Hobart, 5, 1752.
- Grupen, C., Hamdan, M.A., Hansen, S., Thompson, M.G., Wolfendale, A.W., and Young, E.C.M., 1972, J. Phys. A: Gen. Phys., 5, 1713.
- Hamdan, M.A., 1972, Ph.D. Thesis, University of Durham.
- Hayman, P.J., and Wolfendale, A.W., 1962, Proc. Phys. Soc., 80, 710.
- Hayman, P.J., Palmer, N.S., and Wolfendale, A.W., 1963, Proc. Roy. Soc., 275A, 391.
- Hess, V.F., 1912, Phys. Zeitschr., 13, 1084.
- Holmes, J.E.R., Owen, B.G., and Rodgers, A.L., 1961, Proc. Phys. Soc., 78, 505.
- Hume, C.J., Nandi, B.C., Thompson, M.G., Whalley, M.R., and Wolfendale, A.W., 1973, J. Phys. A: Gen. Phys., 6, 673.
- Jacob, M., 1973, CERN Report ref. TH.1639-CERN.
- Johnson, T.H., 1938, Rev. Mod. Phys, 10, 193.
- Johnson, T.H., and Street, J.C., 1933, Phys. Rev., 43, 381.
- Khrishnaswamy, M.R., Menon, M.G.K., Narasimham, V.S., Hinotani, K., Ito, N., Miyake, S., Osborne, J.L., Parsons, A.J., and Wolfendale, A.W., 1971, Proc. Roy. Soc. (London), A323, 511.
- Koenig, H.P., Phys. Rev., 1946, 69, 590,
- Krasilnikov, D.D., Skripin, G.V., Chirkov, N.P., and Shafer, G.V., 1971, P.I.C.C.R., Hobart, 6, 2421.
- Lattes, C.M.G., Muirhead, H., Occhialini, G.P.S., and Powell, C.F., 1947, Nature, London, 159, 694.
- Menon, M.G.K., and Ramana Murthy, P.V., 1967, Prog. in Elem. Part. and Cosmic Ray Phys., 9, 161.
- Meyer, B.S., Sellschop, J.P.F., Crouch, M.F., Kropp, W.R., Sobel H.W., Curr, H.S., Lathrop, J., and Reines, F., 1970, Phys. Rev. D., 1, 2229.

- Miyake, S., Narasimham, V.S., and Ramana Murthy, P.V., 1964, Nuovo Cim., 32, 1505, and 1524.
- Mizutani, K., Shirani, T., Akashi, M., and Watanabe, Z., 1971, P.I.C.C.R., Hobart, 4, 1392.
- Nandi, B.C., and Sinha, M.S., 1972, J. Phys. A: Gen. Phys., 5, 1384.
- Ng, L.K., Wdowczyk, J., and Wolfendale, A.W., 1973(a), P.I.C.C.R., Denver, 3, 1781.
- Ng, L.K., Wdowczyk, J., and Wolfendale, A.W., 1973(b), Internal Communication, University of Durham.
- Osborne, J.L., Palmer, N.S., and Wolfendale, A.W., 1964, Proc. Phys. Soc., 84, 911.
- Osborne, J.L., 1966, Ph.D. Thesis, University of Durham.
- Owen, B.C., and Wilson, J.G., 1955, Proc. Phys. Soc., A68, 409.
- Pak, W., Ozaki, S., Roe, B.P., and Greisen, K., 1961, Phys. Rev., 121, 905.
- Pine, J., Davisson, R.J., and Greisen, K., 1959, Nuovo Cim., 14, 1181.
- Rochester, G.D., and Butler, C.C., 1947, Nature (London), 160, 855.
- Roll, P.G., and Wilkinson, D.T., 1967, Ann. Phys. (U.S.A.), 44, 289.
- Rossi, B., and Greisen, K., 1942, Rev. Mod. Phys., 13, 240.
- Rossi, B., 1948, Rev. Mod. Phys., 20, 537.
- Rossi, B., 1952, "High Energy Particles" (Prentice-Hall).
- Ryan, M.J., Ormes, J.F., and Balasubrahmanyam, V.K., 1972, Phys. Rev. Lett., 28, 985.
- Smith, J.A., and Duller, N.M., 1959, J. Geophys. Res., 64, 2297.
- Sternheimer, R.M., 1956, Phys. Rev., 103, 511.
- Suga, K., Sakuyama, H., Kawaguchi, S., and Hara, T., 1971, P.I.C.C.R., Hobart, 1, 2742.
- Wright, A., 1973(a), P.I.C.C.R., Denver, 3, 1709.
- Wright, A., 1973(b), Private Communication.
- Wdowczyk, J., and Wolfendale, A.W., 1973, J. Phys. A : Gen. Phys., 6, 1594.
- (P.I.C.C.R. = Proc. Int. Conf. on Cosmic Rays)

